Sources, spatio-temporal variation and co-variability of cloud condensation nuclei and black carbon

Von der Fakultät für Physik und Geowissenschaften
der Universität Leipzig
genehmigte

Dissertation

zur Erlangung des Grades
Doktor rerum naturalium
Dr. rer. nat.

vorgelegt von

M. Sc. RWTH, Ovid Oktavian Krüger
geboren am 30.11.1990 in Weilburg

Gutachter: Prof. Dr. Johannes Quaas
Prof. Dr. Ulrich Pöschl

Tag der Verleihung 25. September 2023

UNIVERSITÄT
LEIPZIG

MAX PLANCK INSTITUTE
FOR CHEMISTRY

Diese Arbeit wurde angefertigt zwischen 01.08.2018 und 30.05.2023
am Max-Planck-Institut für Chemie,
Abteilung Multiphasenchemie,
Hahn-Meitner-Weg 1,
55128 Mainz.

Diese Arbeit wurde betreut von
Prof. Dr. Mira Pöhlker und Prof. Dr. Johannes Quaas.

1. Berichterstatter: Prof. Dr. Johannes Quaas
2. Berichterstatter: Prof. Dr. Ulrich Pöschl

Prüfungskomitee:
Jun.-Prof. Dr. Heike Kalesse-Los (Vorsitzende)
Prof. Dr. Johannes Quaas (Betreuer)
Prof. Dr. Manfred Wendisch

Bibliographische Beschreibung

Bibliographische Beschreibung

Ursprünge, räumlich-zeitliche Variation und Co-Variabilität von Wolkenkondensationskeimen und Ruß
Krüger, Ovid Oktavian
Universität Leipzig, Dissertation
150 Seiten, 273 Literaturzitate, 58 Abbildungen, 7 Tabellen.

Referat Die Wechselwirkung von Aerosolen mit Wolken und Strahlung hängt von einer Reihe von Faktoren ab, wie den physikalisch-chemischen Eigenschaften, der geographischen und zeitlichen Variabilität und der vertikalen Verteilung der atmosphärischen Aerosole. Von besonderer Bedeutung sind Wolkenkondensationskeime (CCN) und schwarze Kohlenstoffpartikel (BC) als Untergruppen der atmosphärischen Aerosolpopulation. CCNs sind eine Voraussetzung für die Bildung von Wolkentröpfchen, und Variationen im CCN-Budget können die Wolkeneigenschaften verändern. BC kann Sonnenstrahlung effizient absorbieren, lokale Erwärmung verursachen und die Wolkenbildung hemmen. Um die Auswirkungen von CCN und BC auf Wolken und den Energiehaushalt der Erde zu bestimmen, sind die atmosphärischen Konzentrationen und ihre räumlich-zeitliche Verteilung von großer Bedeutung. Deshalb befasst sich diese Dissertation mit der geographischen, zeitlichen und vertikalen Variabilität des atmosphärischen Aerosols und den Zusammenhängen zwischen CCN und BC und trägt dazu bei, diese anhand umfangreicher Felddaten aus flugzeug- und bodengestützten Messungen zu verstehen. Die Datenanalyse konzentriert sich auf anthropogene Verschmutzung, Waldbrandemissionen und vulkanische Aerosole.

Im Anthropozän hat sich sowohl die Verteilung als auch die Konzentration von Aerosolen drastisch verändert. Die Hauptquelle anthropogener Feinstaubbelastung ist die Verbrennung fossiler Brennstoffe und Biokraftstoffe. Die allgegenwärtige anthropogene Luftverschmutzung, insbesondere über den kontinentalen Regionen der nördlichen Hemisphäre, erschwert die Bewertung des anthropogenen Einflusses auf Aerosole und Klima, da ungestörte Referenzmessungen fehlen. Der abrupte Rückgang menschlicher Aktivitäten während der ersten COVID-19 Lockdowns schuf beispiellose atmosphärische Bedingungen, die es uns ermöglichten, Änderungen der troposphärischen Zusammensetzung als Reaktion auf Änderungen anthropogener Emissionen zu untersuchen und zu quantifizieren. Die Ergebnisse zeigen den starken und direkten Einfluss menschlicher Aktivitäten auf die Luftqualität, die Rolle von BC als wichtiger Luftschadstoff im Anthropozän und die enge Beziehung zwischen den atmosphärischen Konzentrationen von CCN und BC.

Messdaten von fünf Flugzeugmissionen zeigen charakteristische Beziehungen zwischen CCN und BC in städtischem Feinstaub über Europa und Ostasien, hochgealtertem Biomasseverbrennungsrauch über dem tropischen Atlantik und dem Amazonas-Regenwald und leicht gealtertem Biomasseverbrennungsrauch über Europa, Brasilien und Asien. Über Europa und Asien ist die vertikale Verteilung von CCN in der unteren Troposphäre bis zu einer Höhe von etwa 5 km sehr empfindlich auf regionale anthropogene Emissionen. Über dem tropischen Atlantik wird die vertikale Verteilung stark durch den Ferntransport von Mineralstaub und Rauch aus der Verbrennung von Biomasse beeinflusst, aber auch Vulkanausbrüche tragen zur Aerosolbelastung bei.

Bibliographic description

Bibliographic description

Sources, spatio-temporal variation and co-variability of cloud condensation nuclei and black carbon
Krüger, Ovid Oktavian
Leipzig University, dissertation
150 pages, 273 references, 58 figures, 7 tables.

Abstract Aerosol-cloud and aerosol-radiation interactions depend on several factors such as the physico-chemical properties, geographical and temporal variability, and vertical distribution of atmospheric aerosols. Of particular importance are cloud condensation nuclei (CCN) and black carbon (BC) particles as a subset of the atmospheric aerosol population. CCN are a prerequisite for cloud droplet formation, and variations in CCN loading can modify cloud properties. BC can efficiently absorb solar radiation, induce local heating and inhibit cloud formation. In order to determine the effects of CCN and BC on clouds, precipitation, radiation and the Earth's energy budget, atmospheric loading and spatio-temporal distribution of aerosols are highly relevant. Thus this dissertation addresses and helps to elucidate the spatio-temporal variation and co-variability of CCN and BC with extensive field measurement data from aircraft and ground-based measurements. The data analyses focus on anthropogenic pollution, wildfire emissions and volcanic aerosols.

In the Anthropocene, the distribution and abundance of atmospheric aerosols have changed drastically. Major sources of anthropogenic particulate pollution are the combustion of fossil fuels and biofuels as well as emissions from open biomass burning. The ubiquitous presence of anthropogenic air pollution, especially over continental regions in the Northern Hemisphere, hampers the assessment of anthropogenic influence on aerosol and climate due to a lack of unperturbed reference measurements. The abrupt reduction in human activities during the first COVID-19 lockdown created unprecedented atmospheric conditions that allowed us to investigate and quantify changes in the tropospheric composition in response to changes in anthropogenic emissions. The results reflect a strong and immediate influence of human activities on air quality, the role of BC as a major air pollutant in the Anthropocene, and close links between the atmospheric burdens of CCN and BC.

Measurement data from five aircraft missions in polluted environments reveal characteristic relationships between CCN and BC in urban haze from Europe and East Asia, highly aged biomass burning smoke over the tropical Atlantic and the Amazon rainforest, and lightly aged biomass burning smoke over Europe, Brazil, and Asia. Over Europe and Asia, the vertical distribution of CCN in the lower troposphere up to altitudes about 5 km is highly sensitive to regional anthropogenic emissions. Over the tropical Atlantic ocean, the vertical distribution is strongly influenced by the long-range transport of mineral dust and biomass burning smoke, but volcanic eruptions also contribute to the aerosol load.

Contents

CHAPTER 1

Introduction

1.1 Perturbed atmosphere in the Anthropocene

At the latest since industrialisation human actions have exerted profound and manifold influences on the atmosphere and environment. The fast growth in human population and economic activities as well as a general increasing wealth boosted global energy, food and goods demand. To meet these immense demands, humanity became a major geological force on Earth (Monastersky, 2015). This includes the rapid transformation of the biosphere for food and energy production as well as the exploitation of fossil energy resources and natural resources. Especially the deforestation and transformation of wetlands into cropland and the combustion of fossil fuels caused a rapid and unprecedented increase in atmospheric greenhouse gas concentrations in Earth's records. The changed atmospheric composition is most prominent in carbon dioxide, but also other trace gases as methane and nitrous oxide increased drastically, as well as the aerosol burden. The increased greenhouse gas and aerosol burden are associated with climate system adjustments and caused the well recorded increasing trend in global temperatures (e.g., Szopa et al., 2021). As these changes are dominated by human activities, the current epoch has been termed the Anthropocene (Steffen et al., 2011).

1.2 Aerosols and their climate impact

Aerosols are a major constituent of global change. In addition to their importance for the climate, they also play key roles in public health as a major air pollutant and are accountable for millions of premature deaths (e.g., Lelieveld et al., 2019b). Aerosols only remain in the atmosphere for relatively short periods. Thus, the geographical and vertical distribution are highly variable and sensitive to emission sources, both in the temporal and the spatial dimension. Differently, the most relevant greenhouse gases have atmospheric residence times in the range of years, decades or even centuries and are therefore termed long-lived climate forcers. The long residence time leads to a relatively equal distribution in the atmosphere and well predicable variability in their vertical and geographical distribution. The distinct variability in the distribution of aerosol engenders the need for in situ measurements at different locations around the globe covering both the vertical and spatial variability, while long-term measurements can help to better understand the temporal variability.

Atmospheric aerosol are liquid or solid particles suspended in air (Seinfeld and Pandis, 2006). They can be natural aerosols, such as sea spray, mineral dust, biological particles and sulfates from the oxidation of carbonyl and dimethyl sulfide, or volcanic sulfur dioxide which dominated the pre-industrial atmospheric aerosol burden (Andreae, 2007; Després et al., 2012; Kremser et al., 2016). However, the industrialization greatly enhanced the number and strength of aerosol sources worldwide (e.g., Andreae, 2009; Carslaw et al., 2017; Crutzen, 2006). Combustion of biomass and fossil fuels has become an aerosol source of particular importance as it is the basis for energy production, mobility and land clearing and management in agricul-

ture (e.g., Bond et al., 2013; Ramanathan and Carmichael, 2008). Thereby, large amounts of primary particulate pollutants, such as black and brown carbon are emitted directly into the boundary layer. In addition, fuel combustion also emits gaseous pollutants such as aerosol precursor gases. This anthropogenic particulate pollution can be distributed over thousands of kilometers by large-scale atmospheric circulations. Thus, there are only a few places on Earth unperturbed by human aerosols (Andreae, 2007), while anthropogenic greenhouse gas emissions influence the atmosphere globally.

Generally, aerosol concentrations within the planetary boundary layer over continents exceed concentrations over oceans. Aerosol can be emitted directly into the atmosphere, referred to as primary aerosol, or form as secondary aerosol by oxidation and clustering of gaseous precursor substances. Thereby, the sizes of atmospherically relevant aerosol span from a few nanometer up to hundreds of micrometer (e.g., Pöhlker et al., 2021; Seinfeld and Pandis, 2006). The size distribution of the atmospheric aerosol burden has typically one or several maxima at distinct size ranges. The mono- or multimodal structure of the aerosol size distribution reflects the aerosol source and sinks as well as aerosol dynamics and chemical processing. The most important processes in aerosol physics are nucleation, coagulation, condensation and evaporation. Condensation and evaporation keep particle number concentrations conserved with changing mass fluxes, particle coagulation has a conserved aerosol mass while the number concentration reduces (e.g., Ketzel and Berkowicz, 2004). Nucleation, however, leads to variations in both aerosol mass and number concentration. The smallest mode of the aerosol size distribution is called nucleation mode and consists of particles after they have been formed through oxidation and subsequent nucleation of precursor gases, such as volatile organic compounds (Hallquist et al., 2009; Kulmala, 2003). Aerosol at diameters larger than $\sim 10\,\mathrm{nm}$ is counted among the Aitken mode. The growth in the Aitken mode is driven by condensation and partly by coagulation. Particles with diameters exceeding $100\,\mathrm{nm}$ account for the accumulation mode. These three modes have the highest relevance for aerosol number concentrations, whereas aerosol larger than $1\,\mu\mathrm{m}$, also referred to as coarse mode, tend to dominate the aerosol mass concentration (e.g., Seinfeld and Pandis, 2006).

During their atmospheric residence time, particles interact with solar radiation and reactive atmospheric constituents. In this process, they undergo complex physical and chemical transformations, also referred to as aerosol aging. Aerosol aging can alter the initial size, shape, and composition, with significant impacts on their atmospheric importance (Pöschl, 2005). The typical atmospheric residence times of airborne aerosol ranges from days to weeks in the troposphere. Stratospheric aerosol, however, can remain airborne for months up to several years (Kremser et al., 2016). For sub-micrometer aerosol there are two major scavenging processes: Wet deposition, which can happen in-cloud, where aerosols are nucleated and subsequently grow to large droplets and rain out or below-cloud, where precipitation can wash out aerosol by impaction. Therefore this process is also referred to as impaction scavenging, a major removal process for black carbon (BC) and other hydrophobic aerosol (Ohata et al., 2016). Another atmospheric removal pathway is dry deposition, by either sedimentation of larger particles or diffusion.

Before-mentioned processes outline the removal of aerosol from the atmosphere, however, coagulation can also decrease the number concentration of aerosol. Coa-

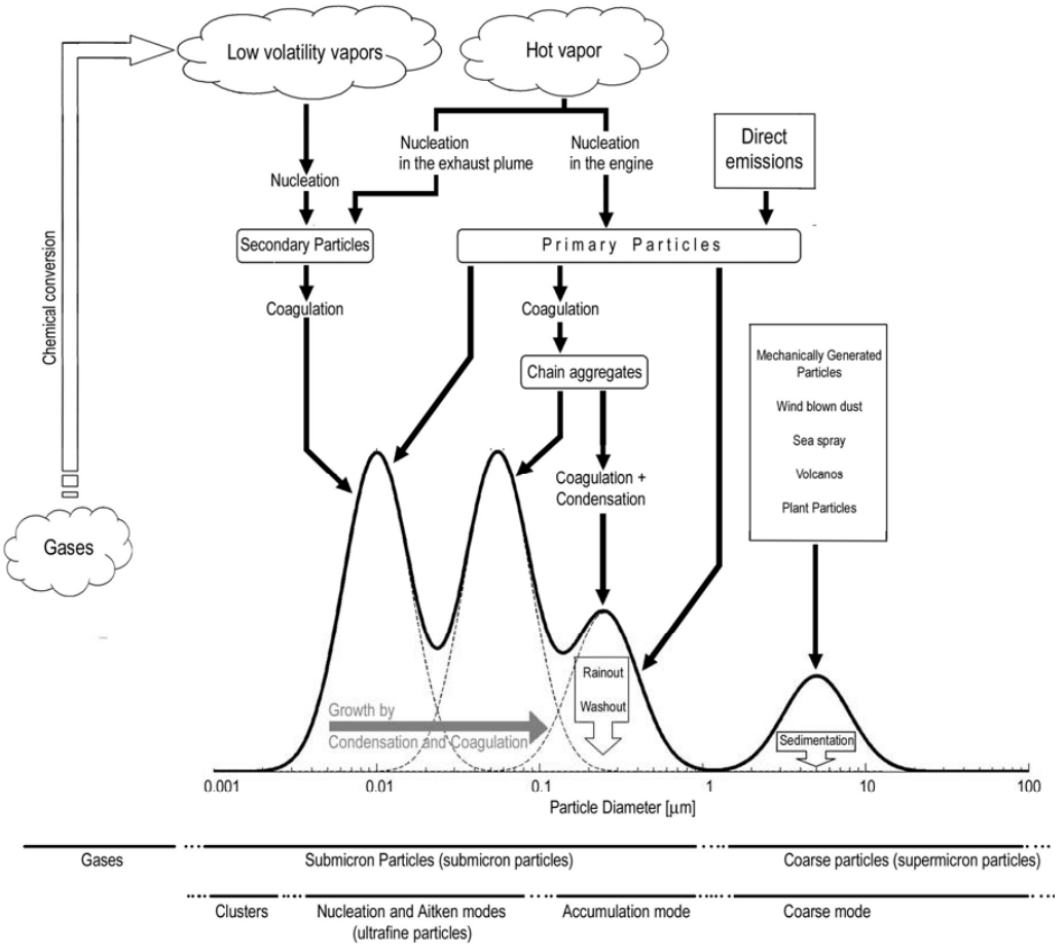

Figure 1.1: Figure from Hussein, 2005 Aerosol life cycle for anthropogenic pollution with formation and transformation processes.

lescence is especially important in decreasing the number of smaller particles with diameters below $\sim 50\,\mathrm{nm}$ (e.g., Birmili and Hoffmann, 2006). Thereby, aerosols coagulate with each other, altering the number concentration whilst the aerosol mass concentration remains conserved (e.g., Ketzel and Berkowicz, 2004). Coalescence is also of great relevance for the formation of particle agglomerations close to the particle sources, such as in vehicle exhausts (Ketzel and Berkowicz, 2004; Pohjola et al., 2003; Vignati et al., 1999).

Aerosol residence times and deposition, however, are not only highly relevant for atmospheric chemistry and physics, but they are also proven to be of crucial importance in the transmission of respiratory aerosol carried pathogens and generally for hygienic indoor air conditions (e.g., Pöhlker et al., 2021). Globally, the population density of humans is increasing and, thus, the likelihood of disease transmission between individuals as well. At the same time, our understanding and awareness of efficient preventive measures increased, too (e.g., Pöhlker et al., 2021). Due to relatively low relative humidity and stable thermodynamic conditions, for aerosol driven pathogen transmission, dry deposition from diffusion and sedimentation are the most relevant sinks. However, neither are of great importance for the transmission of airborne pathogens due to small aerosol size. Meanwhile, the diffusion of smaller particles and impaction of larger aerosols can be highly efficient in the hu-

man respiratory tract (e.g., Pöhlker et al., 2021). Therefore, to prevent human to human infections with airborne pathogens, a good ventilation (e.g., Helleis et al., 2023) and efficient filtration (e.g., Bagheri et al., 2021; Cheng et al., 2021) should be the measures of choice.

In the climate system, aerosols play a fundamental role (e.g., Andreae and Crutzen, 1997; Bellouin et al., 2020; Szopa et al., 2021). They scatter and absorb solar and terrestrial radiation and therefore alter the energy balance directly. This interplay of aerosol with radiation is termed direct radiative effect or aerosol radiation interactions (ARI) (Boucher et al., 2013). The absorption and scattering efficiency depends on several factors. The wavelength of the radiation and the particle size determine the way of scattering. For aerosol in a size rage comparable to the radiation wavelength, Mie scattering is the prevailing scattering (Bohren and Huffman, 1998). For particles much smaller than the wavelength, Rayleigh scattering dominates (Bohren and Huffman, 1998). Also, the particles' shape and refractive index, determined by the aerosol source, chemical composition, atmospheric aging and mixing state influence ARI (Bohren and Huffman, 1998; Hansen and Travis, 1974). Scattering and absorption of aerosol contribute to the extinction of radiation. Thereby, aerosols induce a rapid adjustment in the vertical and spatial distribution of radiative fluxes and heating rates with significant impacts on temperature and water vapor profiles, the atmospheric stability, and consequently cloud formation (Koch and Del Genio, 2010; Samset and Myhre, 2015; Stjern et al., 2017). In addition to the semi-direct effect on clouds as described above, aerosols also provide a necessary surface area for water vapor condensation and thereby affect clouds directly through aerosol-cloud interactions (ACI), inducing an indirect forcing on the climate system (Boucher et al., 2013; Mülmenstädt and Feingold, 2018). A subset of atmospheric aerosols act as cloud condensation nuclei (CCN) or ice nuclei (IN) and, thus, influence the cloud droplet number and size distribution, referred to as cloud microphysics, but also the cloud albedo and lifetime, which is counted among the cloud macrophysics (Ackerman et al., 2000; Andreae and Rosenfeld, 2008; Rosenfeld et al., 2014; Rosenfeld et al., 2008a; Twomey, 1974; Twomey, 1977).

1.2.1 Aerosol-radiation interactions

As pointed out before, for ARI, a general distinction between two aerosol types is reasonable. First, aerosol where the scattering of incoming shortwave solar radiation dominates and second, aerosol with a dark and thus absorbing surface which absorbs and scatters solar radiation. The different mechanisms and aerosol types will be outlined in the following.

Dominantly scattering aerosols have manifold sources. They can be emitted either directly into the atmosphere as primary aerosol or they are secondary formed from precursor gases. The formation of secondary aerosol can happen in different altitudes based on the precursor gases and atmospheric conditions. Secondary aerosol can form in highly polluted environments, such as major metropolis and industrial hot spots, however, also in clean and unperturbed atmospheric conditions, such as the upper troposphere or large forests (e.g., Andreae et al., 2018; Brock et al., 1995; Kerminen et al., 2018; Kulmala et al., 2013; Lee et al., 2019). Regions where new particle formation is not well understood are the Amazon rain forest where ongoing research tries to find the location of particle nucleation in order to fundamentally

understand how the aerosol burden in a nearly pristine environment is maintained (Andreae et al., 2018). This knowledge is essential to understanding the impact of the ongoing deforestation on the rain forest aerosol burden and hydrological cycle and thus to understanding the ecosystem atmospheric coupling and resilience.

Besides the overall cooling due to scattering of solar radiation back to space, aerosols such as black and brown carbon or some mineral and industrial dusts also absorb incoming solar radiation, leading to a sensitive heat flux from these aerosols.

Black carbon as a major constituent of the subset of absorbing aerosol receives special attention in the scope of this thesis. It exclusively originates in processes of incomplete combustion by the clustering of graphene spheres (Frenklach and Mebel, 2020; Johansson et al., 2018). However, the inception and growth from gaseous polycyclic aromatic hydrocarbons (PAHs), formed in pyrolysis of fuel, to soot remains uncertain (e.g., Frenklach and Mebel, 2020; Howard, 1992; Johansson et al., 2018; Thomson and Mitra, 2018). Albeit the formation of BC is not fully understood to date, it is non-controversial that the accumulated graphene spheres after coagulation are emitted as BC aerosol directly into the atmosphere as the major absorbing species for short-wave radiation, significantly affecting Earth energy balance (Andreae and Ramanathan, 2013; Bond et al., 2013; Ramanathan and Carmichael, 2008; Szopa et al., 2021). A large fraction of atmospheric BC originates from anthropogenic sources (Bond et al., 2013). Pure BC is insoluble in water and chemically inert in the atmosphere (Bond et al., 2013; Sedlacek et al., 2022). According to the most recent assessment report of the Intergovernmental Panel on Climate Change (IPCC), the best estimate of industrial-era climate forcing of BC is $+0.063\,\mathrm{W\,m^{-2}}$, with an uncertainty spanning from -0.28 to $+0.42\,\mathrm{W\,m^{-2}}$ (Szopa et al., 2021; Thornhill et al., 2021).

The distribution of BC is highly heterogeneous in space and time, inducing large uncertainties in assessing its influence on the climate system (Laj et al., 2020). Further, also the physicochemical properties of BC vary during atmospheric aging and thereby influence radiative properties. Condensation of semivolatile gases on the BC surface as well as coagulation with aerosols alter the morphology and mixing state of BC. Both condensation and coagulation can lead to a surface coating of the BC aerosol, resulting in an enhanced absorption of solar radiation (Cappa et al., 2012; Fuller et al., 1999; Yuan et al., 2021). The coating and the external mixing of BC with more hydrophilic species may also lead to a stronger interaction with water vapor and potential activation as CCN (Liu et al., 2013; Zuberi et al., 2005).

Absorption of radiation leads to local sensitive heating and thus perturbs the temperature structure of the atmosphere, with a potential influence on the cloud cover. The effect, however, can have different directions and strongly depends on the altitude of the absorbing aerosol relative to the cloud and the cloud type. Koch and Del Genio, 2010 summarizes the effects as following: The cloud cover decreases with absorbing aerosol embedded in the cloud layer, whereas absorbing aerosols below clouds tend to enhance convection and the cloud cover. Both aforementioned scenarios are typical for urban pollution which is emitted with rather low thermal energy and from a larger spatial area. Therefore it remains within the planetary boundary layer and in its transition zone (e.g., Hernández et al., 2022). In contrast to that, smoke from biomass burning tends to be lifted above the boundary layer (e.g., Holanda et al., 2020; Krüger et al., 2022; Ohneiser et al., 2020; Ohneiser et al., 2022; Zhang et al.,

2019), and thus the absorption layer is located above cloud top and tends to stabilize the underlying atmosphere and therefore to enhance stratocumulus and potentially reduce cumulus clouds. Also, a potential brightening on the stratocumulus by entrained aerosol from biomass burning layers over the Atlantic is reported (Lu et al., 2018). The effects of absorbing aerosol on cloud cover, however, tend to have large regional variability. Also, the interactions of absorbing aerosol and clouds remain uncertain to date, however, improvements in model- and observational constraints are made (Allen et al., 2019). Overall, there is generally a net negative semi-direct feedback from the cloud cover response (Koch and Del Genio, 2010).

1.2.2 Aerosol-cloud interactions

Besides its direct effect on radiation and semi-direct effect on cloud coverage, aerosols are a major driver of cloud variability and a prerequisite for cloud formation at atmospheric conditions. The cooling induced by ACI exceeds the direct radiative effects (Szopa et al., 2021), however, due to the larger diameters of cloud droplets and ice crystals there is also absorption of long-wave terrestrial radiation. The interactions with long-wave radiation induce a warming of the atmosphere, whereas the overall ACI induces a cooling of the atmosphere (Szopa et al., 2021). The potential importance of ACI effects on cloud radiative forcing is especially relevant in shallow marine cloud systems where the clouds have an albedo tenfold larger than that of the ocean surface (Stevens and Feingold, 2009).

Water vapor in the atmosphere needs a surface to condense on and form a liquid water droplet. A subset of aerosols can provide this surface and acts as nuclei for cloud droplets and ice crystals. Generally, homogeneous nucleation of water vapor to cloud droplets is possible, however, the supersaturation needed would exceed atmospheric conditions (e.g., Krüger et al., 2014) and thus is neglectable. For ice crystals in cirrus clouds, on the other hand, homogeneous nucleation of aqueous solution droplets is a common pathway (Kärcher and Lohmann, 2002).

The existence of aerosol is not only necessary for cloud droplet formation, it also alters cloud micro- and macrophysics, such as the clouds latent heat release vertical profile, dynamic evolution, and precipitation onset (e.g., Albrecht, 1989; Andreae et al., 2004; Martins et al., 2011; Ramanathan et al., 2001; Rosenfeld et al., 2008b; Squires, 1958). Aerosol introduced microphysical changes on clouds can be a cloud brightening and therefore an increased cloud albedo (i.e., the fraction of solar radiative energy reflected back to space relative to the incoming radiation on cloud top Quaas et al., 2020). This cloud albedo effect, also referred to as Twomey effect, can also lead to changed cloud lifetimes due to reduced precipitation efficiency (e.g., Albrecht, 1989; Squires, 1958; Twomey, 1977). The cloud albedo responds to increased aerosol loads with an increase in cloud droplet number concentration (N_d), leading to smaller droplets (Albrecht, 1989; Twomey, 1977). The combination of smaller but more N_d in unchanged thermodynamic and atmospheric conditions lead to more reflective clouds (Twomey, 1977). The smaller but more N_d not solely change the cloud albedo, they also influence the onset of precipitation. The precipitation efficiency is reduced for shallow clouds with increased aerosol concentrations (e.g., Albrecht, 1989; Andreae and Rosenfeld, 2008; Penner et al., 2004; Rosenfeld, 2000), while deep convective clouds react nonlinear and highly depend on meteorology and enhanced aerosol burdens (Campos Braga et al., 2021; Khain et al., 2008;

Rosenfeld et al., 2008b). The later onset of precipitation increases cloud lifetimes and tends to shift precipitation onset into higher altitudes and regions, while low-level rainout is suppressed (Andreae et al., 2004; Feingold, 2005; Lin et al., 2006). The changed precipitation patterns due to ACI not only affect the radiative balance, but can also substantially affect ecosystems and the hydrosphere (Ramanathan et al., 2001; Trenberth, 2011).

A subset of aerosol, called cloud condensation nuclei (CCN), can provide a surface area or solutes to initiate the condensation of water vapor and thus droplet formation in the atmosphere. To initiate droplet nucleation, the solid CCN must be either soluble in water or have sufficient size and a hydrophilic surface. Thereby the size of the CCN tends to dominate the CCN characteristics of an aerosol (Dusek et al., 2006). But also aqueous and thus liquid aerosol, such as aqueous sulfate aerosol, can serve as CCN if it is large enough (Petters and Kreidenweis, 2007).

Generally, for droplet growth, condensation on the CCN needs to exceed evaporation. The Köhler theory describes the CCN activity of an aerosol and can be separated thereby in two opposing drivers, the curvature and solute effects (Koehler et al., 2006; Kreidenweis et al., 2005). The curvature effect, described in the Kelvin term (1.1), is taking into account the surface tension of water over a curved surface, which describes the resulting equilibrium of an aqueous solution droplet with water vapor in the surrounding air (Koehler et al., 2006; Kreidenweis et al., 2005). Therefore, a higher supersaturation is necessary for the activation of smaller aerosols to droplets. It is assumed that the partial molar volume of water approximates the molar volume of pure water. Following the Kelvin term is as follows,

$$K_e = \exp\left(\frac{4\sigma_{sol} M_w}{\rho_w D_{wet} T R}\right) \tag{1.1}$$

for a spherical aqueous droplet with wet diameter D_{wet}. The surface tension of the solution droplet is $\sigma_s ol$, ρ_w and M_w are the molar density and mass of pure liquid water, T is the absolute temperature of the droplet, and R is the universal gas constant.

The solute effect in the Köhler theory is based on the slower evaporation rate of water molecules in a solution than in pure water due to the lower partial pressure as described in the Raoult's law. Therefore the solute effect is referred to as Raoult's term. In the process of droplet formation, watery solutions occur when water vapor condenses on CCN that fully or partly dissolve in the evolving water droplet. The solute effect can partially compensate the higher evaporation on small particles emerging from curvature effect and therefore allow smaller aerosol to serve as CCN.

$$s = a_w \cdot K_e \tag{1.2}$$

The water vapor saturation ratio, s, is the actual partial pressure of water to the equilibrium pressure over a flat surface of pure water. The relative humidity (RH) can be expressed by s in percent ($RH\% = (s - 1) \times 100\%$). Typically RH is used in water vapor sub-saturated conditions, whereas in supersaturated conditions the relative humidity is expressed as supersaturation ($S\% = RH\% - 100\%$, when $RH\% > 100\%$). To solve equation 1.2, information about the water activity of the solution

(a_w) constituting the droplet is needed. In Koehler et al., 2006 the water activity is described as follows,

$$a_w^{-1} = 1 + \nu\Phi\frac{n_s}{n_w}. \tag{1.3}$$

where n_s is the moles of solute, n_w is the moles of water, and Φ is the osmotic coefficient, which expresses the non-ideality of the solution. The number of ions each solute molecule dissociates into is ν, which indicates the molecular structure for complete dissociation under infinitely dilute conditions (Koehler et al., 2006). However, a_w can be approximated as (Kreidenweis et al., 2005; Petters and Kreidenweis, 2007; Rose et al., 2008),

$$a_w \approx \exp -\frac{B}{D_{wet}^3} \tag{1.4}$$

where B is,

$$B = \kappa \cdot D_{dry}^3 \tag{1.5}$$

with the aerosol dry diameter D_{dry} and the hygroscopicity parameter κ, which defines as follows,

$$\kappa = i_s\frac{\rho_s M_w}{\rho_w M_s} \tag{1.6}$$

with the van't Hoff factor, i_s, the solutes ($_s$) and water ($_w$) density and mass (ρ, M).

The Köhler activation curve can serve to study cloud droplet nucleation. Figure 1.2 illustrates an example of a numerical solution for the Köhler curve of the water vapor and an ammonium sulfate aerosol with a dry diameter of $30\,\mathrm{nm}$, with the isolated Raoult's and Kelvin Terms. The Kelvin term curve can be understood as a Köhler curve for pure water. It increases exponentially with decreasing droplet diameters, therefore, homogeneous nucleation of pure water vapor becomes extremely unlikely in the atmosphere. To nucleate a droplet, some water molecules need to cluster, however, the diameter of this forming droplet would be too small to maintain condensation to dominate over evaporation. In contrast to that, for aerosols or droplets with larger diameters, the equilibrium supersaturation for droplet growth decreases, thus, the larger aerosols act more readily as CCN. As demonstrated by the Raoult's term, the presence of some solutes in the droplet can decrease the initial diameter for droplet growth and therefore favors cloud droplet nucleation. The solute effect also leads to hygroscopic growth at sub-saturated conditions. This effect is also of importance in the formation of haze. After reaching a certain supersaturation (the critical supersaturation, S_c), the nucleated aerosol can grow unhindered. As soon as an aerosol reaches this state, the CCN is referred to as activated.

The activation of aerosol to cloud droplets is not only important for ACI, it is also key to the major removal processes which are in-cloud and impaction scavenging (e.g., Ohata et al., 2016). Therefore, the aerosol population in the lower troposphere

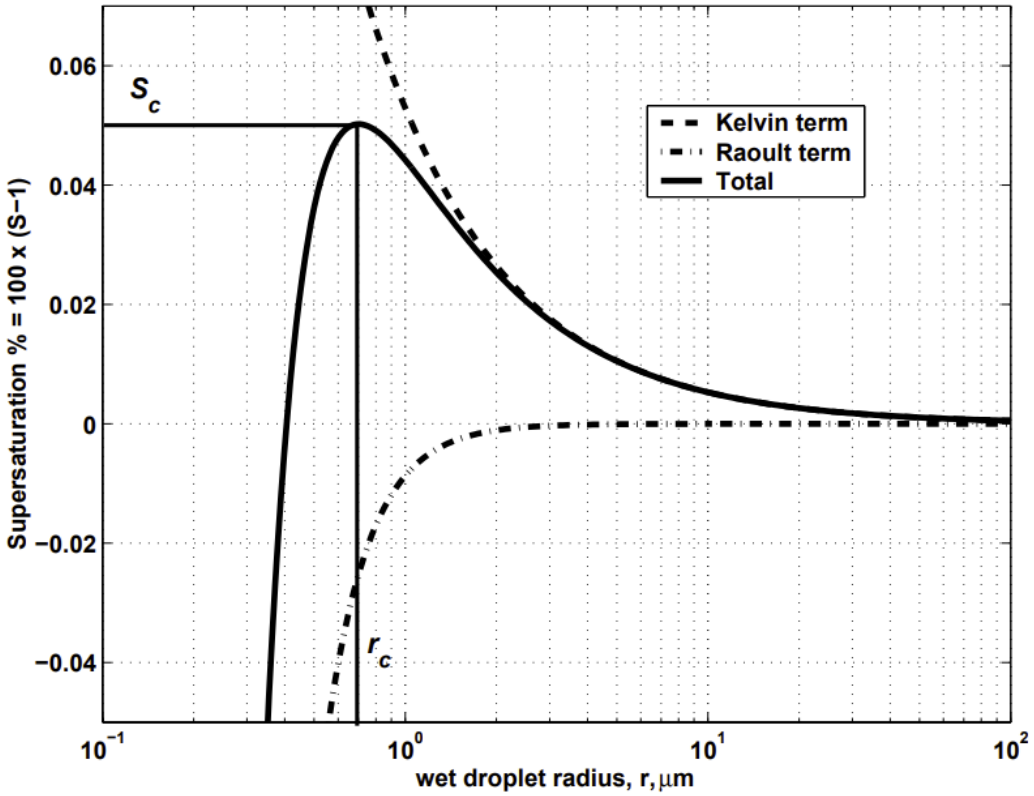

Figure 1.2: Figure from McFiggans et al., 2006: Köhler droplet activation curve for ammonium sulfate aerosol with a dry diameter of $30\,\mathrm{nm}$ and pure water vapor. Dashed lines are the isolated effects of the droplet curvature (Kelvin-Term) and the solute (Raoult-Term).

is tightly linked to cloud formation. However, the appearance and distribution of clouds are frequently patchy and also aerosols are heterogeneously distributed in the troposphere due to their sensitivity on sources and removal processes. To understand the aerosol life-circle in the atmosphere, knowledge about the vertical and spatial distribution of aerosol is of particular value.

1.3 Importance of spatio–temporal variations in atmospheric aerosol burden

As aerosols are a major constituent of global change, the focus of this thesis is on their occurrence in the atmosphere with the aim to extend current knowledge about the variability of their spatio-temporal distribution.

For both ACI and ARI, the spatio-temporal and vertical distribution of the aerosol burden is of great importance (e.g., Andreae et al., 2004; Gryspeerdt and Stier, 2012; Koch and Del Genio, 2010; Ramanathan et al., 2001; Samset et al., 2013). The vertical distribution of absorbing aerosol dominates the ARI and thus the local heating due to absorption. Especially in the upper troposphere and lower stratosphere, the local heating of biomass burning smoke can affect atmospheric conditions and the radiative balance (Ditas et al., 2018). Ohneiser et al., 2022 showed that the heat-

ing of smoke layers can be sufficient for lofting across the tropopause into the lower stratosphere, where aerosol residence times exceed the ones in the troposphere and ozone chemistry is affected by the aerosol enhancements. Also Samset et al., 2013 highlights the sensitivity of ARI on the location of the absorbing aerosol, while Koch and Del Genio, 2010 shows the importance of location of an absorbing aerosol layer relative to the cloud cover. The location relative to cloud layers is also of high importance: When absorbing aerosols are covered relative to the incoming solar radiation by clouds, their ARI turns neglectable, however, absorbing aerosol in the free troposphere, especially when enhanced in smoke layers, can even hinder cloud formation and the radiative effect is enhanced by increasing the surface albedo. On the other hand, clouds with embedded pollution from wildfires or urban areas, can extend to higher altitudes, due to delayed precipitation onset and therefore efficiently work as transport pathways of lower tropospheric pollutants into the upper troposphere or lower stratosphere, where residence times and climatic effects tend to be larger (e.g., Andreae et al., 2004; Ditas et al., 2018; Ohneiser et al., 2022; Samset et al., 2013). But also the near surface effects by ARI from dense wildfire smoke can modify boundary layer meteorology, as winds, air dryness and rainfall leading to a positive feedback loop with severe consequences for ecosystems, health and climate (Huang et al., 2023).

Comparably, also the spatio-temporal variations in the distributions of absorbing aerosol play an important role. Absorbing aerosol in the atmosphere over regions with generally dark surface albedo, as continental regions or oceans, only slightly modify the planetary albedo and therefore absorption of shortwave radiation, whereas over regions with low surface albedo, as the poles, absorbing aerosol accelerates warming due to the absorption of shortwave radiation. Krüger et al., 2022 found the atmosphere over Europe only slightly sensitive to reductions in the BC burden, while Polar regions show a large (Flanner, 2013), however uncertain (Wendisch et al., 2023), sensitivity to BC concentrations in the atmosphere.

Concerning the ACI, the availability of the aerosols for participation in cloud processes is the determining factor. Aerosols are either directly available at cloud base and thus, during cloud initiation, but also during the cloud lifetime they can alter cloud micro- and macrophysics. Large quantities of aerosol can delay or even suppress onset of precipitation due to Twomey effect (Braga et al., 2017; Twomey, 1977). This delay or suppression of precipitation increases the cloud atmospheric lifetime and the radiative properties due to increased total surface of more small droplets. For clouds which form in aerosol limited regimes the precipitation onset is earlier (Braga et al., 2021) and the clouds tend to have stronger convection.

Satellites provide aerosol characteristics often as aerosol optical density (AOD), which is a columnar value. This quantity is of great value for atmospheric science, especially due to its nearly global coverage and long-term records. However, AOD can only provide limited information about the location within the atmospheric column and is often biased for continental and near-urban locations (Wang et al., 2018). Wrong assumptions for the location of the aerosol can lead to significant uncertainties in ARI and ACI. Further satellite measurements are not sensitive to fine aerosol which often dominates the overall aerosol number concentration and are most relevant for ACI.

The satellite retrieved data are receiving a lot of attention in climate modeling, where it can readily be implemented and provides a good measurement based constrain for the columnar aerosol load. Meanwhile, the vertical distribution and the number concentration, especially of fine mode aerosol, remains relatively unconstrained from AOD data. However, these information are of great importance, especially for ACI. Andreae, 2009 found a correlation following a power law between some ground-based measurement of CCN and AOD, however there are large uncertainties within the measurements for both remote marine sites and continental sites.

In situ measurements of aerosol can fill that gap arising from AOD data. Hernández et al., 2022, demonstrated the good agreement between satellite retrieved AOD data and the in situ measurements for a lightly aged and dense plume of biomass burning smoke over the Mediterranean (Fig. 5.7). However, biomass burning plumes are not the only emitter of particulate pollution and are a special case since the density of pollution is very high in relatively fresh plumes. For urban haze, the emission source spans over a large spatial area and emissions are rather constant, with little diurnal and weekly variations, compared to biomass burning, which occurs only occasionally on a relatively narrow spatial extent with high density of emissions. Therefore measurements of urban haze, but also highly aged and therefore diluted biomass burning plumes, are challenging for remote sensing and need accurate in situ measurements. To cover a large spatial and vertical extent, measurements onboard a research aircraft are highly beneficial.

Satellite based LIDAR (Light Imaging, Detection And Ranging) measurements as provided for example from the the Cloud-Aerosol Lidar with Orthogonal Polarization (CALIOP) onboard the Cloud–Aerosol Lidar and Infrared Pathfinder Satellite Observation (CALIPSO) provide valuable data about the vertical structure of the atmosphere, especially in respect to clouds and aerosol layers. Background aerosol, however, can only be measured in densely polluted regions where the resulting aerosol vertical extinction coefficients are sufficient for the instrumental sensitivity. For the aerosol layers detected by CALIOP, CCN retrievals agree in an order of around 1.5 with ground based observations (Choudhury and Tesche, 2022) and also retrievals of aerosol number concentrations for Aitken mode and accumulation mode particles are generally comparable to observations (Choudhury et al., 2022). In situ aerosol measurements provide information about the vertical structure of aerosol out of dense plumes and the aerosol chemical and physical properties.

1.4 Mapping anthropogenic air pollution in the COVID–19 lockdown

The immense emissions of particulate air pollutants produced by civilisation led to an atmosphere with only very few remaining unperturbed regions (Andreae, 2007). Some of these regions are the remote southern oceans and some sites in the remote Amazon rain-forest during the raining-season. However, on highly populated and industrialized continents there is likely no pristine place. The COVID-19 lockdowns in early 2020 led to an unprecedented cut in anthropogenic emissions, giving rise to the opportunity to investigate some sign of the Anthropocene and providing an outlook into a hopefully decarbonized and, therefore, cleaner future.

To subdue the exponential spread of the SARS-CoV-2 (severe acute respiratory syndrome coronavirus type 2), most European countries responded with substantial cuts in mobility and economic activities. This included forced and voluntary confinements such as travel bans, home-office and relinquished travel activities (e.g., Hale et al., 2021; Quaas et al., 2021b). Many of these behaviour modifications decreased fossil fuel combustion, a major source of atmospheric BC (BC) (e.g., Bond et al., 2013; Pöschl, 2005). This decrease is reflected in a roughly $30\,\%$ decreased fossil fuel demand in early 2020 (Fig. 3.8). That reduction is attributed to $90\,\%$ less air traffic in Europe (Schumann et al., 2021b) as well as strongly reduced road traffic (Fig. 3.8). These changes in anthropogenic emissions created unprecedented atmospheric conditions compared to the generally anthropogenic shaped continental aerosol burden (Andreae, 2007) and gave rise to the opportunity to measure particulate pollution.

Several model studies use proxies like the strictness of the confinements or mobile phone data on transportation to show the impact of behavior changes on emissions (e.g., Forster et al., 2020; Le Quéré et al., 2020). Also, satellite-based observations are used to track changes in trace gas concentrations, aerosol optical properties as well as cloud coverage (e.g., Li and Groß, 2021; Quaas et al., 2021a; Schumann et al., 2021a). A more accurate estimate at the cost of spatial resolution is achieved with surface air pollution monitoring stations (e.g., Evangeliou et al., 2021; Petetin et al., 2020; Shi et al., 2021). All these studies have contributed to understanding the COVID-19 confinement's influence on the atmosphere and climate. Nevertheless, they fail to provide a precise quantification of air pollutants over a large spatial area with profiles of the lower tropospheric distribution. In this thesis, airborne in situ observations of BC and CCN during the first COVID-19 lockdown in early 2020 are presented, showing a consistent data set for a large region along with the vertical distribution of BC and CCN.

We used measurements of M_{BC}, N_{BC} and $N_{\mathrm{CCN\,0.3}}$ in the lower troposphere in western and southern Europe (Fig. 1.3) to elucidate the changes in particulate pollution. Therefore the data from in situ measurements during non-confinement conditions in July 2017 (during the EMeRGe EU campaign, Hernández et al., 2022) are compared with that affected by reduced emissions in May and June 2020 (during the BLUESKY campaign, Voigt et al., 2022). The measurements were performed while most of the lockdown confinements were still active, however, the strictest lockdown was from the middle of March until the middle of May (Fig. 2.4 and section 2.6.1). Here we estimate to what extent the BC reductions are due to lower emissions and to other factors such as meteorological conditions and differences in flight tracks. Therefore we modeled M_{BC} along the flight tracks with the ECHAM/MESSy Atmospheric Chemistry (EMAC) model and used the differences in the model results to adjust our in-situ data for changes not related to reduced anthropogenic emissions. For the measurement period in 2020, we show a substantial reduction in BC compared to the measurements from 2017.

The fast response on the aerosol burden to the COVID-19 confinements is due to its relatively short atmospheric residence time, ranging from some days to a few weeks (Bond et al., 2013; Holanda et al., 2020; Lund et al., 2018). Owing to its relatively short residence time, the lower tropospheric aerosol burden response is nearly immediate to emissions changes. This immediacy makes BC and CCN an appropriate tracer for the rapid changes in anthropogenic activities and thus an important quantity in estimating the radiative effect of the 2020 confinements.

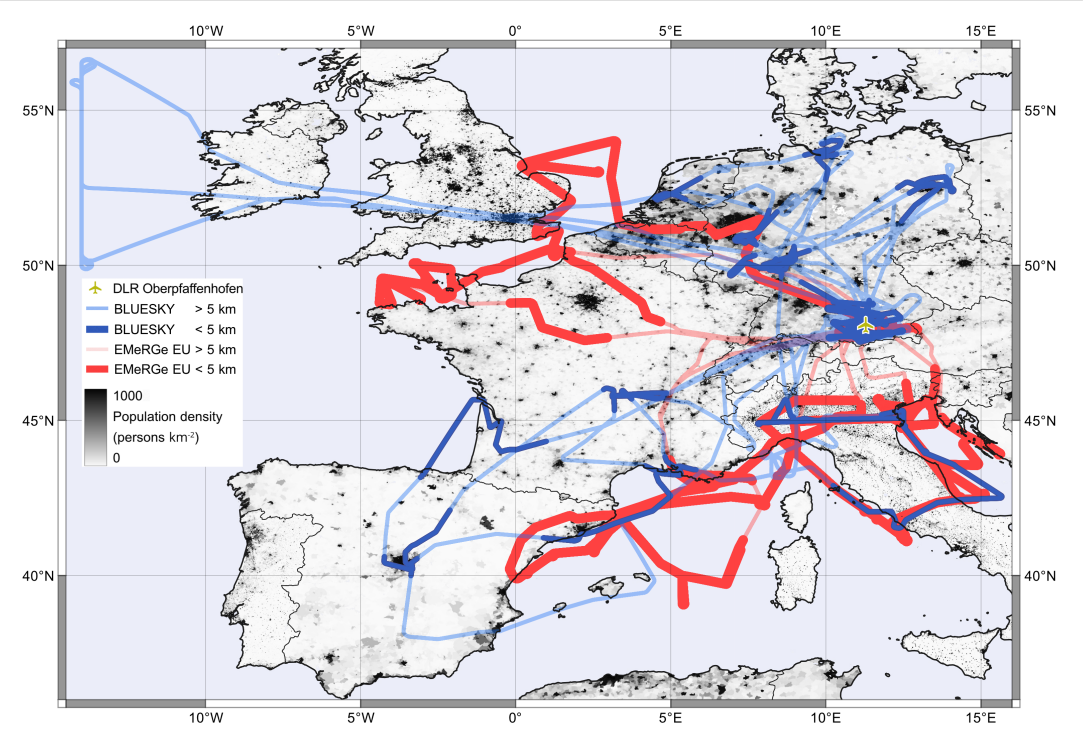

Figure 1.3: Flight tracks of the HALO EMeRGe EU (in July 2017, Hernández et al., 2022) and BLUESKY (in May and June 2020, Voigt et al., 2022) aircraft campaigns. Both campaigns were conducted from the DLR airport in Oberpfaffenhofen in southern Germany. Flight segments with altitudes below 5 km, which yielded the measurement data for the quantification of the BC reductions, are highlighted in the map. The population density is for the year 2020 (CIESIN, 2018).

Besides urban and industrial air pollution, open biomass burning of forests, savannahs and agricultural used areas is another major constituent of particulate pollution in the atmosphere. While there has been a decreasing trend for urban particulate pollution during the last decades (e.g., Kanaya et al., 2020; Kutzner et al., 2018; Querol et al., 2013; Singh et al., 2018), emissions from biomass burning are expected to increase further due to increasing heat and drought stress on ecosystems on a warming planet. To date, biomass burning already contributes to around 60 % of the global BC emissions (Andreae, 2019; Bond et al., 2013). Besides BC, large quantities of organic and inorganic aerosol and numerous gases of different volatility are also co-emitted by open biomass burning (Andreae, 2019; Lobert and Wamatz, 1993). Some of the organic aerosol from biomass burning can also have light absorbing properties. These aerosols are referred to as brown carbon and, unlike black carbon, they have a large spectrum of absorbing properties and precursors. They either form by photo-degradation of initially non absorbing aerosol, or they are already emitted with absorbing properties (Andreae and Gelencsér, 2006). Smoke further contains a large fraction of scattering aerosol. The smoke plumes generally have higher lifetimes in the atmosphere due to their higher emission height and density. There is an increased chance of transport and lofting of smoke plumes above the boundary layer, where wet removal is weaker. Also, rapid adjustments of the

thermal profile due to absorption can vary cloud patterns. There is also evidence that smoke and fires potentially vary meteorological patterns and therefore intensify and spread fires (Huang et al., 2023). Also, transport into the upper troposphere and lower stratosphere is reported (Ditas et al., 2018; Ohneiser et al., 2020; Schill et al., 2020), where the radiative effect of absorbing layers is more destructive to climate (Samset et al., 2013). However, the overall climate impact of biomass burning smoke in the atmosphere is complex due to the mixture of absorbing and scattering aerosol as well as the various impacts on clouds, depending on the smoke layer composition, altitude, location and also meteorological parameters.

1.5 Volcanic eruptions as strong natural aerosol sources

A significant aerosol cooling effect is associated to non absorbing aerosol in the upper troposphere and lower stratosphere (UTLS). In the UTLS aerosols play a crucial role in Earths radiative budget by masking parts of greenhouse gas induced heating. The so called Junge layer (Junge and Manson, 1961) is a well known reservoir of relatively large sulfate rich aerosol in the stratosphere scattering incoming shortwave radiation back to space (e.g., Kremser et al., 2016). A strong but discontinuous source of aerosol in the UTLS are volcanic eruptions. The aerosol size distribution of the volcanic aerosol and the location of the aerosol layers are important parameters for the direct sunlight scattering as well as for the aerosol residence time in the atmosphere.

Sulfur rich precursor gases nucleate and condense to sulfate organics predominantly in the tropical tropopause region, maintaining the aerosol burden of the Junge layer (Brock et al., 1995; Junge and Manson, 1961; Kremser et al., 2016; Murphy et al., 2021). The strongest sources for these sulfate aerosol precursors during volcanic quiescence are natural dimethylsulfide (DMS, $(CH_3)_2S$)) and carbonyl sulfide (OCS) emissions, but also anthropogenic sulfate dioxide (SO_2) emissions contribute to the stratospheric sulfate burden (e.g., Kremser et al., 2016). Volcanic eruptions, however, can exceed other sulfate sources by the large amounts of emitted SO_2. These precursors oxidize in the tropopause region or stratosphere to H_2SO_4 gases which then condense or nucleate to watery sulfuric acid aerosol (H_2SO_4-H_2O). Heterogeneous particle formation on surfaces of upper troposphere nucleation particles is also a potential formation mechanism for these sulfate aerosols (Brock et al., 1995).

The conversion speed from sulfate rich gases into sulfate aerosol in the atmosphere strongly depends on the available hydroxyl-radicals (OH^-). Lelieveld et al., 2016 showed elevated concentrations of OH^- within the tropical tropopause layer (TTL) and tropical lower stratosphere (TLS). Besides OH^- as an oxidation partner, availability of water vapor to form watery sulfuric acid aerosol can determine the speed of the conversion to sulfate. The e-folding time for the SO_2 conversion to sulfate aerosol is in the range of a few weeks to months (e.g., Kremser et al., 2016). Carn et al., 2016 show that the lifetime of SO_2 and thus the conversion from gas- into particle-phase is below one week within the tropopause region. For SO_2 in the stratosphere, the lifetime is around one month (Carn et al., 2016).

Volcanic eruptions with high explosive power can directly inject SO_2 into the stratosphere, whereas some moderate eruptions have their peak injection height within

the free troposphere up to the tropopause region. The subsequently formed aerosol has generally only a small organic mass fraction (e.g., Schmale et al., 2010). The SO_2 and sulfate from moderate non-stratospheric eruptions, however, remain only shortly in the troposphere and are then either removed from the atmosphere through the hydrological circle or lofted into the lower stratosphere (e.g., Aubry et al., 2021). After reaching the stratosphere, the volcanic aerosol enhancements have residence times ranging from months up to several years, mainly depending on the magnitude of emissions, the injection height and the latitude where the eruption occurred. It can take up to half a year until significant sedimentation of volcanic aerosol from the stratosphere into the tropopause occurs (e.g. Borrmann et al., 2010; Borrmann et al., 1997; Keim et al., 1996). The volcanic SO_2 and aerosol also induce a local heating by absorbing radiation (e.g., Bluth et al., 1992; Lary et al., 1994; Read et al., 1993). However, the long residence time and strong scattering properties of the aerosol enhancements lead to an overall surface cooling by reduced incoming shortwave radiation (Robock, 2000).

Moderate volcanic eruptions within the tropics with injection heights in the range of the TTL are relatively frequent (e.g., Carn et al., 2016; Schmidt and Black, 2022). Commonly, these moderate non-stratospheric eruptions do not receive attention in climate models due to their expected short atmospheric residence times (Aubry et al., 2021). For climate engineering considerations, however, the tropical lower stratosphere is meant to be the preferred injection location due to the assumed longest residence time for the sulfate aerosols (e.g., Visioni et al., 2019). The relatively low water vapor concentration in the TTL favors an enhanced aerosol residence time. Also, the air-masses within the TTL have tendencies to either loft into the lower stratosphere or to entrain into the free troposphere. Additional volcanic sulfates and ash can have a significant impact on both the radiative properties of the sulfate aerosol and on the residence time of these aerosols (Aubry et al., 2021; Zhu et al., 2020).

For heterogeneous reactions in the TTL and stratosphere as well as for the radiative budget, the aerosol size distribution is of major relevance. Smaller aerosols in the stratosphere scatter incoming solar shortwave radiation and have minor interactions with outgoing long wave radiation, whereas larger aerosols not only scatter solar radiation but also absorb solar and infrared radiation. The absorption of infrared radiation reduces the overall cooling effect of these aerosols (e.g., Stenchikov et al., 1998). Therefore, information about the aerosol size distribution is an important quantity for volcanic aerosol.

In this dissertation I present in situ aerosol measurements of the physio-chemical properties of a distinct aerosol enhancement in the tropical tropopause layer (TTL) around $14.5\,\mathrm{km}$ over the Atlantic Ocean. I can track the plume back to volcanic activities around 20 days prior to the measurements at the Ambae (15° S 165° E) and the Sierra Negra (1° S 92° W) volcanoes. The mode diameter of the aerosol plume is considerably below reported values for earlier volcanic eruptions and agrees better with the assumed sizes for background stratospheric aerosol. The sulfate aerosol mass is enhanced by a factor around 30, but also organic aerosol mass doubled within the aerosol plume. Moderate volcanic eruptions are expected to be less likely to reach the lower stratosphere in future climate projections (Aubry et al., 2021). Thus, our results provide important information for climate modeling of the aerosol evolution and transport of moderate tropical volcanic eruptions in the upper troposphere.

1.6 Thesis outline

This dissertation addresses the following research objectives with a focus on the spatial and temporal distribution of CCN and BC:

1. **Black carbon aerosol reductions during COVID-19 confinements quantified by aircraft measurements over Europe – chapter 3.1:** The abrupt reduction in human activities during the first lockdown of the COVID-19 pandemic created unprecedented atmospheric conditions. This gave rise to the opportunity to quantify the changes in lower tropospheric air pollution. Therefore, we conducted the BLUESKY aircraft campaign and measured vertical profiles of BC aerosol particles over western and southern Europe in May and June 2020. We compared the results to similar measurements of the EMeRGe EU campaign performed in July 2017 and found that the BC mass concentrations (M_{BC}) were reduced by about $48\,\%$. For BC particle number concentrations, we found comparable reductions. Based on EMAC chemistry-transport model simulations, we found differences in meteorological conditions and flight patterns responsible for about $7\,\%$ of the M_{BC} reductions. Accordingly, $41\,\%$ of M_{BC} reductions can be attributed to reduced anthropogenic emissions. Our results reflect the strong and immediate positive effect of changes in human activities on air quality and the atmospheric role of BC aerosols as a major air pollutant in the Anthropocene.

2. **Changed cloud condensation nuclei burden during COVID-19 lockdown over Europe – chapter 3.2:** Besides the documented changes in the BC burden, other aerosol species also experienced changes during the COVID-19 confinements. In this chapter, the changes in the aerosol population, acting as CCN at a water vapor supersaturation of $0.3\,\%$ ($N_{\mathrm{CCN\,0.3}}$) are analysed. Therefore, vertical profiles of $N_{\mathrm{CCN\,0.3}}$ from measurements during the BLUESKY campaign in 2020 and the EMeRGe EU campaign in 2017 are compared. Besides the comparison of vertical median concentrations, the distribution in the cross section along measurement latitude is analysed. The $N_{\mathrm{CCN\,0.3}}$ is thereby found to agree well with M_{BC}, especially for highly polluted regions, affected by dense urban haze or biomass burning. Also the reduction in the CCN burden agrees well with the overall reductions of M_{BC} during the confinements. In addition to the comparison of in situ measurement data from HALO campaigns, vertical profiles of $N_{\mathrm{CCN\,0.3}}$ from the ECHAM-HAM climate model are also considered. The model data are a ten-year monthly average for the measurement months providing a long-term perspective. Generally, the vertical gradient in $N_{\mathrm{CCN\,0.3}}$ in the model results is too uniform compared to the in situ data, however, in the middle and upper troposphere, the measurements and model results agree well. Also between the measurements in 2020 and 2017 there are only minor differences in the middle and upper troposphere above $5\,\mathrm{km}$.

3. **Variations in the vertical distribution of cloud condensation nuclei burden over Asia and the tropical Atlantic – chapter 4:** In this section, the long-term climate model results, as used for the measurements over Europe, are compared to the vertical profiles from measurement data of the EMeRGe Asia and CAFE Africa campaign. I find that the measurements over the remote tropical Atlantic are in line with the range provided by the long-term expectations from

the climate model, whereas in Asia, the in situ data exceed the model expectations significantly. However, the general shape of the vertical distribution is also captured well over the oceans of Southeast and East Asia. A potential explanation is a strong bias due to the sampling strategy during EMeRGe Asia, targeting on specific pollution hot-spots and therefore over-representing measurements in a more polluted and aerosol enhanced regime. I find a sensitivity of $N_{\text{CCN 0.3}}$ in the lower troposphere to anthropogenic air pollution, as a common feature between the measurements in Asia and Europe. Over the remote tropical Atlantic, $N_{\text{CCN 0.3}}$ also showed a strong enhancement in a highly aged biomass burning smoke layer.

4. **Characteristic relationships between CCN and BC – chapter 5:** We use the results of the comparison of the BLUESKY and EMeRGe EU $N_{\text{CCN 0.3}}$ and M_{BC} to find a general trend between these two quantities. For this purpose, M_{BC} serves as a tracer for $N_{\text{CCN 0.3}}$ from urban areas. Generally the air pollution caused by human activities in the Anthropocene is characterised by burning of biomass or fossil fuel. The ratio of M_{BC} to $N_{\text{CCN 0.3}}$ depends on the emission source, combustion conditions and atmospheric aging. These results are further extended to measurements in other polluted regimes as highly aged biomass burning smoke over the Atlantic and lightly aged smoke in Europe, Asia and over the Amazon rain-forest. Between $N_{\text{CCN 0.3}}$ and M_{BC} a distinct near-linear relation is discovered in the various polluted atmospheric conditions and regions. In all these conditions, the $N_{\text{CCN 0.3}}$ are exceeding the N_{BC}, especially in continental regions where the BC is mostly from anthropogenic sources, but also in highly aged smoke from biomass burning. The ubiquitous presence of enhancements in the CCN number concentrations under polluted conditions reveals the importance of anthropogenic pollution to the CCN burden.

5. **In situ measurements of a volcanic aerosol layer in the tropical tropopause layer – chapter 6:** During the CAFE Africa campaign, a roughly three weeks aged aerosol plume from a volcanic eruption was encountered. The origin of this plume could be traced back either to the Ambae (15° S 165° E) or the Sierra Negra (1° S 92° W) eruption. Onboard the HALO aircraft we could perform in situ measurements of the aerosol chemical composition and $N_{\text{CCN 0.3}}$. Also measurements of the total aerosol number concentration N_{CN} and optical measurements of particles in the size range between 180 to $400\,\text{nm}$ ($N_{\text{CN 180}}$) were taken. Further based on the information about the chemical composition and therefore the theoretical hygroscopicity parameter, κ_{chem}, a size distribution was retrieved from the CCN data and combined with N_{CN} and $N_{\text{CN 180}}$. In situ observations of volcanic aerosol within the TTL are rare and the data may be of relevance for the modeling as well as for the climate engineering community.

Additional to the research presented in the course of this dissertation, I contributed as co-author to 19 articles published in peer-review journals. Further, I am first author of the study Krüger et al., 2022, which is also included in this dissertation in chapter 3. The study is published in the peer-review journal Atmospheric Chemistry and Physics and was selected by the executive editor as "highlight paper". My full publication record is listed in **??**.

CHAPTER 2

Materials and Methods

This chapter contains detailed descriptions of the main measurements and campaigns analysed in this thesis as well as an overview of the large set of supporting data from different instruments and climate models. Thereby this chapter is structured as follows: The measurement techniques and measurement campaigns and sites are outlined in the general methods, since they are relevant for all chapters in the results section. Additional data from models and specific measurements as well as parts of the data analysis approaches are outlined in sub-sections corresponding to the certain chapter in the results section.

2.1 Measurement platforms, sites and campaigns

This thesis consists of in situ measurement data from various research field campaigns at different sites and platforms. These are introduced in the following section.

2.1.1 HALO, the high altitude and long range research aircraft

The aircraft measurements included in this thesis were conducted with the High Altitude and LOng range (HALO) research aircraft. The HALO aircraft is a modified long-range business jet (G550, Gulfstream, USA) with a ceiling flight altitude of $15.5\,\mathrm{km}$ and therefore the capabilities to probe the lower stratosphere in nearly all latitudes. HALO is based at the German Aerospace Center (DLR) in Oberpfaffenhofen, near Munich in Germany and is a joint research platform of several German research organizations (i.e., Leibniz Institute for Tropospheric Research (TROPOS), Max Planck Society, DLR, Karlsruhe Institute of Technology and FZ Jülich) and universities (i.e., University Leipzig, Frankfurt and Mainz). The data from the HALO missions presented in this dissertation is available at the HALO database (https://halo-db.pa.op.dlr.de/).

ACRIDICON-CHUVA

Aerosol, Cloud, Precipitation, and Radiation Interactions and Dynamics of Convective Cloud Systems–Cloud Processes of the Main Precipitation Systems in Brazil: A Contribution to Cloud Resolving Modeling and to the Global Precipitation Measurement. The measurement campaign took place in Manaus in the central Amazon rain forest in Brazil. Cloud properties (e.g., Braga et al., 2021; Braga et al., 2017; Campos Braga et al., 2021) and aerosol characteristics (e.g., Andreae et al., 2018; Liu et al., 2023; Schulz et al., 2018) were probed during 14 measurement flights covering the large geographical extent of the Amazonian Basin and the Brazilian Atlantic shore in September and October 2014, in the Amazonian dry season (Andreae et al., 2018; Machado et al., 2017; Wendisch et al., 2016). Over the Atlantic off the Brazilian shore, a layer of aged biomass burning smoke originated in Africa was probed in the free troposphere (see section 5 and Holanda et al., 2020). In contrast to that aged smoke, also lightly aged biomass burning emissions were observed over the intense deforested region of the southern Amazon, also referred to as the 'arc of deforestation'.

EMeRGe EU

Effect of Megacities on the transport and transformation of pollutants on the Regional and Global scales (EMeRGe EU) was investigated from 10 until 28 July 2017 in Eu-

rope (Hernández et al., 2022). Aim of the EMeRGe EU campaign was to investigate, quantify and record the emissions and the transformation of pollution from highly populated regions in Europe. The campaign base was in Oberpfaffenhofen, close to Munich in Germany. Target regions were large cities and urban accumulations in Belgium, the Netherlands and Luxembourg (Benelux), Germany, France, Italy, Spain, and England (see section 3, Fig. 1.3 and Förster et al., 2023; Hernández et al., 2022; Krüger et al., 2022). Besides the targeted urban emissions, also biomass burning smoke, mineral dust and frequently a mix of pollution regimes were encountered. The focus of EMeRGe EU determined the flight tracks to be in the lower troposphere, where anthropogenic pollution is most abundant. The flights were performed predominantly up- and down-wind of densely populated regions.

EMeRGe Asia

Effect of Megacities on the Transport and Transformation of Pollutants on the Regional to Global Scales in Asia. The campaign was the companion part to the measurements of EMeRGe EU, probing south-east Asian pollution with the aircraft based in Tainan, Taiwan ($22.57°$ N $120.12°$ E). The campaign took place in March and April 2018, probing the outflow of major cities in Taiwan, China, Korea, Japan, the Philippines and Thailand at different aging and mixing states (e.g., Förster et al., 2023). Also, smoke from open biomass burning, especially agricultural residual burning, was probed during the campaign (see section 3.2, 5 and Lin et al., 2023).

CAFE Africa

Chemistry of the Atmosphere: Field Experiment in Africa. The CAFE Africa campaign took place in August and September 2018 based on Sal in Cape Verde ($16.75°$ N, $22.95°$ W). During the 14 scientific measurement flights over western Africa and the Atlantic, focal points were the African outflow of biomass burning emissions in the lower troposphere, the distribution of pollutants in the interplay with the inter tropical convergence zone (ITCZ), effects of deep convection on aerosol and gas burdens and the oxidative capacity in this complex mixture of air-masses (e.g., Nussbaumer et al., 2021; Schneider et al., 2021; Tadic et al., 2021). Further, during one measurement flight, a volcanic aerosol layer was intensely probed (see section 6). In several flights over the southern Atlantic, aged biomass burning smoke layers emitted from African biomass burning were probed in the lower free troposphere (see section 5).

CAFE EU as part of BLUESKY

Chemistry of the Atmosphere: Field Experiment in Europe. The campaign took place from May to June 2020 during the unprecedented social and economical COVID-19 caused confinements in many European countries. The total of 8 measurement flights were carried out in southern and western European airspace (Fig. 1.3, Krüger et al., 2022; Reifenberg et al., 2022; Voigt et al., 2022). Several flights were conducted in the region of the north Atlantic flight corridor, in the upper troposphere and lower stratosphere, west of Ireland. The regions we focus on in this thesis are, however, only countries where we probed the lower troposphere, namely, Germany, France, Spain, Italy and the Benelux countries. These countries are also used for the comparison of the results to other data sets and publications.

2.1.2 Barbados Aerosol and Chemistry Observatory

Barbados as a base for atmospheric research is of particular interest due to its location in the remote Atlantic, dominated by unperturbed air-mass advection from the tropical Atlantic, influenced only by long-range transported African continental air-masses (e.g. Archibald et al., 2015; Quinn et al., 2021; Stevens et al., 2016; Stevens et al., 2021; Wex et al., 2016). The island's east coast with only little recent anthropogenic influence (Prospero et al., 2005; Savoie et al., 2002) houses two major research facilities: the Barbados Aerosol and Chemistry Observatory (BACO) and the Barbados Cloud Observatory (BCO). The BACO measurement site is located at a cliff called Ragged Point ($13.16°$ N and $59.43°$ W) protrude around $30\,\mathrm{m}$ above sea level. It consists of an aerosol lab container connected to a $17\,\mathrm{m}$ sampling tower with a near iso-kinetic inlet. The BACO site is dedicated to in situ aerosol and trace gas studies since the 1970's (e.g. Carlson and Prospero, 1972; Prospero, 1968; Stevens et al., 2016). The BCO however, which is operated by the Caribbean Institute for Meteorology and Hydrology in Bridgetown, Barbados, and the Max Planck Institute for Meteorology in Hamburg, Germany, focuses on remote sensing techniques to elucidate shallow cumulus clouds (e.g., Stevens et al., 2016; Stevens et al., 2021).

EUREC^{4}A and ATOMIC

Aerosol samples for offline analysis and size-resolved CCN measurements (Royer et al., 2023a) were performed at BACO during the EUREC^{4}A and ATOMIC field campaigns in January and February 2020 (Quinn et al., 2021; Stevens et al., 2021). The aim of the measurement campaigns was to advance the understanding of the interplay between clouds, convection and circulation and their role in climate change. EUREC^{4}A stands for Elucidating the Role of Clouds–Circulation Coupling in Climate and ATOMIC for Atlantic Tradewind Ocean-Atmosphere Mesoscale Interaction Campaign. The CCN measurements and size distribution data measured at BACO agree well with the total CCN data measured with a CCNC of the same type and size distributions sampled onboard the research vessel Ronald H. Brown upwind BACO (Quinn et al., 2021).

2.2 General instrumentation

2.2.1 Hygroscopic aerosol properties

The cloud condensation nuclei (CCN) number concentration (N_{CCN}) at different water vapor supersaturation (S, $N_{\mathrm{CCN\,S}}$) and the aerosol hygroscopicity parameter (κ) were measured onboard the HALO research aircraft and at the BACO observatory at Barbados' east coast.

The CCNC measurements in this thesis are performed with commercial continuous-flow streamwise thermal-gradient CCN counter (CCNC, model CCN-200 and model CCN-100, DMT, Longmont, CO, USA, Roberts and Nenes, 2005; Rose et al., 2008). The core of the CCNC instrument is a cylindrical flow tube (column) with an inner diameter of $2.3\,\mathrm{cm}$ and a height of $50\,\mathrm{cm}$. In the column an aerosol sample flow in the center-line is covered by a particle free sheath air. The laminar flows are directed from top to bottom of the column, which has a nearly linear increasing temperature gradient in flow direction. The column is made of a continuous wet

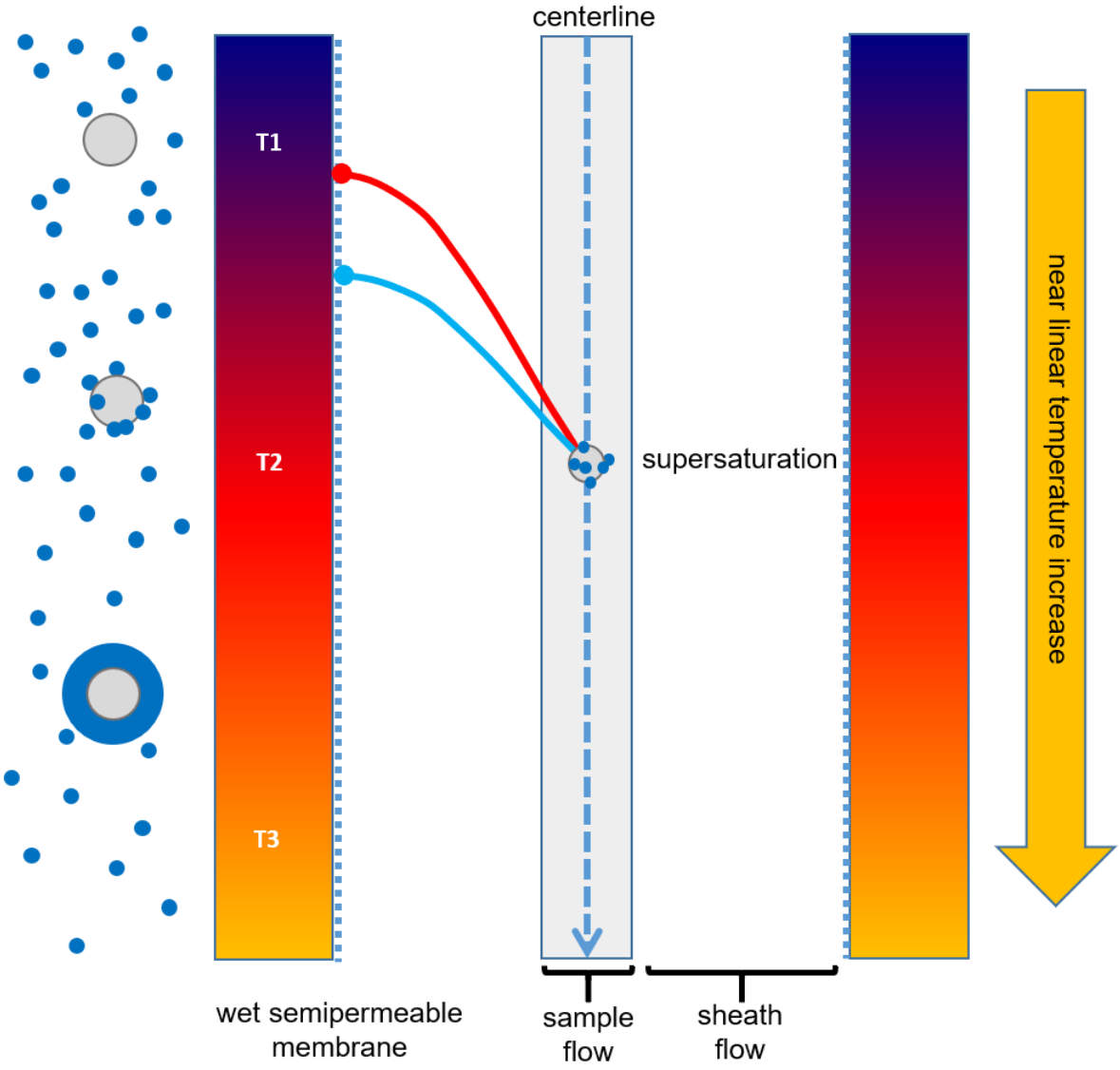

Figure 2.1: Schematic cross section of a CCNC column with general diffusion of heat (red line) and water vapor molecules (blue line). The near linear temperature increase in the CCNC column is slightly larger between T1 and T2 than in the second half between T2 and T3 to ensure early CCN activation and sufficient growth time.

semipermeable porous membrane, allowing water vapor to enter the flow system. Heat and water vapor are transported with the laminar flow towards the center-line, thereby the diffusion of water vapor is faster than the diffusion of heat, a water vapor supersaturation is steadily achieved in the center-line, where the aerosol sample is transported.

Due to the supersaturated conditions in the center-line, aerosol with a critical supersaturation below the prevalent conditions can activate and grow into droplets large enough to be detected by the optical particle counter (OPC). The OPC not only detects droplets larger than $1\,\mu\mathrm{m}$, it also provides the droplet size distribution in the range from 0.75 to $10\,\mu\mathrm{m}$. To ensure sufficient time for the activated CCN to grow into detectable droplets, the temperature gradient in the first half of the column is slightly larger than in the second half. That restricts most of the actual CCN activation to the first part of the column. Besides the instrumental temperature gradient, also the flow

rate, sample pressure and the sample temperature influence the supersaturation in the center-line; these values are monitored and considered in the evaluation of the CCNC data (Rose et al., 2008).

Due to the constant sample flow, the error in the CCNC data are dominated by the calibration uncertainty in a range of $10\,\%$, (Pöhlker et al., 2018). The counting error in N_{CCN} is based on the measured particle number and is ~ $10\,\%$ of N_{CCN} for high concentrations and ~ $20\,\%$ for low concentrations (Krüger et al., 2014). The variability in S is around $\pm 5\,\%$ following Rose et al., 2008 and Moore and Nenes, 2009.

Calibration of CCNC instruments

The water supersaturation is calibrated with size-selected ammonium sulfate aerosols that were analysed by the CCNC set to a designated temperature gradient with constant flow, at BACO and to a constant temperature gradient with designated flow rate for the low pressure HALO setup, as well as a CPC to measure total condensation nuclei (N_{CN}) concentration, according to to (Rose et al., 2008). The ratio between $N_{\mathrm{CCN\,S}}$ to N_{CN} then was used to determine the diameter at which 50 % of the ammonium sulfate aerosol is activated as CCN at a particular S (critical activation diameter, d_{50}). The critical diameter known from theory was then used to determine actual instrumental supersaturation. The relation between flow or temperatures to supersaturation provides a linear correlation that was used to adjust the supersaturation (and flow for HALO data) shown by the instrument to the actual value of the water vapor supersaturation.

2.2.2 Black carbon aerosol mass and number concentration

The refractory black carbon (rBC) was measured with an eight-channel Single Particle Soot Photometer (SP2, Droplet Measurement Technologies, Longmont, USA). The SP2 quantifies rBC and non-absorbing particles using laser-induced incandescence and scatter signals (Schwarz et al., 2006; Stephens et al., 2003). Particles with a rBC core absorb the laser light and evaporate. The emitted incandescence signal is linearly proportional to the mass of the rBC cores (Laborde et al., 2013). The SP2 used for this study is sensitive to rBC cores in the size range between 70 to $500\,\mathrm{nm}$ mass-equivalent diameter, assuming a density of $1.8\,\mathrm{g\,cm^{-3}}$.

The SP2 incandescence signal was calibrated at the beginning, during, and at the end of each campaign with size-selected fullerene soot particles (Alfa Aesar Lot W08A039). The scattering signal was calibrated with spherical polystyrene latex size standards (208, 244, and 288 nm) and size selected ammonium sulfate particles using a differential mobility analyser (Grimm Aerosol Technik, Ainring, Germany). The results of all calibrations for both campaigns agreed within their uncertainty ranges, confirming good instrument stability throughout the comparison. The uncertainty for SP2 measurements is $5\,\%$ for N_{BC} and $10\,\%$ for M_{BC} (Laborde et al., 2012). The measurement data was analysed with the Paul-Scherrer Institute (PSI) SP2 toolkit (Gysel-Beer and Corbin, 2019) and adjusted to standard temperature and pressure (STP, T =273.15 k, p =1013.25 hPa). Throughout the analysis we use the BC data without a correction for the lower cutoff of the SP2. Due to the large contribution of anthropogenic BC emissions to our measurements and the high uncertainty in the size distribution for diameters below the SP2 detection limit we do not fit the size distribution to a log normal distribution. Furthermore, for M_{BC}, diameters below

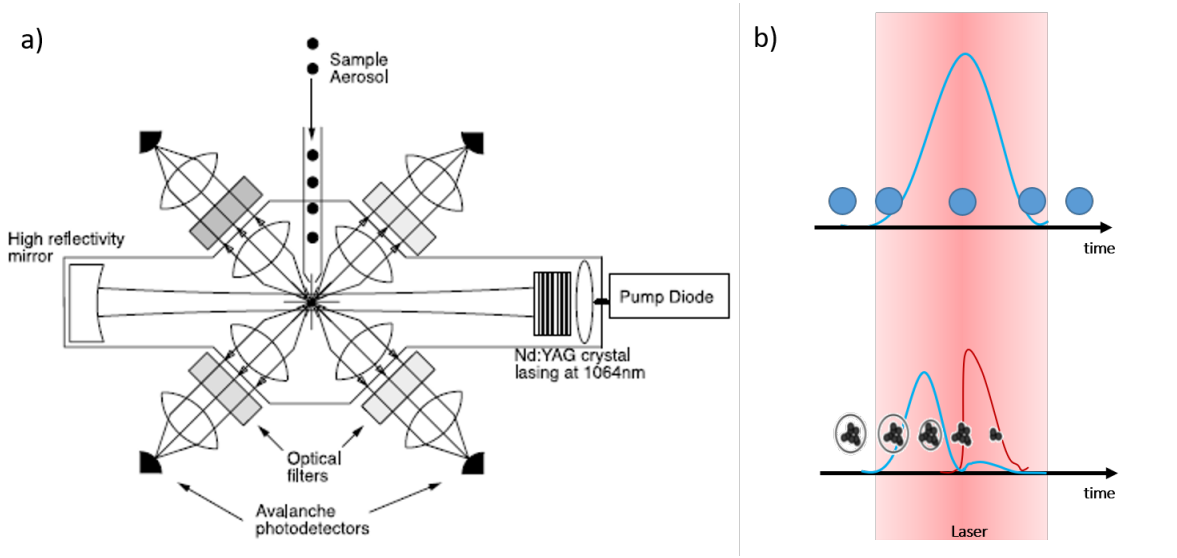

Figure 2.2: Schematic sketch of SP2 (a), adapted from Schwarz et al., 2006. Schematic working principle of SP2 for absorbing and non-absorbing aerosol (b).

100 nm do not play a significant role, regardless of their potentially dominating role for N_{BC} and importance for the BC surface area (Pileci et al., 2021; Reddington et al., 2013; Schwarz et al., 2008; Seinfeld and Pandis, 2006).

The log normal size distributions from the refractory BC data are calculated by using the following function according to Heintzenberg, 1994,

$$f(x) = \frac{A}{\sqrt{2\pi} log(\sigma)} \exp\left[-\frac{(\log(x) - \log(D_g))^2}{2\log^2(\sigma)}\right] \tag{2.1}$$

with A as a free parameter, D_g as mean geometric diameters and the widths (i.e. the standard deviations, σ_g) of the core size distributions.

2.3 HALO instrumentation

2.3.1 Meteorological parameters

General meteorological data were obtained from the Basic HALO Measurement and Sensor System (BAHAMAS) on a 1 Hz resolution. BAHAMAS measures meteorological parameters like pressure, temperature, and the 3-D wind vector as well as the aircraft position and altitude. The water vapor mixing ratio and further humidity parameters are measured by the Sophisticated Hygrometer for Atmospheric ResearCh (SHARC, Kaufmann et al., 2018). The typical absolute accuracy of the general meteorological data are around 0.5 K for temperature, 0.3 hPa for pressure. The hygrometer measurements agree within their combined accuracy (±10 % to 15 %, depending on the humidity regime) and the total mean values agree within 2.5 %. For mixing ratios below 10 ppm H_2O, systematic differences on the order of 10 % and up to a maximum of 15 % are found (e.g., Andreae et al., 2018; Kaufmann et al., 2018).

All aerosol data reported in this study are corrected for standard pressure and temperature (STP, T=273.15 K, p=1013.25 hPa) based on the instrumental monitoring measurements of sample temperature and pressure.

2.3.2 Aerosol sampling

The HALO sub-micrometer aerosol inlet (HASI) allows for up to 30 liters per minute of sample air flow to be provided to aerosol instruments inside the aircraft cabin. It samples the air at the top of the fuselage outside of the aircraft boundary layer and regulates the sample air flow in each of the four forward-facing sample lines to achieve near isokinetic sampling conditions according to the actual aircraft velocity. Therefore, the air stream is aligned and decelerated by a factor around 15 at the front shroud, followed by a two step deceleration in a main diffusor and smaller diffusors at the tips of the sample lines as illustrated in figure 2.3 (Andreae et al., 2018; Minikin et al., 2017). Overall, a deceleration of the air sample by a factor around 40 is achieved (Minikin et al., 2017). All measurements in this thesis were taken from the HASI inlet from one of the four forward heading sampling lines.

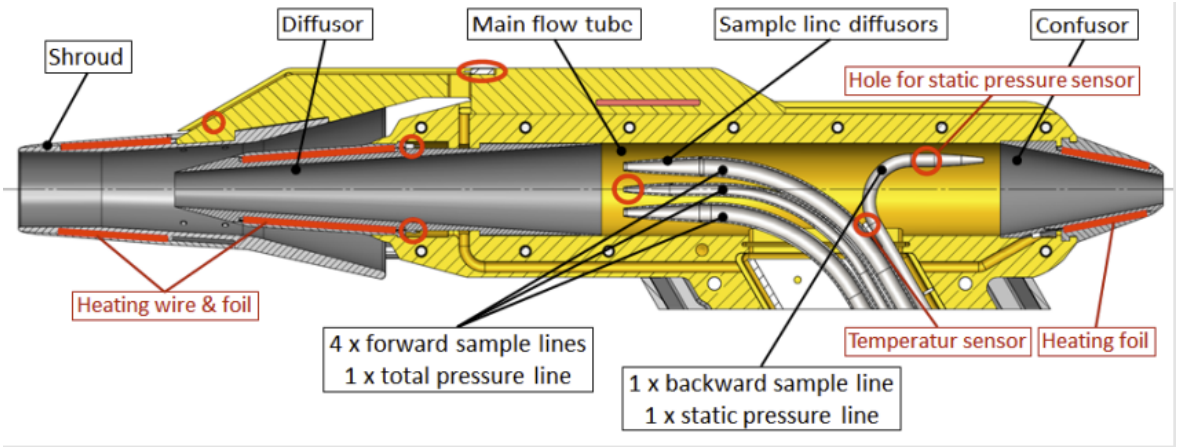

Figure 2.3: Schematic cross section of the HASI inlet system from Minikin et al., 2017.

2.3.3 Constant pressure inlet for aerosol instruments

For some aerosol measurements or the later data analysis a constant sample pressure is crucial. Therefore, a custom-made constant pressure inlet (CPI) was employed at the instrument's inlet of the CCNC and C-ToF AMS. The pressure is controlled with a variable critical orifice maintained by a squeezed O-ring. With a proportional–integral–derivative (PID) controller the squeezing rate is adjusted to achieve the target pressure behind the critical orifice. The transmission losses for sub-micrometer aerosol are discussed in Molleker et al., 2020 and are found to be considerably low for particles below 600 nm and pressure differences between ambient and sample pressure of up to 750 hPa. During most of the measurements the pressure difference between ambient and sample is smaller than that and particles larger than a few hundreds of nm are only of secondary importance for the CCN budget due to their low number concentrations (e.g., Seinfeld and Pandis, 2006). The CPI is well documented and described in Molleker et al., 2020.

2.3.4 HALO CCN measurements

We measured the number concentration of CCN at a water vapor supersaturation S of $0.3\,\%$ ($N_{\text{CCN 0.3}}$) with a dual column continuous-flow streamwise thermal gradient CCN counter (CCNC, model CCN-200, DMT, Longmont, USA, Roberts and Nenes, 2005; Rose et al., 2008). The CCNC consists of two independent columns, in which particles with a critical S smaller than or equal to the instrumental S are activated and form water droplets. Droplets above $1\,\mu\text{m}$ diameter are detected by an optical particle counter. The inlet flow rate of the column was $0.5\,\text{L/min}$ with a sheath-to-aerosol flow ratio of 10. The water supply pump was operated at "high" liquid flow. To avoid variations in S due to pressure instabilities, we deployed a constant pressure inlet (CPI) without significant particle losses in the relevant size range (Molleker et al., 2020). Only data without pressure variations and thus with stable S is included in the further analysis. The instrument was calibrated before and after the campaign at different pressures and flow rates according to Rose et al., 2008.

The second column of the CCNC provided a spectrum of 12 different S with the scanning flow operation mode (Moore and Nenes, 2009). Thereby the hardware settings for temperature in the CCNC instrument are maintained constant and the flow deviates to achieve different S between 0.09 % and 0.7 %, taking advantage of stable and robust hardware settings (Moore and Nenes, 2009). The data for the scanning S, however, is not further used in the context of this dissertation, since it is of particular interest for cloud micro-physics and case studies which are not focus of this thesis.

The CCN employed in HALO was controlled by a dedicated LabVIEW software (National Instruments, Austin, USA), controlling the preinstalled CCN instrumental software from the manufacturer as well as the CPI and the bypass flows to maintain near-isokinetic sampling at the HASI inlet.

2.3.5 Aerosol size distribution and number concentration

HALO AMETYST: Total aerosol concentration N_{CN} was measured with condensation nuclei counters (CPC) of the type CPC 5.410 manufactured by GRIMM Aerosol Technik (Ainring, Germany). The CPC are employed in the Aerosol Measurement System (AMETYST) and have a lower cut off diameter of $18.5\,\text{nm}$ at pressures around $150\,\text{hPa}$ (Andreae et al., 2018). The N_{CN} data are STP corrected. Further details on the CPC measurements in Andreae et al., 2018.

2.3.6 Aerosol mass chemical composition

HALO C-ToF-AMS: With a compact time-of-flight aerosol mass spectrometer (C-ToF-AMS) we measured in situ chemical composition of sub-micrometer aerosol particles (e.g., Drewnick et al., 2005; Schmale et al., 2010). The C-ToF-AMS can provide mass concentrations of particulate organics, nitrate, sulfate, chloride, and ammonium. Therefore, the aerosol particles enter the instrumental cavity behind a constant pressure inlet (Molleker et al., 2020) and an aerodynamic lens focuses the sample flow into a narrow beam. In the vacuum chamber, the aerosols are flash vaporized and the resulting molecules in the gas-phase are ionized by electron impact. The ions are analysed by time-of-flight mass spectrometry, separated by their mass-to-charge

ratio, and detected by a micro-channel plate detector. The temporal resolution of the C-ToF-AMS is 30 s corresponding to roughly 6 km flight distance. Further details in Schulz et al., 2018 and Andreae et al., 2018.

2.4 BACO instrumentation

2.4.1 BACO CCN measurements

The size-resolved CCN activity was determined with a one column continuous-flow streamwise thermal gradient CCN counter (CCNC, model CCN-100, DMT, Longmont, USA, Roberts and Nenes, 2005; Rose et al., 2008) combined with a modified differential mobility analyser (DMA, modified model M, Grimm Aerosol Technik, Ainring, Germany, Wiedensohler, 1988) and a condensation particle counter (CPC, model 5412, Grimm Aerosol Technik, Ainring, Germany). An X-ray aerosol charger (Advanced Aerosol Neutralizer 3088, TSI Incorporate, Shoreview, USA) is used to impart a predictable charge distribution of the aerosol sample. The air sample was dried with a custom made continuous condensation drier to maintain a relative humidity in the sample air between 20 and 30 %. Therefore the sheath air in the DMA was dried in a condensation circuit. The circuit was cooling down the sheath air to 6 °C and the condensed water was drained. The dry sheath air dried the sample within the DMA. In the set-up, diameter (D) between 20 and 243 nm were selected for time periods in the range of one minute. The monodisperse aerosol sample was then split between the CCNC and CPC. The CCNC was operated at five different S (0.08, 0.15, 0.23, 0.41, and 0.71 %), which are maintained by a defined temperature gradient within the CCN column (Fig. 2.1). On each S a full size distribution data set was collected. Including the time for flushing the column between different monodisperse samples and to stabilize S, one size scan per S took around 30 minutes, leading to a total time resolution of 2.5 hours for a full size resolved CCN measurement over the set of five S.

The CCN set up at BACO is controlled by a dedicated LabVIEW software (National Instruments, Austin, USA), controlling the commercial DMT instrumental software as well as the DMA and the CPC.

To calculate the hygroscopicity parameter κ, particles that activate as CCN at each S and D are counted in the CCNC as $N_{\text{CCN S,D}}$, while the whole aerosol population of a selected D is counted in the CPC to determine $N_{\text{CN D}}$. The monodisperse aerosol sample of a range of D at certain S is measured. The resulting $N_{\text{CCN S,D}}$ and $N_{\text{CN D}}$ are then used for the calculation of the critical diameter for the CCN activation (d50). These data, along with the particle number size distribution determined by a scanning mobility particle sizer (SMPS, model 5420, Grimm Aerosol Technik, Ainring, Germany) operating independently to the CCNC setup, are then used to calculate the activation curve and the effective hygroscopicity parameter κ using equation 2.2 according to the κ-Köhler model Petters and Kreidenweis, 2007:

$$\kappa = \frac{4A^3}{27D_p^3 ln^2 S_c rit}, \tag{2.2}$$

with D_{p} as dry particle diameter, S_{crit} is the instrumental water vapor supersaturation, and A is the Kelvin term calculated from equation 2.3:

$$A = \frac{4\sigma M_W}{RT\rho_w}, \tag{2.3}$$

with a surface tension (σ of $0.072\,\mathrm{J\,m^{-2}}$), the universal gas constant (R), and water molecular weight (M_{W}) and density (ρ_{W}). Higher values of κ indicate more hygroscopic particles that are more efficient at water uptake and that activate as CCN at lower S in the κ-Köhler model. Further details on the κ calculations and associated errors can be found in Pöhlker et al., 2016.

2.4.2 Aerosol size distribution and number concentration

BACO measurements: At Barbados, the aerosol size distribution was measured with a commercial scanning mobility particle sizer (SMPS, model 5420, Grimm Aerosol Technik, Ainring, Germany). The SMPS sizes the aerosol mobility diameter with a differential mobility analyser (DMA, model M, Grimm Aerosol Technik, Ainring, Germany). The aerosol sample therefore requires an equal charge distribution, which is achieved with a commercial X-ray aerosol charger (Advanced Aerosol Neutralizer 3088, TSI Incorporate, Shoreview, USA) to impart a predictable charge distribution of the aerosol sample. The sample air is dried with a custom build condense drier, where the sheath flow of the DMA is dried in a chiller loop. The dryer maintained an RH in the range of 20 to 30 % of the sample.

2.4.3 Aerosol mass chemical composition

BACO offline analysis: During the EUREC^{4}A campaign, aerosol particles were sampled with a commercial three-stage size selective micro-analysis particle sampler (MPS-3, California Measurements, USA). The three selected size ranges are below $0.7\,\mu\mathrm{m}$ for stage 3, $0.7\,\mu\mathrm{m}$ to $2.5\,\mu\mathrm{m}$ on stage 2 and $2.5\,\mu\mathrm{m}$ until $5.0\,\mu\mathrm{m}$ on stage 1. The aerosol was sampled on carbon-coated copper grids (Ted Pella, USA) for computer-controlled scanning electron microscopy coupled with energy dispersive x-ray spectroscopy (CCSEM/EDX; Quanta 3D). The CCSEM/EDX analysis determined the elemental composition of individual particle and was performed at the Pacific Northwest National Laboratory. Also, samples on silicon wafers (Ted Pella, USA) were collected and analysed with CCSEM/EDX to confirm the carbon measurements from the samples on the carbon-coated copper grids. Further details on the CCSEM/EDX offline analysis of the BACO samples can be found in Royer et al., 2023a.

2.5 Global climate and air-mass origin modeling

In the context of this thesis, data from two climate models are used in the analysis and evaluation of the in situ measurement data. First, model simulations of M_{BC} are utilized to quantify the effects of meteorology, flight pattern and biomass burning on the M_{BC} reductions during the first COVID-19 lockdown in Europe. Second,

the HALO measurements are set into a broader context by comparing them to ten-year monthly averages of model results of $N_{\mathrm{CCN\,0.3}}$. Besides the climate models, also air-mass origin models were utilized in the context of this thesis. Trajectories and supporting information were calculated with HYSPLIT. The two climate models and details on the HYSPLIT use will be outlined in the following sections.

2.5.1 ECHAM/MESSy model

We used the ECHAM/MESSy Atmopheric Chemistry (EMAC) model at T63 horizontal spectral resolution (approx. $1.8\,^{\circ} \times 1.8\,^{\circ}$) and with 31 hybrid terrain following pressure levels up to $10\,\mathrm{hPa}$ in the lower stratosphere (Jöckel et al., 2010; Jöckel et al., 2005; Lelieveld et al., 2019a; Pozzer et al., 2012). The core atmospheric model employed here is the 5^{th} generation European Centre Hamburg (ECHAM5) general circulation model. EMAC includes multiple sub-models that represent the tropospheric and stratospheric processes and their interaction with the biosphere. We used the Modular Earth Submodel System (MESSy, v.2.54, Beer et al., 2020; Jöckel et al., 2010) to link submodels that describe emission, aerosols, atmospheric chemistry, deposition and other processes. The GMXe (Global Modal Aerosol Extension) submodel (Pringle et al., 2010) was employed to simulate the microphysical processes in aerosols and the gas/aerosol portioning. The GMXe organizes the aerosols into hydrophilic and hydrophobic modes. The hydrophilic mode encompasses aerosols in the entire size spectrum (coarse, accumulation, Aitken and nucleation), whereas the hydrophobic mode does not consider the nucleation mode. We updated the assumption in the GMXe by emitting black and organic carbon in accumulation and Aitken modes following a recent study (Paasonen et al., 2016). The gas phase and heterogeneous chemistry was simulated with the MECCA submodel (Sander et al., 2005; Sander et al., 2019). The ORACLE (Organic Aerosol Composition and Evolution) submodel (Tsimpidi et al., 2014; Tsimpidi et al., 2018) was used to simulate the atmospheric evolution and composition of the organic aerosols. The aerosol optical properties were calculated by the AEROPT (AERosol OPTical properties) submodel (Dietmüller et al., 2016; Klingmüller et al., 2019; Lauer et al., 2007; Pozzer et al., 2012), which assumes the aerosol components in each mode to be spherical, well mixed and with volume averaged refractive indices. The radiation calculations were done with the RAD submodel (Dietmüller et al., 2016) which is equipped with logical switches for diagnostically calling the radiation schemes multiple times within one model setup for calculation radiative forcings. The S4D (Sampling in 4 Dimensions) submodel (Jöckel et al., 2010) was used to interpolate and write the model outputs online at the spatial and temporal steps of the EMeRGe EU and BLUESKY aircraft measurements. Apart from these submodels, the following MESSy submodels were enabled: AIRSEA, BIOBURN, CLOUD, CLOUDOPT, CONVEC, CVTRANS, DDEP, E5VDIFF, H2O, JVAL, LNOX, OFFEMIS, ONEMIS, ORBIT, SCAV, SEDI, SORBIT, SURFACE, TNUDGE and TROPOP [*].

The EMAC global simulations, nudged towards the ERA-5 meteorological re-analyses, were performed for two time periods: from January to July 2017 and from January to June 2020 to coincide with the EMeRGe EU and BLUESKY aircraft campaigns re-

[*]Explicit description of each of these submodels can be found in the MESSy submodel list https://www.messy-interface.org/current/auto/messy_submodels.html. The EMAC model is available under license at https://www.messy-interface.org/.

spectively. Over the past decade, EMAC model simulations of aerosols and trace gases have been extensively evaluated against ground measurements and satellite retrievals (Brühl et al., 2015; Kerkweg et al., 2006; Lelieveld et al., 2007; Lelieveld et al., 2019a; Pozzer et al., 2015; Tsimpidi et al., 2018; Zimmermann et al., 2020). Here, we use the monthly varying Community Emissions Data System (CEDS) anthropogenic emission inventory of 2014, Hoesly et al., 2018 at $0.5^\circ \times 0.5^\circ$ resolution for the primary emitted species including CO (carbon monoxide), NO_2 (oxides of nitrogen), SO_2 (sulfur dioxide), NH_3 (ammonia), BC, OC (organic carbon) and NMVOCs (non methane volatile organic compounds). Biomass burning emissions were obtained from the Global Fire Assimilation System (GFAS) inventory Kaiser et al., 2012. The emissions data were then pre-processed and vertically distributed in six emission heights following Pozzer et al., 2012. Residential and commercial fuel use was the largest emitter of BC (46934 t per year) over the region investigated in this study (Fig. 1.3, i.e., latitude between -5 and 16° and longitude between 37.5 and 54.5°), followed by emissions from land transportation (36023 t per year), power generation (22161 t per year), industrial combustion and process (17737 t per year), agricultural waste burning (1283 t per year) and air traffic (0.4067 t per year). For comparisons with the EMeRGe EU and BLUESKY aircraft measurements, BC concentration was diagnosed along the aircraft routes. A sensitivity model simulation was performed by reducing anthropogenic BC emissions from all sectors by $40\,\%$ to compare the model results to the BLUESKY observations.

2.5.2 ECHAM6.3–HAM2.3 simulations of $N_{\mathrm{CCN\ 0.3}}$

We extracted $N_{\mathrm{CCN\,0.3}}$ data from a multi year model run with the ECHAM–HAM model, version ECHAM6.3–HAM2.3 (Neubauer et al., 2019; Tegen et al., 2019). The model is based on the ECHAM atmospheric general circulation model (Stevens et al., 2013), the HAM interactive aerosol module (Stier et al., 2005; Zhang et al., 2012).

The model output is provided in STP and only the certain months out of the ten year data where the HALO campaigns took place were extracted from the data set for the comparison in the vertical profiles. The original model considers the following aerosol species with their compound-specific κ: sea salt ($\kappa_{\mathrm{SS}} = 1.12$), mineral dust ($\kappa_{\mathrm{DU}} = 0$), black carbon ($\kappa_{\mathrm{BC}} = 0$), primary organic aerosol ($\kappa_{\mathrm{POA}} = 0.06$), and sulfate ($\kappa_{\mathrm{SU}} = 0.60$) (Petters and Kreidenweis, 2007; Zhang et al., 2012; Zieger et al., 2017). Note that the model uses sulfate as a surrogate species for all inorganic ions other than sea salt and dust. The κ associated with secondary organic aerosol (Tegen et al., 2019) is typically $\kappa_{\mathrm{SOA}} = 0.037$ according to Zhang et al., 2012.

2.5.3 HYSPLIT backward trajectories and boundary layer height

To better understand the history of the measured air masses as well as to understand some meteorological drivers for aerosol concentrations, e.g., the planetary boundary layer height, backward trajectories were calculated and analysed.

The backward trajectories (BT) were calculated with the HYSPLIT package (version 4, revision 664, October 2014 Rolph et al., 2017; Stein et al., 2015). BT were calculated every 1-min along the aircraft flight track (longitude, latitude, altitude). The

rainfall shown in chapter 5 is the precipitation along the BTs (compare Pöhlker et al., 2019).

To provide the planetary boundary layer height below the flight track for the BLUESKY, EMeRGe EU, EMeRGe Asia and CAFE Africa campaigns (3.1 and 3.2), as shown in figures 2.7, 3.3, 4.3 and 4.7, we used the HYSPLIT BT results and extracted the mixed layer height from each BT starting point (e.g., the first entry in each BT file).

To provide the arithmetic mean of planetary boundary layer below the flight track shown in figures 2.7 and 3.3, we binned the data along the latitude in 0.2° steps. Then we calculated the arithmetic mean for each of these bins.

2.6 Methods to map air pollution in the COVID–19 lockdown (chapters 3 and 4)

2.6.1 Temporal course of response measures to COVID-19

The regional severity of the COVID-19 outbreak and thus the response by the European states was not concerted. A dynamic and scattered change in restrictions was the outcome. Nevertheless, all countries covered by our measurements experienced substantial restrictions during the COVID-19 lockdown. The responses with the largest impact on air pollution include closings of schools and workplaces, the cancellation of public events, stay-at-home requirements and relinquished national and international travel activities (Hale et al., 2021). All these restrictions led to a drastic drop in both personal mobility as well as business trips. In Figure 2.4 we show the governmental response index as an indicator of the confinement strengths for selected countries. The data are downloaded from the Oxford Covid-19 Government Response Tracker [*] and further described in Hale et al., 2021. Besides the patchy responses of particular states and provinces, the EU imposed a comprehensive travel ban for non-EU citizens, with a drop in air-traffic as the outcome. This ban was in effect from 18 March 2020 to 30 June 2020 and thus covered the whole measurement period [†]. Generally, the measurement period falls into the later lockdown period, when many confinements were still in effect and travel activities remained low (Fig. 2.4).

We compare the results of EMeRGe EU to BLUESKY including the CAFE EU project (Chemistry of the Atmosphere: Field Experiment in Europe), from 23 May to 09 June 2020 (Voigt et al., 2022). The central point during BLUESKY was to investigate the effects of the COVID-19 confinements on the atmosphere. This included measurements of urban pollution in the lower troposphere, but also effects of reduced air traffic. Therefore, some measurements were performed in passenger aircraft cruising altitudes in the upper troposphere and lowermost stratosphere (Tomsche et al., 2022; Zauner-Wieczorek et al., 2022).

[*] https://github.com/OxCGRT/covid-policy-tracker, last access 06.07.2021

[†] https://data.consilium.europa.eu/doc/document/ST-9208-2020-INIT/de/pdf

[*] Governmental response index data downloaded from https://github.com/OxCGRT/covid-policy-tracker/blob/3143b76020ef83072086853749c950ac0921ba47/data/timeseries/government_response_index.csv, last access 06.07.2021

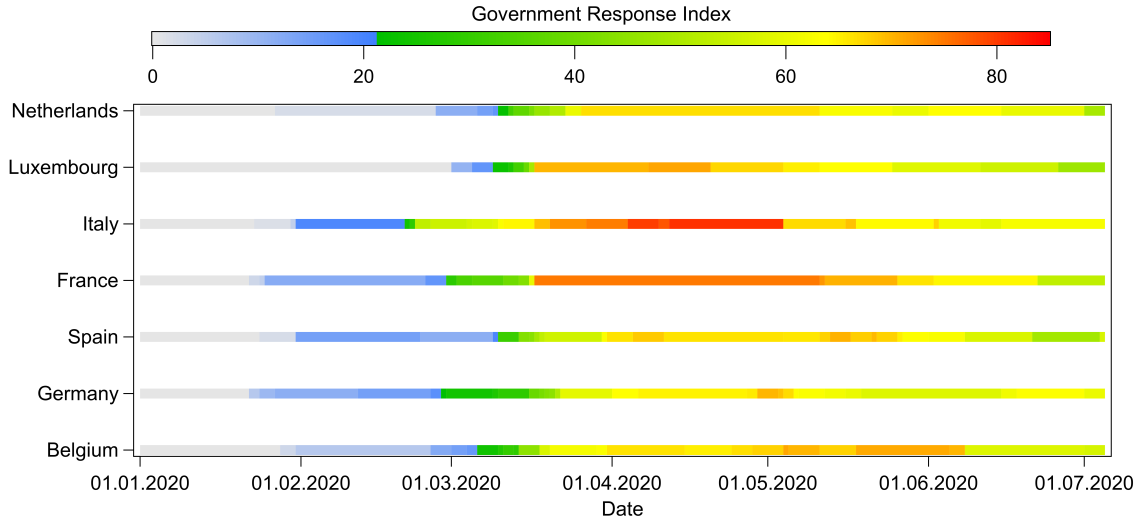

Figure 2.4: Temporal evolution of response on COVID-19 for selected European countries *. Further details on the governmental response index in Hale et al., 2021.

The two compared HALO aircraft campaigns, besides the well comparable studied area, also have some important differences. A major difference, which is also apparent in the vertical distributions of M_{BC} (e.g., Figs. 3.1, 3.3 and 3.2), is that during BLUESKY in 2020, low air traffic volume allowed us to perform more near surface measurement flights. These measurements also include manoeuvres referred to as low approaches (Voigt et al., 2022), i.e. a landing manoeuvre without ground contact followed by a take off. This manoeuvre enabled us to perform more measurements within the PBL during BLUESKY compared to EMeRGe EU in 2017, when high air traffic volume inhibited these low approaches. We later account for these differences in the flight pattern with the EMAC model simulations (sections 2.6.2 and 2.5.1).

The short lifetime of BC hinders it from getting well mixed in the free troposphere and leads to a strong vertical gradient in its concentration. An accumulation of BC can be found in the lower troposphere and especially in the PBL. On top of the PBL there is some turbulent and convective mixing taking place, introducing PBL pollutants, like BC, into the lower troposphere (Andreae et al., 2018; Schwarz et al., 2017). Moreover, BC concentrations in the middle and upper troposphere are rather driven by wildfires and long range transport (Ditas et al., 2018; Holanda et al., 2020) than by anthropogenic pollution. These properties of atmospheric BC led us to focus on the lower troposphere, up to 5000 m above mean sea level.

Albeit both field campaigns have a focus on emissions from major pollution centers (MPC) in Europe, the vertical distribution we report in this study (e.g., Figs. 3.1 and 3.2) is rather representative for M_{BC} in European background conditions (Querol et al., 2013). This can be explained by the fact that large fractions of the measurement flights were performed out of the MPC outflows or in highly aged air masses which also reach remote regions in Europe. All measurement flights were performed during daytime, thus there is no diurnal influence expected in our data set.

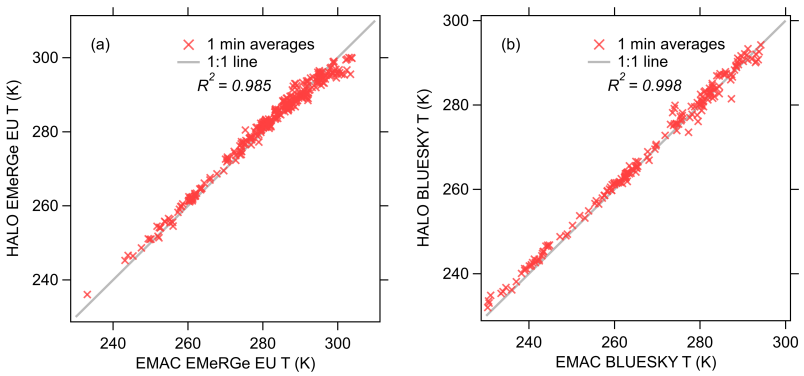

Figure 2.5: Scatter plot for ambient temperature (T) in k from HALO measurements and EMAC model simulations. Grey line is the one to one ratio. (a) corresponds to measurements from 2017 with $R^2 = 0.985$. (b) are 2020 measurements with $R^2 = 0.998$.

2.6.2 Accounting for flight pattern, seasonality and meteorology

The major difficulty in comparing atmospheric aerosol measurements is the strong dependence on multivariate factors as e.g., meteorological, regional and seasonal influence on the distribution and concentration of aerosol. This is due to (I) removal processes driven by the hydrological circle, dominated by cloud processing (Liu et al., 2020; Ohata et al., 2016). (II) The extent of the PBL, determining the concentration and vertical extent of bulk BC and other aerosol species (S. Raj et al., 2021a). (III) Seasonal variations in emission types and strengths. Besides these factors, influencing the actual BC burden, also the flight tracks and the emissions transportation pathways have an essential influence on the measurement results.

We therefore used EMAC model simulations of M_{BC} along the flight tracks with different emission scenarios (details on the EMAC model set up in section 2.5.1). First, we run the model for 2017 and 2020 with unmodified 2014 emission inventories (Hoesly et al., 2018). For the comparison and evaluation we use one minute average measurement data 30 s prior and 30 s after each model output (see 2.6.6, Fig. 2.6 and 2.5). In the next step we calculate the descriptive statistics for vertical bins of 500 m (see section 2.6.3). The difference for each altitude bin between the results of the EMAC runs for 2017 and 2020 is added to the 2020 measurement results to account for differences unrelated to emission changes (e.g., flight pattern, meteorology, and differences in emission patterns as well as emissions from wildfires). The adjusted vertical profile for the 2020 measurements is then compared to the 2017 measurements to quantify the emission reductions according to equation 2.4.

$$BC_{\mathrm{red}} = \frac{M_{\mathrm{BC2017H}} - \left(M_{\mathrm{BC2020H}} + \left(M_{\mathrm{BC2017M}} - M_{\mathrm{BC2020M}}\right)\right)}{M_{\mathrm{BC2017H}}} \tag{2.4}$$

Where BC_{red} is the unit-less reduction factor in M_{BC} attributed to the COVID-19 confinements, M_{BC2017H} and M_{BC2020H} stands for HALO measurements, while the difference between the EMAC results (M_{BC2017M} and M_{BC2020M}) is the adjustment factor introduced earlier.

2.6.3 Vertical and latitudinal distribution of $N_{\mathrm{CCN\,0.3}}$, N_{BC} and M_{BC}

The vertical profiles of M_{BC}, N_{BC}, $N_{\mathrm{CCN\,0.3}}$ (Figs. 3.1, 3.11) and the microphysical BC properties in Figures 3.1 d and 3.5 represent all measurement data with the model output during the two campaigns. For the model evaluation we only used measurement data from 30 seconds prior to and 30 seconds after an EMAC model output (Figs. 2.6 and 2.5). No EMAC simulations for N_{BC} and $N_{\mathrm{CCN\,0.3}}$ were conducted. To obtain the vertical profiles, the measurement and model data are concatenated in 500 m altitude bins. The statistical values given in the particular figure and table are calculated for each bin with IGOR Pro (WaveMetrics Inc. version 7.08). We calculated the arithmetic mean, also referred to as mean within this study.

Also, the log-normal size distributions, given in Figures3.1 d and 3.5, are calculated for the concatenated data in each altitude bin. We used the function according to (Heintzenberg, 1994), provided in equation 2.1.

The cross-section along the latitude for M_{BC} and $N_{\mathrm{CCN\,0.3}}$ in chapter 3 consists of arithmetic averages for all measurement data falling into a grid of $0.2°$ latitude and $500\,\mathrm{m}$ altitude. The terrain height is the arithmetic average height for each certain $0.2°$ latitude grid. The terrain height below the HALO flight track was computed with the online tool GPS visualizer based on the 1 second resolution coordinates of the HALO aircraft [*]. The PBL height is the arithmetic average for the certain $0.2°$ latitude grid for all data with flight altitudes below or equal to $10\,\mathrm{km}$.

2.6.4 Vertically integrated M_{BC} burden

The vertically integrated M_{BC} burden per surface area is calculated as the integral of the median vertical M_{BC} concentration. We only considered vertical bins for the comparison where, during both campaigns, measurements were performed along with EMAC model outputs. Note that the M_{BC} per cubic meter in the vertical profiles is STP corrected. Thus, we scaled the altitude bins with a scaling factor (S_{P}, Table 3.2) based on the pressure altitude. Equation 2.5 shows the calculation of (S_{P}) with h_{bin} as the altitude of the corresponding altitude bin in the vertical profile.

$$S_{\mathrm{P}} = \frac{1}{(1 - \frac{h_{\mathrm{bin}}}{4307.69396\,\mathrm{m}})^{5.2553026}} \tag{2.5}$$

2.6.5 EMAC regional radiative impact of the changed M_{BC}

The radiative effect due to a $40\,\%$ reduction in M_{BC} is calculated with EMAC for the local radiative forcing (longitude between -5 and $16°$ and latitude between 37.5 and $54.5°$ N) for the months May and June. The radiative effect is the difference between one run with full aerosol emissions and one with $40\,\%$ reduced anthropogenic M_{BC} emissions. The calculations are done for short wave radiation with clear sky conditions.

[*] Online accessible at https://www.gpsvisualizer.com/elevation, last access 20.02.2022

2.6.6 EMAC model evaluation

Besides the comparison between the EMAC results for M_{BC} (Fig. 2.6), we also compare the modeled and observed ambient temperature as an independent variable (Fig. 2.5). The R^2 for the ambient temperature observation-model comparison is close to unity, indicating a successful nudging of synoptic variables and that the meteorological conditions during the relevant time period are simulated adequately. Locations of peaks in M_{BC} due to biomass burning emissions during EMeRGe EU (Fig. 2.7a) are captured by the model, whereas concentrations are underestimated (Figs. 2.6, 3.2a and 2.7a). The median for the $500\,\mathrm{m}$ bins, however, turns out to be robust against these outliers (R^2 of 0.76 with a median absolute deviation (MAD) of $0.12\,\mu\mathrm{g\,m^{-3}}$ for 2017 and $R^2 = 0.90$, MAD $= 0.07\,\mu\mathrm{g\,m^{-3}}$ for 2020), whereas the average for the vertical profiles is more sensitive to peak concentrations, leading to a significantly smaller $R^2 = 0.43$ with a high standard deviation (STD) of $0.57\,\mu\mathrm{g\,m^{-3}}$ for EMeRGe EU. For BLUESKY the $R^2 = 0.94$ with STD $= 0.16\,\mu\mathrm{g\,m^{-3}}$ is slightly higher, compared to median values.

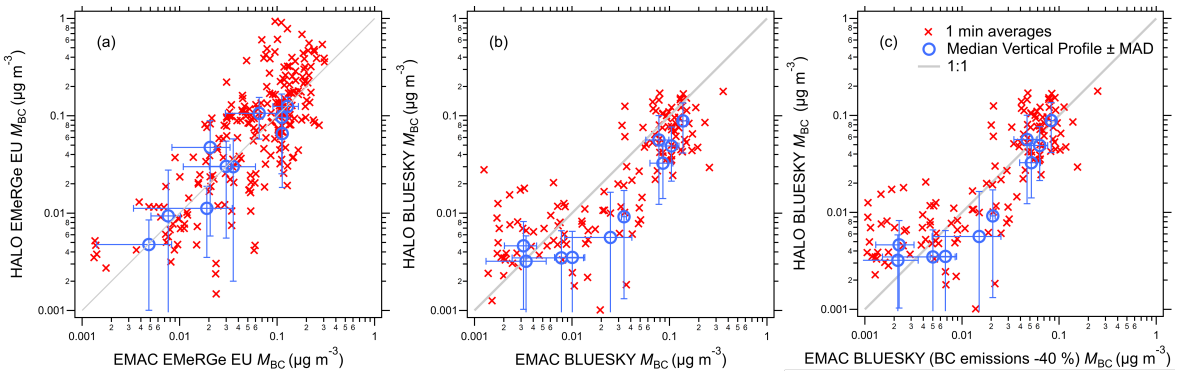

Figure 2.6: Scatter plot for median M_{BC} values of HALO measurements and EMAC model results. Red data shows the comparison of 1 minute averages. In blue, median concentrations as used for the vertical profiles are shown. Error bars are one median absolute deviation (MAD) for the vertical merged data in $500\,\mathrm{m}$ altitude bins. Data shown is for the compared altitude up to $5000\,\mathrm{m}$. (a) corresponds to measurements from 2017 with $R^2 = 0.76$. (b) are 2020 measurements with initial emissions in the EMAC model and $R^2 = 0.90$. (c) as (b) but with $40\,\%$ reduced anthropogenic emissions in EMAC simulation and $R^2 = 0.90$.

2.6.7 EUROSTAT data for fossil and solid fuels

Data published by EUROSTAT is used to investigate the reductions in fossil fuel demand during the confinement period in 2020 *. For figure 3.8, we use the terminology suggested by EUROSTAT. However, to make these rather technical terms more clear, we refer, in section 3.1.1, to motor spirits as gasoline and to kerosene as aircraft fuel. Furthermore, the difference in solid fossil fuel (which is the compilation of hard coal, including anthracite, coking coal and other bituminous coal; brown coal, including sub-bituminous coal and lignite; and coal products, including patent fuel, coke oven coke, gas coke, coal tar and brown coal briquettes †) demand between

*Data downloaded from https://ec.europa.eu/eurostat/databrowser/view/NRG_JODI__custom_482779/default/table last access 25.01.2021

†Data described here https://ec.europa.eu/eurostat/statistics-explained/index.php?oldid=449721, last access 19.04.2022)

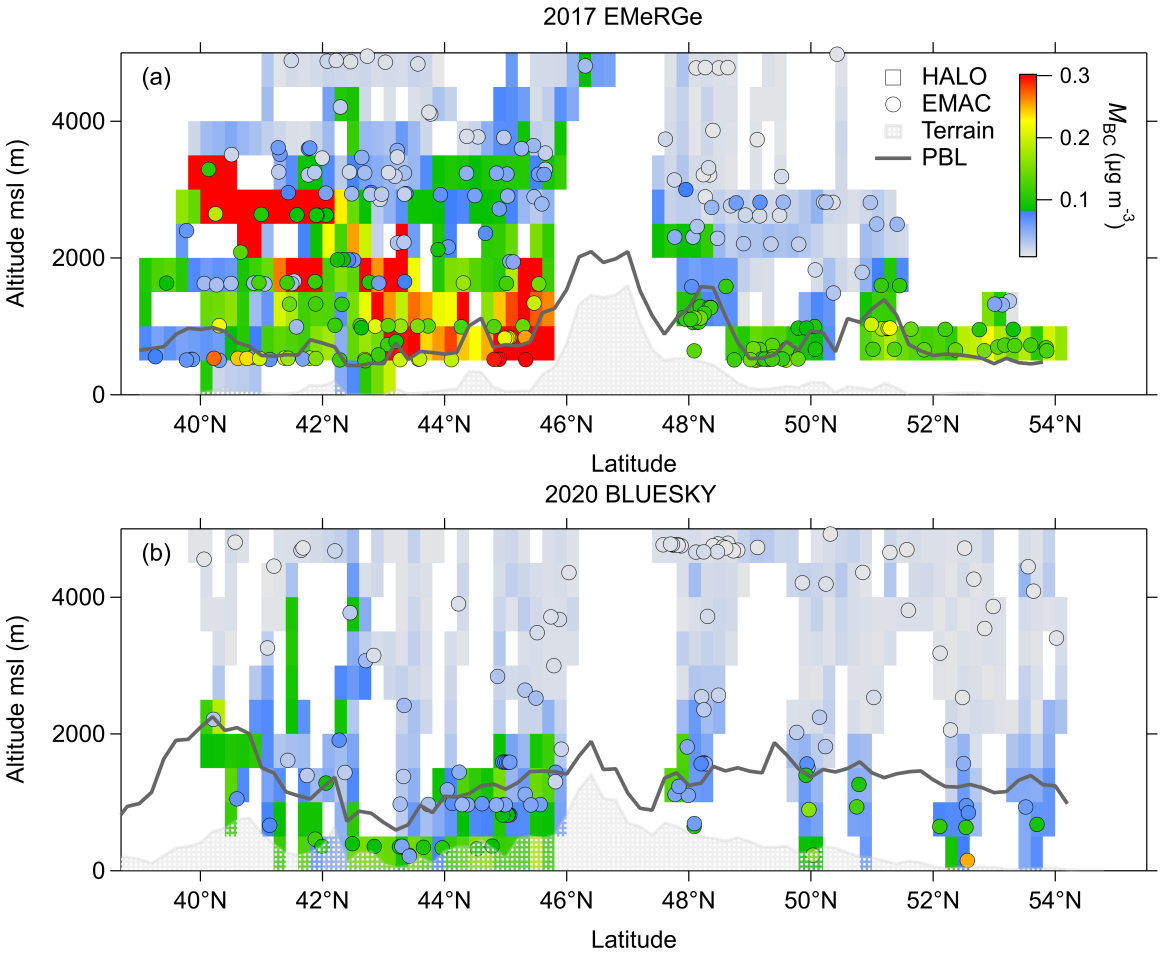

Figure 2.7: (a) Cross section of M_{BC} for 2017 EMeRGe EU measurements (rectangle marker). Arithmetic mean for all measurement data falling into a grid point of 0.2 ° latitude and $500\,\mathrm{m}$ altitude. The color scale ranges from 0 to $0.3\,\mu\mathrm{g\,m^{-3}}$. Means exceeding this range are shown in red. Round marker EMAC model results are displayed without further modification. (b) like (a) but for the 2020 BLUESKY measurements. The grey shading is the mean terrain height below flight track and the grey solid line shows the planetary boundary layer height below flight track (details in section 2.5.3).

2017 and 2020 is used to analyse important drivers for the BC reduction, other than the COVID-19 confinements in 2020 *.

2.6.8 Data availability

The data set for the vertical distribution of M_{BC} (Table 2.1), N_{BC} (Table 3.1), the rBC core size distribution (Table 3.3) and the vertically integrated M_{BC} burden (Table 3.2) is provided in the supplementary material. The original data set is available under https://doi.org/10.17617/3.GKRXCN. Further data from the two HALO missions is available at the HALO database (https://halo-db.pa.op.dlr.de/).

*Data downloaded from https://ec.europa.eu/eurostat/databrowser/view/NRG_CB_SFF__custom_1131819/default/table?lang=en last access 08.07.2021 and https://ec.europa.eu/eurostat/databrowser/view/NRG_CB_SFFM__custom_1558586/default/table?lang=en last access 12.11.2021

Table 2.1: Average and median M_{BC} from HALO observations and EMAC simulations. Values in column altitude represent centre of corresponding $500\,\mathrm{m}$ altitude bin.

	EMeRGe EU				BLUESKY					
	Observations		EMAC		Observations		EMAC		EMAC 40 % reduced	
Altitude [m]	Avg [$\mu g\,m^{-3}$]	Median [$\mu g\,m^{-3}$]	Avg [$\mu g\,m^{-3}$]	Median [$\mu g\,m^{-3}$]	Avg [$\mu g\,m^{-3}$]	Median [$\mu g\,m^{-3}$]	Avg [$\mu g\,m^{-3}$]	Median [$\mu g\,m^{-3}$]	Avg [$\mu g\,m^{-3}$]	Median [$\mu g\,m^{-3}$]
250	0.083	0.066	0.113	0.113	0.099	0.089	0.156	0.137	0.110	0.097
750	0.172	0.125	0.143	0.128	0.064	0.049	0.109	0.105	0.077	0.073
1250	0.132	0.097	0.119	0.112	0.072	0.056	0.079	0.078	0.056	0.055
1750	0.174	0.106	0.069	0.065	0.045	0.033	0.079	0.086	0.055	0.060
2250	0.119	0.030	0.043	0.030	0.034	0.009	0.031	0.034	0.022	0.024
2750	0.140	0.030	0.044	0.036	0.019	0.006	0.027	0.025	0.019	0.017
3250	0.103	0.047	0.028	0.021	0.012	0.004	0.015	0.010	0.011	0.008
3750	0.023	0.011	0.028	0.019	0.010	0.003	0.011	0.008	0.008	0.006
4250	0.029	0.009	0.010	0.008	0.011	0.005	0.004	0.003	0.003	0.002
4750	0.013	0.005	0.007	0.005	0.008	0.003	0.006	0.003	0.004	0.002

2.7 Methods to analyse relationships between CCN and BC (chapter 5)

The methods for the chapter 5 and the selected flight segments with characteristic CCN to BC signatures from the HALO aircraft campaigns are outlined below.

2.7.1 Selection of characteristic atmospheric conditions

The plumes with dominant contribution of a specific combustion source were identified according to the geographical location and season, as outlined below, in order to define their characteristic regimes in the BC-CCN scatter plots. Here, we first present the selected plumes where we encountered stable conditions of one single combustion aerosol source (5.1). Second, we show the criteria for plume selection in more diverse atmospheric conditions, where we either had comparably few data points or a superposition of different pollution sources (5.2 and 5.3):

- **Urban pollution:** A focal point of the CAFE EU aircraft campaign was the investigation of urban pollution at low altitudes over a variety of European cities. During the time the campaign took place, biomass emissions did not affect the flights to a significant extent, according to satellite-based fire maps and associate BTs. For our analysis, we only included the city plumes with high CCN levels (i.e., $N_{CCN} > 1000\,\mathrm{cm^{-3}}$). In total, 62 1-min averages fulfilled these criteria.
- **Lightly aged Amazonian BB:** The smoke from fires in the Amazon was investigated during ACRIDICON-CHUVA. We selected the flights AC12 and AC13 (18 and 19 September 2014) over the deforestation area and selected the periods where the rBC geometric mean diameter is smaller than $195\,\mathrm{nm}$, which corresponds mostly to measurements below 2 km altitude. In total, 70 1-min averages fulfilled this criterion.
- **Highly aged African BB:** The westerly outflow of highly aged African BB smoke over the Atlantic Ocean – which also reaches the Amazon eventually – was probed during CAFE Africa. Flight segments were selected according to the geographic area, restricted to the South Atlantic Ocean with latitude $< 9.5\circ$ and longitude $< 0\circ$. This area was chosen in order to avoid influences of urban

pollution from Western Africa or mineral dust in higher latitudes (Holanda et al., 2023). In total, 305 1-min averages fulfilled these criteria.

Also, plumes with more diverse atmospheric conditions were probed, with either comparably few data points or a superposition of different pollution sources. These plumes are shown in the case study section and classified based on the three predefined regimes. The selection criteria for the individual cases are given in Table 2.2 and the criteria listed below:

- **Case studies on lightly aged BB smoke over Europe and Asia:** We defined BB plumes based on the strongly increased M_{BC} and N_{BC} within our measurements and on information from the corresponding flight reports. The specific data selection criteria can be found in Table 2.2.
- **Case study on highly aged African BB smoke over the Amazon:** For African BB emissions transported into the Amazon basin, the deconvolution method presented in Holanda et al., 2023 (with the same parameters and constraints) was applied to distinguish African from South American smoke. Therefore, a bimodal fit was applied to every rBC mass size distribution. Two distinctive flight segments of the ACRIDICON-CHUVA flight AC07 (06 September 2014) agreed with the size distribution of African smoke. In total, 21 1-min averages fulfilled these criteria.
- **Case study on highly aged African BB over the Brazilian shore:** For the LRT African BB smoke encountered over the Brazilian shore we used the plumes identified in Holanda et al., 2020. The event day of particular relevance was 30 September 2014, during ACRIDICON-CHUVA flight AC19. In total, 87 1-minute averages fulfilled these criteria.
- **Case studies on urban pollution over Europe and Asia:** The outflow of mega populated centers were selected according to following criteria (i) specific measurement flights, (ii) geographical coordinates, (iii) elevated M_{rBC} and (iv) analysis of backward trajectories. The parameters for the specific case studies are summarized in Table 2.2.

Table 2.2: Selected BB and urban plumes during aircraft mission in Europe and Asia with relevant parameters. Number of observations is the total count of 1-minute averages shown in the respective BC-CCN scatter plot.

Case study denomination	Figure	Flight date	Flight	M_{rBC} [$\mu\mathrm{g\,m^{-3}}$]	Latitude [°]	Longitude [°]	Altitude [m]	Observations number
BB dominated plumes								
Thailand	5.5	12 March 2018	E-A-03			< 104.0		170
Thailand	5.5	07 April 2018	E-A-14			< 104.0		
Marseille pure BB	5.7A	24 July 2017	E-EU-07	> 0.23	< 43.2			13
Marseille BB and urban	5.7A	24 July 2017	E-EU-07	> 0.23	> 43.2			7
Portugal BB	5.8	28 July 2017	E-EU-09		< 44.0	< 10.0	> 2200	103
Italian and Croatian aged BB	5.9	20 July 2017	E-EU-06		< 42.0	< 12.6	> 1000	14
Urban dominated plumes								
Barcelona urban	5.14	20 July 2017	E-EU-09		< 44.0	< 10.0	< 2200	74
Nagoya urban	5.15	30 March 2018	E-A-13		> 137.0			66
Rome urban mixed 1	5.16	11 July 2017	E-EU-03		$42.0 < \mathrm{Lat} < 44.5$	$13.0 < \mathrm{Lon} < 16.0$		105
Rome urban mixed 2	5.16	20 July 2017	E-EU-06		$42.0 < \mathrm{Lat} < 44.5$	$13.0 < \mathrm{Lon} < 16.0$		
London urban 1	5.17A	17 July 2017	E-EU-05			< 0		135
London urban 2	5.17A	26 July 2017	E-EU-08		> 52.0			
Po Valley urban mix 1	5.17B	11 July 2017	E-EU-03		$44.6 < \mathrm{Lat} < 46.0$	> 9.0		134
Po Valley urban mix 2	5.17B	20 July 2017	E-EU-06		$44.6 < \mathrm{Lat} < 46.0$	> 9.0		
China urban 1	5.18	22 March 2018	E-A-07		$25.0 < \mathrm{Lat} < 33.0$			
China urban 2	5.18	24 March 2018	E-A-08		$25.0 < \mathrm{Lat} < 33.0$			513
China urban 3	5.18	26 March 2018	E-A-09		$25.0 < \mathrm{Lat} < 33.0$			

2.7.2 Backward trajectories and MODIS data products

The backward trajectories (BT) were calculated with the HYSPLIT package (version 4, Revision 664, October 2014) (Rolph et al., 2017; Stein et al., 2015). BTs were calculated every 1-min along the aircraft flight track (longitude, latitude, altitude). Only BTs below $10\,\mathrm{km}$ altitude were included. The rainfall is the precipitation along the BT (compare Pöhlker et al., 2019). Information retrieved from the BT analysis are combined with the Moderate Resolution Imaging Spectroradiometer (MODIS) "Fires and Thermal Anomalies (Day and Night)" and "Corrected Reflectance (True Color)" product, downloaded from https://worldview.earthdata.nasa.gov/ (last access 06 Sep 2021).

2.8 Methods for the analysis of volcanic aerosols (chapter 6)

2.8.1 Trace gas measurements

The O_3 mixing ratios are measured via UV absorption and chemiluminescence by the FAIRO instrument (chemiluminescence data with a total uncertainty of 2.5 % Zahn et al., 2012). Further details on the trace gas measurements in Nussbaumer et al., 2021.

2.8.2 Aerosol size distribution retrieved from CCN measurements

We determine a theoretical critical diameter for the HALO CCN measurements at $S = 0.3\,\%$. Therefore we used the hygroscopicity parameter κ_{chem} calculated from the measured organic (ϵ_{org}) and inorganic mass fraction ($\epsilon_{\mathrm{inorg}}$) following (Pöhlker et al., 2023).

$$\kappa = \epsilon_{\mathrm{org}}\kappa_{\mathrm{org}} + \epsilon_{\mathrm{inorg}}\kappa_{\mathrm{inorg}} \tag{2.6}$$

This allows us to use κ in equation 2.7 (Köhler, 1936; Petters and Kreidenweis, 2007; Rose et al., 2008) and to iteratively solve the equation for D_{crit}. It has to be noted that this method to determine a theoretical lower cut off diameter for $N_{\mathrm{CCN\ 0.3}}$ and the data has large uncertainty for the following reasons. The aerosol chemical composition has a lower-cut-off diameter not including all potential $N_{\mathrm{CCN\ 0.3}}$, thus the actual chemical composition may differ from the one applied in equation 2.6. The resulting critical diameter retrieved from CCN data, however, agrees well with what to expect from literature values (e.g., Petters and Kreidenweis, 2007) and provides helpful data for further studies on volcanic aerosol plumes in the TTL region.

The critical diameter of particles detected by the CCNC was calculated using a κ of 0.6 by the modified Köhler equation (Köhler, 1936) presented in Petters and Kreidenweis, 2007, as following:

$$S(D_s) = \frac{D_{wet}^3 - D_s^3}{D_{wet}^3 - (1-\kappa)D_s^3} \exp\left(\frac{4\sigma_s M_w}{RT\rho_w D_{wet}}\right) \tag{2.7}$$

While σ_s is the solution droplet's surface tension, M_w is the molar weight of water, ρ_w is the water density, R is the universal gas constant, T is the absolute temperature, and D_{wet} is the droplet diameter at a given S or RH, with $S = RH/100\,\%$ and D_s is the diameter of the solid particle.

2.8.3 Vertical distribution of $N_{CCN\ 0.3}$

We compare the vertical distribution of $N_{CCN\ 0.3}$ from the ECHAM–HAM model with our in situ measurements conducted onboard the HALO aircraft with the HALO CCNC (see 2.2.1). The area of comparison is indicated in figure 4.1 and comprises all HALO measurements within 23 °N and 10 °S over the Atlantic Ocean. Both data sets are corrected to standard conditions (STP, T=273.15 K, p=1013.25 hPa). While the measurements were conducted in 2018 (see 2.1.1), the ECHAM-HAM results are monthly means for August and September in the years 2003 until 2012. This comparison facilitates a classification of the HALO measurements with snapshot character into a bigger context.

2.8.4 HYSPLIT backward trajectory analysis

Due to longer aerosol residence times in the UTLS, 30 days backward trajectories were calculated with the HYSPLIT package (version 4, revision 664, October 2014 Rolph et al., 2017; Stein et al., 2015). Three circles with a diameter of $1°$ were defined, one out of the volcanic plume at $30.5°$ W and $14.3°$ N. This circle corresponds to the measurements on the plume's altitude and on the same flight leg as the plume was measured (Fig. 6.3 around 16:15 UTC). The other two circles correspond to measurements within the volcanic plume at $26.5°$ W and $12°$ N and $25°$ W and $10°$ N (in Fig. 6.3 at 17:00 and 17:50 UTC respectively). From each circle 100 single BT were emitted from random locations within the circle. All BT are starting at 17:00 UTC at the 17. August 2018 in an altitude of $14.5\,\mathrm{km}$. The BT density was then calculated for each 1 times $1°$ grid. The BT age since measurement is the average age of each BT falling into one grid cell with a total of at least 15 BT points within the grid.

2.8.5 Radiative transfer modeling of heating rate in aerosol plume

To test whether these changes can be explained by absorption of UV radiation by the remaining SO_2 and LW radiation by the sulfate aerosol, the heating rate is calculated with a radiative transfer model (libRadtran, Emde et al., 2016; Mayer and Kylling, 2005) combined with the MOPSMAP tool (Gasteiger and Wiegner, 2018) to calculate the vertical optical properties of the in situ measured aerosol data.

The vertical profiles for pressure, temperature, air density, O_3, O, water vapor, CO_2, NO_2, CH_4, N_2O, CO are from the Anderson et al., 1986 reference atmospheric model "Tropical". The solar zenith angle in the calculations is the maximum of the particular measurement day with $12°$ N $25°$ W at 13:44:11. The aerosol layer has a log-normal size distribution with a count median radius of $50\,\mathrm{nm}$ and a $\sigma_g = 2$. The aerosols are assumed to be spherical with a hygroscopicity, $\kappa = 0.6$ and a relative humidity of 20%.

The OPAC software (Optical Properties of Aerosols and Clouds Hess et al., 1998) was used to compute the refractive indices.

CHAPTER 3

Changed aerosol burden during COVID-19 confinements

This chapter is based on the peer-reviewed and published manuscript and includes figures from another peer-reviewed study and unpublished work outlined below:

Krüger, O. O.; Holanda, B. A.; Chowdhury, S.; Pozzer, A.; Walter, D.; Pöhlker, C.; Andrés Hernández, M. D.; Burrows, J. P.; Voigt, C.; Lelieveld, J.; Quaas, J.; Pöschl, U., and Pöhlker, M. L.: "Black carbon aerosol reductions during covid-19 confinement quantified by aircraft measurements over europe". *Atmospheric Chemistry and Physics*, 22, 13. (2022), pp. 8683–8699. DOI: 10.5194/acp-22-8683-2022

I wrote the manuscript with input from my co-authors and I carried out the peer-review process in ACP. The original idea for the study was developed by B. Holanda, M. Pöhlker and myself. For the BLUESKY data set, I conducted the measurements of soot aerosol onboard the HALO aircraft. For the EMeRGe EU data set I was involved in the campaign preparations and during the measurement campaign in data evaluation. The SP2 raw data treatment was performed by B. Holanda. The HYSPLIT backward trajectories (BT) were calculated by D. Walter. A. Pozzer and S. Chowdhury provided the EMAC model data. I performed the data evaluation, analysis and produced all figures.

Hernández, M. D. A.; Hilboll, A.; Ziereis, H.; Förster, E.; Krüger, O. O.; Kaiser, K.; Schneider, J.; Barnaba, F.; Vrekoussis, M.; Schmidt, J.; Huntrieser, H.; Blechschmidt, A.-M.; George, M.; Nenakhov, V.; Harlass, T.; Holanda, B. A.; Wolf, J.; Eirenschmalz, L.; Krebsbach, M.; Pöhlker, M. L.; Hedegaard, A. B. K.; Mei, L.; Pfeilsticker, K.; Liu, Y.; Koppmann, R.; Schlager, H.; Bohn, B.; Schumann, U.; Richter, A.; Schreiner, B.; Sauer, D.; Baumann, R.; Mertens, M.; Jöckel, P.; Kilian, M.; Stratmann, G.; Pöhlker, C.; Campanelli, M.; Pandolfi, M.; Sicard, M.; Gómez-Amo, J. L.; Pujadas, M.; Bigge, K.; Kluge, F.; Schwarz, A.; Daskalakis, N.; Walter, D.; Zahn, A.; Pöschl, U.; Bönisch, H.; Borrmann, S.; Platt, U., and Burrows, J. P.: "Overview: on the transport and transformation of pollutants in the outflow of major population centres –observational data from the emerge european intensive operational period in summer 2017". *Atmospheric Chemistry and Physics*. (2022). DOI: 10.5194/acp-22-5877-2022

I was in the lead author team, for this publication. For the EMeRGe EU data set I was involved in the campaign preparations and during the measurement campaign in data evaluation. I analysed the data after the campaign. I prepared figure 12 and 21 and provided the original idea and measurement data for figure 31c in the original publication.

I wrote and designed the evaluation of the changed CCN burden during the confinements. For the BLUESKY data set, I conducted the CCN-measurements onboard the HALO aircraft. For the EMeRGe EU data set I was involved in the campaign preparations and during the measurement campaign in data evaluation. I analysed the HYSPLIT backward trajectories which were calculated by D. Walter. I defined the grids and performed the comparison between the ECHAM-HAM CCN data and the HALO measurements. ECHAM-HAM data was provided by M. Salzmann and J. Quaas.

This manuscript includes data sets from the following field experiment:
EMeRGe EU and BLUESKY

3.1 Black carbon aerosol reductions during COVID-19 confinement quantified by aircraft measurements over Europe

The focal point of this chapter is the comparison between two HALO measurement campaigns, conducted over south and west Europe in 2017 and 2020 (Fig. 1.3 and section 2.1.1). By using EMAC model simulations we quantify to what extent the pandemic-related confinements in 2020, on one hand, and other factors such as meteorology, on the other hand, influenced the observed M_{BC} reduction. In addition, the atmospheric distribution of BC and its dependency on the magnitude of emissions is analysed. Furthermore, we examine the regional direct radiative effect of the BC reduction.

Determining the adjusted vertical distribution of the 2020 measurements (Fig. 3.1 d and section 2.6.2) enables us to quantify the anthropogenic emission reductions between both campaigns. Consequently, we calculated the difference between the two vertical distributions of M_{BC}, retrieved from the two initial EMAC model simulations (Fig. 3.1 a and b). In the following we added this difference to the 2020 measurements (section 2.6.2), to generate an adjusted vertically integrated M_{BC} burden (section 2.6.4) of $129\,\mu\mathrm{g\,m^{-2}}$ for 2020, whereas the actual measured burdens are $113\,\mu\mathrm{g\,m^{-2}}$ for 2020 and $219\,\mu\mathrm{g\,m^{-2}}$ for 2017. Accordingly, the difference between the adjusted M_{BC} burden for 2020 to the actual measurements from 2017 of $90\,\mu\mathrm{g\,m^{-2}}$ is attributable to reduced anthropogenic emissions. This value corresponds to a $41\,\%$ reduction in median M_{BC} burden.

In accordance with the analysis described above (also, section 2.6.2), we performed an evaluation of the regional sensitivity of the emission reductions. Therefore we separated our data set at a latitude of 47° N due to different vertical distributions and absolute concentrations north and south of that threshold (Fig 3.3). Beside the differences M_{BC} the threshold also represents a rough estimate of the Alps corresponding to the HALO flight tracks. South of 47° N the median adjusted vertically integrated M_{BC} burden is 37 % reduced whereas concentrations north of 47° N are 38 % lower in 2020 compared to 2017 (Fig. 3.2). These results are in a good agreement with the reductions of 41 % we found for all data, showing that there is only little regional sensitivity for the reported M_{BC} reductions.

Beside an emission reduction, also other factors influence the differences in measured M_{BC}. Figure 3.1 shows the median vertical distribution of measured and modeled M_{BC}. For the two initial model runs (Figs. 3.1 a and 3.1 b) we used identical emission inventories for the year 2014 (Hoesly et al., 2018). This approach enables us to compare our measurements with an quantity independent from anthropogenic emissions (i.e. we apply the same emissions for both campaigns) and only account for drivers other than emission reductions for differences in M_{BC}. While the 2017 measured mass burden is $4\,\%$ overestimated by the model (Fig. 3.1 a and Table3.2), the measurements under confinement conditions are overestimated by $47\,\%$ in the model, when considering 2014 emissions (Fig. 3.1 b). These results demonstrate that meteorological influences, different flight patterns and differences in seasonal emissions cannot explain the observed change in lower tropospheric M_{BC}. As metric for the direct comparison of the two measurement campaigns, we use the model results

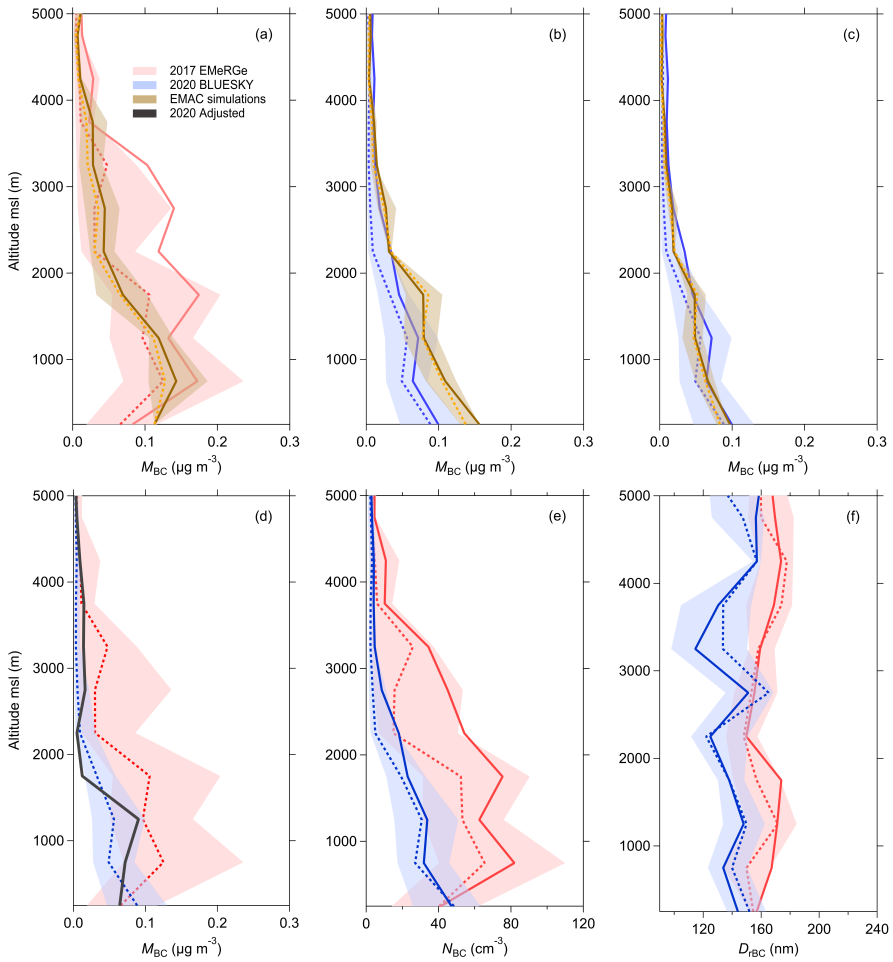

Figure 3.1: Vertical distributions of measured and modeled M_{BC} (a, b, c, and d). Solid lines represent arithmetic mean values, dashed lines represent median values shading marks the interquartile range. (a) shows EMeRGe EU 2017 measurements and EMAC simulations with initial 2014 emission inventories. (b) shows BLUESKY 2020 measurements and EMAC simulations with initial 2014 emission inventories. (c) shows BLUESKY measurements and EMAC simulations with anthropogenic BC emission reduced by $40\,\%$. (d) shows EMeRGe EU and BLUESKY measurements (as also shown in panels (a) and (b)) for comparison between the two campaigns. The grey solid line shows the adjusted median M_{BC} concentration expected for BLUESKY measurements in 2020 (details see section 2.6.2). The adjusted value is based on non-confinement influences retrieved from the difference in the EMAC simulations for BLUESKY and EMeRGe EU with the 2014 emission inventories. It represents the expected measurement value, assuming the same meteorological and seasonal conditions for both campaigns. The difference between the medians of EMeRGe EU and adjusted BLUESKY represents the emission reduction. (e) shows the measured N_{BC} for EMeRGe EU in 2017 and BLUESKY in 2020. (f) shows the geometric mean refractory BC core diameters (D_{rBC}) for EMeRGe EU in 2017 and BLUESKY in 2020. Further details about the vertical distributions in 2.6.3 and 2.5.3.

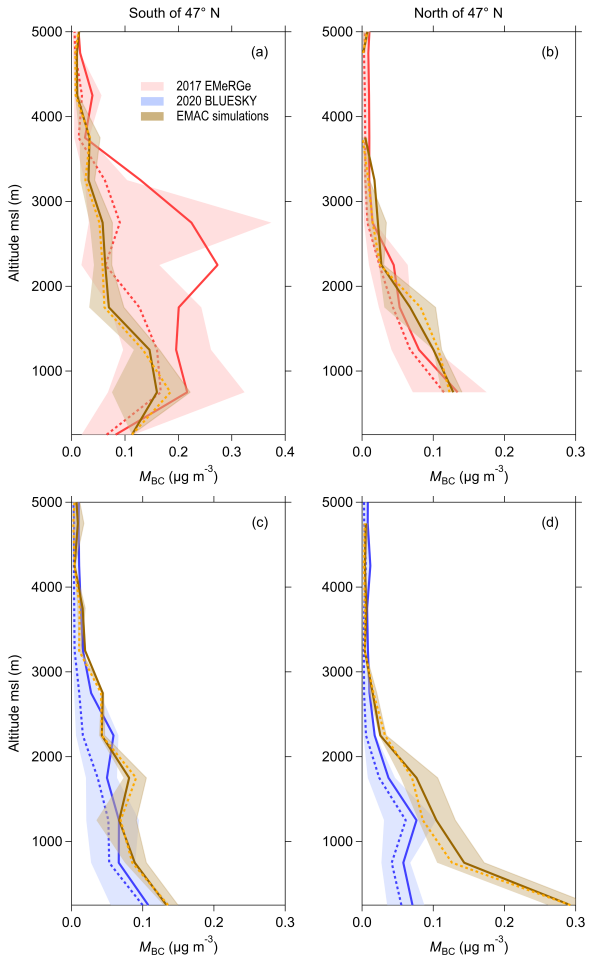

Figure 3.2: Vertical distribution of M_{BC} north and south of $47°$ N. Solid lines represent arithmetic mean values, dashed lines represent median values shading marks the interquartile range. (a) and (b) show data for EMeRGe EU from 2017, (c) and (d) for BLUESKY from 2020. Note that the x-axis in (a) ranges between 0 to $0.4\,\mu\mathrm{g\,m^{-3}}$.

to adjust our measurements. Therefore, we calculate the difference of the model results for 2017 and 2020 for each altitude bin. Overall, the difference in modeled M_{BC} between 2020 and 2017 accounts for a reduction of $7\,\%$ relative to 2017. This difference is a consequence of different flight pattern, meteorological conditions and seasonal variations in emissions.

We find a good agreement for the the shape of the vertical BC distribution for measured and modelled M_{BC} profiles. Even though the concentrations in 2020 are strongly overestimated the vertical extent is well described by the EMAC simulations (see also 3.1 c with reduced anthropogenic emissions). The Pearson coefficient of determination (R^2) for the vertical profiles of the observation-model comparison is 0.76 for 2017 and 0.90 for 2020 (Fig. 2.6). Based on the good agreement for the general vertical distribution during both campaigns, we conclude, that the shape of the vertical distribution of anthropogenic BC in the lower troposphere remains unaffected by the emission changes in 2020.

We compare the median vertical profiles in this study to simplify the heterogeneously distributed M_{BC} over Europe (Fig. 3.3). The vertical distribution of BC is strongly influenced by the planetary boundary layer (PBL) height, whereas its geographic pat-

Table 3.1: Average and median N_{BC} from HALO observations. Values in column altitude represent centre of corresponding $500\,\mathrm{m}$ altitude bin.

	EMeRGe EU Observation		BLUESKY Observation	
Altitude [m]	Avg [cm^{-3}]	Median [cm^{-3}]	Avg [cm^{-3}]	Median [cm^{-3}]
250	41.1	40.3	47.1	48.5
750	81.8	65.4	31.8	27.0
1250	62.5	53.1	33.7	30.7
1750	75.3	52.3	22.9	19.3
2250	54.2	15.0	18.0	5.1
2750	45.0	15.6	8.6	3.5
3250	34.4	25.8	4.7	2.4
3750	10.2	6.0	4.1	2.4
4250	10.8	4.7	4.2	3.2
4750	4.6	2.9	3.2	2.6

Table 3.2: Vertically integrated M_{BC} burden per surface area. BLUESKY adjusted is the BLUESKY observation and the EMAC model retrieved adjustment (see section 2.6.2). Values in column altitude represent centre of corresponding $500\,\mathrm{m}$ altitude bin. Pressure altitude scaling factor calculated as described in section 2.6.4. Last row provides column sum of vertically integrated M_{BC} burden.

Altitude [m]	Pressure altitude scaling factor	EMeRGe EU Median [$\mu g\,m^{-2}$]	BLUESKY Median [$\mu g\,m^{-2}$]	BLUESKY Adjusted Median [$\mu g\,m^{-2}$]
250	1.03	31.86	43.00	31.23
750	1.09	57.14	22.40	32.87
1250	1.16	41.51	24.26	38.88
1750	1.24	42.88	13.19	4.97
2250	1.32	11.48	3.49	1.89
2750	1.40	10.71	2.01	5.84
3250	1.49	15.86	1.18	4.70
3750	1.59	3.52	1.09	4.61
4250	1.70	2.75	1.36	2.67
4750	1.81	1.31	0.88	1.28
Sum		219.04	112.86	128.95

tern is more sensitive to emission hot spots like large cities or industrial areas. Elevated M_{BC} during BLUESKY were mostly confined to the PBL in good agreements with observations for western Europe in the course of EMeRGe EU and literature (e.g., Ding et al., 2019). In southern Europe, however, M_{BC} was stronger decoupled from the PBL and we also observed high concentrations within the lower free troposphere in 2017 and occasionally in 2020. During both campaigns, M_{BC} in southern Europe exceeds values in western Europe (at latitudes North of $47°$ N). The measurements in 2020 were not significantly influenced by biomass burning emissions (Fig. 3.4). While in 2017, we also encountered mixed biomass burning smoke (Fig. 3.4 a) and anthropogenic pollution in and above the PBL. The biomass burning influence was prominent in southern Europe from $40°$ N and $42°$ N latitude (Figs. 3.3 a and 3.4 a). The defined BC plume between 2000 and $3500\,\mathrm{m}$ altitude in southern Europe is dominated by biomass burning emissions. This biomass burning influence also caused the large discrepancies between the median and mean concentrations between $2000\,\mathrm{m}$ and $3500\,\mathrm{m}$ in figures 3.1 a and 3.2 a. An analogy can be drawn to previous studies, which reported a similar pronounced stratification of biomass burning smoke above the PBL (Holanda et al., 2020). To be less sensitive to event-like measurements, we

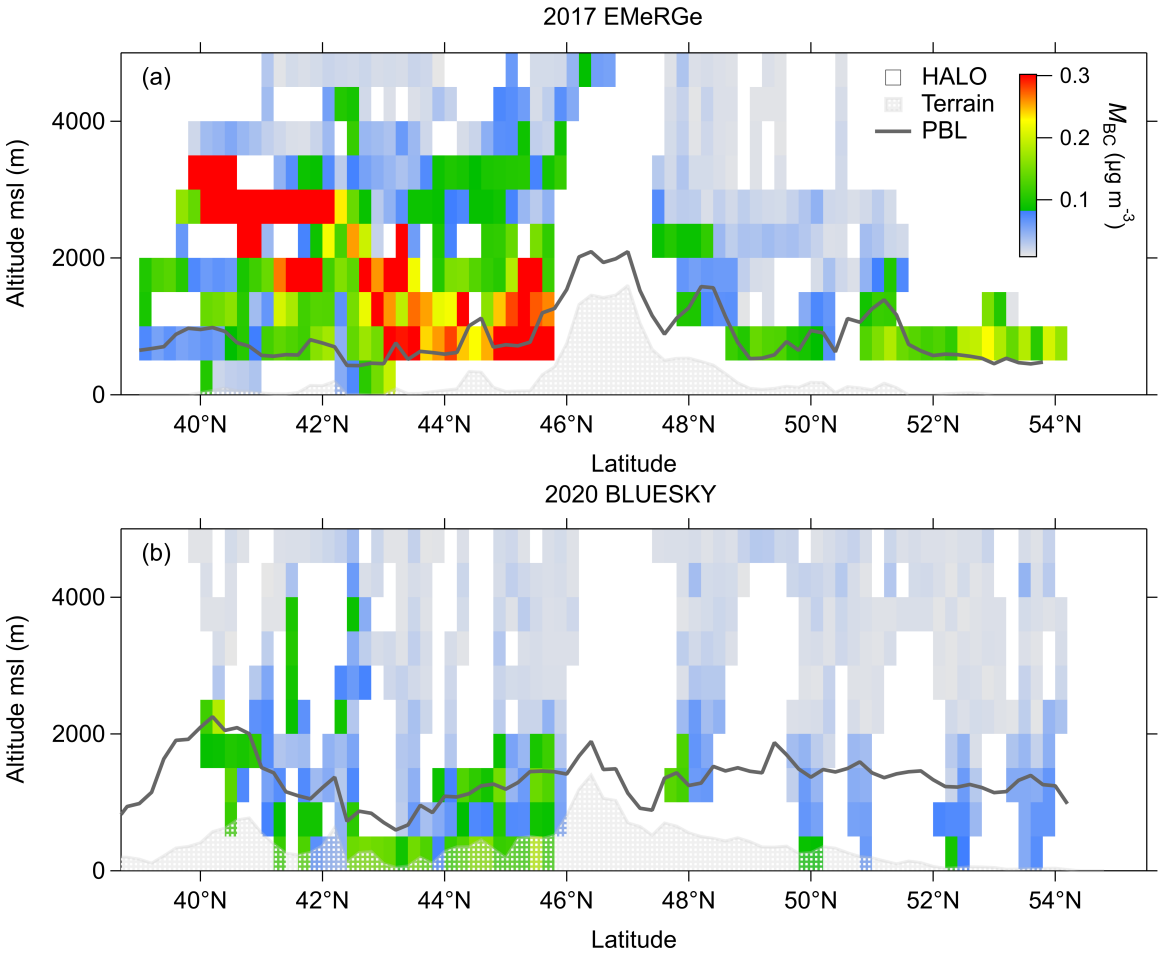

Figure 3.3: (a) Cross section of M_{BC} for 2017 EMeRGe EU measurements. Arithmetic mean for all data falling into a grid point of $0.2°$ latitude and $500\,\mathrm{m}$ altitude. The color scale ranges from 0 to $0.3\,\mu\mathrm{g\,m^{-3}}$. Means exceeding this range are shown in red. (b) as (a) but for the 2020 BLUESKY measurements. The grey shading is the mean terrain height below flight track and the grey solid line shows the planetary boundary layer height below flight track (details in section 2.5.3).

use median values for the comparison of the two aircraft campaigns (see also section 2.6.6).

The measured values for M_{BC} in 2020 are $48\,\%$ lower, when disregarding the model-based adjustment described above. For the refractory BC particle number concentration (N_{BC}), we also find $48\,\%$ lower concentrations (Fig. 3.1 e). The good agreement between M_{BC} and N_{BC}, is in accordance with the constant M_{BC} to N_{BC} ratios over its vertical distributions (Fig. 3.5 a). Also, the comparable median size distribution of the rBC particles between the two measurement campaigns, with rBC core diameters (D_{rBC}) ranging between ~ 120 to $180\,\mathrm{nm}$ (Fig. 3.5) shows the good agreement. The larger D_{rBC} during the measurements in 2017 are likely due to influences of biomass burning smoke which tend to have larger D_{rBC} compared to urban emissions (e.g., Holanda et al., 2020; Liu et al., 2014; Schwarz et al., 2008). The consistent ratio between M_{BC} and N_{BC} (Fig. 3.5 b) indicates that differences in coagulation growth are unlikely to play a significant role for the vertical profiles of D_{rBC} reported

*Data downloaded from https://firms.modaps.eosdis.nasa.gov/, last access 2023.03.08.

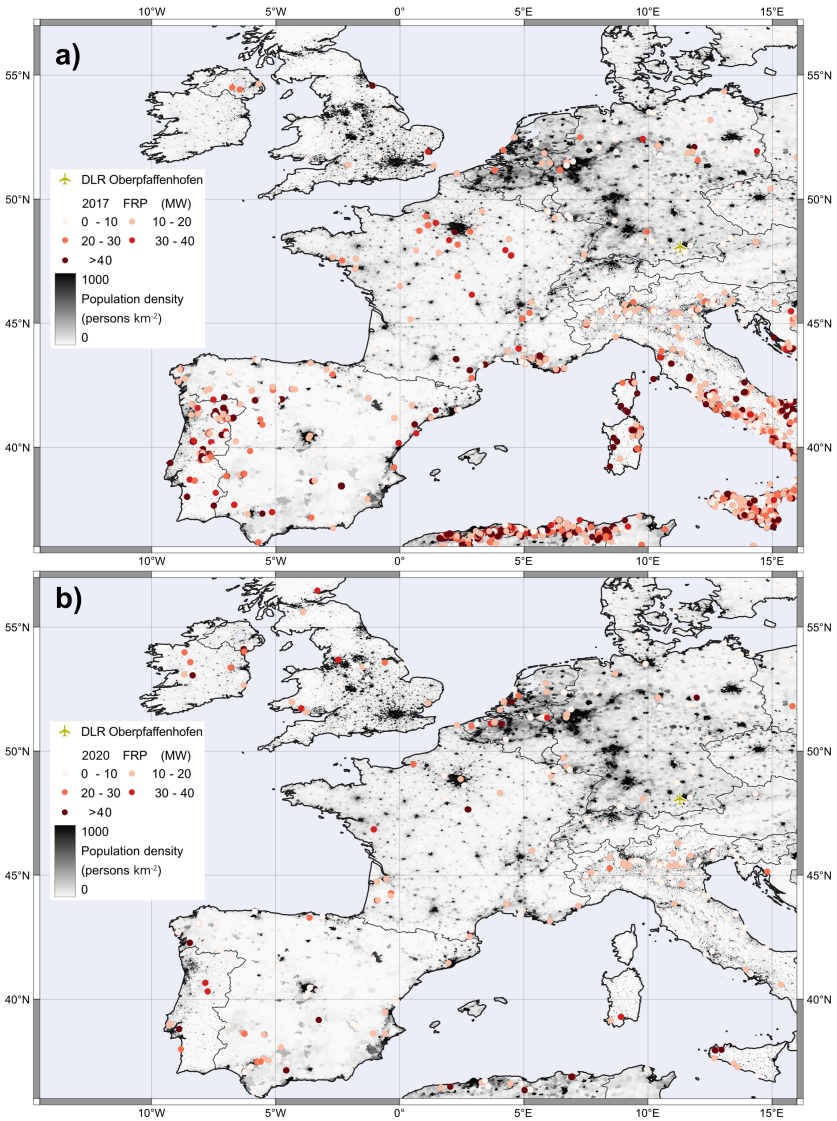

Figure 3.4: MODIS fires and thermal anomalies for the measurement periods in 2017 (a) and 2020 (b) color coded by Fire Radiative Power (FRP) in megawatts *.

here. Coagulation tends to predominately remove smaller particles and thus has a stronger impact on number concentrations than on the mass concentration (Ketzel and Berkowicz, 2004). This trend is not observable in our data (Fig. 3.5 b). Also anthropogenic BC emissions in Europe tend to get diluted before significant coagulation initiates (Ketzel and Berkowicz, 2004; Pohjola et al., 2003; Vignati et al., 1999). Beside coagulation and different sources, also size selective removal of BC cores with larger diameters by scavenging (e.g., Liu et al., 2020; Ohata et al., 2016) could play a role in the differences between 2017 and 2020. However there are no significant differences in precipitation in the summer months in Europe. Furthermore the range for D_{rBC} agrees with literature values for urban emissions (e.g., Liu et al., 2014; Schwarz et al., 2008).

To estimate the effect the reductions have on Earth's radiative budget, we calculated the regional aerosol direct radiative effect in the measurement area (see sec-

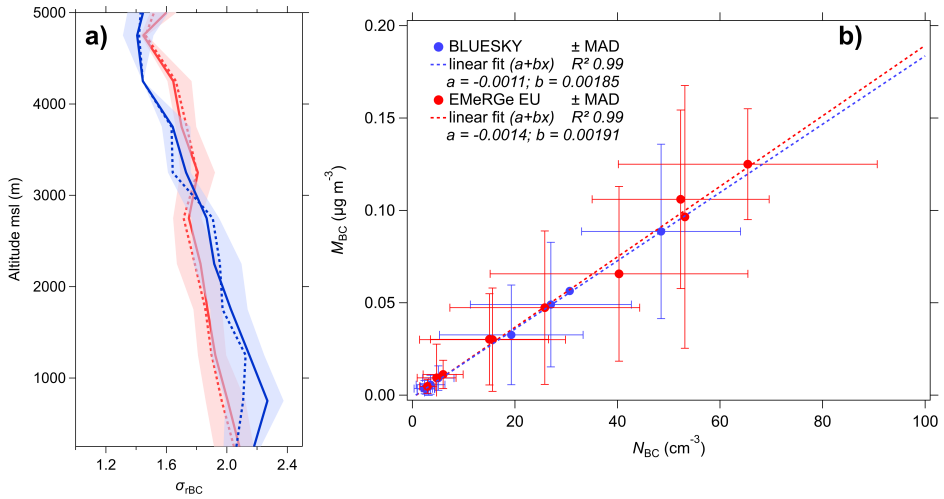

Figure 3.5: a) Vertical profiles of M_{BC} microphysical properties, the geometric standard deviation (σ_{rBC}) of the core size distributions. 2020 BLUESKY measurements in blue and 2017 EMeRGe EU measurements in red. Dashed lines show the median, solid lines the mean concentration and shaded areas represent interquartile range for each altitude bin of $500\,\mathrm{m}$. b) Scatter plot for data from vertical distribution of M_{BC} and N_{BC}. In red, data from 2017 collected during EMeRGe EU, in blue data from BLUESKY in 2020. Median absolute deviation (MAD) is shown as whiskers. Dashed lines are linear fits for each campaign.

tion 2.6.5). Therefore we reduced anthropogenic BC emissions in our EMAC simulation by $40\,\%$ and found a cooling effect of $0.06\,\mathrm{W\,m^{-2}}$ (Fig. 3.6) at the top of the atmosphere (TOA). This reduction due to a reduction of anthropogenic BC emissions by $40\,\%$ is as large as the global-mean BC radiative forcing, as assessed by the IPCC AR6 (Szopa et al., 2021).

3.1.1 Implications of M_{BC} reductions

We present the first measurement study showing the influence of the unprecedented reduction in atmospheric pollution in 2020 on BC vertical distribution. Our measurements cover a large spatial area, measured on a rather short time scale. Thus, we deliver a representative data set, showing the changes in atmospheric BC concentra-

Table 3.3: Average and median of M_{BC} microphysical properties, geometric mean diameters (D_{rBC}) and the geometric standard deviation (σ_{rBC}) of the core size distributions. Values in column altitude represent centre of corresponding $500\,\mathrm{m}$ altitude bin.

	EMeRGe EU				BLUESKY			
	D_{rBC}		σ_{rBC}		D_{rBC}		σ_{rBC}	
Altitude [m]	Avg [nm]	Median [nm]	Avg	Median	Avg [nm]	Median [nm]	Avg	Median
250	157	155	2.083	2.047	144	152	2.180	2.063
750	167	150	2.006	1.966	134	140	2.268	2.108
1250	171	172	1.924	1.900	148	150	2.149	2.124
1750	174	157	1.872	1.858	138	138	2.027	1.972
2250	150	148	1.826	1.789	125	122	1.917	1.954
2750	155	153	1.749	1.714	151	165	1.866	1.907
3250	159	158	1.808	1.803	115	134	1.731	1.642
3750	169	174	1.701	1.735	130	134	1.642	1.634
4250	174	178	1.645	1.663	157	157	1.444	1.444
4750	170	160	1.447	1.463	157	148	1.392	1.405

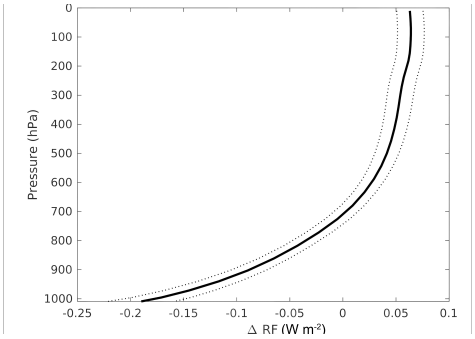

Figure 3.6: Profile for difference in aerosol radiative effect due to a reduction of $40\,\%$ in M_{BC}. The profile is averaged for the months May and June over the region of HALO measurements (latitude between -5 and $16°$ and longitude between 37.5 and $54.5°$, Fig. 1.3).

tion. We benefit in this comparison from the large spatial coverage, measured with the same instrumentation. In addition, the vertical extent of pollutants emitted in the PBL is observed with a high accuracy. In the discussion section we compare our aircraft data with recent studies, quantifying the impact of the COVID-19 confinements with other metrics. We find a general agreement, even though most studies use 2019 or a multiyear average as reference for the comparison, while we compare two rather short periods in 2017 and 2020. We also investigate potential reasons for the reduction of atmospheric BC and other pollutants and consequently analyse data published by EUROSTAT (details in supplementary material) on fossil and solid fuel demand.

The $41\,\%$ reduced M_{BC} we find, exceeds the mean value for Europe ($11\,\%$) reported by Evangeliou et al., 2021. Nevertheless, our results fall within the reported range from $42\,\%$ to $8\,\%$ for southern and western Europe. Also studies with stronger regional focus agree well with our results. Moreda-Piñeiro et al., 2021 found for the southwest Atlantic region of Spain, BC reductions between 29 to $51\,\%$. Beside BC, also other atmospheric constituents were found to be reduced during the 2020 confinements. For the Po Valley, Lonati and Riva, 2021 found benzene reduced by roughly $40\,\%$ in May 2020. Benzene is a volatile organic compound (VOC) primarily emitted by road traffic and in good correlation with anthropogenic BC emissions (Wren et al., 2018). Petetin et al., 2020 found NO_2, as another traffic-related pollutant, decreased between 41 and $55\,\%$ in Spain. By combining satellite and surface in-situ measurements with numeric modeling, Venter et al., 2020 found fine particulate matter (PM2.5) reduced by $31\,\%$. Apart from measurements, also proxy data are used to quantify the effect of the confinements on the atmosphere. Forster et al., 2020 shows globally a decrease in BC of up to $22\,\%$ for the lockdown period and around $15\,\%$ in May 2020. When only considering the countries probed in our measurement flights, the reduction is $40\,\%$ in May and $20\,\%$ in June 2020 (Fig. 3.7*). These literature values, based on mobility data from Google and Apple, agree well with our measurements. All of the above-mentioned studies, analysing the reductions in traffic related pollutants and proxies, are in a similar range as our results.

Less traffic is identified as the driving force for improved air quality in 2020 (Le Quéré et al., 2020). This is reinforced by the drop in fossil fuel demand during the

*Data downloaded from https://github.com/Priestley-Centre/COVID19_emissions, last access 02.03.2023.

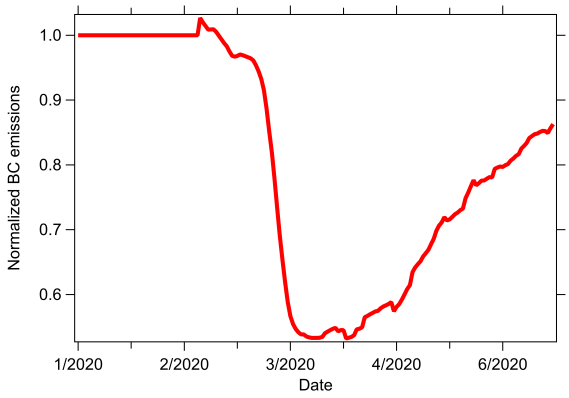

Figure 3.7: Temporal evolution of normalized daily BC mass emissions for Germany, Italy, France, Spain, Netherlands and Luxembourg. Data published in Forster et al., 2020.

confinements in 2020 (Fig. 3.8). For May 2020, fossil fuel demand was $30\,\%$ below the 2017 level (Fig. 3.8). We found the largest reduction in aircraft fuel demand with $75\,\%$ (Fig. 3.8 e, g). For road traffic fuels, the decrease is roughly $20\,\%$ (Diesel $-18\,\%$, Fig. 3.8 b, d, and gasoline $-32\,\%$, Fig. 3.8 f, i). Other than gasoline, Diesel is widely used in the transportation sector and thus the impact of the confinements in 2020 is relatively smaller. On German highways, heavy goods traffic was reduced around 25 % compared to a more than 50 % reduction in passenger cars (Goecke et al., 2020). Studies found large differences in real-world emission factors between Diesel and gasoline vehicles as well as passenger and heavy goods vehicles (Ban-Weiss et al., 2009; Ban-Weiss et al., 2008; Peitzmeier et al., 2017; Wiesner et al., 2021), however, a source apportionment and thus a quantification of the single sources impacts on the M_{BC} reductions in 2020 is not possible based on our measurement data. The higher decrease in gasoline and aircraft fuels demand can be attributed to the drop in passenger traffic, due to travel bans, home-office, and relinquished traveling activities.

Beside reduced emissions due to the COVID-19 confinements, other emission reductions took place between the two measurement campaigns. The total consumption of solid fuels (i.e. all common coal products, details in supplementary material) in 2020 was around $42\,\%$ below the corresponding value for 2017 (3.9). However, solid fossil fuel, only accounts for a small fraction ($3\,\%$) of the BC emissions from power generation (McDuffie et al., 2020). Accordingly, reductions in solid fossil fuel combustion for power generation have only little influence ($< 1\,\%$) on the absolute M_{BC} burden. Due to higher emission standards there are multi-year declines of the BC burden reported for the Northern Hemisphere (e.e., Kutzner et al., 2018; Querol et al., 2013; Singh et al., 2018). Based on surface measurement stations Kutzner et al., 2018 found an annual reduction between 1 and $3\,\%$ for German urban background and rural sites in the period between 2005 until 2014. At traffic sites the annual reduction was as high as $5\,\%$. For a kerbside station in London, Singh et al., 2018 found up to $8\,\%$ annual reduction in BC, whereas the reduction at rural and remote sites was as little as $0.6\,\%$. Querol et al., 2013 obtains similar results for Spain with a high BC reduction in urban areas and little to statistically insignificant reductions

*data are downloaded for countries considered in this study from the EUROSTAT website with last access 08.07.2021 (https://ec.europa.eu/eurostat/databrowser/view/NRG_CB_SFF__custom_1131819/default/table).

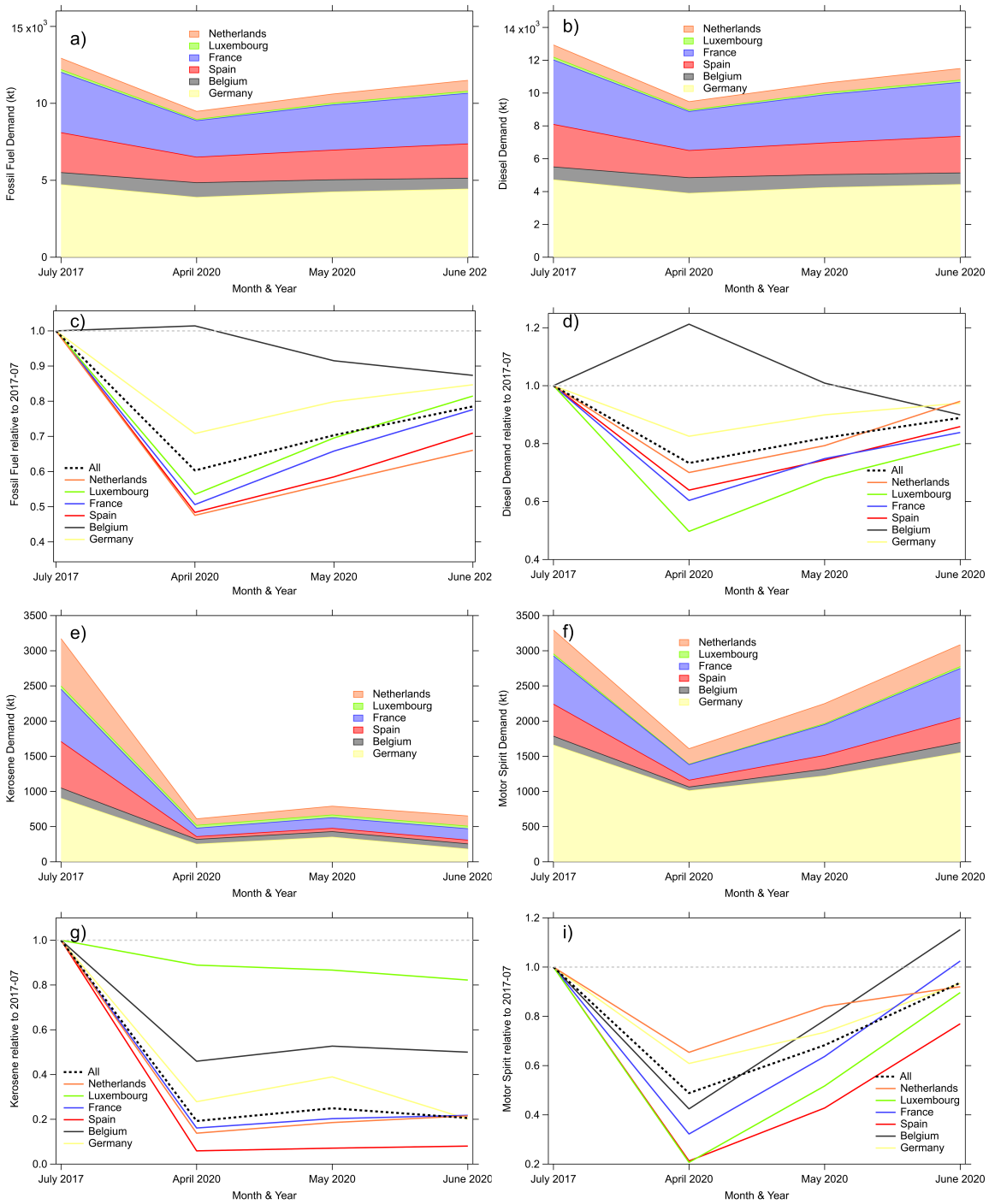

Figure 3.8: EUROSTAT data for fossil fuel demand for the July 2017, April 2020, May 2020 and June 2020. Panel a) and c) combines demand for diesel, kerosene (aviation fuel) and motor spirit (gasoline) *. Panel b) and d) provides the Diesel demand, e) and g) the Kerosene (aviation fuel) and, f) and i) the motor spirit (gasoline) demand.

in rural regions. The BC concentrations in our study falls within the range reported by Querol et al., 2013 for remote and rural sites in Spain. It has to be noted that BC concentrations show both a strong vertical gradient and a geographic pattern, highly sensitive to emission hot spots like traffic sites, domestic combustion sources or industrial areas. Thus the median vertical profiles shall be understood as lower tropospheric background concentrations with an anticipated annual reduction in the

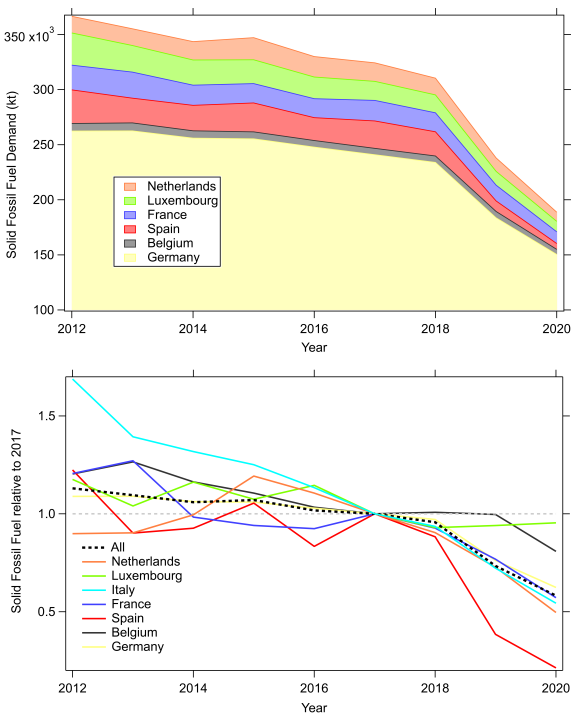

Figure 3.9: Cumulative EUROSTAT data for solid fossil fuel inland consumption for the years 2012 to 2020 *.

range of rural and urban background concentrations. Hence, around 3 to $9\,\%$ of the reduction we found should be attributed to long-term trends in emission reductions.

The local top of the atmosphere direct radiative effect of BC over continental Europe is considerably small, due to the low surface albedo and relatively low BC concentrations (Heald et al., 2014). Due to BC's ability to absorb solar radiation the reduced emissions show a net warming effect in the lower troposphere, by increasing the incoming radiation. However, there is a change of sign at pressure levels below $700\,\mathrm{hPa}$ ($\backsim 3000\,\mathrm{m}$) resulting in an overall cooling effect at the top of the atmosphere. Nevertheless, to get a full picture of the atmospheric response to the unprecedented atmospheric situation during the COVID-19 pandemic, more sophisticated studies are needed at this point. In particular the long-range transport of anthropogenic pollutants to remote regions like higher latitudes, where its climate impact is amplified by a high surface albedo and an increased ice melting due to deposition of atmospheric BC on snow and ice will be of interest. Also, research on the long- and short-term radiative effects in combination with other relevant species will be very valuable for atmospheric science and policy makers. For these studies we present a good estimate for the near immediate response of M_{BC} in the area of southern and western Europe. Furthermore, we show that proxy data as used by Forster et al. (2020) or EUROSTAT data can serve well for the improvement and the definition of emission inventories during the exceptional atmospheric circumstances during the pandemic.

*data are downloaded for countries considered in this study from the EUROSTAT website with last access 08.07.2021 (https://ec.europa.eu/eurostat/databrowser/view/NRG_CB_SFF__custom_1131819/default/table).

3.1.2 Summary of M_{BC} reductions

We showed that lower tropospheric median M_{BC} was decreased by $41\,\%$ in southern and western Europe in 2020 compared to 2017. This reduction is attributed to two main reasons, the general decreasing trends of BC emissions in Europe accounting for 3 to $9\,\%$ and the confinement of human movement as a result the measures taken to minimize the spread of COVID-19 accounting for 32 to $38\,\%$. The effect of COVID-19 confinements on the atmospheric M_{BC} found in this study generally agrees with earlier studies using ground based and proxy data to estimate the confinement's effect. In addition to earlier studies, we present the first measurement results of airborne BC in 2020. We provide a consistent data set for a large spatial area and the vertical extent of M_{BC} and N_{BC}.

Our results confirm the near immediate atmospheric response of M_{BC} and N_{BC} to anthropogenic activities. Reduced mobility drives the BC reductions in the lower troposphere. Some of these changes in mobility, such as reduced road and air traffic due to home-office and video conferences, should be sustained into working culture. Model studies using our results can quantify the positive effects on public health and the atmosphere due to reductions in air pollution. Our study extends current knowledge about the distribution of pollutants in the atmosphere. It demonstrates that the impact of measures, which improve air quality, also influence climate. It thereby contributes to one of the most important challenges of this century, namely how to mitigate climate change.

3.2 Changed cloud condensation nuclei burden during COVID-19 lockdown over Europe

Besides the outlined reduction in M_{BC} and N_{BC}, the N_{CCN} budget was also affected by the COVID-19 confinements in Europe. In the following, I compare the measurements of $N_{\mathrm{CCN\ 0.3}}$ from the EMeRGe EU campaign during business as usual conditions and the BLUESKY measurements characterized by the COVID-19 lockdown.

The sources for aerosol acting as CCN are diverse. They can originate from biogenic emissions, as primary biogenic aerosol, or form secondarily from precursor gases emitted from the biosphere. Aerosol from the burst of ocean waves, referred to as sea spray, can also contribute to the CCN burden in marine environments. In the Anthropocene, however, in most continental and even coastal regions, the CCN burden is dominated by anthropogenic emissions of primary particulate pollution and secondary aerosol nucleated from precursor gases (e.g., Andreae, 2007). Due to the more diverse sources, the analysis of CCN is more complex compared to BC which is emitted exclusively during incomplete combustion processes. Therefore, the following section focuses on a qualitative analysis of the changes in the CCN burden due to the COVID-19 confinements in Europe.

In 2020, the $N_{\mathrm{CCN\ 0.3}}$ was generally lower than in 2017, with a remarkably stronger confinement to the PBL (Fig. 3.10). For the measurements in 2017, Hernández et al., 2022 report a good agreement between CO and $N_{\mathrm{CCN\ 0.3}}$ in the lower troposphere. CO is primarily emitted in the combustion of fossil and bio fuels and is therefore a good general tracer for pollutants originating from combustion processes. The good correlation with CO as well as the confinement to the PBL are good indications that the bulk of the CCN budget over Europe is dominated by anthropogenic emissions and combustion processes.

Besides the anthropogenic combustion of fossil- and bio-fuels for housing, industry, traffic and agriculture, also biomass burning emissions from wildfires in south Europe (Fig. 3.4) are apparent in $N_{\mathrm{CCN\ 0.3}}$. These wildfire emissions are mostly lofted into the free troposphere due to the high thermal energy of the fires leading to convective upward transport, whereas urban haze is more confined to the PBL since the single emission sources have rather small thermal energy which is not sufficient to trigger convective processes. Intrusions of urban haze into the free troposphere happen more likely due to turbulent mixing in the interface between the PBL and the free troposphere. The layers dominated by lightly aged biomass burning smoke feature a high concentration of both BC and $N_{\mathrm{CCN\ 0.3}}$.

During EMeRGe EU, long-range transport of biomass burning emissions from North America was probed (Förster et al., 2023; Hernández et al., 2022). Remarkable are the enhancements in CO in these layers, however, only average or even below average $N_{\mathrm{CCN\ 0.3}}$ were measured (Hernández et al., 2022). Also M_{BC} within these plumes is remarkably low. A possible explanation is that particulate pollution in these layers already scavenged and got diluted by background aerosol.

The anthropogenic origin of the lower tropospheric CCN, driven by combustion processes, allows a direct transfer of the results for the M_{BC} reductions to correct the CCN budget for the changed conditions in 2020. Important to note are thereby the generally similar but different scavenging processes for BC and CCN. As outlined

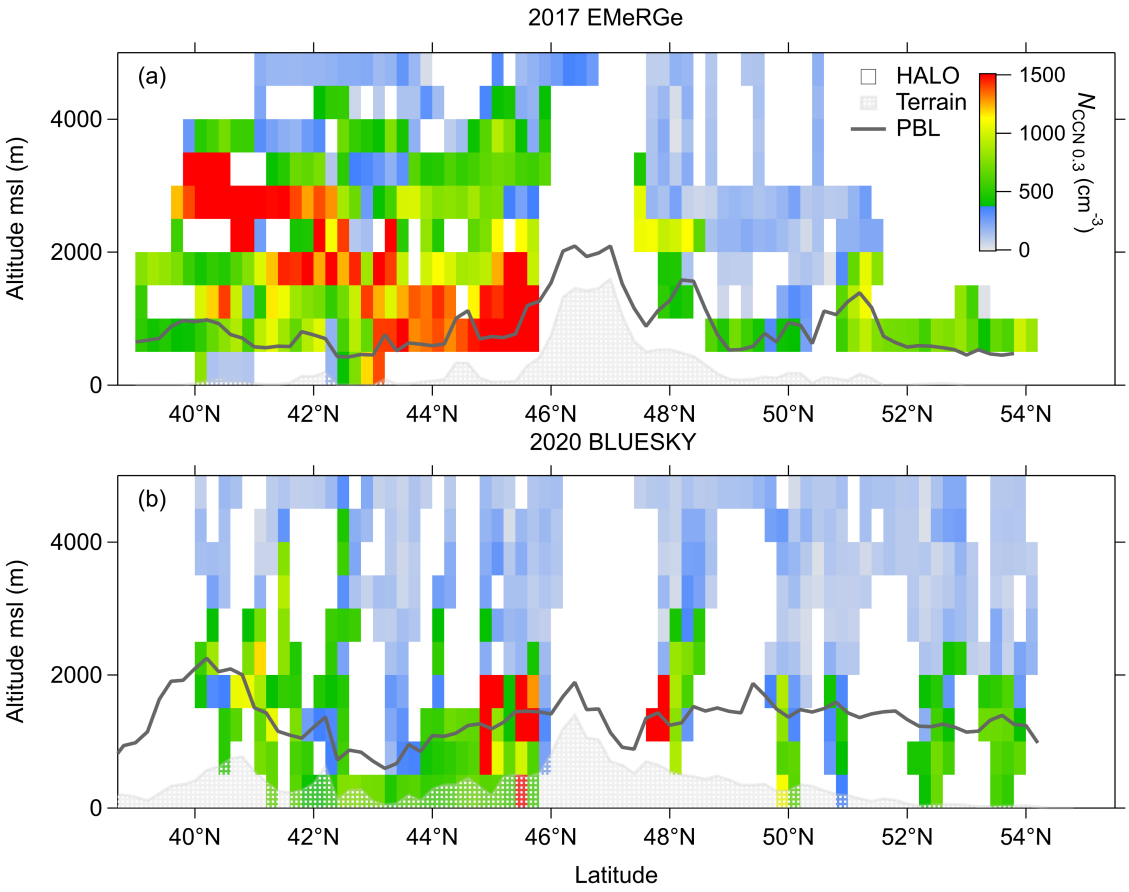

Figure 3.10: (a) Cross section of $N_{CCN\,0.3}$ for 2017 EMeRGe EU measurements. Arithmetic mean for all data falling into a grid point of $0.2°$ latitude and $500\,\mathrm{m}$ altitude. The color scale ranges from 0 to $0.3\,\mu\mathrm{g\,m^{-3}}$. Means exceeding this range are shown in red. (b) as (a) but for the 2020 BLUESKY measurements. The grey shading is the mean terrain height below flight track and the grey solid line shows the planetary boundary layer height below flight track (details in section 2.5.3).

in section 1.2 BC is mostly removed by impaction scavenging, whereas for CCN, hygroscopic growth and subsequent sedimentation, droplet activation and rainout as well as heterogeneous chemistry dominate the atmospheric removal processes. Nonetheless, the good agreement in the vertical and spatial distribution of CCN and BC (Figs. 3.3 and 3.10) motivates us to use the results of the BC data for the analysis of the CCN measurements. Figure 3.11 shows nicely that a 35 % reduction of the CCN budget over Europe for 2017 agrees better with the CCN burden measured in 2020.

The measurement, however, had significant differences in the flight pattern and manoeuvres. The most notable difference are probably the low approaches (i.e., a landing manoeuvre without ground contact followed by a take off) which were possible due to the low air traffic during the COVID-19 confinements. The low approaches allowed more measurements within the PBL during the BLUESKY campaign. During the EMeRGe EU campaign only few flight segments were possible within the lowest flight altitudes. Further details on the flight pattern are outlined in chapters 2.1.1

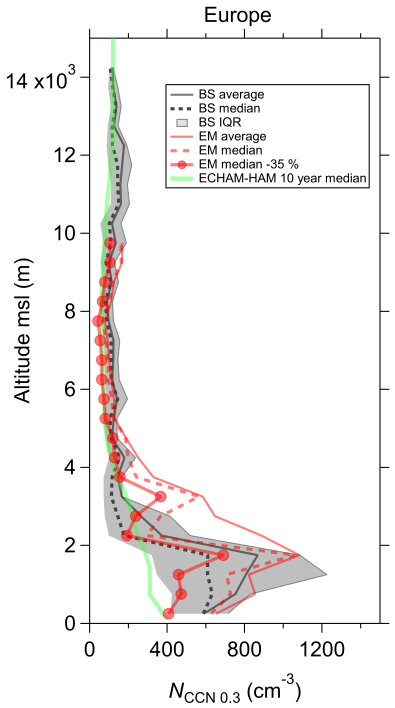

Figure 3.11: Vertical profiles for all $N_{\mathrm{CCN\ 0.3}}$ data from the EMeRGe EU (red) and BLUESKY (grey and black). The dashed lines show the median, the solid lines the average, for BLUESKY the grey shading represents the first and third quartile. The red solid line with round markers is the EMeRGe EU median reduced by 35 % to match the reductions found for M_{BC}. The solid green line is the median ECHAM-HAM data from ten-year monthly average data in the time from 2003 until 2012 for the months May, June and July of each year.

and 2.6. These differences likely explain the lower M_{BC} and $N_{\mathrm{CCN\ 0.3}}$ in the vertical profile for 2017 close to the surface.

The strong vertical gradient in the lower troposphere is expected for measurements over Europe where the major sources of CCN are of anthropogenic origin (e.g., Hernández et al., 2022). Particle nucleation from biogenic precursors plays only a minor role for the overall CCN budget within the lower troposphere over Europe due to large and ubiquitous amounts of background pollution. Also aerosol cloud interactions in the interface of boundary layer and free troposphere as well as limited transport of particulate pollution across the boundary layer engender the strong vertical gradient in the vertical profile of $N_{\mathrm{CCN\ 0.3}}$.

The distinct difference between the measurements in 2017 and 2020 in the lowest $5\,\mathrm{km}$ of the troposphere levels out with increasing altitudes. A potential explanation are smaller direct anthropogenic influences in higher altitudes. This decreased impact of anthropogenic aerosol in higher altitudes may also explain the lower sensitivity of the CCN budget to anthropogenic emissions. To better understand how representative the HALO measurement data are against the general climatology, the measured vertical distribution of $N_{\mathrm{CCN\ 0.3}}$ is compared with the average vertical profile retrieved from a ten-year monthly average of ECHAM-HAM simulations ($N_{\mathrm{CCN\ 0.3\ ECHAM}}$). The significant drop in CCN concentrations at altitudes between 2 and $3\,\mathrm{km}$ observed in the HALO measurement data are not present in the model results, which show a rather linear decrease in $N_{\mathrm{CCN\ 0.3\ ECHAM}}$ over the vertical distribution in the lower troposphere. Therefore, the model results below $3\,\mathrm{km}$ are

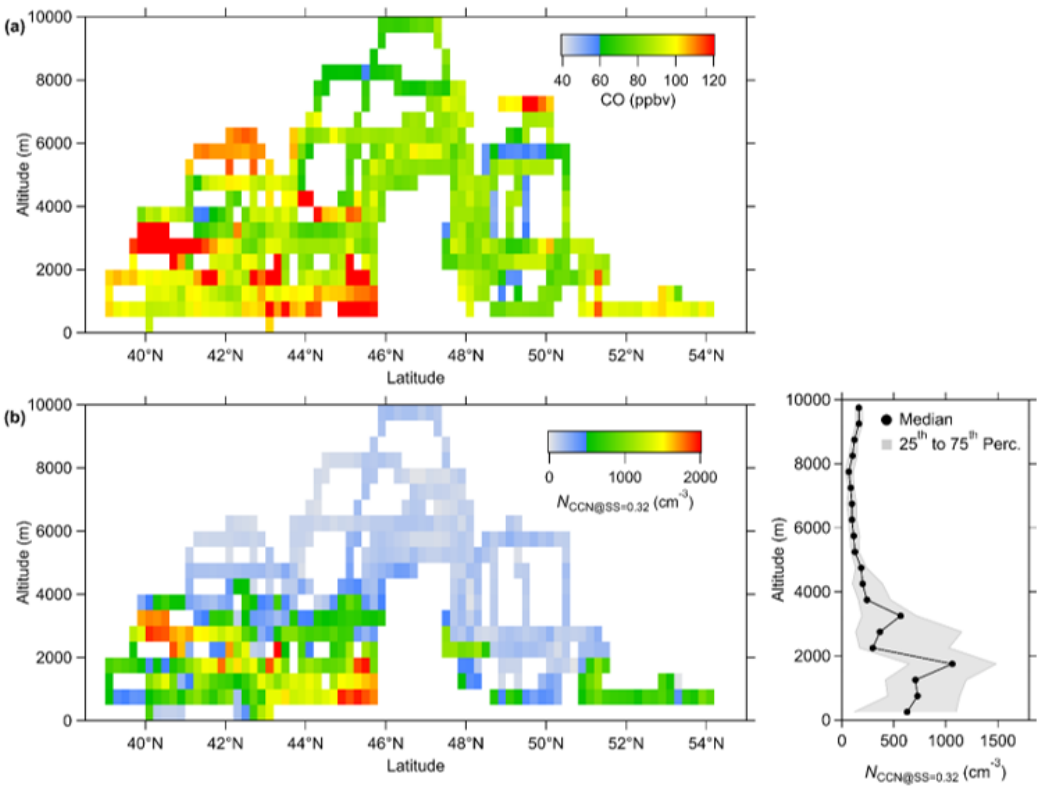

Figure 3.12: Figure and caption from Hernández et al., 2022, Figure 12: Vertical and latitudinal distribution observed during the EMeRGe IOP of (a) CO mixing ratios and (b) CCN number concentration at a supersaturation (S) of 0.32 % (except for E-EU-04, due to instrumental failure). The CCN curtain plot on the bottom left is made with latitude- (0.2°) and altitude-binned (500 m) CCN number concentrations. On the right, the median vertical $N_{CCN\,0.32}$ profile is represented by a solid black line and the interquartile range by a grey-shaded area. CCN data are standard temperature and pressure (STP) corrected.

substantially lower than the measurements. For the measurements above the lower troposphere, however, the two HALO campaigns and the ten-year average retrieved from model data agree well. This good agreement illustrates the lower sensitivity of the CCN budget in the middle and upper troposphere to anthropogenic emission pattern.

3.2.1 Summary of $N_{CCN\,0.3}$ changes

In the vertical profiles and the distribution in the cross section the occurrence of $N_{CCN\,0.3}$ agrees well with M_{BC}, especially in highly polluted regions, affected by dense urban haze or biomass burning. Also the reduction in the CCN burden agrees well with the overall reductions of M_{BC} during the confinements. The ECHAM-HAM climate model data are a ten-year monthly average for the measurement months providing a long-term perspective. Generally, the vertical gradient in $N_{CCN\,0.3}$ in the model results is too uniform compared to the in situ data, however, in the middle and upper troposphere, the measurements and model results agree well. Also between the measurements in 2020 and 2017 there are only minor differences in the middle and upper troposphere above $5\,\mathrm{km}$.

Based on the good correlation between CCN and BC but also CO within the lower troposphere, the CCN burden there can be regarded as strongly influenced by anthropogenic emissions. In contrast, the insensitivity of $N_{\mathrm{CCN\,0.3}}$ in higher altitudes over Europe to the general pollution levels indicates that other processes than local pollution from combustion are dominating the CCN burden in the free and upper troposphere.

CHAPTER 4

Vertical distribution of $N_{\text{CCN 0.3}}$ in various environments

This chapter includes data sets from the following field experiments:
EMeRGe Asia and CAFE Africa.

Contribution to this chapter by Ovid O. Krüger: I wrote and designed the presented study. For the EMeRGe Asia and CAFE Africa data sets, I conducted the CCN-measurements onboard the HALO aircraft. I defined the grids and performed the comparison between the ECHAM-HAM CCN data and the HALO measurements. ECHAM-HAM data was provided by M. Salzmann and J. Quaas.

The tendencies of a decoupling for the CCN budget within the lower troposphere and the free and upper troposphere as pointed out in the previous section is further examined with more HALO aircraft measurements of $N_{CCN\ 0.3}$ and $N_{CCN\ 0.3\ ECHAM}$ for the measurement regions. The measurement regions for the median vertical profiles are in East and Southeast Asia (Fig. 4.5) and over the tropical Atlantic Ocean (Fig. 4.1).

4.1 Vertical distribution of $N_{CCN\ 0.3}$ over the tropical Atlantic

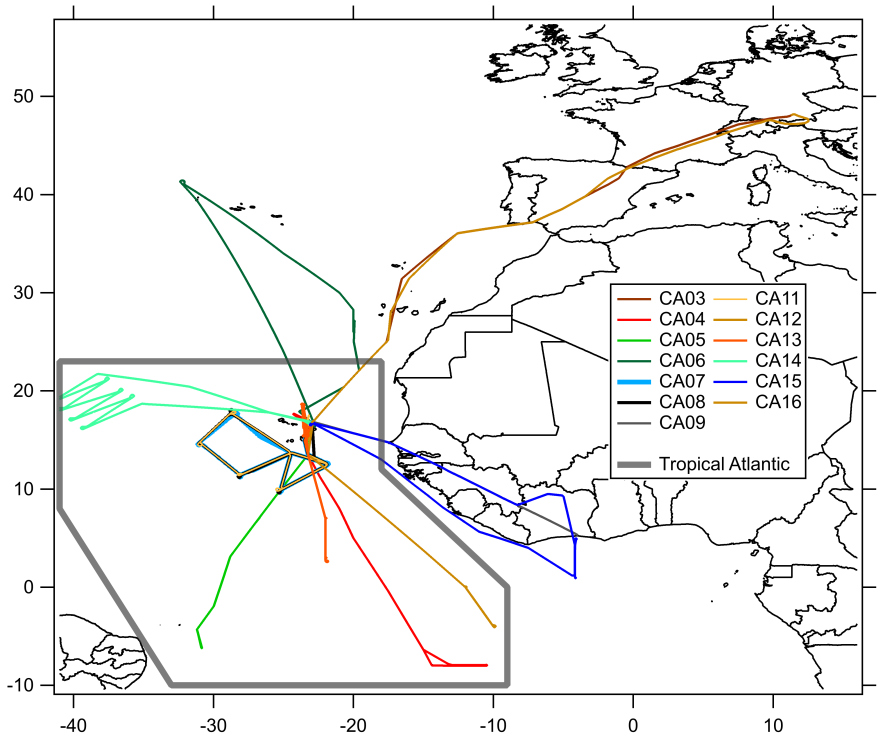

Figure 4.1: Flight map with measurement flights of the CAFE Africa field campaign from August and September 2018. Different measurement flights are color coded according to legend. The grey polygon represents the region extracted from the global ECHAM-HAM data set for the comparison of the vertical distribution of $N_{CCN\ 0.3}$.

The measurement data from the tropical Atlantic are from CAFE Africa, conducted in August and September 2018 from Sal, Cape Verde (details in section 2.1.1). Measurements in the tropical northern hemisphere predominate, but the data set also includes measurements across the intertropical convergence zone (ITCZ) down to about 8°S (Fig. 4.2). The location of the ITCZ during the measurements was around 8 to 13°N, thus data from both tropical hemispheres over the Atlantic is well represented in the analysis.

The cross section along the latitude for M_{BC} illustrates the impact of biomass burning emissions as a strong but local and periodical aerosol source in the lower free troposphere (Fig. 4.3). These influences on the aerosol population are also remarkable in the CCN burden (Fig. 4.2). In the biomass burning smoke we encountered

the highest concentrations of $N_{CCN\,0.3}$ in the lower free troposphere, also exceeding the measurements in the marine boundary layer. The influence of biomass burning over the tropical Atlantic is confined to altitudes below $5\,\mathrm{km}$ in the presented data set. These findings are also reported in Holanda et al., 2023 for highly aged biomass burning smoke measured over the Atlantic near the Brazilian coast. These stable smoke layers are transported as compact layers of particulate pollution above the marine boundary layer. Thermal inversion thereby inhibits these smoke layers from mixing with surrounding air-masses (e.g., Holanda et al., 2023; Lareau and Clements, 2015). Accordingly, we measured only low concentrations of M_{BC} out of the biomass burning plumes.

Another, and also discontinuous, source of CCN is the southbound transport of mineral dust from African deserts. The transport of dust layers was measured north of the ITCZ during the CAFE Africa campaign and coincides with enhanced $N_{CCN\,0.3}$ and some intrusions of anthropogenic pollution, which increased M_{BC} (13 to $19°$N in figures 4.3 and 4.2). The aerosol enhancements due to mineral dust transport are in a comparable altitude range as the smoke plumes originated from biomass burning, however, the upward transport for both aerosol types is generally different (e.g., Royer et al., 2023a).

We observed only low M_{BC} in the middle free troposphere, above $5\,\mathrm{km}$. The long range transport of mineral dust layers also occurred in lower altitudes during the CAFE Africa measurements in late summer 2018. Therefore, the $N_{CCN\,0.3}$ budget in the middle and upper troposphere is considered as background concentrations for the remote tropical Atlantic.

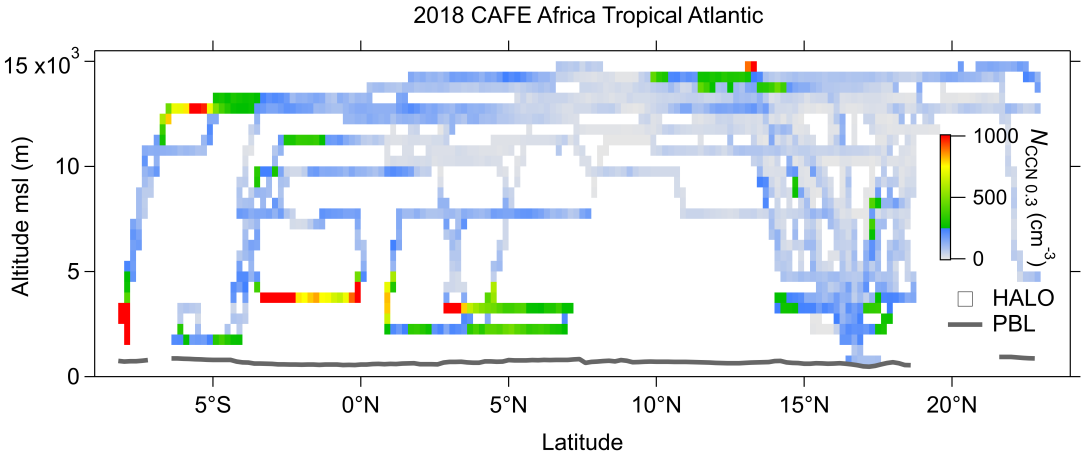

Figure 4.2: Cross section of $N_{CCN\,0.3}$ for 2018 CAFE Africa measurements. Arithmetic mean for all data falling into a grid point of $0.2°$ latitude and $500\,\mathrm{m}$ altitude. The color scale ranges from 0 to $1000\,\mathrm{cm}^{-3}$. Means exceeding this range are shown in red. The grey solid line shows the planetary boundary layer height below flight track retrieved from HYSPLIT backward trajectories (details in section 2.5.3).

In general, the vertical profiles for the HALO measurement data from the CAFE Africa campaign in 2018 over the tropical Atlantic and the ECHAM-HAM data agree well. With the exceptions of the above discussed distinct biomass burning smoke plumes and the transport of mineral dust, the measurement data consists of marine background conditions. The third quartile as well as the average vertical profile react

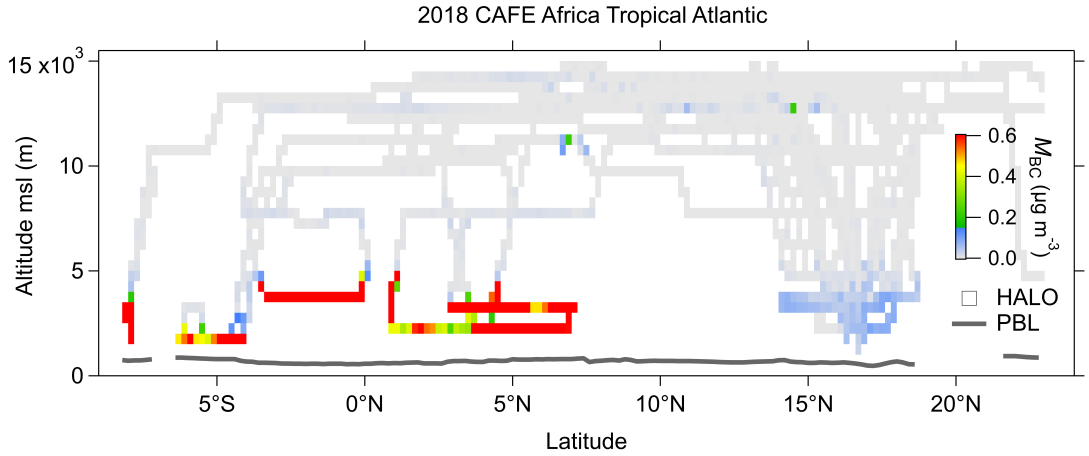

Figure 4.3: Cross section of M_{BC} for 2018 CAFE Africa measurements. Arithmetic mean for all data falling into a grid point of $0.2°$ latitude and $500\,\mathrm{m}$ altitude. The color scale ranges from 0 to $0.6\,\mu\mathrm{g\,m^{-3}}$. Means exceeding this range are shown in red. The grey solid line shows the planetary boundary layer height below flight track retrieved from HYSPLIT backward trajectories (details in section 2.5.3).

sensitively to these smoke and dust plumes with a comparably small spatial extent but strong enhancements (Fig. 4.4. It is important to note that during CAFE Africa, biomass burning smoke was one of the key research targets, therefore the frequent occurrence in the measurement data is potentially due to a sampling bias and only hardly representative for the general marine free troposphere. Due to the small horizontal extent of the biomass burning smoke and urban haze plumes, these emissions will not outweigh the marine background when comparing the median value.

The agreement between the ten-year median of monthly model data averages with the in situ measurements over the tropical Atlantic supports the hypothesis of pollution driven variations in the CCN budget of the lower troposphere and only minor sensitivity of CCN in higher altitudes to both variations in emission and meteorological factors. The model results capture the general shape and the absolute concentration of $N_{CCN\,0.3}$ well over the whole vertical extent.

In the model data as well as in the measurements, a considerable increase in $N_{CCN\,0.3}$ appears in altitudes between 1 and $4\,\mathrm{km}$, followed by a drop. The enhancement in both the model and in situ data are associated with typical altitudes for long range transport of biomass burning smoke and mineral dust (e.g., Holanda et al., 2023; Royer et al., 2023a). The model tends to capture these measured enhancements of aerosols well. Above 4 to $5\,\mathrm{km}$, the $N_{CCN\,0.3}$ drops and remains rather linear for in situ and model data in the middle free troposphere. In the upper troposphere and lower stratosphere, however, the CCN burden tends to increase due to formation of secondary aerosol species from sulfuric precursor gases (e.g., Brock et al., 1995; Williamson et al., 2019) as well as due to downward transport and mixing of stratospheric sulfate aerosols (e.g. Kremser et al., 2016). The measurements over the tropical Atlantic generally agree well with the climatology data retrieved from the ECHAM-HAM model and the overall processes controlling the CCN burden in the tropical troposphere tend to be little sensitive to anthropogenic pollution and small scale meteorological parameters.

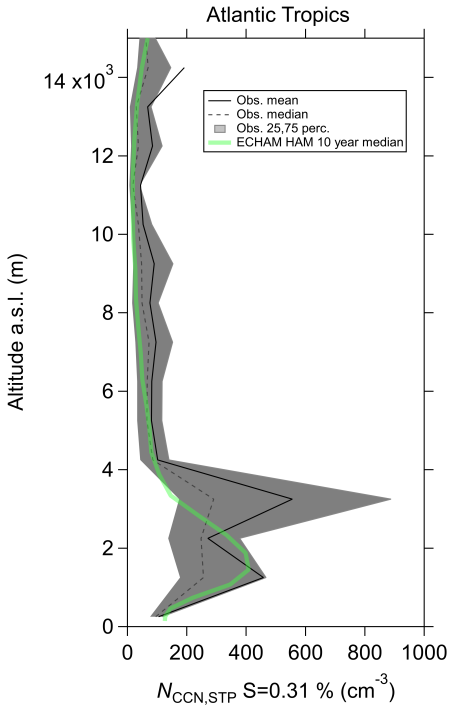

Figure 4.4: Vertical profiles for $N_{CCN\ 0.3}$ data from region defined as tropical Atlantic in this study (grey and black). The dashed lines show the median, the solid lines the average, for BLUESKY the grey shading represents the first and third quartile. The red solid line with round markers is the EMeRGe EU median reduced by 35 % to match the reductions found for M_{BC}. The solid green line is the median ECHAM-HAM data from ten year monthly average data in the time from 2003 until 2012 for the months May, June and July of each year.

4.2 Vertical distribution of $N_{CCN\ 0.3}$ over Asia

EMeRGe Asia focused, like its companion campaign EMeRGe EU, on anthropogenic pollution from major population centres. Flights were carried out in March and April 2018 from Tainan in Central Taiwan. The targeted outflows of urban haze originated from Beijing and Shanghai in China, Manila on the Philippines, Nagoya in Japan, Bangkok in Thailand and several major cities in Taiwan (further details in section 2.1.1) and had various atmospheric aging times. For the analysis of the EMeRGe Asia data in the context of the vertical CCN burden, the overall observations are separated into East and Southeast Asia. The separation is at a latitude of $21.5°$ N, south of Taiwan (Fig. 4.5).

In Asia the pollution encountered was generally less confined to the PBL compared to measurements in Europe. The overall concentrations also exceed the observations in Europe. Please note therefore the different color scale in figures 4.7 and 3.3. We measured high concentrations of M_{BC} also in the middle free troposphere (Fig. 4.7). The BC aerosol consisted of aged urban haze (see also section 5.3) occasionally mixed with emissions from biomass burning in Indochina (Lin et al., 2023) and Northeast China (see also section 5.2). The remarkably high concentrations of M_{BC} measured between 30 and $34°$N originate from the metropolitan area of Beijing and Shanghai and were measured after few days of ageing over the Yellow Sea. The concentrations of pollution are often higher above the boundary layer than within, especially over Taiwan, located in the outflow of the Yangtze River delta and in the

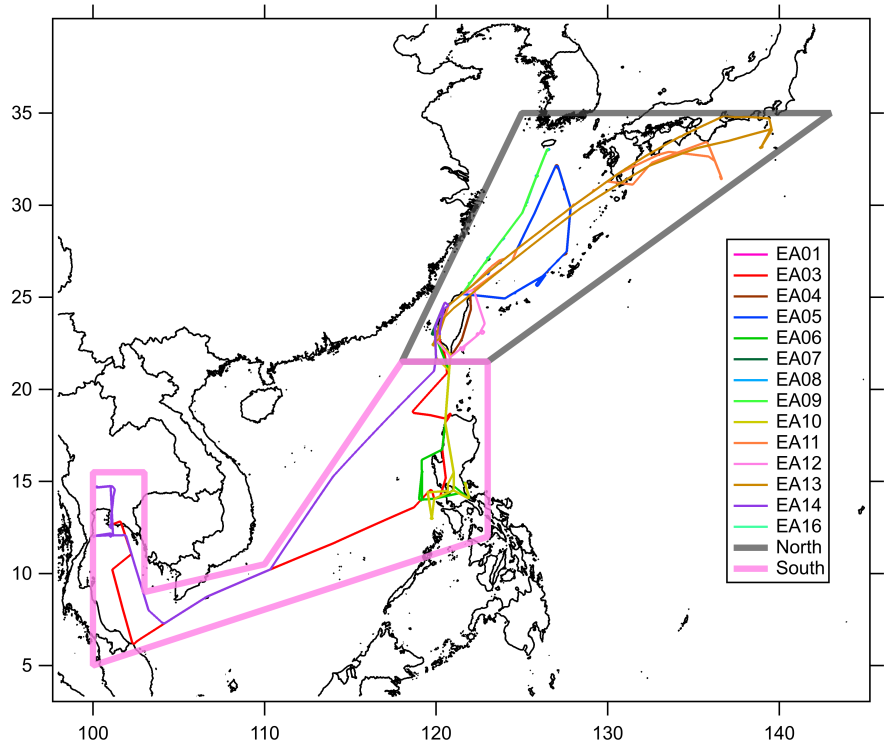

Figure 4.5: Flight map with measurement flights of the EMeRGe Asia field campaign from 2018. Different measurement flights are color coded according to legend. The grey polygon represents the region extracted from the global ECHAM-HAM data set for the comparison of the vertical distribution of $N_{CCN\ 0.3}$ for the vertical profiles north of Taiwan. The pink polygon is for the comparison south of Taiwan.

transportation pattern of highly aged pollution from the Beijing region, both some of the most polluted regions globally (e.g., Chan and Yao, 2008; Ramanathan and Carmichael, 2008). This suggests that the vertical distribution of M_{BC} can be assumed as dominated by aged urban haze.

The higher aerosol burden encountered in Asia is not only apparent in M_{BC} but also in the measured $N_{CCN\ 0.3}$ exceeding concentrations over Europe and the tropical Atlantic. The ECHAM-HAM concentrations for the probed regions in Asia are higher as well, however, they are still underestimating the measurements. Different to the results over Europe, in the probed regions over Asia the model also diverges from the measurements in the upper troposphere. One potential explanation for this divergence could be the higher pollution in the free troposphere in Asia. Whereas the overall measured CCN burden exceeds the model expectations, the shape of the vertical distribution is captured well in the ECHAM-HAM results.

In the upper troposphere, however, there are some event-like measurements of high $N_{CCN\ 0.3}$. These measurements tend to diverge strongly from the model expectations for the upper troposphere where no significant increase in $N_{CCN\ 0.3\ ECHAM}$ is expected up to altitudes of $14\,km$ in the tropical regions (Fig. 4.8 a) and around $13\,km$ in the extratropical regions (fig. 4.8 b). To understand the origin of these high $N_{CCN\ 0.3}$ in the upper troposphere we will need further investigation.

The lower $N_{CCN\ 0.3\ ECHAM}$ compared to the measurements can also be due to the very heterogeneous region of measurements regarding landmass and population. As ap-

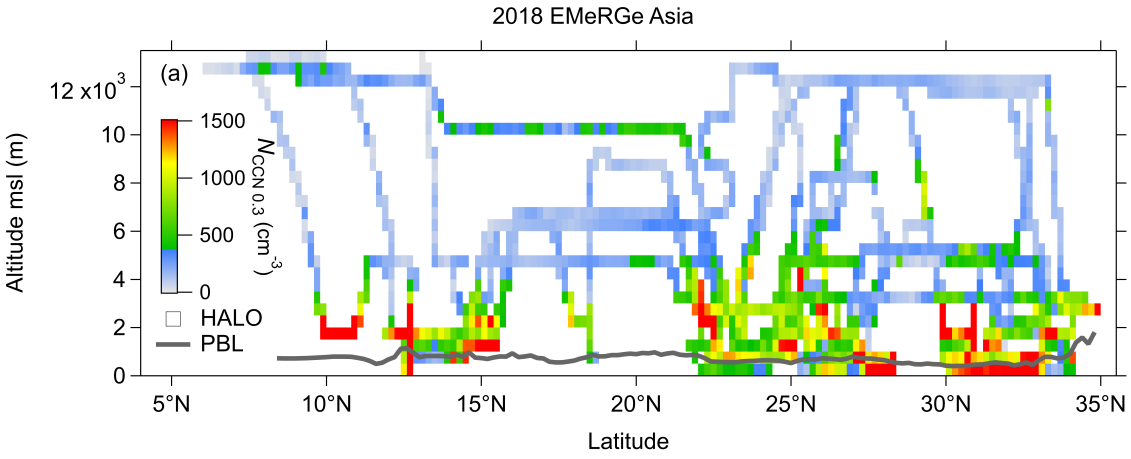

Figure 4.6: Cross section of $N_{CCN\ 0.3}$ for 2018 EMeRGe Asia measurements. Arithmetic mean for all data falling into a grid point of $0.2°$ latitude and $500\,\mathrm{m}$ altitude. The color scale ranges from 0 to $1500\,\mathrm{cm}^{-3}$. Means exceeding this range are shown in red. The grey solid line shows the planetary boundary layer height below flight track retrieved from HYSPLIT backward trajectories (details in section 2.5.3).

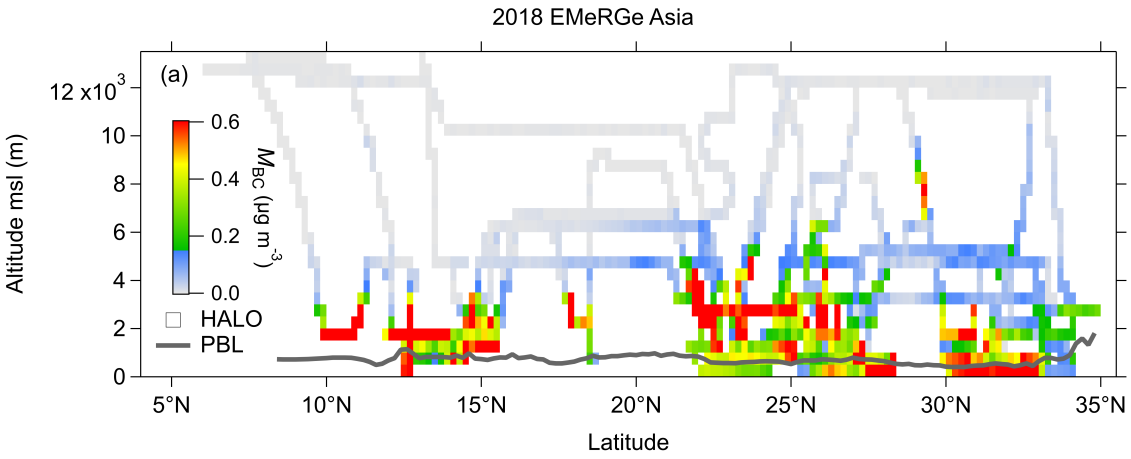

Figure 4.7: Cross section of M_{BC} for 2018 EMeRGe Asia measurements. Arithmetic mean for all data falling into a grid point of $0.2°$ latitude and $500\,\mathrm{m}$ altitude. The color scale ranges from 0 to $0.6\,\mu\mathrm{g\,m}^{-3}$. Means exceeding this range are shown in red. The grey solid line shows the planetary boundary layer height below flight track retrieved from HYSPLIT backward trajectories (details in section S1) The grey solid line shows the planetary boundary layer height below flight track retrieved from HYSPLIT backward trajectories (details in section 2.5.3).

parent in figure 4.5, large areas of the extracted polygons for the ECHAM-HAM data are over ocean, whereas the measurements over ocean were generally in higher altitudes or targeting expected transport of urban haze based on satellite observations and model forecasting. This sampling method leads to biases towards higher concentrations and makes a straight forward comparison with long term trends from not nudged modeling only little robust.

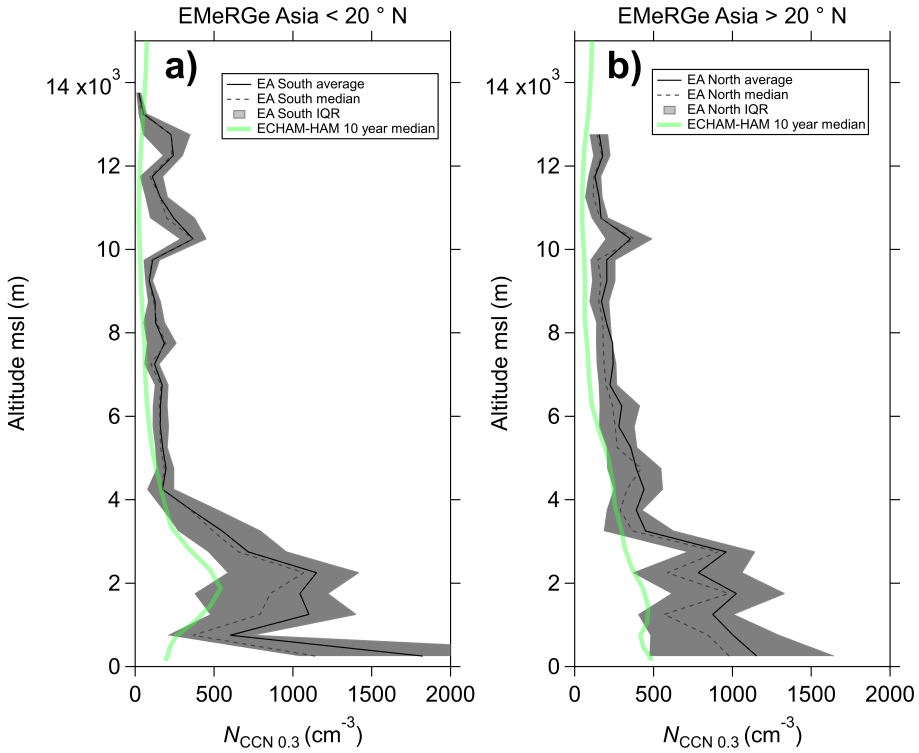

Figure 4.8: Vertical profiles for all $N_{CCN\ 0.3}$ data from the EMeRGe Asia north of $20°$ N (a) and south of $20°$ N (b). The dashed lines show the median, the solid lines the average and the grey shading represents the first and third quartile. The solid green line is the median ECHAM-HAM data from ten-year monthly average data in the time from 2003 until 2012 for the months March and April of each year.

4.3 Sensitivity of $N_{CCN\ 0.3}$ to anthropogenic perturbations

Over the tropical Atlantic the measured $N_{CCN\ 0.3}$ agrees well with the profiles retrieved from the ECHAM-HAM data. Therefore, the measurements of the CAFE Africa field campaign can be assumed to be representative for the more general vertical distribution of $N_{CCN\ 0.3}$ over the remote tropical Atlantic and second, anthropogenic pollution does not have strong impacts on the vertical distribution of $N_{CCN\ 0.3}$ in this region.

The comparison of the two HALO campaigns in 2017 and 2020, combined with the ECHAM-HAM model results, illustrates the high sensitivity of the CCN burden to local anthropogenic air pollution in the lower troposphere over Europe. In Europe $N_{CCN\ 0.3}$ is remarkably altitude dependent and shows a distinguished drop at the interface between planetary boundary layer and free troposphere. Above this drop at altitudes around $3\,\mathrm{km}$ the in-situ measurement data agrees well with the median of ten-years monthly average values from a global climate model. Further, there are only minor differences between the measurements in 2017 and 2020 although anthropogenic emissions were drastically reduced. Consequently, the CCN budget in the middle and upper troposphere over Europe can be considered as little sensitive to local anthropogenic air pollution.

These findings can not be confirmed based on measurements in East and Southeast Asia, where the CCN concentrations are higher over the whole vertical extent com-

pared to Europe. Also, the ECHAM-HAM model results tend to underestimate $N_{\text{CCN 0.3}}$ across its measured vertical extent. The influence of the targeted sampling strategy during EMeRGe Asia and the heterogeneous population and landmass distribution within the sampling region also remains uncertain.

The general sensitivity of $N_{\text{CCN 0.3}}$ in the lower troposphere to anthropogenic air pollution, however, is a common feature between the measurements in Asia and Europe. Over the remote tropical Atlantic, $N_{\text{CCN 0.3}}$ also showed a strong enhancement in a highly aged biomass burning smoke layer. For improved understanding of sources and properties of different pollution types, the co-variability of black carbon as a conserved tracer for combustion aerosol and cloud condensation nuclei as a highly climate relevant quantity can be analysed.

CHAPTER 5

Characteristic relationships between CCN and BC

This chapter is based on a manuscript draft published in Holanda, 2021 and contains figures and data sets of two further publications (Royer et al., 2023a; S. Raj et al., 2021a). My contributions are outlined below.

Holanda, B. A.: "Atmospheric processing and relevance of biomass burning aerosols over the amazon and the atlantic. chapter 6: co-variability of black carbon and cloud condensation nuclei in different polluted environments". *Dissertation, Johannes Gutenberg Universität Mainz*. (2021)

I designed and wrote the study in shared authorship with B. Holanda. I was responsible for the CCN measurements during EMeRGe EU and Asia, CAFE Africa and BLUESKY and supported the BC measurements led by B. Holanda. I calculated the HYSPLIT backward trajectories and did the satellite data analysis. Together with B. Holanda I selected the plumes and wrote the manuscript draft.

Royer, H. M.; Pöhlker, M. L.; Krüger, O. O.; Blades, E.; Sealy, P.; Lata, N. N.; Cheng, Z.; China, S.; Ault, A. P.; Quinn, P. K.; Zuidema, P.; Pöhlker, C.; Pöschl, U.; Andreae, M., and Gaston, C. J.: "African smoke particles act as cloud condensation nuclei in the wintertime tropical north atlantic boundary layer over barbados". *Atmospheric Chemistry and Physics*, 23, 2. (2023), pp. 981–998. DOI: 10.5194/acp-23-981-2023

I was responsible for the size resolved CCN measurements and the aerosol size distribution set up at BACO. I monitored the data quality and the instrumental performance throughout the measurement period. Further, together with H. Royer and M. L. Pöhlker, I performed the data analysis for the CCN and aerosol size distribution set up. H. Royer wrote the final publication and prepared the figures.

S. Raj, S.; Krüger, O. O.; Sharma, A.; Panda, U.; Pöhlker, C.; Walter, D.; Förster, J.-D.; Singh, R. P.; S., S.; Klimach, T.; Darbyshire, E.; Martin, S. T.; McFiggans, G.; Coe, H.; Allan, J.; R., R.; Soni, V. K.; Su, H.; Andreae, M. O.; Pöschl, U.; Pöhlker, M. L., and Gunthe, S. S.: "Planetary boundary layer height modulates aerosol—water vapor interactions during winter in the megacity of delhi". *Journal of Geophysical Research: Atmospheres*, 126, 24. (2021). DOI: https://doi.org/10.1029/2021JD035681

I supported S. Raj in the data evaluation and interpretation. Further, I commented and edited the manuscript and discussed the data presentation.

This chapter includes data sets from the following field experiments:
ACRIDICON-CHUVA, EMeRGe EU, EMeRGe Asia, CAFE Africa and BLUESKY.

As shown in chapter 3.2, the CCN burden in the lower troposphere can be highly sensitive to anthropogenic emissions. During the unprecedented reductions of anthropogenic emissions in the first COVID-19 lockdown in Europe, the lower tropospheric CCN burden dropped in a similar range as the black carbon mass and number concentrations. While the COVID-19 confinements strongly affected the CCN burden in the lower troposphere, the in situ measurements and model results of the free and upper troposphere revealed only little variability.

Based on ground based measurements in Delhi, S. Raj et al., 2021a found synoptic parameters, namely the planetary boundary layer height, to dominate the aerosol population density (Fig. 5.1) for M_{BC} and N_{CCN} at different supersaturation. The planetary boundary layer in Delhi during wintertime has periods of weak inversion, where the PBL height does not decrease considerably during nighttime. During days with a high nighttime PBL the aerosol burden is substantially lower. In contrast, on days with normal inversion, the low nocturnal PBL traps the urban haze in a much smaller volume, leading to high aerosol loads. Overall, M_{BC} and $N_{\mathrm{CCN\ (S)}}$ follow the same trends for the reported measurements in Delhi.

Both above mentioned cases, for Europe and Delhi, suggest some coherence or even linearity between the concentrations of black carbon and the overall budget of hygroscopic aerosol. It is worth noting that BC may also interact with water vapor and participate in cloud formation processes, however, the considerably small number concentration of BC compared to $N_{\mathrm{CCN\ 0.3}}$ (Fig. 5.3 b) illustrates that the role of BC is only of secondary importance for the overall CCN burden in urban haze.

Apart from urban haze emitted by anthropogenic activities, open biomass burning such as wildfires or agricultural residual burning also emits vast amounts of smoke. Smoke plumes are typically confined layers with aerosol and gas enhancements lofted into the free troposphere with a limited spatial extent (e.g., Holanda et al., 2023; Wu et al., 2021; Wu et al., 2020). During observations in high latitudes, smoke plumes from wildfires were found lofted into the upper troposphere and lower stratosphere (Ditas et al., 2018; Ohneiser et al., 2020; Ohneiser et al., 2022). The smoke plumes contain high fractions of black carbon aerosol, but also significant enhancements of hygroscopic aerosol as shown in figure 4.4 for HALO measurements over the tropical Atlantic. Likewise, Royer et al., 2023a finds long range transport of biomass burning smoke to increase $N_{\mathrm{CCN\ 0.16}}$ in the remote marine boundary layer of Barbados some thousands of kilometers downwind of the fire emissions in Africa (Fig. 5.2). The Barbados Aerosol Cloud Observatory (BACO) experiences nearly exclusive advection of marine air masses without recent continental or anthropogenic influences (section 2.1.2); therefore, recent continental or anthropogenic sources of these elevated aerosol loads rich in black carbon can be excluded. The two examples demonstrate the importance of smoke from biomass burning, not only for absorbing black carbon aerosol, but also for hygroscopic aerosol and therefore for aerosol-cloud interactions.

In situ measurements of N_{CCN} in biomass burning smoke remain sparse (Andreae, 2019). Unlike BC, N_{CCN} is subject to significant secondary formation (Ahern et al., 2019) and since the N_{CCN} is highly sensitive to the aerosol size distribution and aerosol surface chemistry, the concentrations can change substantially during the plumes' atmospheric residence time. However, the smoke plumes tend to stabilize in a temporal range where aircraft measurements are performed (Andreae, 2009).

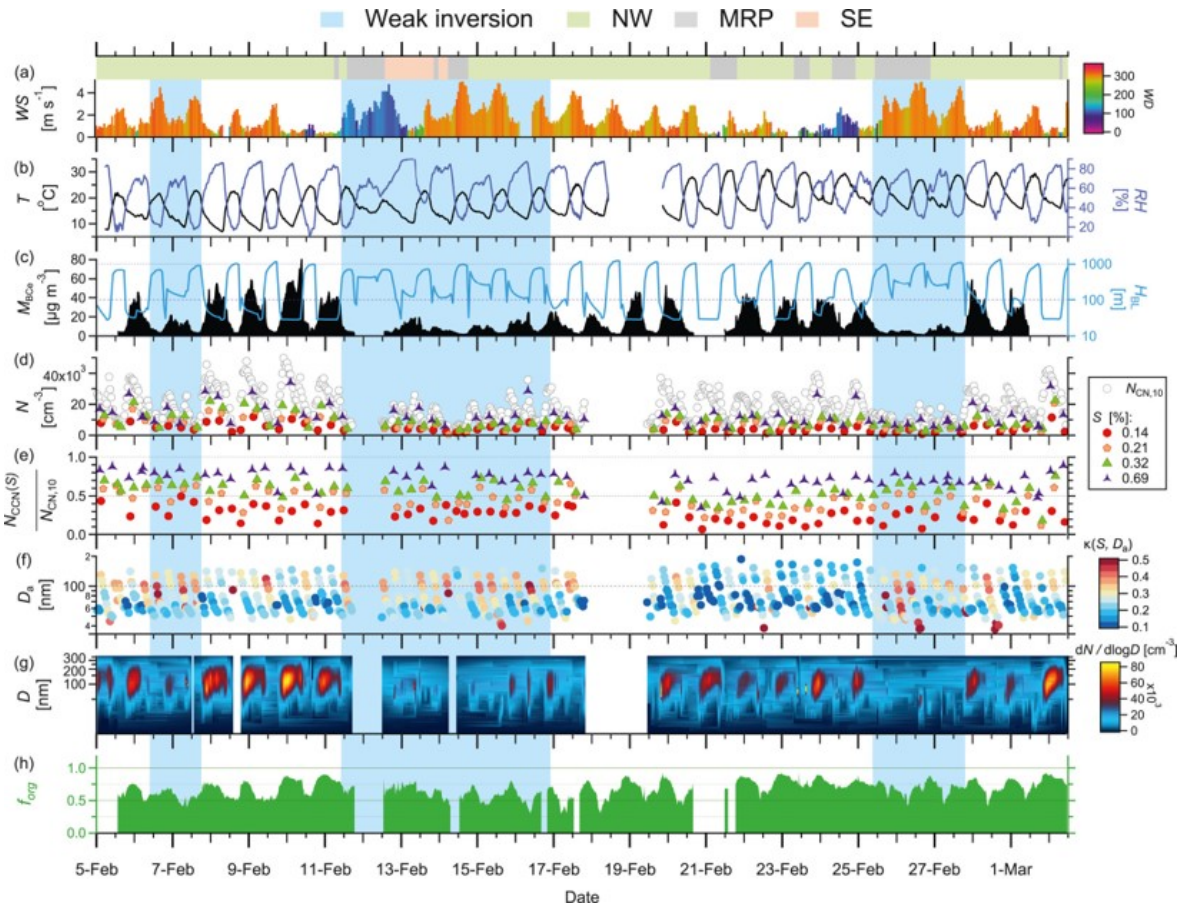

Figure 5.1: Figure and modified caption from S. Raj et al., 2021a. Evolution of meteorological and aerosol parameters shown as a function of local time. Strong radiative inversion periods and weak radiative inversion periods are indicated by white and blue graph background, respectively. The shading on top indicates the air mass observed: north-west (green); south-east (orange) and mixed regional pollution (gray). Temporal evolution of (a) wind speed (WS, $\mathrm{m\,s^{-1}}$ color-scaled by wind direction (WD, °); (b) temperature (T, °C) on the left axis and relative humidity (RH, %) on the right axis; (c) mass concentration of elemental black carbon (BCe, $M_{\mathrm{BC,\,e}}, \mu\mathrm{g\,m^{-3}}$) on the left axis and boundary layer height (HBL, m) from the WRF model on the right axis; (d) total particle number concentration in the size range ~10–370 nm ($N_{\mathrm{CN\,10}}\,\mathrm{cm^{-3}}$) and CCN concentration at selected S levels ($N_{\mathrm{CCN\,(S)}}, \mathrm{cm^{-3}}$); (e) CCN efficiency ($N_{\mathrm{CCN\,(S)}}/N_{\mathrm{CN\,10}}$) at selected S levels; (f) hygroscopicity Kappa ($\kappa_{\mathrm{(S,Da)}}$) is plotted as color of dots against the midpoint activation diameter (Da, nm) as y-axis. Larger Da corresponds to lower supersaturation and vice versa; (g) particle number size distribution (dN/d log D, $\mathrm{cm^{-3}}$) shown as a heat map from 10 to 370 nm; (h) organic mass fraction of non-refractory submicron aerosols (NR-PM1, f_{org}).

That can be explained by the dilution of the plumes which lowers the coagulation rate which is the driving factor for considerable shifts in the aerosol size-distribution and number concentration (Andreae, 2019; Janhäll et al., 2010). As a result, the HALO in situ data can be expected to be within a relatively stable state of the plume life cycle.

Black carbon is a relatively well conserved tracer of anthropogenic pollution and wildfires (e.g., Andreae, 2019; Sedlacek et al., 2022) and hence it can serve as a link between the influence of pollution from combustion on the CCN budget. The BC aerosol mass is nonvolatile and chemically inert and thus shows only minor changes

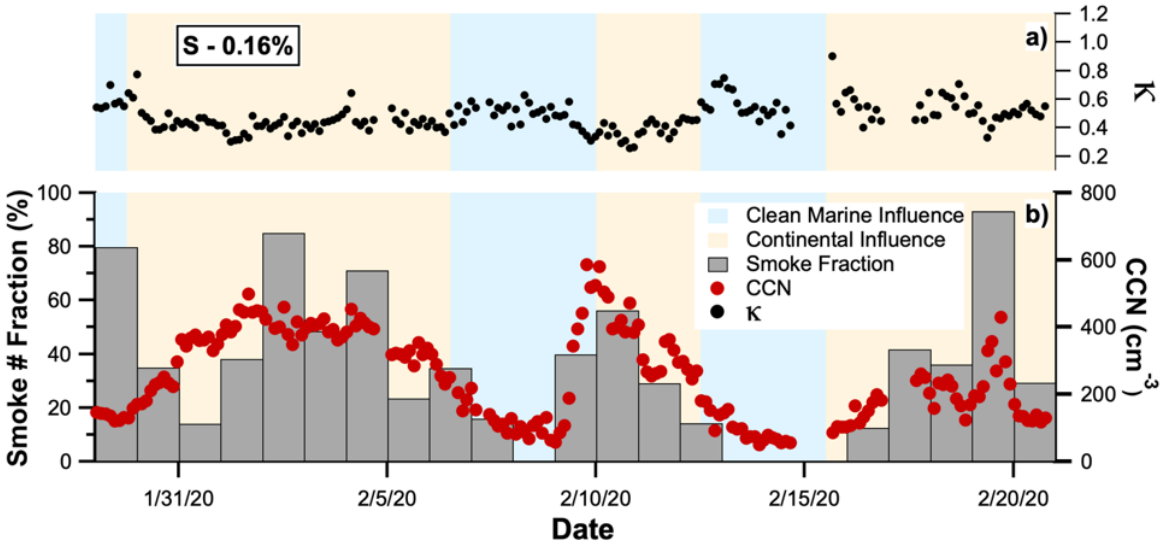

Figure 5.2: Figure and caption from Royer et al., 2023a. Temporal evolution of hygroscopicity parameter κ (black dots, upper panel) and CCN number concentration (red dots, lower panel), both measured at S = 0.16%, and smoke particle number fraction (grey bars, left axis, lower panel). Background color shadings indicate periods of continental influence (orange) and clean marine influence (blue) determined by HYSPLIT backward trajectories and dust mass concentrations.

during atmospheric aging. Therefore, the relationship between $N_{\mathrm{CCN\,0.3}}$ and M_{BC} for typical emission sources is characterised based on HALO measurement data. For highly and lightly aged open biomass burning smoke and aged urban haze, a distinct relation between BC and CCN is identified. The relationships are further compared with some case studies from HALO in situ measurements in various environments. For the case studies, HYSPLIT backward trajectories and MODIS satellite data are also considered in the source apportionment. Based on the typical emission sources, a general parametrisation of the CCN budget related to the M_{BC} in polluted environments is retrieved.

5.1 Typical $N_{\mathrm{CCN\,0.3}}$ and M_{BC} regimes in polluted environments

In this section, the three typical regimes for highly and lightly aged biomass burning smoke and for urban haze are identified for HALO in situ data from measurements in one of the three distinct pollution regimes without significant influences of other combustion aerosol sources.

The reference case for the highly aged biomass burning smoke consists of data from the CAFE Africa campaign where we measured highly aged smoke plumes in different stages of aging states over the tropical Atlantic during three measurement flights. The plumes were transported well above the marine boundary layer (Fig. 4.3) and did not show implications of recent mixing with other air masses.

The core diameters of the refractory black carbon aerosol (D_{rBC}) in the highly aged biomass burning smoke are comparably large, with a mean of $D_{\mathrm{rBC}} = 225\,\mathrm{nm}$ and a

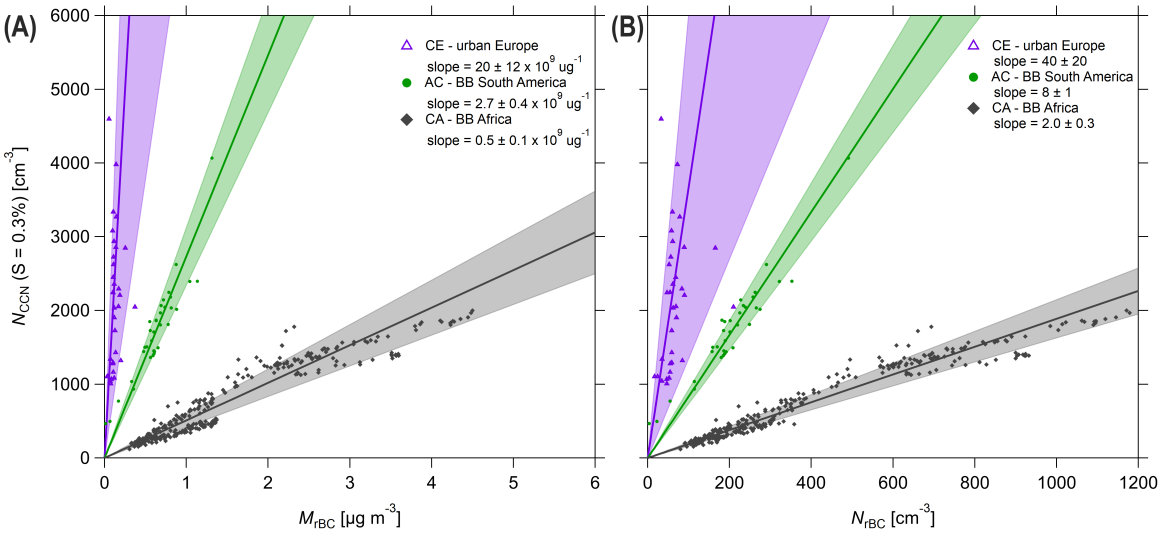

Figure 5.3: Relationships between **(A)** $N_{CCN\ 0.3}$ and M_{BC}; and **(B)** $N_{CCN\ 0.3}$ and N_{BC} for the selected pollution conditions: urban pollution (violet), lightly aged Amazonian BB (green) and highly aged African BB (grey). The solid lines represent linear orthogonal distance regression (ODR) applied to the 1-min averaged data (as markers) with shadings representing ± one standard deviation. The fit parameters of the regressions are shown in Table 5.1.

narrow distribution with $\sigma_{rBC} = 1.5$ (Fig. 5.4 A1 and B1). While highly aged biomass burning smoke has the largest D_{rBC} in our data set, it represents the lower end of the $N_{CCN\ 0.3}$ to M_{BC} regimes ($\Delta CCN/\Delta BC \approx 0.5 \pm 0.1 \cdot 10^9\ \mu g^{-1}$).

During the transatlantic transport, the smoke plumes dilute with cleaner air masses in the free troposphere. This dilution causes a decrease in absolute concentrations, however, the ratio of $N_{CCN\ 0.3}$ to M_{BC} and N_{BC} remains nearly unaffected. The narrow size distribution and small spread between mean, median and within the interquartile range (IQR) are also remarkable for measurement data from three independent measurement flights with different geographical locations over the tropical Atlantic. Further, the observed size range is in good agreement with ground based measurements at the ATTO site, as discussed in Holanda et al. (2023).The low variability of the highly aged smoke plumes over large geographical areas suggests that there is little aging of the persistent layers of smoke that form from the pyro-convective smoke clouds.

Lightly aged biomass burning smoke over the Amazon rain forest was intensively probed during the ACRIDICON-CHUVA campaign. In the measurement period in September 2014, however, long-range transport of smoke emitted in Africa comprises a large fraction of the Amazon's aerosol burden (Holanda et al., 2023; Holanda et al., 2020; Saturno et al., 2018). Therefore, we only selected periods when emissions from regional fires in the Amazon were dominant. Most of the selected data were

Table 5.1: The fit parameters of the ODR fits presented in Figure 5.3: slope ± standard deviation (SD), R^2 and the number of observations (N, i.e., observations of one minute averages of data in 1 Hz temporal resolution) shown in the respective BC-CCN scatter plot.

	Urban	Lightly aged BB	Highly aged BB
$\Delta CCN/\Delta BC \pm SD\ [\cdot 10^9\ \mu g^{-1}]$	20 ± 12	2.7 ± 0.4	0.5 ± 0.1
R^2	0.90	0.99	0.97
N	62	70	305

collected within the PBL of the southern Amazon rain forest, known as 'Arc of Deforestation'. These data fall within $N_{\mathrm{CCN\,0.3}}$ to M_{BC} ratios with a slope of $\Delta\mathrm{CCN}/\Delta\mathrm{BC} \approx 2.7 \pm 0.4 \cdot 10^9\ \mu\mathrm{g}^{-1}$ (Fig. 5.3). With $D_{\mathrm{rBC}} = 195\,\mathrm{nm}$ and $\sigma_{\mathrm{rBC}} = 1.6$, the size distribution of lightly aged smoke is also well confined and the BC core diameters are below the ones for highly aged smoke.

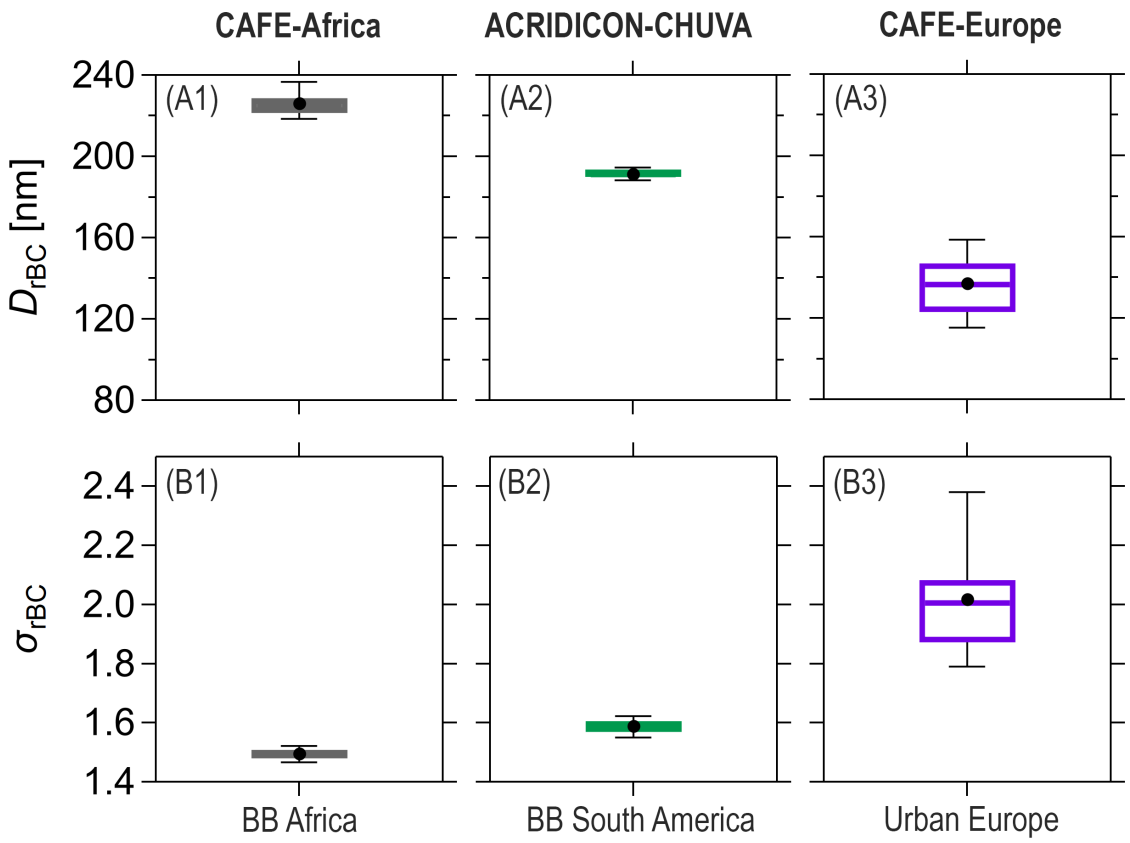

Figure 5.4: Properties of rBC cores during pollution conditions shown in Fig. 5.3, showing significant differences in agreement with Holanda et al. (2023). Specifically, geometric mean diameters, D_{rBC}, in **(A)** and (B) the geometric standard deviation, σ_{rBC}, in **(A)** are shown, both retrieved from lognormal fits of 1 minute averaged rBC mass size distributions for the different pollution conditions presented in Figure 5.3. In the box-whisker plots, the horizontal bars represent the median, circles the mean, boxes the interquartile range (IQR, i.e., 25$^{\mathrm{th}}$ and 75$^{\mathrm{th}}$ percentiles), and whiskers the 9$^{\mathrm{th}}$ and 91$^{\mathrm{th}}$ percentiles.

In the urban haze of several European cities we found the highest $N_{\mathrm{CCN\,0.3}}$ per N_{BC} and M_{BC} presented in this study, reaching up to $\sim 4600\,\mathrm{cm}^{-3}$, while N_{BC} does not exceed $\sim 160\,\mathrm{cm}^{-3}$, and M_{BC} $\sim 0.2\,\mu\mathrm{g\,cm}^{-3}$ leading to a ratio of $\Delta\mathrm{CCN}/\Delta\mathrm{BC} \approx 20 \pm 12 \cdot 10^9\ \mu\mathrm{g}^{-1}$ accordingly. The measurements were taken from May to June 2020, without significant biomass burning events in Europe and out of the domestic heating season where domestic wood burning enriches the BC burden significantly (e.g., Kalogridis et al., 2018). Therefore, these measurements serve as a benchmark for the typical $N_{\mathrm{CCN\,0.3}}$ to M_{BC} signature of urban haze. The urban haze presented here is dominated by anthropogenic combustion emissions, which include, to a significant degree, emissions from traffic and energy production (Bond et al., 2013; Krüger et al., 2022, and chapter 3). The rather broad size distribution ($\sigma_{\mathrm{rBC}} = 2.0$) combined with relatively small $D_{\mathrm{rBC}} = 137\,\mathrm{nm}$ are also typical attributes of urban pollution (Liu et al., 2014;

Reddington et al., 2013; Schwarz et al., 2006; Schwarz et al., 2008). It is notable that, for N_{BC}, probably a large fraction is not detectable with the SP2 due to the lower cut-off around $70\,\mathrm{nm}$. For M_{BC}, however, the smaller particles are only of secondary importance.

5.2 Co-variability of $N_{CCN\ 0.3}$ and M_{BC} in aged biomass burning emissions

Biomass burning smoke is an important constituent of atmospheric pollution, accounting for up to 60 % of atmospheric M_{BC} (e.g., Andreae, 2019; Bond et al., 2013; Bowman et al., 2009). While urban emissions show an overall decreasing trend (e.g., Kanaya et al., 2020; Kutzner et al., 2018; Querol et al., 2013; Singh et al., 2018), smoke from open biomass burning is globally increasing due to land use and climate change (e.g., Guerreiro et al., 2018; Jolly et al., 2015; Senande-Rivera et al., 2022). The smoke emitted from open biomass burning is a punctual and periodic source of air pollution. In the global context, however, there are emissions from wildfires throughout the year and also, BC is ubiquitous, affecting air quality and climate (Schill et al., 2020).

Lightly aged biomass burning smoke was also measured in the lower troposphere over Europe and Asia, besides the smoke probed over the Amazon (Fig. 5.3). The lightly aged biomass burning plumes presented in the following are from measurements over the Gulf of Thailand and originated from evergreen broad leaf forest fires in the border area between Cambodia and Vietnam (Fig. 5.5), from the region around Marseille (Fig. 5.7), from Portugal, measured over Spain (Fig. 5.8), and from Italy, measured over the Tyrrhenian Sea (Fig. 5.9). Apart from the data for lightly aged smoke, we also show data for highly aged smoke originated from Africa and measured over the Amazon and the coast of Northeast Brazil (Fig. 5.11).

Two smoke plumes were probed over the Gulf of Thailand during the ferry flights of the EMeRGe Asia campaign on 12 March and 07 April 2018. Both plumes match the lower end of the $N_{CCN\ 0.3}$ to M_{BC} regime found for the reference case of Amazonian smoke (Fig. 5.5A). Similar to Brazil, fire is also a widespread tool for land clearance in the highlands of Vietnam and Cambodia (Nguyen et al., 2008; Scheidel and Work, 2016; Vadrevu et al., 2019). The MODIS fire maps in Figure 5.5B reveal some fire clusters in the transition area of agriculturally used terrains and savannahs as well as tropical evergreen broad leaf forest vegetation (Fig. 5.5B, 5.6A). According to the air mass history (Figs. 5.5C and 5.6), the smoke plumes we measured over the Gulf of Thailand are likely to have originated from these deforestation and agricultural fires. The plumes were intercepted above the PBL (Fig 4.7) in altitudes between 1500 and 2000 m and some hundreds of kilometers away from the emission sources, and thus, have aged for one and two days prior to the measurements (Fig. 5.5C, 5.6B). What is remarkable here is the good agreement between the two measurements even though in the second flight we encountered cloudy conditions and precipitation (Fig. 5.6B). The slightly larger BC fraction in the Asian smoke compared to the reference case can be explained by the contribution of agricultural fires and the larger distance to the emission sources as well as the aging time and potential scavenging of hygroscopic aerosol due to high humidity and clouds.

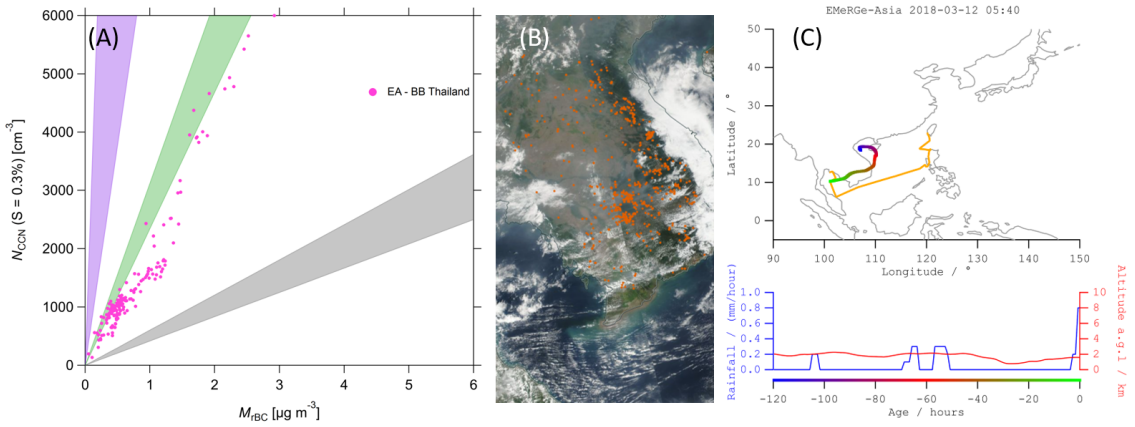

Figure 5.5: **(A)** Relationship between $N_{CCN\ 0.3}$ and M_{BC} for BB emissions in Southeast Asia, measured over the Gulf of Thailand during two measurement flights (12 March and 07 April 2018). The plumes are emitted from BB fires in Vietnam and Cambodia with evergreen broad leaf forest vegetation, savannahs as dominant combustion fuels. **(B)** MODIS "Corrected Reflectance (True Color)" image for 10 March 2018, two days prior to measurement flight. Red dots indicate "Fires and Thermal Anomalies (Day and Night)". **(C)** HYSPLIT BT for measurements of BB plume. The color code indicates time passed prior to measurement, suggesting a plume age of one to two days. Note, BT and MODIS image for the flight on 07 April 2018 can be found in Fig. 5.6.

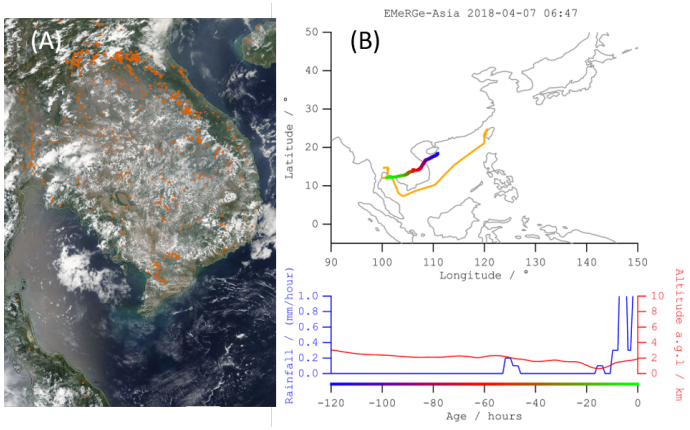

Figure 5.6: **(A)** MODIS "Corrected Reflectance (True Color)" image for 05 April 2018, two days prior to measurement flight. Red dots indicate "Fires and Thermal Anomalies (Day and Night)". **(B)** HYSPLIT BT for measurements of BB plume. The color code indicates time passed prior to measurement, suggesting a plume age of one to two days.

A smoke plume was encountered twice, once onshore and once over the Mediterranean, during the EMeRGe EU campaign on 24 July 2017. Figure 5.7B shows fire spots close to Marseille, France that likely originated from the burn of subtropical mixed forests. We measured the smoke plumes near their emission source, thus we probed relatively fresh smoke conditions. Figure 5.7A reveals an excellent agreement between the BB smoke over the Mediterranean and the lightly aged BB over the Amazon (green shading). For the BB smoke measured over land, however, a higher CCN to BC ratio is observed, falling in between the lightly aged smoke (green) and the urban haze (violet) ratios. This may result from intrusions of urban haze from the nearby metropolitan area of Marseille and Toulon with a population over 3 million

and France's largest cargo harbor *. These observations highlight the sensitivity of the $N_{CCN\,0.3}$ to M_{BC} ratio to additional air-pollution or other strong aerosol emitters.

The comparison of the HALO in situ measurements with SEVIRI satellite retrieved aerosol optical thickness (AOT) in Figure 5.7B highlights the capabilities of satellites to identify the geographical location of smoke plumes. This information can be extended with information about the vertical plume distributions and the distinct aerosol properties within the smoke plumes. The in situ measurements found the plume to be located in altitudes around $2\,\mathrm{km}$ with peak concentrations of $7\,\mu\mathrm{g\,m^{-3}}$, while M_{BC} within the PBL was around $1\,\mu\mathrm{g\,m^{-3}}$ (Hernández et al., 2022).

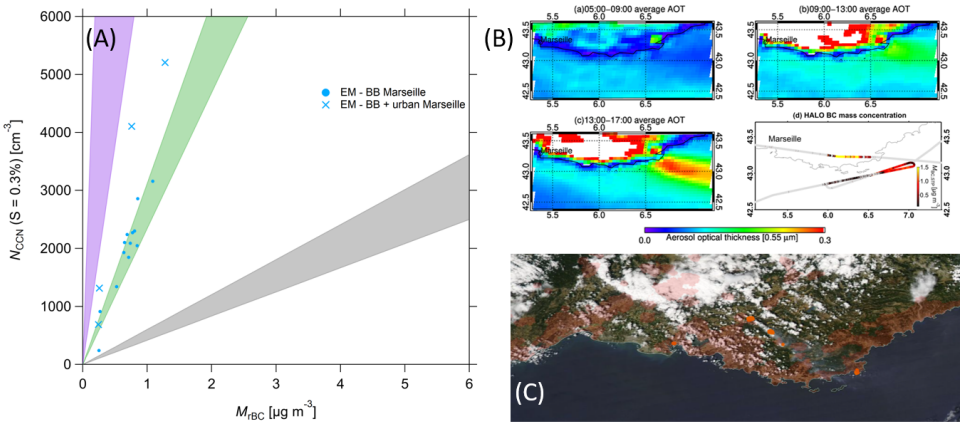

Figure 5.7: (A) Relationship between $N_{CCN\,0.3}$ and M_{BC} for BB emissions in southern Europe, measured over France and the Mediterranean close to Marseille (24 July 2017). (B)(a - c) Aerosol optical thickness at $0.55\,\mu\mathrm{m}$ as retrieved from SEVIRI from 05:00 to 17:00 UTC on 24 July 2017. **(B)**(d) E-EU-07 flight track, color coded with M_{BC}. For better contrast, the scale for M_{BC} ranges from 0.1 to $1.5\,\mu\mathrm{g\,m^{-3}}$. Grey color on flight track indicates values below $0.1\,\mu\mathrm{g\,m^{-3}}$. M_{BC} reached values up to $7\,\mu\mathrm{g\,m^{-3}}$ at the French coast. Figure adapted from Hernández et al., 2022. **(C)** MODIS "Corrected Reflectance (True Color)" image for 24 July 2017, the day of measurement flight. Red dots indicate "Fires and Thermal Anomalies (Day and Night)". The grey shading emerging from fire dots is the image of smoke plumes. The red shading indicates "Human Built-up And Settlement Extent" showing the high density of urban settlements at BB origin.

At relatively low concentrations a higher $N_{CCN\,0.3}$ to M_{BC} ratio is observed for smoke originated from savannah, grassland and evergreen conifer forest fires in Portugal (Fig. 5.8A), compared to the reference case. For higher concentrations of M_{BC}, the ratio agrees well with lightly aged amazonian smoke. The fires had already started five days prior to our measurement flight and persisted over several days. The higher $N_{CCN\,0.3}$ observed in this roughly one day aged plume (Fig. 5.8C) may result from intrusions of urban pollution. The BTs pass over Madrid at altitudes around 2 to 3 km (Fig. 5.8C) as a major source of anthropogenic emissions in Spain. Nevertheless, there is a clear difference in the $N_{CCN\,0.3}$ to M_{BC} ratio of the plume containing predominately wildfire smoke and the outflow of urban haze from Barcelona (section 5.3) as another major pollution region in Spain (Fig. 5.14).

Over the Tyrrhenian Sea we measured roughly two days aged biomass burning smoke from fires in southern Italy and Croatia during EMeRGe EU (Fig. 5.9). The $N_{CCN\,0.3}$

*https://www.marseille-port.fr/en

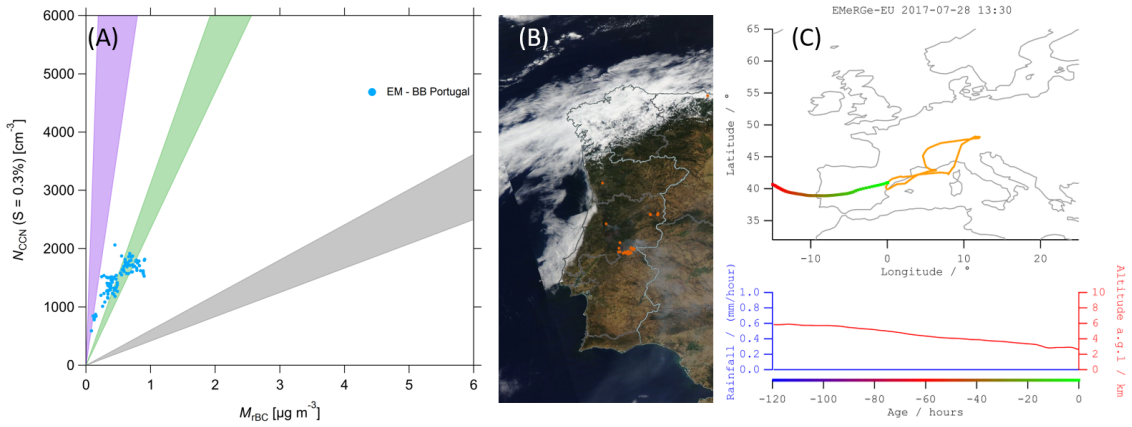

Figure 5.8: (A) Relationship between $N_{CCN\ 0.3}$ and M_{BC} for BB emissions in Southern Europe, measured over Spain. The plumes are emitted from BB fires in Portugal, where savannahs, grassland and evergreen conifer forests are the dominant combustion fuels. The day of measurement was 28 July 2017. **(B)** MODIS "Corrected Reflectance (True Color)" image for 27 July 2017, one day prior to measurement flight. Red dots indicate "Fires and Thermal Anomalies (Day and Night)". The grey shading emerging from fire dots is the image of smoke plumes. **(C)** HYSPLIT BT for measurements of BB plume. The color code indicates time passed prior to measurement, suggesting a plume age of about one day.

to M_{BC} ratio for this lightly aged smoke falls below the ratio found for Marseille (Fig. 5.7) and the reference case (Fig. 5.3). The main combustion fuels were savannahs in Italy and grasslands in Croatia. Savannahs and grasslands tend to burn more efficiently than forests, where the water content is higher (e.g., Andreae, 2019). It can therefore be assumed that fires in more humid regions tend to emit larger amounts of gaseous aerosol precursors and primary aerosol in addition to BC. Thus, a drift towards a lower CCN fraction is in good agreement with the results for highly aged African smoke. The measurements over the Tyrrhenian Sea show nicely the importance of the combustion fuel for the plumes' composition. Andreae, 2019 summarized different biomass burning fuels and found, for savannahs, the co-emitted CCN to be considerably lower than for forest fires (Fig.5.10).

Holanda et al., 2020 reported in situ measurements of highly aged African smoke probed twice in the northern Amazon Basin on the 06 September 2014 and over the Atlantic near the Brazilian coast on 30 September 2014 during the ACRIDICON-CHUVA campaign. The African smoke over South America was encountered mainly in defined and stable atmospheric layers with high aerosol concentrations above the marine boundary layer (Holanda et al., 2020) as well as after downward mixing into the marine and continental boundary layer. As shown in Figure 5.11, many of the data points fall within the region defined as highly aged smoke (grey shading). These plumes, even though lower in overall concentration, agree remarkably well with the CAFE Africa measurements. The points that fall above the grey shading correspond to measurements in the marine or Amazonian boundary layers, where marine and biogenic emissions from the Amazon rain forest potentially contribute to the overall CCN burden. Nevertheless, consistent $N_{CCN\ 0.3}$ to M_{BC} ratios were obtained between independent measurement regions and different campaigns taken four years apart from each other. This result indicates that African smoke layers tend not to age significantly after the pyro-convective intrusion into the free troposphere. The potential formation of secondary formed CCN also seems to happen within the

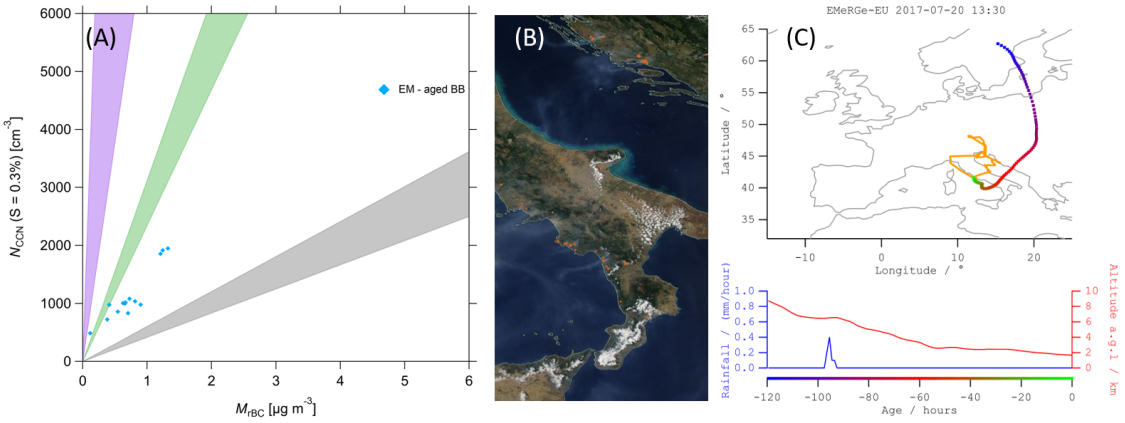

Figure 5.9: **(A)** Relationship between $N_{CCN\ 0.3}$ and M_{BC} for BB emissions in Southern Europe, measured over the Tyrrhenian Sea close to Rome. The plumes are emitted from BB fires in Italy and Croatia, where savannahs and grassland are the dominant combustion fuels. The day of measurement was 20 July 2017. **(B)** MODIS "Corrected Reflectance (True Color)" image for 18 July 2017, two days prior to measurement flight. Red dots indicate "Fires and Thermal Anomalies (Day and Night)". The grey shading emerging from fire dots is the image of smoke plumes. **(C)** HYSPLIT BT for measurements of BB plume. The color code indicates time passed prior to measurement, suggesting a plume age between two and three days.

first days, before the transatlantic transport of the smoke plumes. However, the influence of secondary and primary aerosols on the CCN budget within the smoke layers cannot be answered from our in situ data and will require further modelling and measurement efforts. Since we did not find further aging and processing between the measurements from CAFE Africa and Brazil for BC and CCN in the smoke layers, the only varying factor is the overall concentration which is subject to dilution with surrounding comparatively clean air-masses. Any other aerosol scavenging or processing will lead to a shift in the ratio between $N_{CCN\ 0.3}$ and M_{BC}. Wet scavenging processes would predominately reduce $N_{CCN\ 0.3}$, while sedimentation deposition is unlikely to play an important role in the $N_{CCN\ 0.3}$ size ranges (Pöhlker et al., 2021; Seinfeld and Pandis, 2006).

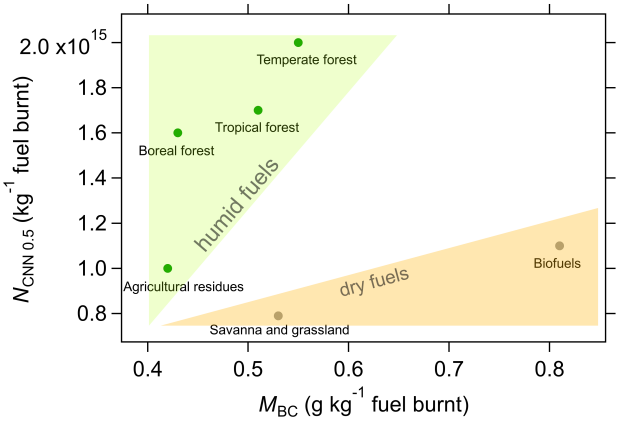

Figure 5.10: Relative emissions of $N_{CCN\ 0.5}$ and M_{BC} per kilogram of burnt combustion fuel. Data taken from table 1 in Andreae, 2019. Note that due to different measurement methods and data reporting, elemental carbon (EC) is also included in the provided $M_{BC\ and\ EC}$ values.

After mixing of the stratified layers of African smoke into the PBL in the central Amazon, no significant aging of the BC is observed either. Figure 5.13 shows $N_{\mathrm{CCN\ 0.3}}$ to M_{BC} ratios for the lightly aged regional and highly aged African smoke measured at the ATTO site (Holanda et al., 2023) and reveals that mixing into the PBL over the central Amazon does not significantly shift the ratios between CCN and BC into other regimes either. The three years of ATTO data were separated with a deconvolution method based on the differences in the BC size distributions, presented in Holanda et al., 2023. The $N_{\mathrm{CCN\ 0.3}}$ was retrieved from the aerosol size distribution measured with an SMPS, following the parametrisation by Pöhlker et al., 2018. The M_{BC} was directly measured with an SP2 (Holanda et al., 2023). The good agreement between the spatial highly resolved HALO measurements and the ground based long-term measurements covering different seasons reveals the robustness of the typical $N_{\mathrm{CCN\ 0.3}}$ to M_{BC} regimes for highly aged African smoke, introduced in this study.

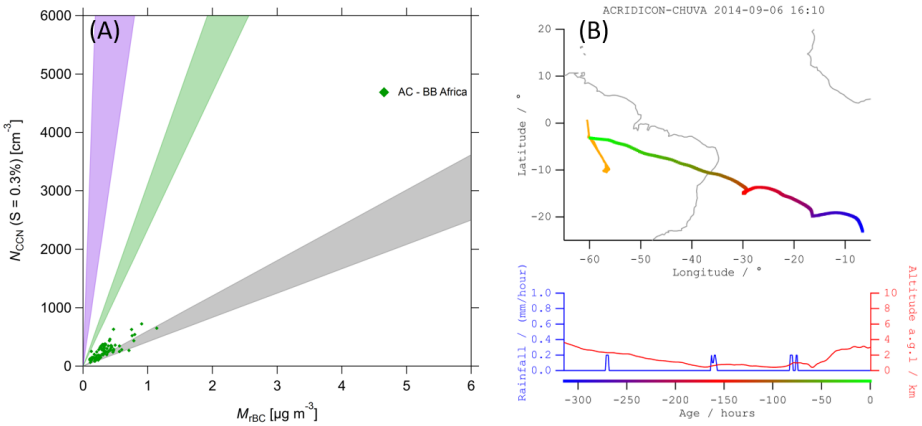

Figure 5.11: (A) Relationship between $N_{\mathrm{CCN\ 0.3}}$ and M_{BC} for BB emissions from African fires, measured over the Amazon rain forest on 06 September 2014 and the Brazilian coast on 30 September 2014. **(B)** HYSPLIT BT calculated 315 hours backward. The color code indicates time passed prior to measurement, showing that the plume roughly travelled over Brazil for four days prior to measurement. Note, the BT for the second plume can be found in figure 5.12.

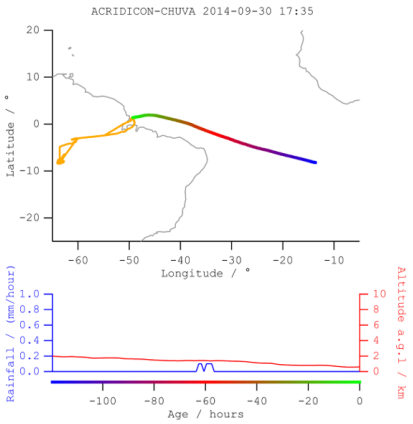

Figure 5.12: HYSPLIT BT for measurements of African BB plumes at Brazilian coast. The color code indicates time passed prior to measurement.

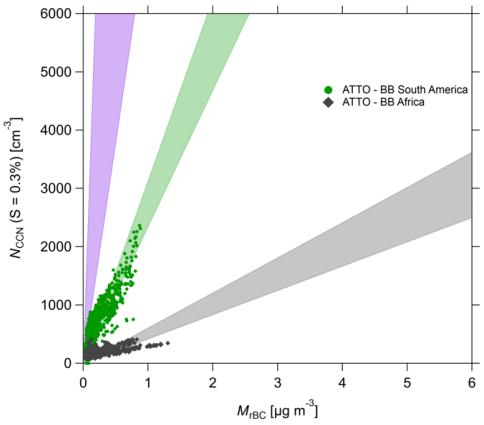

Figure 5.13: Relationship between $N_{CCN\ 0.3}$ and M_{BC} for South American BB emissions (green dots) and African BB smoke (black squares) at the ATTO site. The data separation was performed according to Holanda et al., 2023, further details and methods can be found therein.

5.3 Co-variability of $N_{CCN\ 0.3}$ and M_{BC} in urban haze

In the following, we show measurements of urban pollution from Europe and East Asia. Based on air-mass history modeling, we could identify plumes of urban haze from Barcelona, Spain (Fig. 5.14), Nagoya, Japan (Fig. 5.15), mixed urban and lightly aged smoke from Rome and the Po Valley, Italy (Fig. 5.16, 5.17B) and London, England (Fig. 5.17A). The outflow from Shanghai and Beijing, China was potentially mixed with aged biomass burning smoke (Fig. 5.18). Ground based measurements from Delhi (S. Raj et al., 2021a) are also included in this chapter.

The plume of urban haze originating from Barcelona was measured in summer 2017 during EMeRGe EU (Fig. 5.14A). The $N_{CCN\ 0.3}$ to M_{BC} ratio is in a comparable range to the typical ratio found for urban haze (5.14A, violet shading). During the measurement period, smoke from wildfires in Portugal affected the lower troposphere of the Iberian peninsula (Fig. 5.8). It is possible that the measured urban haze is also influenced to some extent by biomass burning smoke. However, as apparent in figure 5.14B, the probed air-mass is probably not directly affected by the smoke from Portugal and a substantial fraction of the air-masses has not passed the free troposphere over the Iberian Peninsula, where transport of biomass burning smoke preferentially occurs (see e.g., Figs. 3.3, 5.8 and 4.3). The good agreement of the measurements from Barcelona and the reference cases also suggests urban haze to be the dominant aerosol source.

We measured relatively dense pollution downwind of Nagoya in the Ise Bay. The urban haze from the Nagoya metropolitan area shows $N_{CCN\ 0.3}$ to M_{BC} properties that are comparable to the ones encountered in Europe (Fig. 5.15A). The pollution layer was measured in spring 2018 during the EMeRGe Asia campaign. The Nagoya metropolitan area is one of Japan's major industrial centres and, with more than 9 million inhabitants, it is one of Japan's most densely populated areas (Japan, 2020). The major industrial sector is the Toyota main manufacturing plant with numerous sub-component suppliers. Similar to the observations of urban pollution influenced by biomass burning smoke in Europe (Fig. 5.16, 5.17B), there might be some impact of long-range transported smoke from cropland fires in China. The satellite

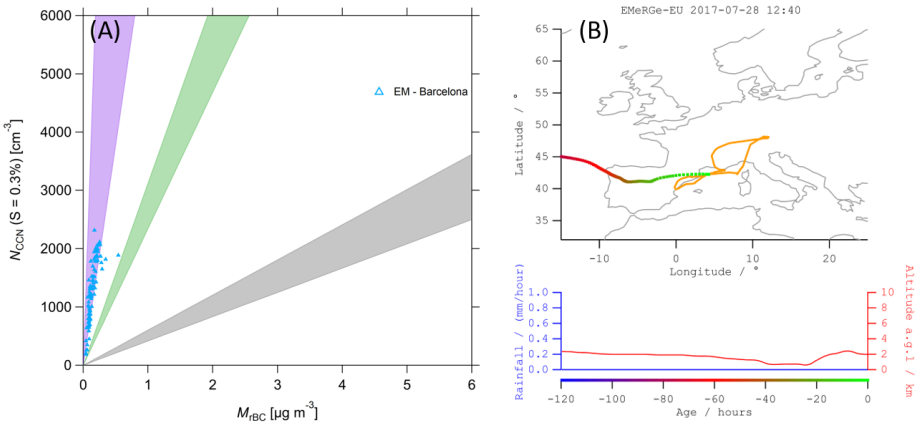

Figure 5.14: **(A)** Relationship between $N_{CCN\,0.3}$ and M_{BC} for urban emissions from Barcelona. The plume was measured over the Mediterranean close to Barcelona (20 July 2017). **(B)** HYSPLIT BT for measurements of the Barcelona plume. The color code indicates time passed prior to measurement, suggesting a plume age of only a few hours.

image reveals a smoke layer on the measurement day in proximity to the measurements (Fig. 5.15B, C). Nevertheless, a large fraction of the observed CCN is expected to have originated from urban emissions in Nagoya metropolitan area. Also, the shorter distance to the source region may explain the high CCN concentration within the Japanese plume. Furthermore, the plume in the Ise Bay was measured within the PBL, while long-range transport of open biomass burning smoke typically occurs above the PBL (see Fig. 3.3 and Holanda et al., 2023; Holanda et al., 2020).

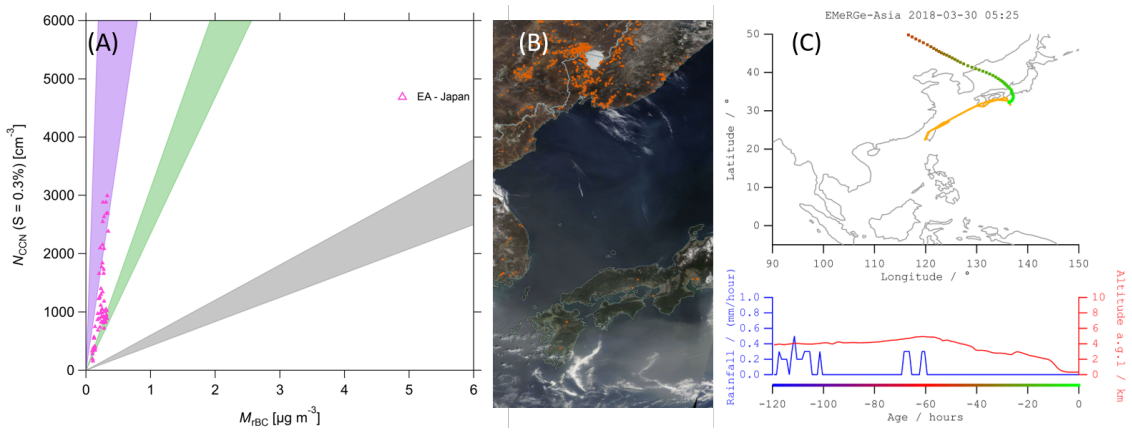

Figure 5.15: **(A)** Relationship between $N_{CCN\,0.3}$ and M_{BC} for urban emissions from metropolitan area of Nagoya (30 March 2018). **(B)** MODIS "Corrected Reflectance (True Color)" image for the day of measurement. Red dots indicate "Fires and Thermal Anomalies (Day and Night)". The grey shading over the ocean is possibly BB and urban smoke from China. **(C)** HYSPLIT BT for measurements of plume. The color code indicates the time elapsed before the measurement, indicating relatively fresh emissions with a residence time of a few hours.

The observed $N_{CCN\,0.3}$ to M_{BC} ratio in the haze plumes from Rome and the Po Valley probed in summer 2017 during EMeRGe EU diverges strongly from the typical case (Figs. 5.16A and 5.17B). As shown in section 3.2, the emission reductions during the COVID-19 confinements have a similar behaviour for black carbon and CCN. Therefore, the $N_{CCN\,0.3}$ to M_{BC} ratio should not diverge significantly either. The lower

$N_{CCN\ 0.3}$ per M_{BC} can likely be explained by the widespread of biomass burning smoke in Europe during the measurements in the summer of 2017. The wildfires contributed to a local background of regional haze in the lower troposphere, affecting some measurements taken in 2017. Nevertheless, there is a good agreement between the results for Rome and the Po Valley with the observations of relatively fresh wildfire smoke mixed with urban haze from the Marseille metropolitan area (Fig. 5.7A). These results illustrate the relevance of biomass burning smoke for the atmospheric BC burden as well as the hygroscopic and radiative properties of pollution plumes from some of Europe's largest metropolitan areas.

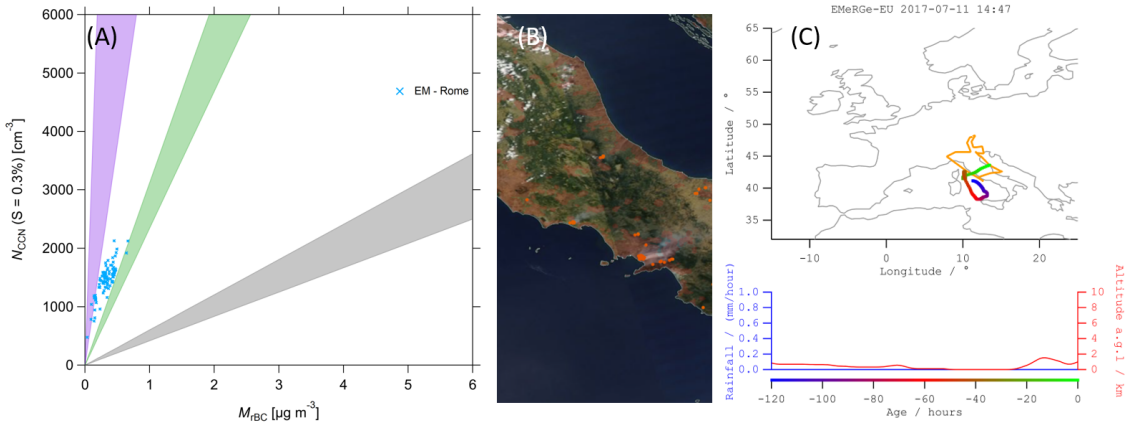

Figure 5.16: (A) Relationship between $N_{CCN\ 0.3}$ and M_{BC} for mixed urban and BB emissions in southern Europe, measured over the Adriatic Sea downwind of Rome. The data are from two measurement flights (11 and 20 July 2017). The BB plumes are emitted from fires in Italy, where savannahs and mixed forests are the dominant combustion fuels. **(B)** MODIS "Corrected Reflectance (True Color)" image for 11.07.2017, the day of measurement flight. Red dots indicate "Fires and Thermal Anomalies (Day and Night)". The grey shading emerging from fire dots is the image of smoke plumes. The red shading indicates "Human Built-up And Settlement Extent" showing the high density of urban settlements at BB origin. **(C)** HYSPLIT BT, the color code indicates time passed prior to measurement, suggesting a plume age of around one day.

The observed $N_{CCN\ 0.3}$ to M_{BC} ratio for the urban plumes of London probed during two measurement flights on 17 and 26 July 2017 (Fig. 5.17A) reveals lower $N_{CCN\ 0.3}$ per M_{BC} compared to the reference case of urban haze. Unlike the reference case with 2020 data, we measured the emissions from London mostly above the marine PBL. Thus, processes in the PBL and the transition into the free troposphere may strongly alter the $N_{CCN\ 0.3}$ to M_{BC} ratio for urban pollution. The good agreement between the two independent measurements of the pollution layers from the London area (Fig. 5.17A) just above the PBL suggests some cloud processing as a potential sink for CCN. The data points are between the reference cases of urban haze and lightly aged biomass burning smoke, however, there is no indication for biomass burning emissions in the recent air-mass history (120 h before measurements). Also, the BT analysis clearly suggests the metropolitan area of London as the source region. Therefore, the overlay with lightly aged biomass burning smoke might be a coincidence due to removal of hygroscopic aerosol at the interface between PBL and free troposphere. Also notable is the good agreement between the slopes of the London plume for $N_{CCN} < 1000\,\mathrm{cm}^{-3}$ and the pollution measured close to Nagoya (5.15).

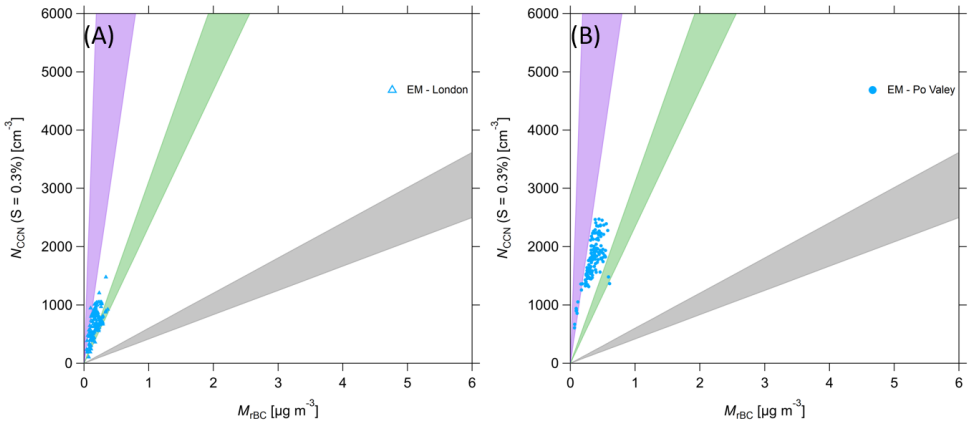

Figure 5.17: (A) Relationship between $N_{\mathrm{CCN\,0.3}}$ and M_{BC} for urban emissions from London. The data are from two measurement flights (17 and 26 July 2017). **(B)** Relationship between $N_{\mathrm{CCN\,0.3}}$ and M_{BC} for mixed urban and BB emissions in Southern Europe, measured over the Po Valley and the Adriatic Sea. The data are from two measurement flights (11 and 20 July 2017).

For the outflow of China's largest cities, Shanghai and Beijing, measured over the East China Sea during EMeRGe Asia, we find a lower $N_{\mathrm{CCN\,0.3}}$ to M_{BC} ratio than for urban haze measured in Europe and Japan. We measured the Chinese outflow over the East China Sea during three consecutive measurement flights (22, 24 and 26 March 2018). Backward trajectory analysis suggests that the urban haze originated mostly from Shanghai, with some contribution of more aged pollution from Beijing (Figs. 5.18C and 5.19). Besides urban pollution, aged smoke from cropland fires may also have contributed to the measured pollution layers (Fig. 5.18B). These fires inflamed 5 days prior to the first measurement flight and lasted over all three flights. While the transportation time of the urban pollution was one to three days prior to the measurements, the smoke aged around five days (Figs. 5.18C and 5.19). The MODIS satellite image reveals a probable mixing of the two pollution types (Fig. 5.18B). The constant aerosol conditions for this mix of urban haze and biomass burning smoke from China over a time period of five days are remarkable and may find application in approaches to understand aged air pollution in the proximity of global aerosol hot spots (e.g., Ramanathan and Carmichael, 2008).

Ground based measurements within the PBL in the mega-city of Delhi compare well to the BC to CCN ratios in biomass burning smoke (Fig. 5.20). The presented data are from measurements during the domestic heating season in Delhi. Commonly, dry solid biomass fuels are burnt for heating in Delhi, enhancing the PBL with biomass burning smoke (Mondal et al., 2021). A significant enhancement in M_{BC} in the evening and nighttime during heating season is reported by e.g., Bhandari et al., 2020; Reyes-Villegas et al., 2021; S. Raj et al., 2021a. Thus, the Delhi data presented in figure 5.20 are likely dominated by pollution from solid biofuel combustion for domestic heating. However, also traffic and other anthropogenic emissions may interfere with the domestic heating emissions. The lower concentrations during daytime are also associated with increasing PBL height and, thus, a dilution of the air pollution. While the daytime data and a few of the nighttime data fall well in between the conditions for relatively fresh and highly aged biomass burning, the nighttime data are dominated by a low $N_{\mathrm{CCN\,0.3}}$ to M_{BC} ratio in the range of highly aged biomass burning smoke.

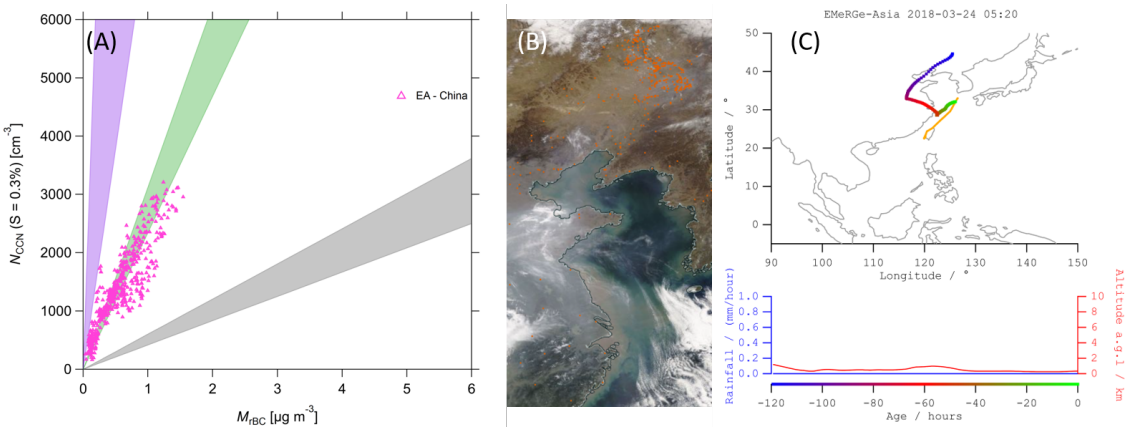

Figure 5.18: **(A)** Relationship between $N_{CCN\ 0.3}$ and M_{BC} for Chinese emissions, measured over the East China Sea downwind of Shanghai and Beijing. The data are from three measurement flights (22, 24 and 26 March 2018). **(B)** MODIS "Corrected Reflectance (True Color)" image for 22 March 2018. Red dots indicate "Fires and Thermal Anomalies (Day and Night)". Croplands are the dominant combustion fuel for these fires. The grey shading shows the urban and BB smoke mixing over the East China Sea. **(C)** HYSPLIT BT for the measurements of the mixed plume. The color code indicates time passed prior to measurement, suggesting a plume age of around two days for the urban pollution and five days for the BB emissions.

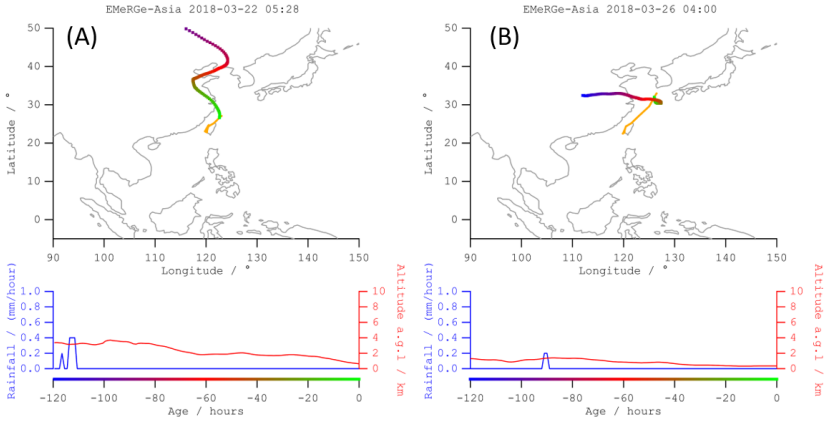

Figure 5.19: HYSPLIT BT for measurements of Chinese plumes. The color code indicates time passed prior to measurement. **(A)** shows the measurements conducted 22 March 2018, with an approximate plume age of around one day for Shanghai, two days for Beijing and four days for agricultural BB. **(B)** shows the measurements from 26 March 2018, with three to four days residence time for the plume from Shanghai.

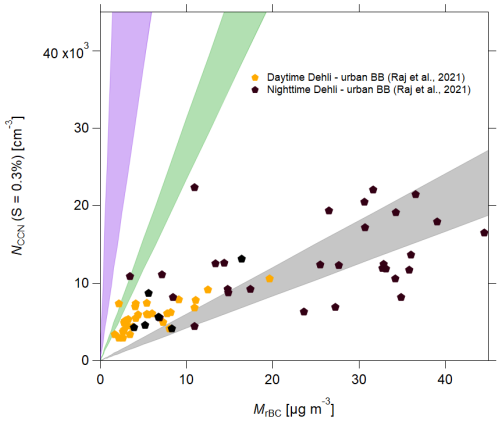

Figure 5.20: (A) Relationship between $N_{\mathrm{CCN\,0.3}}$ and M_{BC} for urban haze, measured from February to March 2018 in Delhi. Orange markers indicate daytime measurements and black markers indicate nighttime measurements. Details on the data separation and the measurements in S. Raj et al., 2021a.

5.4 Parametrisation of $N_{\mathrm{CCN\,0.3}}$ and M_{BC} in various polluted environments

Based on the typical ratios and the case studies, we found characteristic relationships between CCN and BC for the most relevant combustion sources in the Anthropocene. We found typical regimes for urban haze within the planetary boundary layer in high emission-standards countries, lightly aged smoke from open biomass burning from evergreen broadleaf forest vegetation, savannahs and grassland as well as highly aged long-range transported smoke from Africa. In addition to that, we show the effect on the $N_{\mathrm{CCN\,0.3}}$ per M_{BC} when pollution from different sources mixes. The results from the HALO data are confirmed with independent long-term measurements at the ATTO site for lightly and highly aged smoke from open biomass burning.

The radiative impact of biomass burning smoke and urban haze is discussed in several studies (e.g., Ramanathan and Carmichael, 2008; Szopa et al., 2021). The direct effects on cloud physics are primarily a function of N_{CCN}, altering cloud droplet number (e.g., Twomey, 1974; Twomey, 1977) and cloud albedo. However, semi-direct effects where the BC-rich smoke can either accelerate the evaporation of the clouds (so-called "cloud burning") or impede cloud formation by introducing atmospheric heating aloft can alter aerosol-cloud interactions and residence times of the smoke but also other aerosol. The semi-direct effect of absorbing aerosol on clouds is a major source of uncertainty in model predictions of past and future precipitation change (Samset, 2022). A more detailed analysis of the impact of the CCN to BC ratios found in this study on cloud physics, removal processes and thus on the atmospheric residence time is desirable.

In urban pollution within the PBL, N_{CCN} dominates the aerosol burden in respect to M_{BC} and N_{BC}. We found consistent ratios between CCN and BC for Europe in 2017 and 2020 as well as for Japan in 2018. The most significant difference for urban haze from high emission-standard countries is observed between measurements taken within the PBL and above. Based on this observation, we assume the mixing

from the PBL to the free troposphere to be a major force on the composition of urban haze. Apart from some transformation of the plume itself, mixing with biomass burning smoke reduces the N_{CCN} to M_{BC} ratio by introducing high amounts of BC and relatively little N_{CCN}. Consequently, mixing of air-masses and cloud processing at the interface of PBL and free troposphere are the main drivers in diverging the $N_{CCN\ 0.3}$ to M_{BC} ratio for urban haze.

Lightly aged smoke from evergreen broadleaf forest vegetation, savannahs and grasslands have higher M_{BC} compared to urban pollution. Our study shows consistent observations for the Amazon rain forest taken in 2014, Southern Europe from 2017 and Southeast Asia from 2018. Regionally, lightly aged smoke plays a crucial role in pollution levels and for public health. This smoke type also tends to superpose with other aerosol, especially urban haze, within the PBL and the lower troposphere. In our analysis, we can distinguish typical N_{CCN} to M_{BC} regimes for plumes with atmospheric residence times of up to four days. Nevertheless, we do not find evidence or clear indications of removal processes of these smoke layers. In fact, we reveal consistent data for two plumes in Southeast Asia showing no impact of cloudiness and precipitation. Thus, the atmospheric residence time of this lightly aged biomass burning smoke may exceed previous assumptions (Lund et al., 2018). However, further analysis considering the thermodynamic conditions and the meteorological situation during the smoke emissions and transport is needed to understand the importance of removal processes and the smoke layers' residence time.

Highly aged smoke from Africa has the lowest ratio between N_{CCN} and M_{BC} in this study. The relatively larger BC fraction in these plumes favors the rather unperturbed transport of the smoke layers over long distances. Clouds and precipitation can also initiate at low N_{CCN}. However, the typical injection height of African smoke plumes is in the lower free troposphere and is thus less affected by cloud processing and wet removal of aerosol. Also, the absorbing properties of the BC particles can lead to an atmospheric heating and, thereby, to a thermal inversion of the smoke layer, causing self-lofting into dry and non-convection regions of the free troposphere. Also, the large-scale subsidence in the descending arm of the Hadley cell can suppress wet removal. These characteristics make the BC-rich layers rather inert and enable transport over large distances with high atmospheric residence times.

CHAPTER 6

Volcanic aerosol in the tropical tropopause layer

This chapter is based on a manuscript draft for submission in the peer reviewed journal: Atmospheric Chemistry and Physics

This manuscript draft includes data sets from the following field experiment:
CAFE Africa.

Contribution to this manuscript draft by Ovid O. Krüger: I had the original idea for this study, performed the research, analysed the results, prepared the figures, and wrote the manuscript draft. I was responsible for the measurements and analysis of the CAFE Africa CCNC data set. I analysed the satellite data sets. I initiated and performed the analysis and linked the in situ aerosol measurements to the volcanic eruptions occurring in the Pacific Ocean. The aerosol chemical composition data was provided by J. Schneider, K. Kaiser and C. Schulz. J. Schneider provided figure 6.8. The O_3 data was provided by A. Zahn. D. Walter provided the HYSPLIT backward trajectories as defined by the research question. M. Salzmann and J. Quaas provided the ECHAM-HAM data, I performed the analysis and visualization of the data. I initialized the libradTran modeling of the atmospheric heating of the aerosol layer which was performed by K. Klingmüller and A. Pozzer. K. Klingmüller provided the figures. The ERA5 analysis and figure 6.5 were provided by D. Akriditis.

As pointed out in 3.2, the CCN budget in the upper troposphere is only slightly driven by anthropogenic pollution and biomass burning smoke. Especially over remote tropical regions like the tropical Atlantic, the CCN budget tends to be controlled by the oxidation of carbonyl and dimethyl sulfide (e.g., Andreae et al., 1988; Andreae and Raemdonck, 1983; Kremser et al., 2016) and local nucleation events (e.g., Brock et al., 1995; Williamson et al., 2019). These are rather continuous sources of CCN, however, there are also discontinuous but highly relevant sources of CCN. The most prominent of these are aerosol layers formed after SO_2 injections from volcanic eruptions. During the CAFE Africa campaign, a strong enhancement of CCN from volcanic origin was measured in the tropical tropopause layer over the tropical Atlantic.

6.1 In situ measurements of volcanic aerosol

During the CAFE Africa campaign on 17 August 2018 (measurement flight CA07), we encountered significantly elevated aerosol concentrations in the tropical tropopause layer (TTL). Based on in situ measurements, satellite and model data, we can infer a volcanic origin. Here we report on the physio-chemical properties of the volcanic aerosol plume. We employed measurements of aerosol hygroscopic properties from a dual column cloud condensation nuclei counter (CCN-200), combined with the total aerosol number concentration from a condensation particle counter (CPC) and the aerosol size distribution in the range between 180 and $400\,\mathrm{nm}$ measured with a single particle soot photometer (SP2) to provide information about the aerosol size distribution of the volcanic plume. We also report the bulk aerosol chemical composition retrieved with an aerosol mass spectrometer (C-ToF AMS). Further, we show the aerosol enhancements within the volcanic plume based on a model-observation comparison for in situ measured cloud condensation nuclei number concentration at a water vapor suppuration around 0.3 % ($N_{\mathrm{CCN\,0.3}}$) with the ten-year ECHAM-HAM monthly average for August and September over the tropical Atlantic region defined in figure 4.1.

In June and July 2018, some moderate volcanic eruptions occurred within the tropics, injecting SO_2, directly into the lower stratosphere and TTL. These include the Ambae eruption (15° S 165° E) at the end of July 2018 (e.g., Kloss et al., 2020; Malinina et al., 2021) and the Sierra Negra eruption (1° S 92° W) on the Galapagos Islands (e.g., Bell et al., 2021). Apart from these two stratospheric eruptions, the Kilauea eruption in Hawaii (19° N 155° W) peaked at the end of its active phase during this period. The Kilauea volcano, however, did not directly penetrate the upper troposphere (e.g., Crawford et al., 2021; Vernier et al., 2020). Bourassa et al., 2012 showed the impact of the Asian summer monsoon on the lofting of volcanic plumes from the free troposphere into the TTL and lower stratosphere. Therefore, all these three moderate volcanic eruptions can be considered as a potential source of the volcanic aerosol layer.

The aerosol plume was probed at a pressure around $147\,\mathrm{hPa}$ and at an altitude of approximately $14.4\,\mathrm{km}$ (Figs. 6.3 and 6.4). The average potential temperature (θ) increased from 357.9 ($\sigma = 0.39$) to 360 ($\sigma = 1.91$) K, well correlated with the increased aerosol concentration, whereas the altitude and flight direction remained

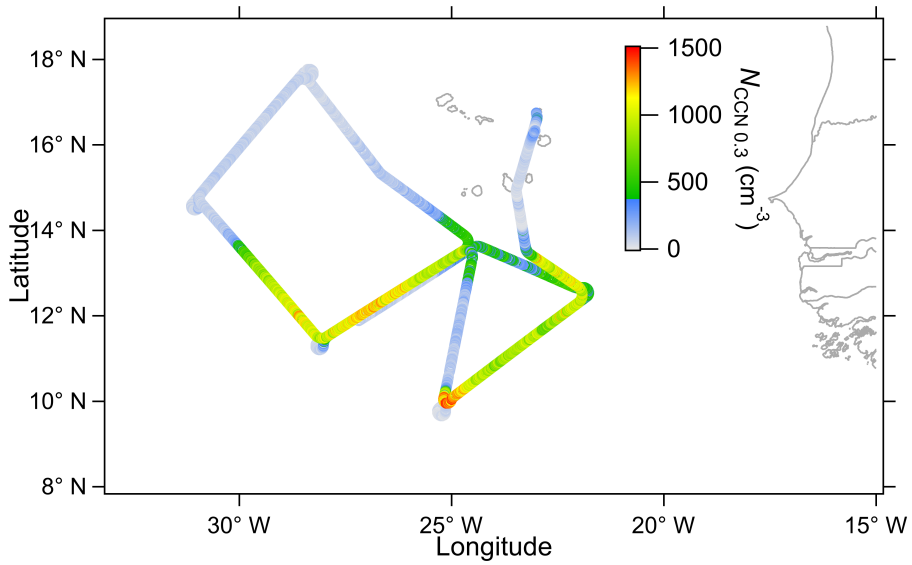

Figure 6.1: Flight track of the CAFE Africa flight at 17 August 2018 (CA07). The color code represents $N_{\mathrm{CCN,\,0.3}}$ in a range from 0 to $1500\,\mathrm{cm}^{-3}$. Note that the bird-view illustration can not provide information about the altitude and some flight passages are overlapped, where only the highest flight level is shown.

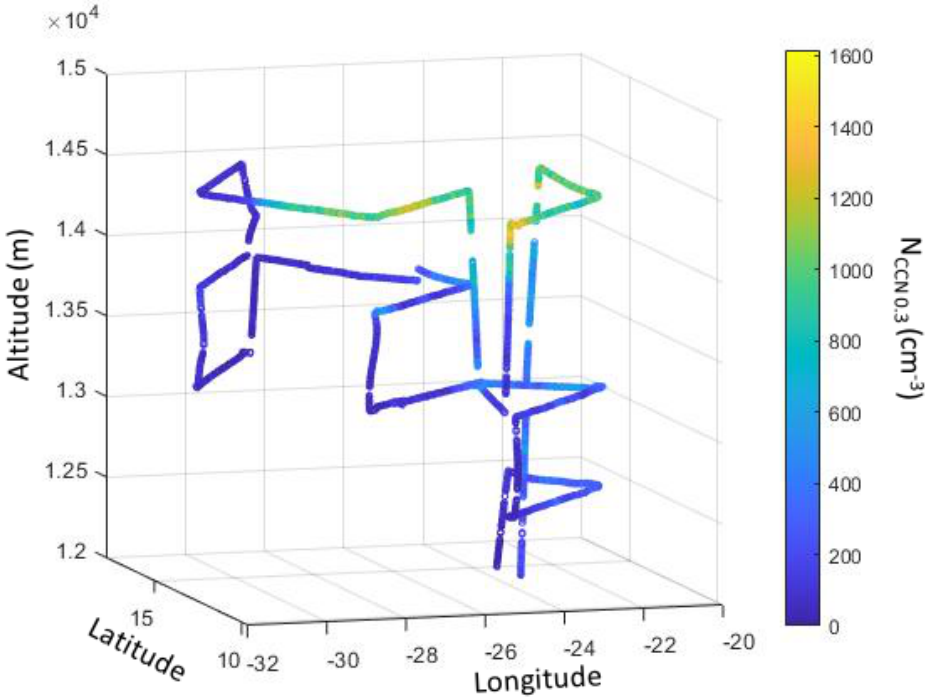

Figure 6.2: Flight track of CA07 in three dimensional space. The color code represents $N_{\mathrm{CCN,\,0.3}}$ in a range from 0 to $1600\,\mathrm{cm}^{-1}$.

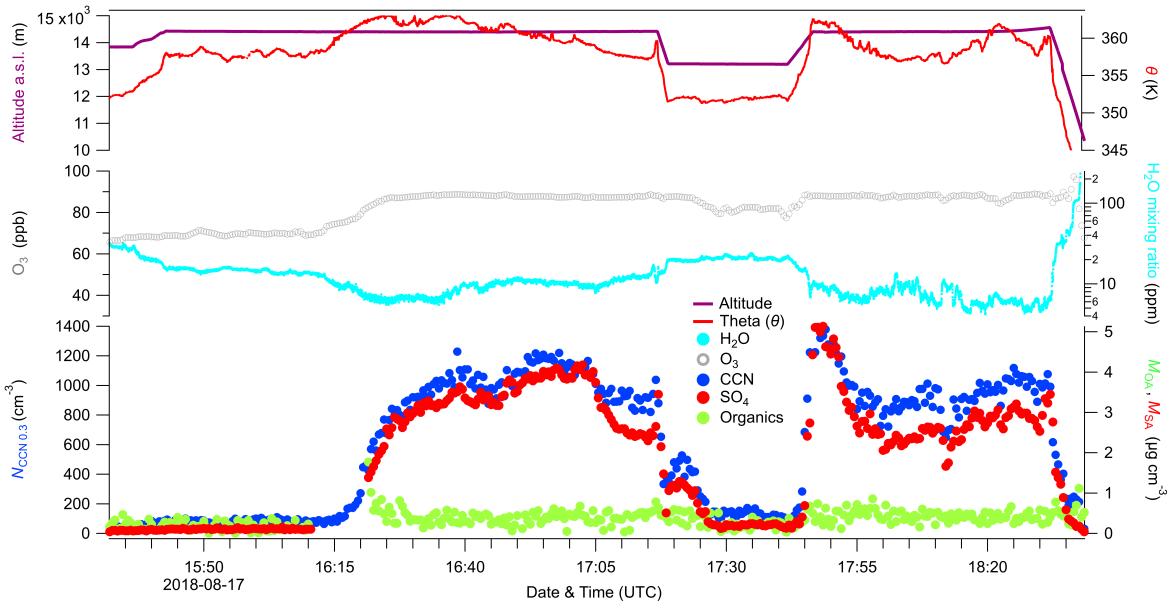

Figure 6.3: Measurement data for CA07. First panel left, HALO flight altitude above sea level. Right, 30 seconds averages of absolute humidity, note the logarithmic scale. Second panel left, 30 seconds averages of ozone as stratospheric tracer. Right, 30 seconds averages of water vapor mixing ratio as tropospheric tracer. Third panel left, 30 seconds averages of $N_{\mathrm{CCN,\,0.3}}$. Right, organics and sulfate mass concentration with a temporal resolution of 60 seconds.

unchanged (Figs. 6.2 and 6.3). The state variables fall into the definition of the TTL by Fueglistaler et al., 2009.

The relative humidity within the plume was low, compared to observations outside the plume (Fig. 6.3). This is in good agreement with Jensen et al., 2018, where a volcanic ash layer was observed in the lower tropical stratosphere. However, there is also a high chance that the low humidity and increased θ indicate an air-mass origin from higher altitudes. Also, the ERA5 reanalysis for specific humidity data suggest a larger region of relative low water vapor at $150\,\mathrm{hPa}$ (Fig. 6.5).

The vertical distribution of $N_{\mathrm{CCN\,0.3}}$ from the ten-year monthly average ECHAM-HAM model data agrees well with the in situ observations (Figs. 4.1 and 6.4 a). The modeled and observed $N_{\mathrm{CCN\,0.3}}$ deviate in lower altitudes, probably due to influences of biomass burning pollution transported from Africa westwards across the Atlantic (Holanda et al., 2023). For higher altitudes, however, the good agreement for the vertical distribution of $N_{\mathrm{CCN\,0.3}}$ allows us to use the ECHAM-HAM data to investigate the assumed vertical profile of $N_{\mathrm{CCN\,0.3}}$ in the lower stratosphere. This comparison illustrates that there is no source in the lower stratosphere which is strong enough to explain the increased aerosol concentration in the TTL. Thus, downward transport of stratospheric air as the origin of the aerosol plume is unlikely.

Besides the high $N_{\mathrm{CCN\,0.3}}$, we also find remarkably high sulfate aerosol mass (M_{SA}) and a moderate enhancement in organic aerosol mass (M_{OA}) compared to the TTL background aerosol (Fig. 6.3 and 6.6). The ratio between M_{SA} and M_{OA} can serve as a tracer for volcanic aerosol (e.g., Saturno et al., 2018; Schmale et al., 2010). We find ratios ranging from 2 to 16 exceeding the values reported in Schmale et al., 2010 for a roughly 80 days aged volcanic plume in the UTLS over Europe. As

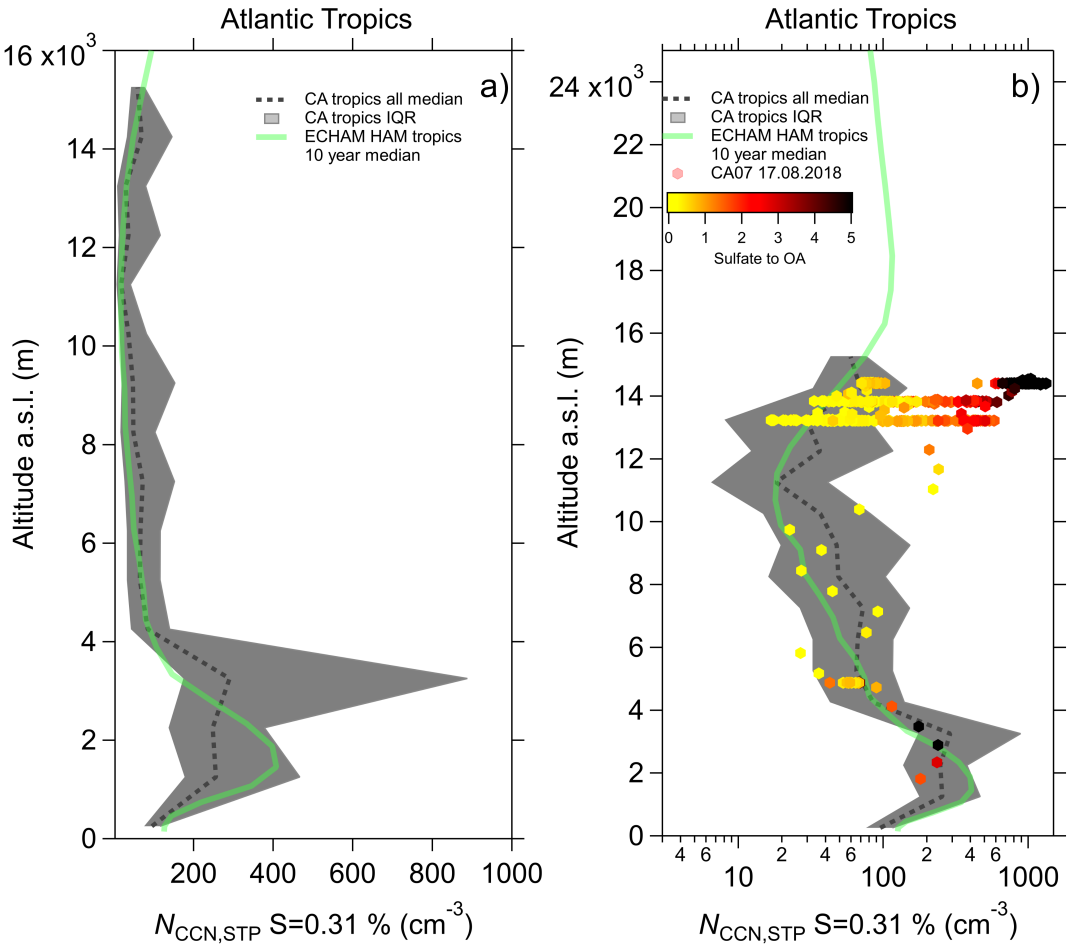

Figure 6.4: (A) Vertical distribution of $N_{\mathrm{CCN}\ 0.3}$ over the tropical Atlantic Ocean region as indicated in figure 4.1. The grey dashed line represents the median with the grey shading as the interquartile range of all measurement flights of the CAFE Africa campaign conducted within the comparison region. The solid green line represents the median of ten-years monthly averaged ECHAM-HAM data (2003 until 2012). (B) As (A) but in logarithmic scale for $N_{\mathrm{CCN}\ 0.3}$ and with model data up to $24\,\mathrm{km}$. The color coded markers on top of the other data are $N_{\mathrm{CCN}\ 0.3}$ for measurement flight CA07 (17.08.2018). The color code shows the M_{SA} to M_{OA} ratio as marker for volcanic origins in a range between 0 and 5, please note that maximum ratios reach up to 16.

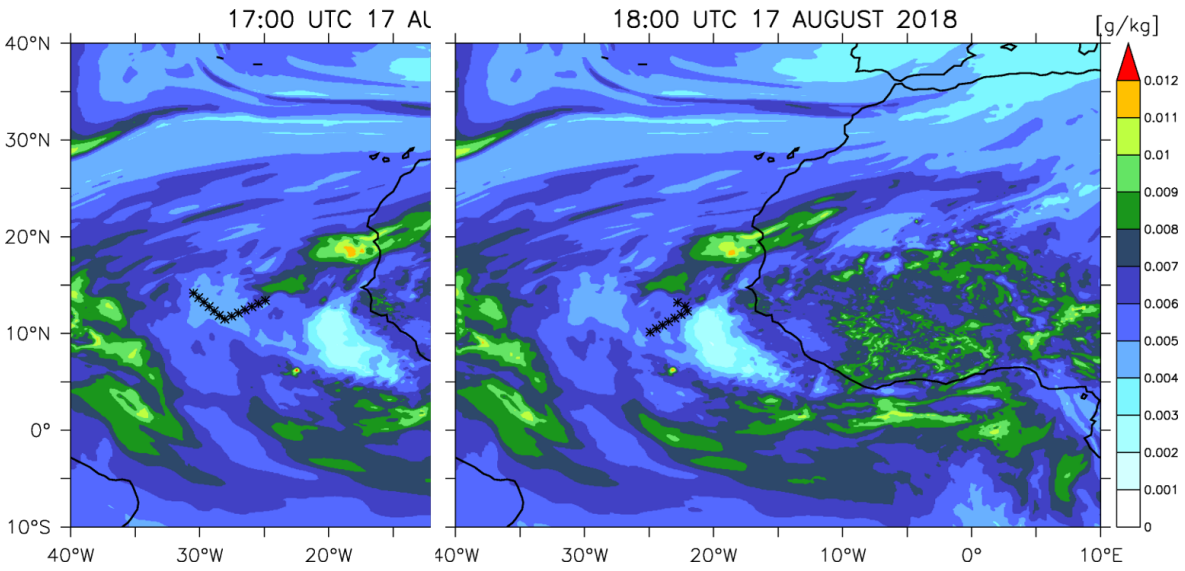

Figure 6.5: HALO flight track (black markers, 17:00 UTC is also referred to as t2, 18:00 UTC as t3 in further analysis) when the volcanic aerosol plume was measured overlaid with ERA5 water vapor at $150\,\mathrm{hPa}$.

shown in Murphy et al., 2021, background M_{OA} is generally lower in the Southern Hemisphere, where the measured plume likely originated (Fig. 6.7). Apart from the M_{SA} to M_{OA} ratio, the neutralization of sulfuric acid by ammonia can also be used to trace back volcanic aerosols. The very low amount of ammonia within the observed aerosol plume in the TTL (Fig. 6.8) reinforces the hypothesis of a volcanic origin of the aerosol plume.

Based on the combined BT analysis with satellite retrieved SO_2, we identified the Ambae ($15°$ S $165°$ E) and the Sierra Negra ($1°$ S $92°$ W) eruptions as the most likely origin of the aerosol plume (Fig. 6.7). The BT density plots in figure 6.7 consist of tree times 100 independent BT emitted from three locations on the flight path; those indicating a westerly origin are from locations inside the aerosol plume, whereas the measurements outside the plume at constant altitude and direction show an easterly origin. The potential eruption dates combined with the BT results suggest a plume aging time of around 20 days. This aging time within the relatively OH^- rich TTL (Lelieveld et al., 2016) is sufficient to convert gas phase SO_2 into particulate sulfate (e.g., Kremser et al., 2016).

The measured vertical extent of the plume reaches down to roughly $13\,\mathrm{km}$ (Fig. 6.2). This lower bound for the plume's vertical extent agrees with CALIPSO observations from 11 August 2018 (Fig. 6.9). Yet, it has to be kept in mind that the measurements generally show a horizontal cross section and do not cover the entire vertical extent of the volcanic plume. Also, we can not provide measurements for the plume-top, however, based on the CALPISO data from 11 August 2018, we assume the top of the plume to penetrate the lower stratosphere up to an altitude of $17\,\mathrm{km}$ (Fig. 6.9). Since the maxima in concentrations were measured at the highest altitudes of observation, the layer likely extends further into the TTL and potentially the lower stratosphere.

*Data downloaded from https://geoservice.dlr.de/web/maps/s5p:tropomi:l3. Last access 14.02.2023.

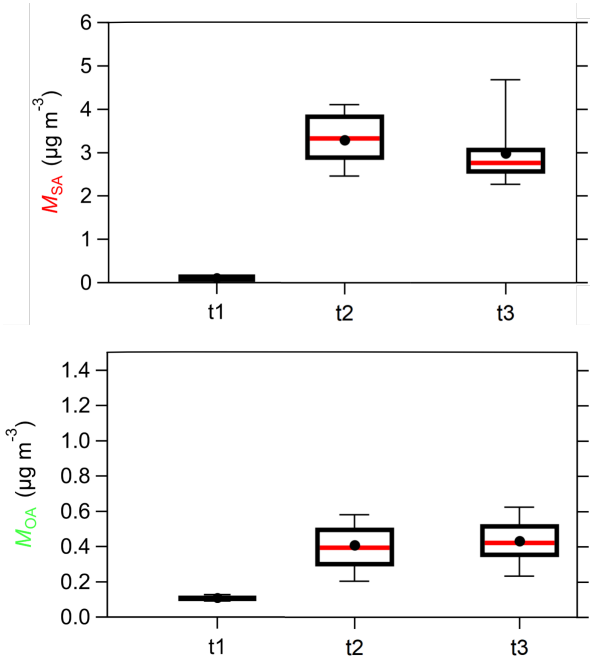

Figure 6.6: Sulfate aerosol (M_{SA}) and organic aerosol (M_{OA}) mass concentrations within (t2 and t3) and outside (t1) the volcanic aerosol layer. The data are derived from the C-ToF AMS measurements with a temporal resolution of $60\,\mathrm{s}$.

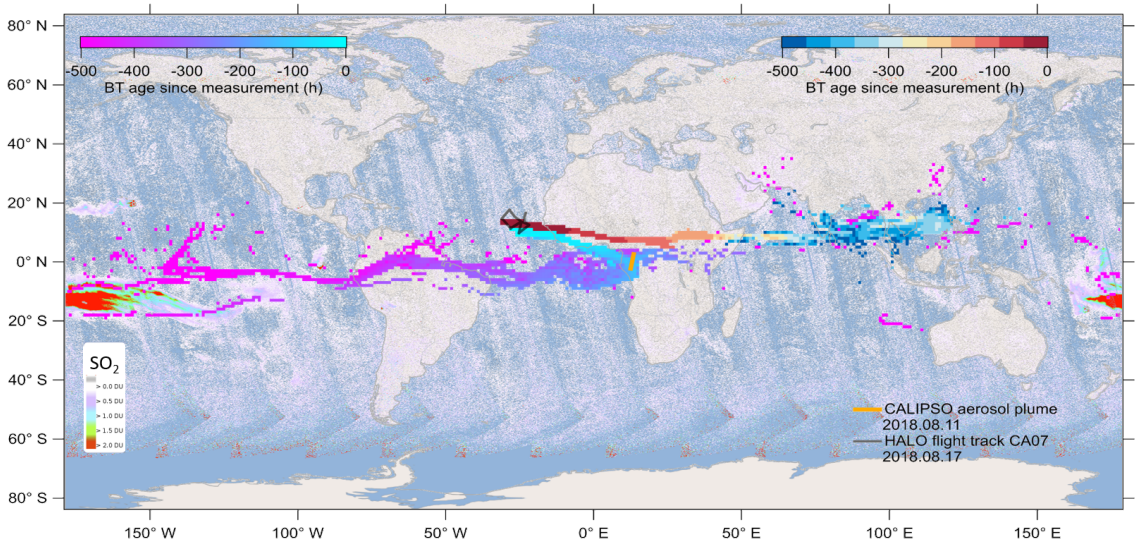

Figure 6.7: Flight track of the CAFE Africa flight at 17 August 2018 (CA07) in grey. The color code in the world map represents satellite retrieved SO_2 from 30 July 2018 measured by Sentinel 5 *. The pink to blue color and blue to red code present the air mass age for a $1°$ times $1°$ density distribution for BT emitted at three locations of the flight track with a runtime of 500 h back in time (details 2.8.4). The yellow line indicates the rough location of the volcanic aerosol plume detected by CALIPSO on 11 August 2018.

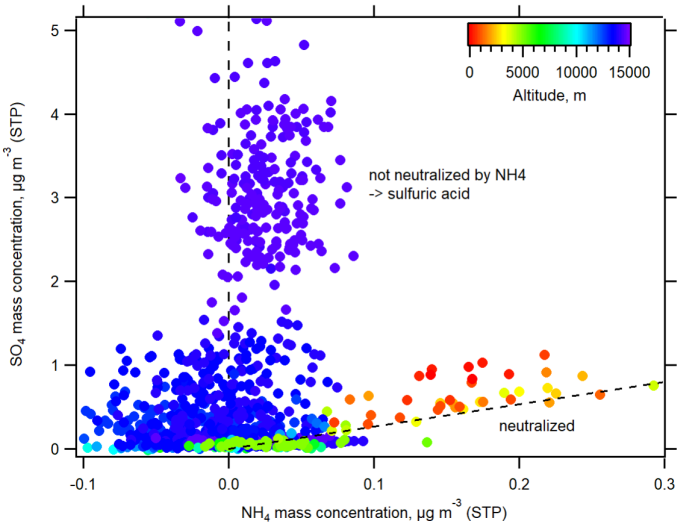

Figure 6.8: Scatter plot of M_{SA} and M_{NH4} measured with a $60\,s$ time resolution with the C-ToF AMS. NH_4 data points are color coded with flight altitude. Vertical dashed line shows the zero NH_4 concentration, angular dashed line shows the neutralized M_{SA} by M_{NH4}. Data points far above this line are not neutralized, which indicates that the M_{SA} is sulfuric acid.

This larger vertical extent is also supported by the CALIPSO overpass (Fig. 6.9) coincidence with the aerosol plumes' air-mass history (Fig. 6.7).

The aerosol enrichment due to the volcanic plume in the TTL is most dominant for aerosol in the size range between 50 and $180\,nm$ (Fig. 6.10). The median $N_{CCN\,0.3}$ in the TTL is 83 ($\sigma = 29$) cm^{-3} (Figs. 6.3, 6.4 a and 6.10). Within the volcanic plume, measured $N_{CCN\,0.3}$ is 935 ($\sigma = 243$) cm^{-3}. For larger aerosol in the range between 180 to $400\,nm$, we observe a comparable pattern. The concentration increases from 12 ($\sigma = 6$) to 93 ($\sigma = 36$) cm^{-3}. For N_{CN}, we can observe a contrary behaviour. Within the volcanic aerosol plume, N_{CN} is lower than outside the plume. In the lowest measured size range between 18 and $50\,nm$, the size bin width normalized concentration within the volcanic plume decreased nearly by half.

Volcanic emissions do not only scatter incoming solar radiation, but also absorb it. In the first days after eruptions, this absorption is dominated by the SO_2 absorption of short wavelengths in the solar spectrum. SO_2 absorbs most strongly at wavelengths between 180 and $235\,nm$, less strongly between 260 to $340\,nm$ and least strongly between 340 and $390\,nm$ (Bekki and Pyle, 1992). For heating rates in the Earth's atmosphere, however, only absorption in wavelengths above $310\,nm$ is of interest since the ultra violet (UV) radiation with smaller wavelengths is already absorbed by O_3 and does not get through the upper atmosphere (e.g., Lary et al., 1994). As shown for a model of the Mount Pinatubo plume from the 1991 eruption (Bluth et al., 1992; Read et al., 1993), the absorption and thus heating of the volcanic plume is only of relevance for the first 10 days after eruption due to dispersion of the plume and transformation of SO_2 into sulfate aerosol with different radiative properties (Lary et al., 1994).

But also the sulfate aerosol absorbs radiation in the long-wave (LW) spectra, causing an atmospheric heating around the volcanic layer (e.g., Robock, 2000). The in situ measurements also reveal an increase in θ and static temperature. To test whether these changes can be explained by the absorption of UV radiation by the remaining

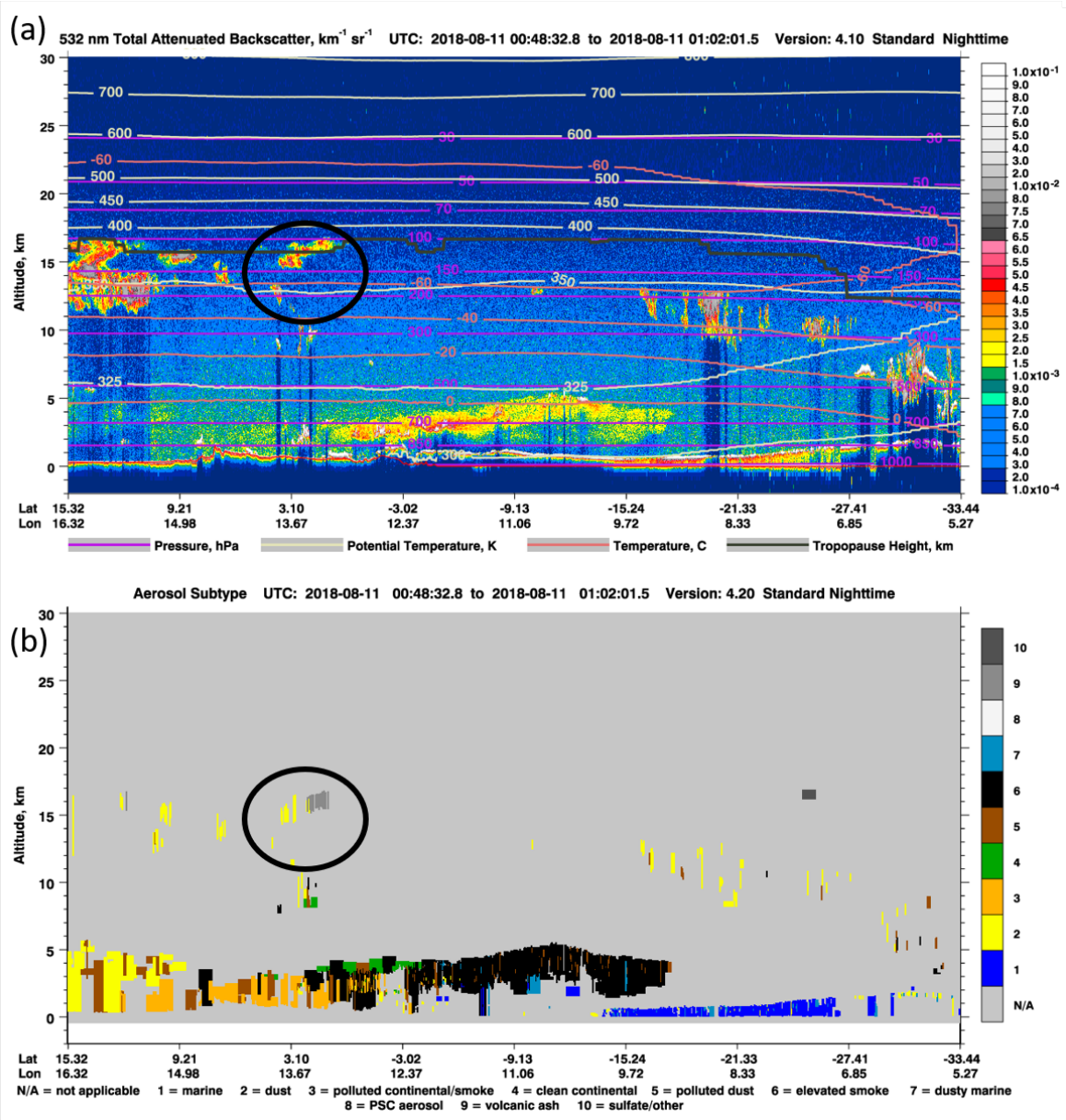

Figure 6.9: Images of the volcanic aerosol layer detected by CALIPSO August 11, 2018 over Africa. (a) shows the 532 nm total attenuated backscatter. The aerosol layer is lactated within the TTL and tip crosses the tropopause (shown as black line), the potential temperature (grey line) is between 350 and 400 K. The Aerosol classification from CALIPSO marks layer partly as dust and volcanic ash aerosol types (b).

SO_2 and LW radiation by the sulfate aerosol, the heating rate is calculated with a radiative transfer model (libRadtran, Emde et al., 2016; Mayer and Kylling, 2005) combined with the MOPSMAP tool (Gasteiger and Wiegner, 2018) to calculate the vertical optical properties of the in situ measured aerosol data (see methods section 2.8.5). We used different vertical extents for the calculations since our in situ measurements do not provide an upper boundary of the plume. However, the heating rates due to the aerosol and SO_2 layer can not solely explain the increased temperatures measured within the volcanic plume.

In the radiative transfer calculations, ash aerosol did not find attention, however, some fraction of the coarse mode aerosol is expected to be volcanic ash. A significant

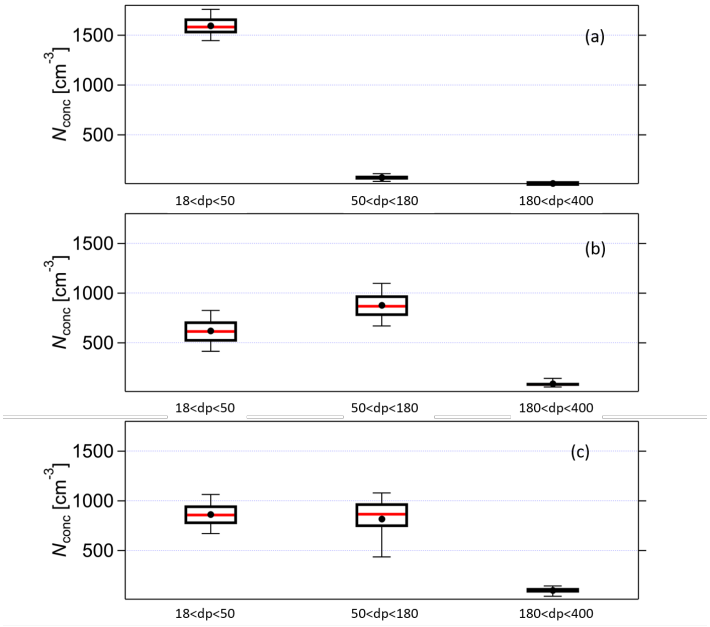

Figure 6.10: Aerosol number concentrations within (b = t2 and C = t3) and out (a = t1) of the volcanic aerosol layer. Aerosol number concentrations for $18 < dp < 50\,\mathrm{nm}$ is the difference between CPC measurements with $N_{\mathrm{CCN,\,0.3}}$ and N_{SC}, $50 < dp < 180\,\mathrm{nm}$ is the difference between $N_{\mathrm{CCN,\,0.3}}$ and N_{SC}.

influence of ash aerosol on the heating rates of volcanic plumes is expected for the first few days after eruption (Niemeier et al., 2009).

The calculation for the atmospheric heating due to the volcanic aerosol layer only leads to heating rates of around $0.12\,\mathrm{K\,d^{-1}}$ (Fig. 6.11), which is more than an order of magnitude below the observed increase in θ. Combined with the results regarding the elevated O_3 and low H_2O, downward transport of air-masses from higher altitudes is the more likely explanation for the temperature increase during the observations of the volcanic aerosol layer.

6.1.1 Discussion and implications of measurements

The peak in the aerosol size range below $180\,\mathrm{nm}$ agrees well with the data reported for the Ambae volcano plume roughly one year after the eruption (Kloss et al., 2020, and published data set) and is considerably smaller than previously reported aerosol size distributions for volcanic aerosol plumes in the UTLS region (Schmale et al., 2010; Wilson et al., 1993). Schmale et al., 2010 discuss lower SO_2 emissions from weaker volcanic eruptions as a potential reason for smaller aerosol sizes. Also, the premeasurement aging time in Schmale et al., 2010 and Wilson et al., 1993 is 80 days, which is longer than the 20 days in our study, but the comparable sizes measured about a year after the eruption do not support a different aging time as an explanation, especially since the e-folding time for the SO_2 to aerosol conversion is in the range of weeks (Kremser et al., 2016).

The decrease in smaller particles along with more particles in the size range between 50 and $180\,\mathrm{nm}$ can have different reasons. Large amounts of free tropospheric and boundary layer air-masses are injected into the TTL, thus the lower fraction of the smaller particles may be due to the displacement of actual TTL air-masses. Also, con-

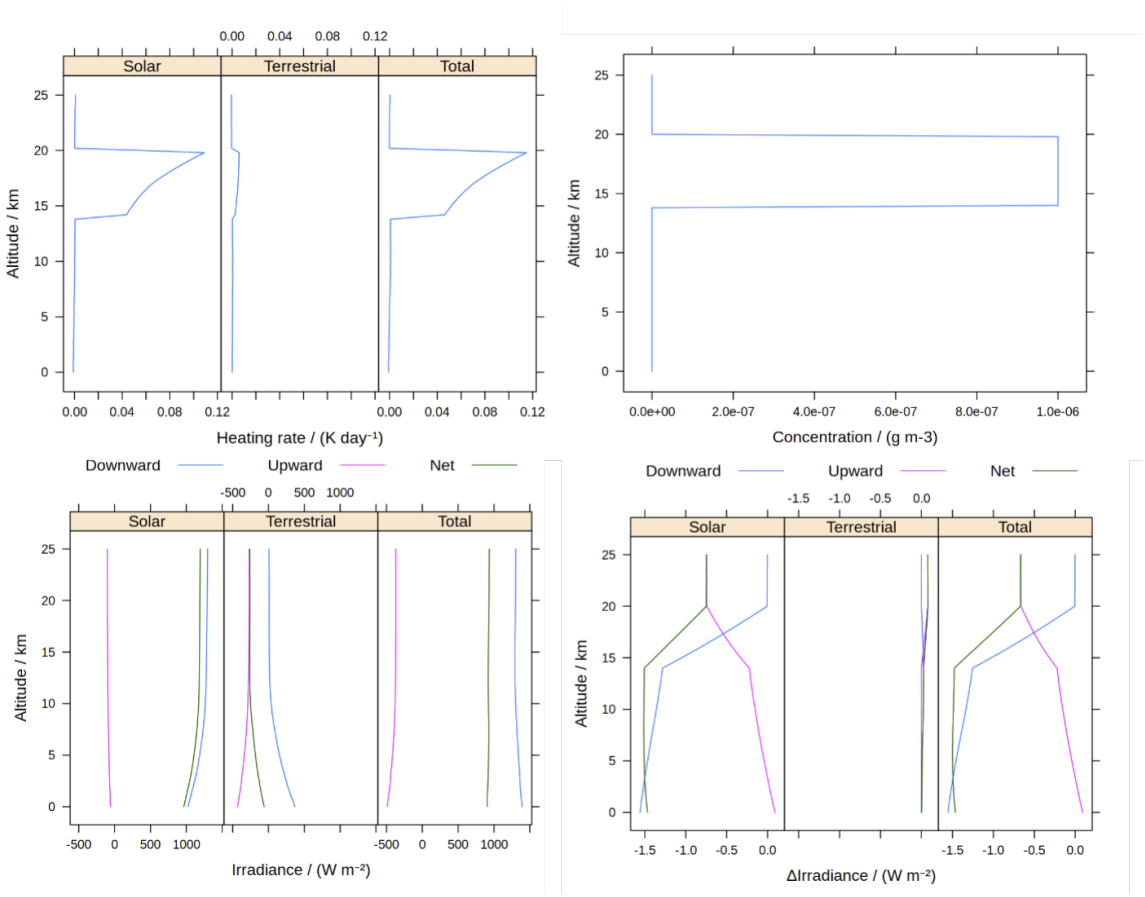

Figure 6.11: Impact of the volcanic aerosol layer on the atmospheric heating rate with assumed aerosol layer thickness of $5.5\,\mathrm{km}$, based on the CALIPSO data. The aerosol type assumed for the calculation is water soluble sulfate aerosol and the calculations are performed for the daily peak solar zenith angle of $12°$ N $25°$ W at 13:44:11. Further details on the calculations in section 2.8.5.

densation growth due to gaseous H_2SO_4 on the smaller particles into larger sizes is a possible explanation. Besides condensation, coagulation is also an important process in aerosol aging. There is the chance that, due to the rather high concentrations in the volcanic plume, there is also some coagulation growth.

The vertical extent agrees with the previous reported analysis of infrared brightness temperature in Kloss et al., 2020. While Kloss et al., 2020 chose the upper intercept with the ERA5 temperature profile for their analysis as the injection height (18 to $19\,\mathrm{km}$), our data suggest the lower intercept with the ERA5 data at $14.5\,\mathrm{km}$ as the potential plume injection height.

Kloss et al., 2020 and Malinina et al., 2021 show a global effect of the Ambae volcanic eruption on radiative forcing. In both studies, the plume is emitted directly into the lower stratosphere. However, we find most of the plume in the TTL about 20 days after the eruption and only small fractions in the lower stratosphere (Fig. 6.9). Due to the long-lasting effect of the eruptions on radiative forcing, it is to expect that the plume passed the tropopause and entered the lower stratosphere. This transport should be of interest since volcanic eruptions not penetrating the stratosphere tend to be neglected in climate models due to a short residence time of the sulfate aerosol (e.g., Aubry et al., 2021). These aerosols should receive more attention, not only to adequately address global stratospheric radiative forcing, but also to address and evaluate their impact on aerosol size distribution and chemistry in interplay with potential man-made sulfate injections in the context of geo-engineering. Laakso et al., 2016 pointed out that for large volcanic eruptions, that penetrate the stratosphere, the climate response is not additional during an geo-engineering scenario, but rather the residence time of the volcanic and man-made aerosol is reduced due to larger and fewer aerosol. The change in aerosol number size distribution also leads to a lower surface cooling (e.g., Laakso et al., 2016; Rasch et al., 2008).

Aubry et al., 2021 estimates the impact of changing climate on the life-cycle of volcanic aerosol and its interaction with radiation. In a warmer climate, moderate-magnitude volcanic eruptions tend not to reach directly into the stratosphere anymore. Thus, the SO_2 from these eruptions is often not considered in models. However, we find a volcanic plume within the TTL, a region with only little humidity, which makes wet deposition of aerosol only slightly relevant. As the TTL is a mixing region of tropospheric and stratospheric air masses, where air parcels with different compositions and lifetimes are dispersed, upward transport into the lower stratosphere is also a possible pathway. Thus, the aerosol enhancements may remain in the TTL for a longer period or can be transported across the TTL into the lower stratosphere. In Kloss et al., 2020, stratospheric aerosol optical density (SAOD) increases later than the maximum radiative forcing occurred shown in Malinina et al., 2021. Thus, some direct transport of sulfate from TTL may have occurred later.

The in situ measurements of a volcanic aerosol layer in the TTL presented here may provide a value input for validating and improving remote sensing retrievals and climate models. Physio-chemical properties of volcanic aerosol in the TTL can also help the geo-engineering community, with better understand the fate and development of large sulfate injections into this region. For estimates of the radiative impact of medium magnitude volcanic eruptions the reported aerosol properties are important input parameter. Within the around three-week aged aerosol plume from either the Ambae or Sierra Negra eruptions, measured sulfates were strongly en-

hanced, but also the organic aerosol mass concentration doubled compared to the TTL background. For the smallest size range measured, between 18 and $50\,\mathrm{nm}$, the concentration within the volcanic plume was reduced by almost half, for the range between 50 and $180\,\mathrm{nm}$ concentrations were increased by a factor of about 12, and particles between 180 and $400\,\mathrm{nm}$ were about 8 times higher than in TTL background conditions.

CHAPTER 7

Conclusions and Outlook

This dissertation can provide some insights into relevant questions concerning the spatio-temporal variability of CCN and BC. Based on HALO in situ measurements of $N_{\text{CCN 0.3}}$, M_{BC} and N_{BC}, constraints for these aerosol parameters are provided. The main findings of this dissertation are summarized in the following.

The in situ measurements of M_{BC} during the first COVID-19 lockdown in Europe revealed a confinement-related M_{BC} reduction between 32 and 38 % compared to 2017. The total difference between the 2020 and 2017 measurements is 48 %, of which a fraction of 7 % is due to differences in atmospheric parameters as well as flight patterns and BC emissions from biomass burning. Another 3 to 9 % of the reduction can be attributed to a general long-term trend of BC reductions in Europe. The reduced BC mass is in good agreement with the results of modelling studies using proxy data from Apple and Google on user mobility behaviour, but also with statistical data from the European Union on fuel demand over the two periods. The results highlight the immediate positive effect that changed human behavior has on the atmospheric pollution and thereby on climate and public heath.

In addition to the unprecedented changes in atmospheric M_{BC} and N_{BC}, the CCN burden also shows a comparable change during the confinements in Europe. The lower tropospheric $N_{\text{CCN 0.3}}$ load is highly sensitive to local anthropogenic pollution. The result illustrates the ability of BC from anthropogenic combustion processes to serve as a conserved tracer of the anthropogenic CCN budget. Based on the spatial analysis of CCN and BC data in other global regions, i.e. for urban haze in East and Southeast Asia and biomass burning smoke layers over the tropical Atlantic, a high sensitivity of the CCN load to the level of anthropogenic and biomass burning pollution is demonstrated within the lower troposphere. In the middle and upper troposphere, above about $5\,\text{km}$, the in situ measured $N_{\text{CCN 0.3}}$ shows little variability and is in good agreement with long-term model data.

The close relationship between the CCN and BC burden is used for a correlation analysis between $N_{\text{CCN 0.3}}$ and M_{BC} of HALO measurements in different polluted environments. Typical relationships between $N_{\text{CCN 0.3}}$ and M_{BC} are identified and summarized in Table 7.1.

Table 7.1: The fit parameters of the characteristic relationships between$N_{\text{CCN 0.3}}$ and M_{BC} (± standard deviation (SD), R^2 and the number of observations (N) as shown in the respective CCN to BC scatter plots).

	urban haze	lightly aged BB	highly aged BB
ΔCCN/ΔBC ± SD [$\cdot 10^9\ \mu\text{g}^{-1}$]	20 ± 12	2.7 ± 0.4	0.5 ± 0.1
R^2	0.90	0.99	0.97
N	62	70	305

For the emissions of $N_{\text{CCN 0.3}}$ and M_{BC} from biomass burning, we find higher fractions of BC for dryer fuels such as savannah, grassland, agricultural residues and coniferous forests, whereas larger amounts of hygroscopic aerosol are found for tropical evergreen forests. Smoke emitted from fires in Africa did not undergo significant processing during transport across the Atlantic, and we found consistent BC and CCN properties for all measurements over the Atlantic and in northeastern Brazil.

The close and approximately linear relationship between $N_{\text{CCN 0.3}}$ and M_{BC} shows both sides of the effect that reducing emissions can have on the atmosphere. While

BC particles are highly light absorbing, the co-emitted scattering and hygroscopic aerosol tend to overcompensate for this atmospheric heating through direct and semi-direct radiative effects. However, particulate pollution also affects precipitation patterns, an increasingly important issue as both droughts and heavy rainfall events with flooding have increased dramatically in recent decades. A lower CCN load can lead to faster droplet growth and thus earlier onset of rain.

The CCN burden in the upper troposphere and lower stratosphere is relatively insensitive to local anthropogenic pollution in the presented data set. This is confirmed by the good agreement between the HALO measurements and model results of ten-year monthly averages from regions comparable to the measurement area. However, for the lower stratosphere and the upper troposphere there are also some discrepancies between model results and in situ measurements. A significant increase in aerosol mass and number is found due to a volcanic aerosol plume in the tropical tropopause layer from an eruption about 20 days before the measurements. The in situ measurements of this plume provide insights into the physical properties of the aerosol with high number concentrations of the accumulation mode aerosol. The chemical aerosol properties show, apart from the dominance of sulfate aerosol, an increase of organic aerosol by a factor of 2 compared to reference measurements outside the plume. For the smallest size range measured between 18 and $50\,\mathrm{nm}$, the concentration inside the volcanic plume decreased by almost half, for the range between 50 and $180\,\mathrm{nm}$ the plume shows the largest increase, by a factor of about 12, and the larger particles between 180 and $400\,\mathrm{nm}$ were about 8 times higher than in TTL background conditions. These observations demonstrate the role of moderate volcanic eruptions in the aerosol load and should serve as input to climate models to study the transport and fate of moderate volcanic eruptions with eruption columns that do not penetrate the stratosphere.

The in situ measurements presented in this thesis can also be of considerable value in validating and improving remote sensing retrievals. This is shown in the comparison of EMeRGe EU measurements of biomass burning smoke near Marseilles with satellite retrievals for aerosol optical thickness (Fig. 5.7) and in the analysis of the volcanic aerosol plume in the tropical tropopause layer supported by CALIPSO space-borne LIDAR measurements (Fig. 6.9). By collocating HALO in situ measurements in a representative grid with ground-based and space-borne remote sensing profiles of the atmosphere, the retrievals, which provide valuable long-term data on the vertical variability of aerosol and clouds, can be validated and potentially improved, but also the HALO data can be seen in a broader context of atmospheric variability.

In the scope of this dissertation I focused on urban pollution, biomass burning smoke and volcanic aerosol in the upper troposphere. However, mineral dust is another particulate constituent of the atmosphere which still lacks in situ measurements within the transported and suspended atmospheric layers. The potential participation of mineral dust aerosol in atmospheric chemistry and cloud formation as well as external mixing with biomass burning smoke and anthropogenic pollution also deserves further investigations. Therefore, the presented data set combined with impaction samples on silicon nitrate substrates for offline analysis collected during the HALO aircraft campaigns can find application.

As illustrated in chapter 4, the vertical distribution of $N_{\mathrm{CCN\,0.3}}$ in models can be improved, especially in highly polluted regions like East and Southeast Asia. Therefore,

nudged model simulations with reanalysis meteorological data for $N_{\mathrm{CCN\ 0.3}}$ and other atmospheric constituents along the actual HALO flight tracks are desirable. This analysis can provide great value in the validation and improvement of sources for different CCN and the evaluation of the actual hygroscopicity of anthropogenic pollution. These results may help to constrain aerosol-cloud interactions in global models and thus, for future climate projections.

Bibliography

Ackerman, A. S.; Toon, O. B.; Taylor, J. P.; Johnson, D. W.; Hobbs, P. V., and Ferek, R. J.: "Effects of aerosols on cloud albedo: evaluation of twomey's parameterization of cloud susceptibility using measurements of ship tracks". *Journal of the Atmospheric Sciences*, 57, 16. (2000), pp. 2684 –2695. DOI: 10.1175/1520-0469(2000)057<2684:EOAOCA>2.0.CO;2.

Ahern, A. T.; Robinson, E. S.; Tkacik, D. S.; Saleh, R.; Hatch, L. E.; Barsanti, K. C.; Stockwell, C. E.; Yokelson, R. J.; Presto, A. A.; Robinson, A. L.; Sullivan, R. C., and Donahue, N. M.: "Production of secondary organic aerosol during aging of biomass burning smoke from fresh fuels and its relationship to voc precursors". *Journal of Geophysical Research: Atmospheres*, 124, 6. (2019), pp. 3583–3606. DOI: https://doi.org/10.1029/2018JD029068.

Albrecht, B. A.: "Aerosols, cloud microphysics, and fractional cloudiness". *Science*, 245, 4923. (1989), pp. 1227–1230. DOI: 10.1126/science.245.4923.1227.

Allen, R. J.; Amiri-Farahani, A.; Lamarque, J. F.; Smith, C.; Shindell, D.; Hassan, T., and Chung, C. E.: "Observationally constrained aerosol–cloud semi-direct effects". *npj Climate and Atmospheric Science*, 2, 1. (2019), pp. 1–12. DOI: 10.1038/s41612-019-0073-9.

Anderson, G. P.; Clough, S. A.; Kneizys, F. X.; Chetwynd, J. H., and Shettle, E. P.: "Afgl (air force geophysical laboratory) atmospheric constituent profiles (0. 120km). environmental research papers". (May 1986). URL: https://www.osti.gov/biblio/6862535.

Andreae, M. O.: "Correlation between cloud condensation nuclei concentration and aerosol optical thickness in remote and polluted regions". *Atmospheric Chemistry and Physics*, 9, 2. (2009), pp. 543–556. DOI: 10.5194/acp-9-543-2009.

Andreae, M. O.: "Emission of trace gases and aerosols from biomass burning – an updated assessment". *Atmospheric Chemistry and Physics*, 19, 13. (2019), pp. 8523–8546. DOI: 10.5194/acp-19-8523-2019.

Andreae, M. O.; Afchine, A.; Albrecht, R.; Holanda, B. A.; Artaxo, P.; Barbosa, H. M. J.; Borrmann, S.; Cecchini, M. A.; Costa, A.; Dollner, M.; Fütterer, D.; Järvinen, E.; Jurkat, T.; Klimach, T.; Konemann, T.; Knote, C.; Krämer, M.; Krisna, T.; Machado, L. A. T.; Mertes, S.; Minikin, A.; Pöhlker, C.; Pöhlker, M. L.; Pöschl, U.; Rosenfeld, D.; Sauer, D.; Schlager, H.; Schnaiter, M.; Schneider, J.; Schulz, C.; Spanu, A.; Sperling, V. B.; Voigt, C.; Walser, A.; Wang, J.; Weinzierl, B.; Wendisch, M., and Ziereis, H.: "Aerosol characteristics and particle production in the upper troposphere over the amazon basin". *Atmospheric Chemistry and Physics*, 18, 2. (2018), pp. 921–961. DOI: 10.5194/acp-18-921-2018.

Andreae, M. O.; Browell, E. V.; Garstang, M.; Gregory, G. L.; Harriss, R. C.; Hill, G. F.; Jacob, D. J.; Pereira, M. C.; Sachse, G. W.; Setzer, A. W.; Dias, P. L. S.; Talbot, R. W.; Torres, A. L., and Wofsy, S. C.: "Biomass-burning emissions and associated haze layers over Amazonia". *Journal of Geophysical Research*, 93, D2. (1988), p. 1509. DOI: 10.1029/JD093iD02p01509.

Andreae, M. O. and Gelencsér, A.: "Black carbon or brown carbon? The nature of light-absorbing carbonaceous aerosols". *Atmospheric Chemistry and Physics*, 6, 10. (2006), pp. 3131–3148. DOI: 10.5194/acp-6-3131-2006.

Andreae, M. O. and Ramanathan, V.: "Climate's Dark Forcings". *Science*, 340, 6130. (2013), pp. 280–281. DOI: 10.1126/science.1235731.

Andreae, M. O.; Rosenfeld, D.; Artaxo, P.; Costa, A. A.; Frank, G. P.; Longo, K. M., and Silva-Dias, M. A. F.: "Smoking rain clouds over the amazon". *Science*, 303, 5662. (2004), pp. 1337–1342. DOI: 10.1126/science.1092779.

Andreae, M. O.: "Aerosols before pollution". *Science*, 315, 5808. (2007), pp. 50–51. DOI: 10.1126/science.1136529.

Andreae, M. O. and Crutzen, P. J.: "Atmospheric aerosols: biogeochemical sources and role in atmospheric chemistry". *Science*, 276, 5315. (1997), pp. 1052–1058. DOI: 10.1126/science.276.5315.1052.

Andreae, M. O. and Raemdonck, H.: "Dimethyl sulfide in the surface ocean and the marine atmosphere: a global view". *Science*, 221, 4612. (1983), pp. 744–747. DOI: 10.1126/science.221.4612.744.

Andreae, M. and Rosenfeld, D.: "Aerosol–cloud–precipitation interactions. Part 1. The nature and sources of cloud-active aerosols". *Earth-Science Reviews*, 89, 1-2. (2008), pp. 13–41. DOI: 10.1016/j.earscirev.2008.03.001.

Archibald, A.; Witham, C.; Ashfold, M.; Manning, A.; O'Doherty, S.; Greally, B.; Young, D., and Shallcross, D.: "Long-term high frequency measurements of ethane, benzene and methyl chloride at Ragged Point, Barbados: Identification of long-range transport events". *Elementa: Science of the Anthropocene*, 3. (2015). 000068. DOI: 10.12952/journal.elementa.000068.

Aubry, T. J.; Staunton-Sykes, J.; Marshall, L. R.; Haywood, J.; Abraham, N. L., and Schmidt, A.: "Climate change modulates the stratospheric volcanic sulfate aerosol lifecycle and radiative forcing from tropical eruptions". *Nature Communications*, 12, 1. (2021). DOI: 10.1038/s41467-021-24943-7.

Bagheri, G.; Thiede, B.; Hejazi, B.; Schlenczek, O., and Bodenschatz, E.: "An upper bound on one-to-one exposure to infectious human respiratory particles". *Proceedings of the National Academy of Sciences*, 118, 49. (2021), e2110117118. DOI: 10.1073/pnas.2110117118.

Ban-Weiss, G. A.; Lunden, M. M.; Kirchstetter, T. W., and Harley, R. A.: "Measurement of black carbon and particle number emission factors from individual heavy-duty trucks". *Environmental Science and Technology*, 43, 5. (2009), pp. 1419–1424. DOI: 10.1021/es8021039.

Ban-Weiss, G. A.; McLaughlin, J. P.; Harley, R. A.; Lunden, M. M.; Kirchstetter, T. W.; Kean, A. J.; Strawa, A. W.; Stevenson, E. D., and Kendall, G. R.: "Long-term changes in emissions of nitrogen oxides and particulate matter from on-road gasoline and diesel vehicles". *Atmospheric Environment*, 42, 2. (2008), pp. 220–232. DOI: 10.1016/j.atmosenv.2007.09.049.

Beer, C. G.; Hendricks, J.; Righi, M.; Heinold, B.; Tegen, I.; Groß, S.; Sauer, D.; Walser, A., and Weinzierl, B.: "Modelling mineral dust emissions and atmospheric dispersion with MADE3 in EMAC v2.54". *Geosci. Model Dev.*, 13, 9. (2020), pp. 4287–4303. DOI: 10.5194/gmd-13-4287-2020.

Bekki, S. and Pyle, J. A.: "Two-dimensional assessment of the impact of aircraft sulphur emissions on the stratospheric sulphate aerosol layer". *Journal of Geophysical Research: Atmospheres*, 97, D14. (1992), pp. 15839–15847. DOI: https://doi.org/10.1029/92JD00770.

Bell, A. F.; La Femina, P. C.; Ruiz, M.; Amelung, F.; Bagnardi, M.; Bean, C. J.; Bernard, B.; Ebinger, C.; Gleeson, M.; Grannell, J.; Hernandez, S.; Higgins, M.; Liorzou, C.; Lundgren, P.; Meier, N. J.; Möllhoff, M.; Oliva, S. J.; Ruiz, A. G., and Stock, M. J.: "Caldera resurgence during the 2018 eruption of Sierra Negra volcano, Galápagos Islands". *Nature Communications*, 12, 1. (2021), pp. 1–9. DOI: 10.1038/s41467-021-21596-4.

Bellouin, N.; Quaas, J.; Gryspeerdt, E.; Kinne, S.; Stier, P.; Watson-Parris, D.; Boucher, O.; Carslaw, K. S.; Christensen, M.; Daniau, A. L.; Dufresne, J. L.; Feingold, G.; Fiedler, S.; Forster, P.; Gettelman, A.; Haywood, J. M.; Lohmann, U.; Malavelle, F.; Mauritsen, T.; McCoy, D. T.; Myhre, G.; Mülmenstädt, J.; Neubauer, D.; Possner, A.; Rugenstein, M.; Sato, Y.; Schulz, M.; Schwartz, S. E.; Sourdeval, O.; Storelvmo, T.; Toll, V.; Winker, D., and Stevens, B.: "Bounding Global Aerosol Radiative Forcing of Climate Change". *Reviews of Geophysics*, 58, 1. (2020), pp. 1–45. DOI: 10.1029/2019RG000660.

Bhandari, S.; Gani, S.; Patel, K.; Wang, D. S.; Soni, P.; Arub, Z.; Habib, G.; Apte, J. S., and Hildebrandt Ruiz, L.: "Sources and atmospheric dynamics of organic aerosol in new delhi, india: insights from receptor modeling". *Atmospheric Chemistry and Physics*, 20, 2. (2020), pp. 735–752. DOI: 10.5194/acp-20-735-2020.

Birmili, W. and Hoffmann, T.: "Environmental pollutants | particulate and dust pollution, inorganic and organic compounds". In: *Encyclopedia of Respiratory Medicine*. Ed. by G. J. Laurent and S. D. Shapiro. Oxford: Academic Press, 2006, pp. 110–120. ISBN: 978-0-12-370879-3. DOI: https://doi.org/10.1016/B0-12-370879-6/00133-2.

Bluth, G. J. S.; Doiron, S. D.; Schnetzler, C. C.; Krueger, A. J., and Walter, L. S.: "Global tracking of the so2 clouds from the june, 1991 mount pinatubo eruptions". *Geophysical Research Letters*, 19, 2. (1992), pp. 151–154. DOI: https://doi.org/10.1029/91GL02792.

Bohren, C. F. and Huffman, D. R.: "Frontmatter". In: *Absorption and Scattering of Light by Small Particles*. John Wiley & Sons, Ltd, 1998. ISBN: 9783527618156. DOI: https://doi.org/10.1002/9783527618156.fmatter.

Bond, T. C.; Doherty, S. J.; Fahey, D. W.; Forster, P. M.; Berntsen, T.; Deangelo, B. J.; Flanner, M. G.; Ghan, S.; Kärcher, B.; Koch, D.; Kinne, S.; Kondo, Y.; Quinn, P. K.; Sarofim, M. C.; Schultz, M. G.; Schulz, M.; Venkataraman, C.; Zhang, H.; Zhang, S.; Bellouin, N.; Guttikunda, S. K.; Hopke, P. K.; Jacobson, M. Z.; Kaiser, J. W.; Klimont, Z.; Lohmann, U.; Schwarz, J. P.; Shindell, D.; Storelvmo, T.; Warren, S. G., and Zender, C. S.: "Bounding the role of black carbon in the climate system: A scientific assessment". *Journal of Geophysical Research Atmospheres*, 118, 11. (2013), pp. 5380–5552. DOI: 10.1002/jgrd.50171.

Borrmann, S.; Kunkel, D.; Weigel, R.; Minikin, A.; Deshler, T.; Wilson, J. C.; Curtius, J.; Volk, C. M.; Homan, C. D.; Ulanovsky, A.; Ravegnani, F.; Viciani, S.; Shur, G. N.; Belyaev, G. V.; Law, K. S., and Cairo, F.: "Aerosols in the tropical and subtropical ut/ls: in-situ measurements of submicron particle abundance and volatility". *Atmospheric Chemistry and Physics*, 10, 12. (2010), pp. 5573–5592. DOI: 10.5194/acp-10-5573-2010.

Borrmann, S.; Solomon, S.; Dye, J. E.; Baumgardner, D.; Kelly, K. K., and Chan, K. R.: "Heterogeneous reactions on stratospheric background aerosols, volcanic sulfuric acid droplets, and type i polar stratospheric clouds: effects of temperature fluctuations and differences in particle phase". *Journal of Geophysical Research: Atmospheres*, 102, D3. (1997), pp. 3639–3648. DOI: https://doi.org/10.1029/96JD02976.

Boucher, O.; Randall, D.; Artaxo, P.; Bretherton, C.; Feingold, G.; Forster, P.; Kerminen, V.-M.; Kondo, Y.; Liao, H.; Lohmann, U.; Rasch, P.; Satheesh, S.; Sherwood, S.; Stevens, B., and Zhang, X.: "Clouds and aerosols". In: *Climate Change 2013: The Physical Science Basis. Contribution of Working Group I to the Fifth Assessment Report of the Intergovernmental Panel on Climate Change*. Ed. by T. Stocker; D. Qin; G.-K. Plattner; M. Tignor; S. Allen; J. Boschung; A. Nauels; Y. Xia; V. Bex, and P. Midgley. Cambridge, United Kingdom and New York, NY, USA: Cambridge University Press, 2013. Chap. 7, 571–658. ISBN: ISBN 978-1-107-66182-0. DOI: 10.1017/CBO9781107415324.016.

Bourassa, A. E.; Robock, A.; Randel, W. J.; Deshler, T.; Rieger, L. A.; Lloyd, N. D.; Llewellyn, E. J., and Degenstein, D. A.: "Large volcanic aerosol load in the stratosphere linked to Asian monsoon transport". *Science*, 336, 6090. (2012), pp. 78–81. DOI: 10.1126/science.1219371.

Bowman, D. M.; Balch, J. K.; Artaxo, P.; Bond, W. J.; Carlson, J. M.; Cochrane, M. A.; D'Antonio, C. M.; DeFries, R. S.; Doyle, J. C.; Harrison, S. P.; Johnston, F. H.; Keeley, J. E.; Krawchuk, M. A.; Kull, C. A.; Marston, J. B.; Moritz, M. A.; Prentice, I. C.; Roos, C. I.; Scott, A. C.; Swetnam, T. W.; Van Der Werf, G. R., and Pyne, S. J.: "Fire in the earth system". *Science*, 324, 5926. (2009), pp. 481–484. DOI: 10.1126/science.1163886.

Braga, R. C.; Rosenfeld, D.; Krüger, O. O.; Ervens, B.; Holanda, B. A.; Wendisch, M.; Krisna, T.; Pöschl, U.; Andreae, M. O.; Voigt, C., and Pöhlker, M. L.: "Linear relationship between effective radius and precipitation water content near the top of convective clouds: measurement results from acridicon–chuva campaign". *Atmospheric Chemistry and Physics*, 21, 18. (2021), pp. 14079–14088. DOI: 10.5194/acp-21-14079-2021.

Braga, R. C.; Rosenfeld, D.; Weigel, R.; Jurkat, T.; Andreae, M. O.; Wendisch, M.; Pöschl, U.; Voigt, C.; Mahnke, C.; Borrmann, S.; Albrecht, R. I.; Molleker, S.; Vila, D. A.; Machado, L. A. T., and Grulich, L.: "Further evidence for ccn aerosol concentrations determining the height of warm rain and ice initiation in convective clouds over the amazon basin". *Atmospheric Chemistry and Physics*, 17, 23. (2017), pp. 14433–14456. DOI: 10.5194/acp-17-14433-2017.

Brock, C. A.; Hamill, P.; Wilson, J. C.; Jonsson, H. H., and Chan, K. R.: "Particle formation in the upper tropical troposphere: a source of nuclei for the stratospheric aerosol". *Science*, 270, 5242. (1995), pp. 1650–1653. DOI: 10.1126/science.270.5242.1650.

Brühl, C.; Lelieveld, J.; Tost, H.; Höpfner, M., and Glatthor, N.: "Stratospheric sulfur and its implications for radiative forcing simulated by the chemistry climate model EMAC". *J Geophys Res Atmos*, 120, 5. (2015), pp. 2103–2118. DOI: 10.1002/2014JD022430.

Campos Braga, R.; Ervens, B.; Rosenfeld, D.; Andreae, M. O.; Förster, J.-D.; Fütterer, D.; Hernández Pardo, L.; Holanda, B. A.; Jurkat, T.; Krüger, O. O.; Lauer, O.; Machado, L. A. T.; Pöhlker, C.; Sauer, D.; Voigt, C.; Walser, A.; Wendisch, M.; Pöschl, U., and Pöhlker, M. L.: "Cloud droplet number closure for tropical convective clouds during the acridicon–chuva campaign". *Atmospheric Chemistry and Physics Discussions*, 2021. (2021), pp. 1–17. DOI: 10.5194/acp-2021-80.

Cappa, C. D.; Onasch, T. B.; Massoli, P.; Worsnop, D. R.; Bates, T. S.; Cross, E. S.; Davidovits, P.; Hakala, J.; Hayden, K. L.; Jobson, B. T.; Kolesar, K. R.; Lack, D. A.; Lerner, B. M.; Li, S.-M.; Mellon, D.; Nuaaman, I.; Olfert, J. S.; Petaja, T.; Quinn, P. K.; Song, C.; Subramanian, R.; Williams, E. J., and Zaveri, R. A.: "Radiative Absorption Enhancements Due to the Mixing State of Atmospheric Black Carbon". *Science*, 337, 6098. (2012), pp. 1078–1081. DOI: 10.1126/science.1223447.

Carlson, T. N. and Prospero, J. M.: "The large-scale movement of saharan air outbreaks over the northern equatorial atlantic". *Journal of Applied Meteorology and Climatology*, 11, 2. (1972), pp. 283 –297. DOI: 10.1175/1520-0450(1972)011<0283:TLSMOS>2.0.CO;2.

Carn, S.; Clarisse, L., and Prata, A.: "Multi-decadal satellite measurements of global volcanic degassing". *Journal of Volcanology and Geothermal Research*, 311. (2016), pp. 99–134. DOI: https://doi.org/10.1016/j.jvolgeores.2016.01.002.

Carslaw, K. S.; Gordon, H.; Hamilton, D. S.; Johnson, J. S.; Regayre, L. A.; Yoshioka, M., and Pringle, K. J.: "Aerosols in the pre-industrial atmosphere". *Current Climate Change Reports*, 3, 1. (2017), pp. 1–15. DOI: 10.1007/s40641-017-0061-2.

Chan, C. K. and Yao, X.: "Air pollution in mega cities in china". *Atmospheric Environment*, 42, 1. (2008), pp. 1–42. DOI: https://doi.org/10.1016/j.atmosenv.2007.09.003.

Cheng, Y.; Ma, N.; Witt, C.; Rapp, S.; Wild, P. S.; Andreae, M. O.; Pöschl, U., and Su, H.: "Face masks effectively limit the probability of sars-cov-2 transmission". *Science*, 372, 6549. (2021), pp. 1439–1443. DOI: 10.1126/science.abg6296.

Choudhury, G.; Ansmann, A., and Tesche, M.: "Evaluation of aerosol number concentrations from calipso with atom airborne in situ measurements". *Atmospheric Chemistry and Physics*, 22, 11. (2022), pp. 7143–7161. DOI: 10.5194/acp-22-7143-2022.

Choudhury, G. and Tesche, M.: “Assessment of caliop-derived ccn concentrations by in situ surface measurements”. *Remote Sensing*, 14, 14. (2022). DOI: 10.3390/rs14143342.

CIESIN: “Center for International Earth Science Information Network - CIESIN - Columbia University. 2018. Gridded Population of the World, Version 4 (GPWv4): Population Density, Revision 11. Palisades, NY: NASA Socioeconomic Data and Applications Center (SEDAC). Accessed 24 October 2021.” (2018). DOI: 10.7927/H49C6VHW.

Crawford, B.; Hagan, D. H.; Grossman, I.; Cole, E.; Holland, L.; Heald, C. L., and Kroll, J. H.: “Mapping pollution exposure and chemistry during an extreme air quality event (the 2018 kīlauea eruption) using a low-cost sensor network”. *Proceedings of the National Academy of Sciences*, 118, 27. (2021), e2025540118. DOI: 10.1073/pnas.2025540118.

Crutzen, P. J.: *The Anthropocene*. Ed. by E. E. and K. T. Berlin, Heidelberg: Earth System Science in the Anthropocene. Springer, 2006.

Després, V.; Huffman, J.; Burrows, S. M.; Hoose, C.; Safatov, A.; Buryak, G.; Fröhlich-Nowoisky, J.; Elbert, W.; Andreae, M.; Pöschl, U., and Jaenicke, R.: “Primary biological aerosol particles in the atmosphere: a review”. *Tellus B: Chemical and Physical Meteorology*, 64, 1. (2012), p. 15598. DOI: 10.3402/tellusb.v64i0.15598.

Dietmüller, S.; Jöckel, P.; Tost, H.; Kunze, M.; Gellhorn, C.; Brinkop, S.; Frömming, C.; Ponater, M.; Steil, B.; Lauer, A., and Hendricks, J.: “A new radiation infrastructure for the Modular Earth Submodel System (MESSy, based on version 2.51)”. *Geosci Model Dev*, 9, 6. (2016), pp. 2209–2222. DOI: 10.5194/gmd-9-2209-2016.

Ding, S.; Liu, D.; Zhao, D.; Hu, K.; Tian, P.; Zhou, W.; Huang, M.; Yang, Y.; Wang, F.; Sheng, J.; Liu, Q.; Kong, S.; Cui, P.; Huang, Y.; He, H.; Coe, H., and Ding, D.: “Size-Related Physical Properties of Black Carbon in the Lower Atmosphere over Beijing and Europe”. *Environmental Science and Technology*, 53, 19. (2019), pp. 11112–11121. DOI: 10.1021/acs.est.9b03722.

Ditas, J.; Ma, N.; Zhang, Y.; Assmann, D.; Neumaier, M.; Riede, H., and Karu, E.: “Strong impact of wildfires on the abundance and aging of black carbon in the lowermost stratosphere”. September 2011. (2018). DOI: 10.1073/pnas.1806868115.

Drewnick, F.; Hings, S. S.; DeCarlo, P.; Jayne, J. T.; Gonin, M.; Fuhrer, K.; Weimer, S.; Jimenez, J. L.; Demerjian, K. L.; Borrmann, S., and Worsnop, D. R.: “A New Time-of-Flight Aerosol Mass Spectrometer (TOF-AMS)—Instrument Description and First Field Deployment”. *Aerosol Science and Technology*, 39, 7. (2005), pp. 637–658. DOI: 10.1080/02786820500182040.

Dusek, U.; Frank, G. P.; Hildebrandt, L.; Curtius, J.; Schneider, J.; Walter, S.; Chand, D.; Drewnick, F.; Hings, S.; Jung, D.; Borrmann, S., and Andreae, M. O.: “Size matters more than chemistry for cloud-nucleating ability of aerosol particles”. *Science*, 312, 5778. (2006), pp. 1375–1378. DOI: 10.1126/science.1125261.

Emde, C.; Buras-Schnell, R.; Kylling, A.; Mayer, B.; Gasteiger, J.; Hamann, U.; Kylling, J.; Richter, B.; Pause, C.; Dowling, T., and Bugliaro, L.: “The libradtran software package for radiative transfer calculations (version 2.0.1)”. *Geoscientific Model Development*, 9, 5. (2016), pp. 1647–1672. DOI: 10.5194/gmd-9-1647-2016.

Evangeliou, N.; Platt, S. M.; Eckhardt, S.; Lund Myhre, C.; Laj, P.; Alados-Arboledas, L.; Backman, J.; Brem, B. T.; Fiebig, M.; Flentje, H.; Marinoni, A.; Pandolfi, M.; Yus-Dìez, J.; Prats, N.; Putaud, J. P.; Sellegri, K.; Sorribas, M.; Eleftheriadis, K.; Vratolis, S.; Wiedensohler, A., and Stohl, A.: "Changes in black carbon emissions over Europe due to COVID-19 lockdowns". *Atmospheric Chemistry and Physics*, 21, 4. (2021), pp. 2675–2692. DOI: 10.5194/acp-21-2675-2021.

Feingold, G.: "On smoke suppression of clouds in Amazonia". *Geophysical Research Letters*, 32, 2. (2005), p. L02804. DOI: 10.1029/2004GL021369.

Flanner, M. G.: "Arctic climate sensitivity to local black carbon". *Journal of Geophysical Research: Atmospheres*, 118, 4. (2013), pp. 1840–1851. DOI: https://doi.org/10.1002/jgrd.50176.

Förster, E.; Bönisch, H.; Neumaier, M.; Obersteiner, F.; Zahn, A.; Hilboll, A.; Kalisz Hedegaard, A. B.; Daskalakis, N.; Poulidis, A. P.; Vrekoussis, M.; Lichtenstern, M., and Braesicke, P.: "Chemical and dynamical identification of emission outflows during the halo campaign emerge in europe and asia". *Atmospheric Chemistry and Physics*, 23, 3. (2023), pp. 1893–1918. DOI: 10.5194/acp-23-1893-2023.

Forster, P. M.; Forster, H. I.; Evans, M. J.; Gidden, M. J.; Jones, C. D.; Keller, C. A.; Lamboll, R. D.; Quéré, C. L.; Rogelj, J.; Rosen, D.; Schleussner, C. F.; Richardson, T. B.; Smith, C. J., and Turnock, S. T.: "Current and future global climate impacts resulting from COVID-19". *Nature Climate Change*, 10, 10. (2020), pp. 913–919. DOI: 10.1038/s41558-020-0883-0.

Frenklach, M. and Mebel, A. M.: "On the mechanism of soot nucleation". *Phys. Chem. Chem. Phys.*, 22. (9 2020), pp. 5314–5331. DOI: 10.1039/D0CP00116C.

Fueglistaler, S.; Dessler, A. E.; Dunkerton, T. J.; Folkins, I.; Fu, Q., and Mote, P. W.: "Tropical tropopause layer". *Reviews of Geophysics*, 47, 1. (2009). DOI: https://doi.org/10.1029/2008RG000267.

Fuller, K. A.; Malm, W. C., and Kreidenweis, S. M.: "Effects of mixing on extinction by carbonaceous particles". *Journal of Geophysical Research: Atmospheres*, 104, D13. (1999), pp. 15941–15954. DOI: 10.1029/1998JD100069.

Gasteiger, J. and Wiegner, M.: "Mopsmap v1.0: a versatile tool for the modeling of aerosol optical properties". *Geoscientific Model Development*, 11, 7. (2018), pp. 2739–2762. DOI: 10.5194/gmd-11-2739-2018.

Goecke, H.; Puls, T., and Wendt, J.: "Vollbremsung: die folgen voncorona für den straßenverkehr". *IW-Kurzbericht*, 60. (2020).

Gryspeerdt, E. and Stier, P.: "Regime-based analysis of aerosol-cloud interactions". *Geophysical Research Letters*, 39, 21. (2012). DOI: https://doi.org/10.1029/2012GL053221.

Guerreiro, S. B.; Dawson, R. J.; Kilsby, C.; Lewis, E., and Ford, A.: "Future heat-waves, droughts and floods in 571 european cities". *Environmental Research Letters*, 13, 3. (2018), p. 034009. DOI: 10.1088/1748-9326/aaaad3.

Gysel-Beer, M and Corbin, J: *SP2 toolkit 4.115 (Igor7) (Version 4.115)*. http://doi.org/10.5281/zenodo.3575186. 2019.

Hale, T.; Angrist, N.; Goldszmidt, R.; Kira, B.; Petherick, A.; Phillips, T.; Webster, S.; Cameron-Blake, E.; Hallas, L.; Majumdar, S., and Tatlow, H.: "A global panel database of pandemic policies (Oxford COVID-19 Government Response Tracker)". *Nature Human Behaviour*, 5, 4. (2021), pp. 529–538. DOI: 10.1038/s41562-021-01079-8.

Hallquist, M.; Wenger, J. C.; Baltensperger, U.; Rudich, Y.; Simpson, D.; Claeys, M.; Dommen, J.; Donahue, N. M.; George, C.; Goldstein, A. H.; Hamilton, J. F.; Herrmann, H.; Hoffmann, T.; Iinuma, Y.; Jang, M.; Jenkin, M. E.; Jimenez, J. L.; Kiendler-Scharr, A.; Maenhaut, W.; McFiggans, G.; Mentel, T. F.; Monod, A.; Prévôt, A. S. H.; Seinfeld, J. H.; Surratt, J. D.; Szmigielski, R., and Wildt, J.: "The formation, properties and impact of secondary organic aerosol: current and emerging issues". *Atmospheric Chemistry and Physics*, 9, 14. (2009), pp. 5155–5236. DOI: 10.5194/acp-9-5155-2009.

Hansen, J. E. and Travis, L. D.: "Light scattering in planetary atmospheres". *Space Science Reviews*, 16, 4. (1974), pp. 527–610. DOI: 10.1007/BF00168069.

Heald, C. L.; Ridley, D. A.; Kroll, J. H.; Barrett, S. R.; Cady-Pereira, K. E.; Alvarado, M. J., and Holmes, C. D.: "Contrasting the direct radiative effect and direct radiative forcing of aerosols". *Atmospheric Chemistry and Physics*, 14, 11. (2014), pp. 5513–5527. DOI: 10.5194/acp-14-5513-2014.

Heintzenberg, J.: "Properties of the log-normal particle size distribution". *Aerosol Science and Technology*, 21, 1. (1994), pp. 46–48. DOI: 10.1080/02786829408959695.

Helleis, F.; Klimach, T., and Pöschl, U.: *Wirksamkeit, Energieeffizienz und Nachhaltigkeit verschiedener Lüftungsmethoden hinsichtlich Luftqualität und Infektionsschutz in Innenräumen: Fensterlüften, Abluftventilatoren, Raumlufttechnik und Luftreiniger*. Version 3.0. 2023. DOI: 10.5281/zenodo.7586167.

Hernández, M. D. A.; Hilboll, A.; Ziereis, H.; Förster, E.; Krüger, O. O.; Kaiser, K.; Schneider, J.; Barnaba, F.; Vrekoussis, M.; Schmidt, J.; Huntrieser, H.; Blechschmidt, A.-M.; George, M.; Nenakhov, V.; Harlass, T.; Holanda, B. A.; Wolf, J.; Eirenschmalz, L.; Krebsbach, M.; Pöhlker, M. L.; Hedegaard, A. B. K.; Mei, L.; Pfeilsticker, K.; Liu, Y.; Koppmann, R.; Schlager, H.; Bohn, B.; Schumann, U.; Richter, A.; Schreiner, B.; Sauer, D.; Baumann, R.; Mertens, M.; Jöckel, P.; Kilian, M.; Stratmann, G.; Pöhlker, C.; Campanelli, M.; Pandolfi, M.; Sicard, M.; Gómez-Amo, J. L.; Pujadas, M.; Bigge, K.; Kluge, F.; Schwarz, A.; Daskalakis, N.; Walter, D.; Zahn, A.; Pöschl, U.; Bönisch, H.; Borrmann, S.; Platt, U., and Burrows, J. P.: "Overview: on the transport and transformation of pollutants in the outflow of major population centres –observational data from the emerge european intensive operational period in summer 2017". *Atmospheric Chemistry and Physics*. (2022). DOI: 10.5194/acp-22-5877-2022.

Hess, M.; Koepke, P., and Schult, I.: "Optical properties of aerosols and clouds: the software package opac". *Bulletin of the American Meteorological Society*, 79, 5. (1998), pp. 831 –844. DOI: 10.1175/1520-0477(1998)079<0831:OPOAAC>2.0.CO;2.

Hoesly, R. M.; Smith, S. J.; Feng, L.; Klimont, Z.; Janssens-Maenhout, G.; Pitkanen, T.; Seibert, J. J.; Vu, L.; Andres, R. J.; Bolt, R. M.; Bond, T. C.; Dawidowski, L.; Kholod, N.; Kurokawa, J.-i.; Li, M.; Liu, L.; Lu, Z.; Moura, M. C. P.; O'Rourke, P. R., and Zhang, Q.: "Historical (1750–2014) anthropogenic emissions of reactive gases and aerosols from the Community Emissions Data System (CEDS)". *Geosci. Model Dev.*, 11, 1. (2018), pp. 369–408. DOI: 10.5194/gmd-11-369-2018.

Holanda, B. A.: "Atmospheric processing and relevance of biomass burning aerosols over the amazon and the atlantic. chapter 6: co-variability of black carbon and cloud condensation nuclei in different polluted environments". *Dissertation, Johannes Gutenberg Universität Mainz*. (2021).

Holanda, B. A.; Franco, M. A.; Walter, D.; Artaxo, P.; Carbone, S.; Cheng, Y.; Chowdhury, S.; Ditas, F.; Gysel-beer, M.; Klimach, T.; Kremper, L. A.; Krüger, O. O.; Lavric, J. V.; Lelieveld, J.; Ma, C.; Machado, L. A. T.; Modini, R. L.; Morais, F. G.; Pozzer, A.; Saturno, J.; Su, H.; Wendisch, M.; Wolff, S.; Pöhlker, M. L.; Andreae, M. O.; Pöschl, U., and Pöhlker, C.: "African biomass burning affects aerosol cycling over the Amazon". (2023), pp. 1–15. DOI: 10.1038/s43247-023-00795-5.

Holanda, B. A.; Pöhlker, M. L.; Walter, D.; Saturno, J.; Sörgel, M.; Ditas, J.; Ditas, F.; Schulz, C.; Menezes Franco, M. A. de; Wang, Q.; Donth, T.; Artaxo, P.; Barbosa, H. M. J.; Borrmann, S.; Braga, R. C.; Brito, J.; Cheng, Y.; Dollner, M.; Kaiser, J. W.; Klimach, T.; Knote, C.; Krüger, O. O.; Fütterer, D.; Lavric, J. V.; Ma, N.; Machado, L. A. T.; Ming, J.; Morais, F. G.; Paulsen, H.; Sauer, D.; Schlager, H.; Schneider, J.; Su, H.; Weinzierl, B.; Walser, A.; Wendisch, M.; Ziereis, H.; Zöger, M.; Pöschl, U.; Andreae, M. O., and Pöhlker, C.: "Influx of african biomass burning aerosol during the amazonian dry season through layered transatlantic transport of black carbon-rich smoke". *Atmospheric Chemistry and Physics*. (Apr. 24, 2020). DOI: 10.5194/acp-20-4757-2020.

Howard, J. B.: "Fullerenes formation in flames". *Symposium (International) on Combustion*, 24, 1. (1992). Twenty-Fourth Symposium on Combustion, pp. 933–946. DOI: https://doi.org/10.1016/S0082-0784(06)80111-6.

Huang, X.; Ding, K.; Liu, J.; Wang, Z.; Tang, R.; Xue, L.; Wang, H.; Zhang, Q.; Tan, Z.-M.; Fu, C.; Davis, S. J.; Andreae, M. O., and Ding, A.: "Smoke-weather interaction affects extreme wildfires in diverse coastal regions". *Science*, 379, 6631. (2023), pp. 457–461. DOI: 10.1126/science.add9843.

Hussein, T.: "Indoor and outdoor aerosol particle size characterization in helsinki". In: 2005. ISBN: 952-5027-60-0.

Janhäll, S.; Andreae, M. O., and Pöschl, U.: "Biomass burning aerosol emissions from vegetation fires: particle number and mass emission factors and size distributions". *Atmospheric Chemistry and Physics*, 10, 3. (2010), pp. 1427–1439. DOI: 10.5194/acp-10-1427-2010.

Japan, S. H.: *Statistical Handbook of Japan 2020, Statistics Bureau Ministry of Internal Affairs and Communications Japan*. 2020. URL: https://www.stat.go.jp/english/data/handbook/pdf/2020all.pdf.

Jensen, E. J.; Woods, S.; Lawson, R. P.; Bui, T. P.; Pfister, L.; Thornberry, T. D.; Rollins, A. W.; Vernier, J.-P.; Pan, L. L.; Honomichl, S., and Toon, O. B.: "Ash particles detected in the tropical lower stratosphere". *Geophysical Research Letters*, 45, 20. (2018), pp. 11,483–11,489. DOI: https://doi.org/10.1029/2018GL079605.

Johansson, K. O.; Head-Gordon, M. P.; Schrader, P. E.; Wilson, K. R., and Michelsen, H. A.: "Resonance-stabilized hydrocarbon-radical chain reactions may explain soot inception and growth". *Science*, 361, 6406. (2018), pp. 997–1000. DOI: 10.1126/science.aat3417.

Jolly, W. M.; Cochrane, M. A.; Freeborn, P. H.; Holden, Z. A.; Brown, T. J.; Williamson, G. J., and Bowman, D. M.: "Climate-induced variations in global wildfire danger from 1979 to 2013". *Nature Communications*, 6, May. (2015), pp. 1–11. DOI: 10.1038/ncomms8537.

Jöckel, P.; Kerkweg, A.; Pozzer, A.; Sander, R.; Tost, H.; Riede, H.; Baumgaertner, A.; Gromov, S., and Kern, B.: "Development cycle 2 of the Modular Earth Submodel System (MESSy2)". *Geosci. Model Dev.*, 3, 2. (2010), pp. 717–752. DOI: 10.5194/gmd-3-717-2010.

Jöckel, P.; Sander, R.; Kerkweg, A.; Tost, H., and Lelieveld, J.: "Technical Note: The Modular Earth Submodel System (MESSy) - a new approach towards Earth System Modeling". *Atmos. Chem. Phys.*, 5, 2. (2005), pp. 433–444. DOI: 10.5194/acp-5-433-2005.

Junge, C. E. and Manson, J. E.: "Stratospheric aerosol studies". *Journal of Geophysical Research (1896-1977)*, 66, 7. (1961), pp. 2163–2182. DOI: https://doi.org/10.1029/JZ066i007p02163.

Kaiser, J. W.; Heil, A.; Andreae, M. O.; Benedetti, A.; Chubarova, N.; Jones, L.; Morcrette, J.-J.; Razinger, M.; Schultz, M. G.; Suttie, M., and Werf, G. R. van der: "Biomass burning emissions estimated with a global fire assimilation system based on observed fire radiative power". *Biogeosciences*, 9, 1. (2012), pp. 527–554. DOI: 10.5194/bg-9-527-2012.

Kalogridis, A.-C.; Vratolis, S.; Liakakou, E.; Gerasopoulos, E.; Mihalopoulos, N., and Eleftheriadis, K.: "Assessment of wood burning versus fossil fuel contribution to wintertime black carbon and carbon monoxide concentrations in athens, greece". *Atmospheric Chemistry and Physics*, 18, 14. (2018), pp. 10219–10236. DOI: 10.5194/acp-18-10219-2018.

Kanaya, Y.; Yamaji, K.; Miyakawa, T.; Taketani, F.; Zhu, C.; Choi, Y.; Komazaki, Y.; Ikeda, K.; Kondo, Y., and Klimont, Z.: "Rapid reduction in black carbon emissions from china: evidence from 2009–2019 observations on fukue island, japan". *Atmospheric Chemistry and Physics*, 20, 11. (2020), pp. 6339–6356. DOI: 10.5194/acp-20-6339-2020.

Kaufmann, S.; Voigt, C.; Heller, R.; Jurkat-Witschas, T.; Krämer, M.; Rolf, C.; Zöger, M.; Giez, A.; Buchholz, B.; Ebert, V.; Thornberry, T., and Schumann, U.: "Intercomparison of midlatitude tropospheric and lower-stratospheric water vapor measurements and comparison to ecmwf humidity data". *Atmospheric Chemistry and Physics*, 18, 22. (2018), pp. 16729–16745. DOI: 10.5194/acp-18-16729-2018.

Keim, E. R.; Fahey, D. W.; Del Negro, L. A.; Woodbridge, E. L.; Gao, R. S.; Wennberg, P. O.; Cohen, R. C.; Stimpfle, R. M.; Kelly, K. K.; Hintsa, E. J.; Wilson, J. C.; Jonsson, H. H.; Dye, J. E.; Baumgardner, D.; Kawa, S. R.; Salawitch, R. J.; Proffitt, M. H.; Loewenstein, M.; Podolske, J. R., and Chan, K. R.: "Observations of large reductions in the no/noy ratio near the mid-latitude tropopause and the role of heterogeneous chemistry". *Geophysical Research Letters*, 23, 22. (1996), pp. 3223–3226. DOI: https://doi.org/10.1029/96GL02593.

Kerkweg, A.; Sander, R.; Tost, H., and Jöckel, P.: "Technical note: Implementation of prescribed (OFFLEM), calculated (ONLEM), and pseudo-emissions (TNUDGE) of chemical species in the Modular Earth Submodel System (MESSy)". *Atmos. Chem. Phys.*, 6, 11. (2006), pp. 3603–3609. DOI: 10.5194/acp-6-3603-2006.

Kerminen, V.-M.; Chen, X.; Vakkari, V.; Petäjä, T.; Kulmala, M., and Bianchi, F.: "Atmospheric new particle formation and growth: review of field observations". *Environmental Research Letters*, 13, 10. (2018), p. 103003. DOI: 10.1088/1748-9326/aadf3c.

Ketzel, M. and Berkowicz, R.: "Modelling the fate of ultrafine particles from exhaust pipe to rural background: an analysis of time scales for dilution, coagulation and deposition". *Atmospheric Environment*, 38, 17. (2004), pp. 2639–2652. DOI: https://doi.org/10.1016/j.atmosenv.2004.02.020.

Khain, A. P.; BenMoshe, N., and Pokrovsky, A.: "Factors determining the impact of aerosols on surface precipitation from clouds: an attempt at classification". *Journal of the Atmospheric Sciences*, 65, 6. (2008), pp. 1721 –1748. DOI: 10.1175/2007JAS2515.1.

Klingmüller, K.; Lelieveld, J.; Karydis, V. A., and Stenchikov, G. L.: "Direct radiative effect of dust–pollution interactions". *Atmos Chem Phys*, 19, 11. (2019), pp. 7397–7408. DOI: 10.5194/acp-19-7397-2019.

Kloss, C.; Sellitto, P.; Legras, B.; Vernier, J.-P.; Jégou, F.; Venkat Ratnam, M.; Suneel Kumar, B.; Lakshmi Madhavan, B., and Berthet, G.: "Impact of the 2018 ambae eruption on the global stratospheric aerosol layer and climate". *Journal of Geophysical Research: Atmospheres*, 125, 14. (2020). e2020JD032410 10.1029/2020JD032410, e2020JD032410. DOI: https://doi.org/10.1029/2020JD032410.

Koch, D. and Del Genio, A. D.: "Black carbon semi-direct effects on cloud cover: review and synthesis". *Atmospheric Chemistry and Physics*, 10, 16. (2010), pp. 7685–7696. DOI: 10.5194/acp-10-7685-2010.

Koehler, K. A.; Kreidenweis, S. M.; DeMott, P. J.; Prenni, A. J.; Carrico, C. M.; Ervens, B., and Feingold, G.: "Water activity and activation diameters from hygroscopicity data - part ii: application to organic species". *Atmospheric Chemistry and Physics*, 6, 3. (2006), pp. 795–809. DOI: 10.5194/acp-6-795-2006.

Köhler, H.: "The nucleus in and the growth of hygroscopic droplets". *Transactions of the Faraday Society*, 32, 2. (1936), pp. 1152–1161. DOI: 10.1039/tf9363201152.

Kreidenweis, S. M.; Koehler, K.; DeMott, P. J.; Prenni, A. J.; Carrico, C., and Ervens, B.: "Water activity and activation diameters from hygroscopicity data - part i: theory and application to inorganic salts". *Atmospheric Chemistry and Physics*, 5, 5. (2005), pp. 1357–1370. DOI: 10.5194/acp-5-1357-2005.

Kremser, S.; Thomason, L. W.; Hobe, M. von; Hermann, M.; Deshler, T.; Timmreck, C.; Toohey, M.; Stenke, A.; Schwarz, J. P.; Weigel, R.; Fueglistaler, S.; Prata, F. J.; Vernier, J.-P.; Schlager, H.; Barnes, J. E.; Antuña-Marrero, J.-C.; Fairlie, D.; Palm, M.; Mahieu, E.; Notholt, J.; Rex, M.; Bingen, C.; Vanhellemont, F.; Bourassa, A.; Plane, J. M. C.; Klocke, D.; Carn, S. A.; Clarisse, L.; Trickl, T.; Neely, R.; James, A. D.; Rieger, L.; Wilson, J. C., and Meland, B.: "Stratospheric aerosol—observations, processes, and impact on climate". *Reviews of Geophysics*, 54, 2. (2016), pp. 278–335. DOI: https://doi.org/10.1002/2015RG000511.

Krüger, M. L.; Mertes, S.; Klimach, T.; Cheng, Y. F.; Su, H.; Schneider, J.; Andreae, M. O.; Pöschl, U., and Rose, D.: "Assessment of cloud supersaturation by size-resolved aerosol particle and cloud condensation nuclei (CCN) measurements". *Atmospheric Measurement Techniques*, 7, 8. (2014), pp. 2615–2626. DOI: 10.5194/amt-7-2615-2014.

Krüger, O. O.; Holanda, B. A.; Chowdhury, S.; Pozzer, A.; Walter, D.; Pöhlker, C.; Andrés Hernández, M. D.; Burrows, J. P.; Voigt, C.; Lelieveld, J.; Quaas, J.; Pöschl, U., and Pöhlker, M. L.: "Black carbon aerosol reductions during covid-19 confinement quantified by aircraft measurements over europe". *Atmospheric Chemistry and Physics*, 22, 13. (2022), pp. 8683–8699. DOI: 10.5194/acp-22-8683-2022.

Kulmala, M.: "How particles nucleate and grow". *Science*, 302, 5647. (2003), pp. 1000–1001. DOI: 10.1126/science.1090848. URL: <GotoISI>://WOS:000186396300034.

Kulmala, M.; Kontkanen, J.; Junninen, H.; Lehtipalo, K.; Manninen, H. E.; Nieminen, T.; Petäjä, T.; Sipilä, M.; Schobesberger, S.; Rantala, P.; Franchin, A.; Jokinen, T.; Järvinen, E.; Äijälä, M.; Kangasluoma, J.; Hakala, J.; Aalto, P. P.; Paasonen, P.; Mikkilä, J.; Vanhanen, J.; Aalto, J.; Hakola, H.; Makkonen, U.; Ruuskanen, T.; Mauldin, R. L.; Duplissy, J.; Vehkamäki, H.; Bäck, J.; Kortelainen, A.; Riipinen, I.; Kurtén, T.; Johnston, M. V.; Smith, J. N.; Ehn, M.; Mentel, T. F.; Lehtinen, K. E. J.; Laaksonen, A.; Kerminen, V.-M., and Worsnop, D. R.: "Direct observations of atmospheric aerosol nucleation". *Science*, 339, 6122. (2013), pp. 943–946. DOI: 10.1126/science.1227385.

Kutzner, R. D.; von Schneidemesser, E.; Kuik, F.; Quedenau, J.; Weatherhead, E. C., and Schmale, J.: "Long-term monitoring of black carbon across germany". *Atmospheric Environment*, 185. (2018), pp. 41–52. DOI: https://doi.org/10.1016/j.atmosenv.2018.04.039.

Kärcher, B. and Lohmann, U.: "A parameterization of cirrus cloud formation: homogeneous freezing of supercooled aerosols". *Journal of Geophysical Research: Atmospheres*, 107, D2. (2002), AAC 4–1–AAC 4–10. DOI: https://doi.org/10.1029/2001JD000470.

Laakso, A.; Kokkola, H.; Partanen, A.-I.; Niemeier, U.; Timmreck, C.; Lehtinen, K. E. J.; Hakkarainen, H., and Korhonen, H.: "Radiative and climate impacts of a large volcanic eruption during stratospheric sulfur geoengineering". *Atmospheric Chemistry and Physics*, 16, 1. (2016), pp. 305–323. DOI: 10.5194/acp-16-305-2016.

Laborde, M.; Crippa, M.; Tritscher, T.; Jurányi, Z.; Decarlo, P. F.; Temime-Roussel, B.; Marchand, N.; Eckhardt, S.; Stohl, A.; Baltensperger, U.; Prévôt, A. S.; Weingartner, E., and Gysel, M.: "Black carbon physical properties and mixing state in the European megacity Paris". *Atmospheric Chemistry and Physics*, 13, 11. (2013), pp. 5831–5856. DOI: 10.5194/acp-13-5831-2013.

Laborde, M.; Mertes, P.; Zieger, P.; Dommen, J.; Baltensperger, U., and Gysel, M.: "Sensitivity of the Single Particle Soot Photometer to different black carbon types". *Atmospheric Measurement Techniques*, 5, 5. (2012), pp. 1031–1043. DOI: 10.5194/amt-5-1031-2012.

Laj, P. et al.: “A global analysis of climate-relevant aerosol properties retrieved from the network of global atmosphere watch (gaw) near-surface observatories”. *Atmospheric Measurement Techniques*, 13, 8. (2020), pp. 4353–4392. DOI: 10.5194/amt-13-4353-2020.

Lareau, N. P. and Clements, C. B.: “Cold smoke: smoke-induced density currents cause unexpected smoke transport near large wildfires”. *Atmospheric Chemistry and Physics*, 15, 20. (2015), pp. 11513–11520. DOI: 10.5194/acp-15-11513-2015.

Lary, D. J.; Balluch, M., and Bekki, S.: “Solar heating rates after a volcanic eruption: the importance of so2 absorption”. *Quarterly Journal of the Royal Meteorological Society*, 120, 520. (1994), pp. 1683–1688. DOI: https://doi.org/10.1002/qj.49712052011.

Lauer, A.; Eyring, V.; Hendricks, J.; Jöckel, P., and Lohmann, U.: “Global model simulations of the impact of ocean-going ships on aerosols, clouds, and the radiation budget”. *Atmos Chem Phys*, 7, 19. (2007), pp. 5061–5079. DOI: 10.5194/acp-7-5061-2007.

Le Quéré, C.; Jackson, R. B.; Jones, M. W.; Smith, A. J.; Abernethy, S.; Andrew, R. M.; De-Gol, A. J.; Willis, D. R.; Shan, Y.; Canadell, J. G.; Friedlingstein, P.; Creutzig, F., and Peters, G. P.: “Temporary reduction in daily global CO2 emissions during the COVID-19 forced confinement”. *Nature Climate Change*, 10, 7. (2020), pp. 647–653. DOI: 10.1038/s41558-020-0797-x.

Lee, S.-H.; Gordon, H.; Yu, H.; Lehtipalo, K.; Haley, R.; Li, Y., and Zhang, R.: “New particle formation in the atmosphere: from molecular clusters to global climate”. *Journal of Geophysical Research: Atmospheres*, 124, 13. (2019), pp. 7098–7146. DOI: https://doi.org/10.1029/2018JD029356.

Lelieveld, J.; Brühl, C.; Jöckel, P.; Steil, B.; Crutzen, P. J.; Fischer, H.; Giorgetta, M. A.; Hoor, P.; Lawrence, M. G.; Sausen, R., and Tost, H.: “Stratospheric dryness: model simulations and satellite observations”. *Atmos Chem Phys*, 7, 5. (2007), pp. 1313–1332. DOI: 10.5194/acp-7-1313-2007.

Lelieveld, J.; Gromov, S.; Pozzer, A., and Taraborrelli, D.: “Global tropospheric hydroxyl distribution, budget and reactivity”. *Atmospheric Chemistry and Physics*, 16, 19. (2016), pp. 12477–12493. DOI: 10.5194/acp-16-12477-2016.

Lelieveld, J.; Klingmueller, K.; Pozzer, A.; Burnett, R. T.; Haines, A., and Ramanathan, V.: “Effects of fossil fuel and total anthropogenic emission removal on public health and climate”. *Proc Natl Acad Sci U.S.A*, 116, 15. (2019), pp. 7192–7197. DOI: 10.1073/pnas.1819989116.

Lelieveld, J.; Klingmueller, K.; Pozzer, A.; Poeschl, U.; Fnais, M.; Daiber, A., and Muenzel, T.: “Cardiovascular disease burden from ambient air pollution in Europe reassessed using novel hazard ratio functions”. *Eur Heart J*, 40, 20. (2019), pp. 1590–1596. DOI: 10.1093/eurheartj/ehz135.

Li, Q. and Groß, S.: “Changes of cirrus cloud properties and occurrence over Europe during the COVID-19 caused air traffic reduction”. *Atmospheric Chemistry and Physics Discussions*, March. (2021), pp. 1–25. DOI: 10.5194/acp-2021-172.

Lin, C.-Y.; Chen, W.-C.; Chien, Y.-Y.; Chou, C. C. K.; Liu, C.-Y.; Ziereis, H.; Schlager, H.; Förster, E.; Obersteiner, F.; Krüger, O. O.; Holanda, B. A.; Pöhlker, M. L.; Kaiser, K.; Schneider, J.; Bohn, B.; Pfeilsticker, K.; Weyland, B.; Andrés Hernández, M. D., and Burrows, J. P.: "Effects of transport on a biomass burning plume from indochina during emerge-asia identified by wrf-chem". *Atmospheric Chemistry and Physics*, 23, 4. (2023), pp. 2627–2647. DOI: 10.5194/acp-23-2627-2023.

Lin, J. C.; Matsui, T.; Pielke, R. A., and Kummerow, C.: "Effects of biomass-burning-derived aerosols on precipitation and clouds in the Amazon Basin: a satellite-based empirical study". *Journal of Geophysical Research*, 111, D19. (2006), p. D19204. DOI: 10.1029/2005JD006884.

Liu, D.; Allan, J.; Whitehead, J.; Young, D.; Flynn, M.; Coe, H.; McFiggans, G.; Fleming, Z. L., and Bandy, B.: "Ambient black carbon particle hygroscopic properties controlled by mixing state and composition". *Atmospheric Chemistry and Physics*, 13, 4. (2013), pp. 2015–2029. DOI: 10.5194/acp-13-2015-2013.

Liu, D.; Allan, J. D.; Young, D. E.; Coe, H.; Beddows, D.; Fleming, Z. L.; Flynn, M. J.; Gallagher, M. W.; Harrison, R. M.; Lee, J.; Prevot, A. S.; Taylor, J. W.; Yin, J.; Williams, P. I., and Zotter, P.: "Size distribution, mixing state and source apportionment of black carbon aerosol in London during winter time". *Atmospheric Chemistry and Physics*, 14, 18. (2014), pp. 10061–10084. DOI: 10.5194/acp-14-10061-2014.

Liu, D.; Ding, S.; Zhao, D.; Hu, K.; Yu, C.; Hu, D.; Wu, Y.; Zhou, C.; Tian, P.; Liu, Q.; Wu, Y.; Zhang, J.; Kong, S.; Huang, M., and Ding, D.: "Black Carbon Emission and Wet Scavenging From Surface to the Top of Boundary Layer Over Beijing Region". *Journal of Geophysical Research: Atmospheres*, 125, 17. (2020), pp. 1–15. DOI: 10.1029/2020JD033096.

Liu, Y.; Su, H.; Wang, S.; Wei, C.; Tao, W.; Pöhlker, M. L.; Pöhlker, C.; Holanda, B. A.; Krüger, O. O.; Hoffmann, T.; Wendisch, M.; Artaxo, P.; Pöschl, U.; Andreae, M. O., and Cheng, Y.: "Strong particle production and condensational growth in the upper troposphere sustained by biogenic vocs from the canopy of the amazon basin". *Atmospheric Chemistry and Physics*, 23, 1. (2023), pp. 251–272. DOI: 10.5194/acp-23-251-2023.

Lobert, J. M. and Wamatz, J.: "Emissions from the combustion process in vegetation". In: *Fire in the Environment: The Ecological, Atmospheric and Climatic Importance of Vegetation Fires*. Ed. by P. J. Crutzen and J. G. Goldammer. New York: John Wiley, 1993, pp. 15–37.

Lonati, G. and Riva, F.: "Regional scale impact of the covid-19 lockdown on air quality: Gaseous pollutants in the po valley, northern Italy". *Atmosphere*, 12, 2. (2021). DOI: 10.3390/atmos12020264.

Lu, Z.; Liu, X.; Zhang, Z.; Zhao, C.; Meyer, K.; Rajapakshe, C.; Wu, C.; Yang, Z., and Penner, J. E.: "Biomass smoke from southern Africa can significantly enhance the brightness of stratocumulus over the southeastern Atlantic Ocean". *Proceedings of the National Academy of Sciences*, 115, 12. (2018), pp. 2924–2929. DOI: 10.1073/pnas.1713703115.

Lund, M. T.; Samset, B. H.; Skeie, R. B.; Watson-Parris, D.; Katich, J. M.; Schwarz, J. P., and Weinzierl, B.: "Short Black Carbon lifetime inferred from a global set of aircraft observations". *npj Climate and Atmospheric Science*, 1, 1. (2018), pp. 1–8. DOI: 10.1038/s41612-018-0040-x.

Machado, L. A. T.; Calheiros, A. J. P.; Biscaro, T.; Giangrande, S.; Silva Dias, M. A. F.; Cecchini, M. A.; Albrecht, R.; Andreae, M. O.; Araujo, W. F.; Arttaxo, P.; Borrmann, S.; Braga, R.; Burleyson, C.; Eichholz, C. W.; Fan, J.; Feng, Z.; Fisch, G. F.; Jensen, M. P.; Martin, S. T.; Pöschl, U.; Pöhlker, C.; Pöhlker, M. L.; Ribaud, J.-F.; Rosenfeld, D.; Saraiva, J. M. B.; Schumacher, C.; Thalman, R.; Walter, D., and Wendisch, M.: "Overview: Precipitation Characteristics and Sensitivities to the Environmental Conditions during GoAmazon2014/5 and ACRIDICON-CHUVA". *Atmospheric Chemistry and Physics Discussions*. (2017), pp. 1–41. DOI: 10.5194/acp-2017-990.

Malinina, E.; Rozanov, A.; Niemeier, U.; Wallis, S.; Arosio, C.; Wrana, F.; Timmreck, C.; Savigny, C. von, and Burrows, J. P.: "Changes in stratospheric aerosol extinction coefficient after the 2018 ambae eruption as seen by omps-lp and maecham5-ham". *Atmospheric Chemistry and Physics*, 21, 19. (2021), pp. 14871–14891. DOI: 10.5194/acp-21-14871-2021.

Martins, J. V.; Marshak, A.; Remer, L. A.; Rosenfeld, D.; Kaufman, Y. J.; Fernandez-Borda, R.; Koren, I.; Correia, A. L.; Zubko, V., and Artaxo, P.: "Remote sensing the vertical profile of cloud droplet effective radius, thermodynamic phase, and temperature". *Atmospheric Chemistry and Physics*, 11, 18. (2011), pp. 9485–9501. DOI: 10.5194/acp-11-9485-2011.

Mayer, B. and Kylling, A.: "Technical note: the libradtran software package for radiative transfer calculations - description and examples of use". *Atmospheric Chemistry and Physics*, 5, 7. (2005), pp. 1855–1877. DOI: 10.5194/acp-5-1855-2005.

McDuffie, E. E.; Smith, S. J.; O'Rourke, P.; Tibrewal, K.; Venkataraman, C.; Marais, E. A.; Zheng, B.; Crippa, M.; Brauer, M., and Martin, R. V.: "A global anthropogenic emission inventory of atmospheric pollutants from sector- and fuel-specific sources (1970–2017): an application of the community emissions data system (ceds)". *Earth System Science Data*, 12, 4. (2020), pp. 3413–3442. DOI: 10.5194/essd-12-3413-2020.

McFiggans, G.; Artaxo, P.; Baltensperger, U.; Coe, H.; Facchini, M. C.; Feingold, G.; Fuzzi, S.; Gysel, M.; Laaksonen, A.; Lohmann, U.; Mentel, T. F.; Murphy, D. M.; O'Dowd, C. D.; Snider, J. R., and Weingartner, E.: "The effect of physical and chemical aerosol properties on warm cloud droplet activation". *Atmospheric Chemistry and Physics*, 6, 9. (2006), pp. 2593–2649. DOI: 10.5194/acp-6-2593-2006.

Minikin, A.; Sauer, D.; Ibrahim, A.; Franke, H.; Röschenthaler, T.; Alexanderütterer, D., and Petzold, A.: "The HALO Submicrometer Aerosol Inlet (HASI): Design concept and first characterization". 2017.

Molleker, S.; Helleis, F.; Klimach, T.; Appel, O.; Clemen, H.-C.; Dragoneas, A.; Gurk, C.; Hünig, A.; Köllner, F.; Rubach, F.; Schulz, C.; Schneider, J., and Borrmann, S.: "Application of an o-ring pinch device as a constant-pressure inlet (cpi) for airborne sampling". *Atmospheric Measurement Techniques*, 13, 7. (2020), pp. 3651–3660. DOI: 10.5194/amt-13-3651-2020.

Monastersky, R.: "Anthropocene: the human age". *Nature*, 519, 7542. (2015), pp. 144–147. DOI: 10.1038/519144a.

Mondal, A.; Saharan, U. S.; Arya, R.; Yadav, L.; Ahlawat, S.; Jangirh, R.; Kotnala, G.; Choudhary, N.; Banoo, R.; Rai, A.; Yadav, P.; Rani, M.; Lal, S.; Stewart, G. J.; Nelson, B. S.; Acton, W. J. F.; Vaughan, A. R.; Hamilton, J. F.; Hopkins, J. R.; Hewitt, C. N.; Sahu, L. K.; Tripathi, N.; Sharma, S., and Mandal, T.: "Non-methane volatile organic compounds emitted from domestic fuels in delhi: emission factors and total city-wide emissions". *Atmospheric Environment: X*, 11. (2021), p. 100127. DOI: https://doi.org/10.1016/j.aeaoa.2021.100127.

Moore, R. H. and Nenes, A.: "Scanning flow ccn analysis—a method for fast measurements of ccn spectra". *Aerosol Science and Technology*, 43, 12. (2009), pp. 1192–1207. DOI: 10.1080/02786820903289780.

Moreda-Piñeiro, J.; Sánchez-Piñero, J.; Fernández-Amado, M.; Costa-Tomé, P.; Gallego-Fernández, N.; Piñeiro-Iglesias, M.; López-Mahía, P., and Muniategui-Lorenzo, S.: "Evolution of gaseous and particulate pollutants in the air: What changed after five lockdown weeks at a southwest atlantic european region (northwest of spain) due to the sars-cov-2 pandemic?" *Atmosphere*, 12, 5. (2021). DOI: 10.3390/atmos12050562.

Mülmenstädt, J and Feingold, G: "The radiative forcing of aerosol–cloud interactions in liquid clouds: wrestling and embracing uncertainty". *Current Climate Change Reports*, 4, 1. (2018), pp. 23–40. DOI: 10.1007/s40641-018-0089-y.

Murphy, D. M.; Froyd, K. D.; Bourgeois, I.; Brock, C. A.; Kupc, A.; Peischl, J.; Schill, G. P.; Thompson, C. R.; Williamson, C. J., and Yu, P.: "Radiative and chemical implications of the size and composition of aerosol particles in the existing or modified global stratosphere". *Atmospheric Chemistry and Physics*, 21, 11. (2021), pp. 8915–8932. DOI: 10.5194/acp-21-8915-2021.

Neubauer, D.; Ferrachat, S.; Siegenthaler-Le Drian, C.; Stier, P.; Partridge, D. G.; Tegen, I.; Bey, I.; Stanelle, T.; Kokkola, H., and Lohmann, U.: "The global aerosol–climate model echam6.3–ham2.3 – part 2: cloud evaluation, aerosol radiative forcing, and climate sensitivity". *Geoscientific Model Development*, 12, 8. (2019), pp. 3609–3639. DOI: 10.5194/gmd-12-3609-2019.

Nguyen, T.; Vien, T.; Lam, N.; Tuong, T., and Cadisch, G: "Analysis of the sustainability with the composite swidden agroecosystem: 1. partial nutrient balance and recovery times of uplands swiddens". *Agriculture, Ecosystem and Environment*, 128. (2008), pp. 37–51.

Niemeier, U.; Timmreck, C.; Graf, H.-F.; Kinne, S.; Rast, S., and Self, S.: "Initial fate of fine ash and sulfur from large volcanic eruptions". *Atmospheric Chemistry and Physics*, 9, 22. (2009), pp. 9043–9057. DOI: 10.5194/acp-9-9043-2009.

Nussbaumer, C. M.; Tadic, I.; Dienhart, D.; Wang, N.; Edtbauer, A.; Ernle, L.; Williams, J.; Obersteiner, F.; Gutiérrez-Álvarez, I.; Harder, H.; Lelieveld, J., and Fischer, H.: "Measurement report: in situ observations of deep convection without lightning during the tropical cyclone florence 2018". *Atmospheric Chemistry and Physics*, 21, 10. (2021), pp. 7933–7945. DOI: 10.5194/acp-21-7933-2021.

Ohata, S.; Moteki, N.; Mori, T.; Koike, M., and Kondo, Y.: "A key process controlling the wet removal of aerosols: New observational evidence". *Scientific Reports*, 6. (2016), pp. 1–9. DOI: 10.1038/srep34113.

Ohneiser, K.; Ansmann, A.; Baars, H.; Seifert, P.; Barja, B.; Jimenez, C.; Radenz, M.; Teisseire, A.; Floutsi, A.; Haarig, M.; Foth, A.; Chudnovsky, A.; Engelmann, R.; Zamorano, F.; Bühl, J., and Wandinger, U.: "Smoke of extreme australian bushfires observed in the stratosphere over punta arenas, chile, in january 2020: optical thickness, lidar ratios, and depolarization ratios at 355 and 532 nm". *Atmospheric Chemistry and Physics*, 20, 13. (2020), pp. 8003–8015. DOI: 10.5194/acp-20-8003-2020.

Ohneiser, K.; Ansmann, A.; Kaifler, B.; Chudnovsky, A.; Barja, B.; Knopf, D. A.; Kaifler, N.; Baars, H.; Seifert, P.; Villanueva, D.; Jimenez, C.; Radenz, M.; Engelmann, R.; Veselovskii, I., and Zamorano, F.: "Australian wildfire smoke in the stratosphere: the decay phase in 2020/2021 and impact on ozone depletion". *Atmospheric Chemistry and Physics*, 22, 11. (2022), pp. 7417–7442. DOI: 10.5194/acp-22-7417-2022.

Paasonen, P.; Kupiainen, K.; Klimont, Z.; Visschedijk, A.; Gon, H. A. C. Denier van der, and Amann, M.: "Continental anthropogenic primary particle number emissions". *Atmos. Chem. Phys.*, 16, 11. (2016), pp. 6823–6840. DOI: 10.5194/acp-16-6823-2016.

Peitzmeier, C.; Loschke, C.; Wiedenhaus, H., and Klemm, O.: "Real-world vehicle emissions as measured by in situ analysis of exhaust plumes". *Environmental Science and Pollution Research*, 24, 29. (2017), pp. 23279–23289. DOI: 10.1007/s11356-017-9941-1.

Penner, J. E.; Dong, X., and Chen, Y.: "Observational evidence of a change in radiative forcing due to the indirect aerosol effect". *Nature*, 427, 6971. (2004), pp. 231–234. DOI: 10.1038/nature02234.

Petetin, H.; Bowdalo, D.; Soret, A.; Guevara, M.; Jorba, O.; Serradell, K., and Pérez García-Pando, C.: "Meteorology-normalized impact of the COVID-19 lockdown upon NO2 pollution in Spain". *Atmospheric Chemistry and Physics*, 20, 18. (2020), pp. 11119–11141. DOI: 10.5194/acp-20-11119-2020.

Petters, M. D. and Kreidenweis, S. M.: "A single parameter representation of hygroscopic growth and cloud condensation nucleus activity". *ATMOSPHERIC CHEMISTRY AND PHYSICS*, 7, 8. (2007), pp. 1961–1971. DOI: 10.5194/acp-7-1961-2007.

Pileci, R. E.; Modini, R. L.; Bertò, M.; Yuan, J.; Corbin, J. C.; Marinoni, A.; Henzing, B.; Moerman, M. M.; Putaud, J. P.; Spindler, G.; Wehner, B.; Müller, T.; Tuch, T.; Trentini, A.; Zanatta, M.; Baltensperger, U., and Gysel-Beer, M.: "Comparison of colocated refractory black carbon (rbc) and elemental carbon (ec) mass concentration measurements during field campaigns at several european sites". *Atmospheric Measurement Techniques*, 14, 2. (2021), pp. 1379–1403. DOI: 10.5194/amt-14-1379-2021.

Pohjola, M.; Pirjola, L.; Kukkonen, J., and Kulmala, M.: "Modelling of the influence of aerosol processes for the dispersion of vehicular exhaust plumes in street environment". *Atmospheric Environment*, 37, 3. (2003), pp. 339–351. DOI: https://doi.org/10.1016/S1352-2310(02)00887-7.

Pöhlker, C.; Walter, D.; Paulsen, H.; Könemann, T.; Rodríguez-caballero, E.; Moran-zuloaga, D.; Brito, J.; Carbone, S.; Degrendele, C.; Després, V. R.; Ditas, F.; Pöhlker, M. L.; Praß, M.; Löbs, N.; Saturno, J.; Sörgel, M.; Wang, Q.; Weber, B.; Wolff, S.; Artaxo, P.; Pöschl, U., and Andreae, M. O.: "Land cover and its transformation in the backward trajectory footprint region of the amazon tall tower observatory". *Atmospheric Chemistry and Physics*. (2019), pp. 8425–8470.

Pöhlker, M. L.; Ditas, F.; Saturno, J.; Klimach, T.; Hrabě De Angelis, I.; Araùjo, A. C.; Brito, J.; Carbone, S.; Cheng, Y.; Chi, X.; Ditz, R.; Gunthe, S. S.; Holanda, B. A.; Kandler, K.; Kesselmeier, J.; Könemann, T.; Krüger, O. O.; Lavric, J. V.; Martin, S. T.; Mikhailov, E.; Moran-Zuloaga, D.; Rizzo, L. V.; Rose, D.; Su, H.; Thalman, R.; Walter, D.; Wang, J.; Wolff, S.; Barbosa, H. M.; Artaxo, P.; Andreae, M. O.; Pöschl, U., and Pöhlker, C.: "Long-term observations of cloud condensation nuclei over the Amazon rain forest - Part 2: Variability and characteristics of biomass burning, long-range transport, and pristine rain forest aerosols". *Atmospheric Chemistry and Physics*, 18, 14. (2018), pp. 10289–10331. DOI: 10.5194/acp-18-10289-2018.

Pöhlker, M. L.; Krüger, O. O.; Förster, J.-D.; Berkemeier, T.; Elbert, W.; Fröhlich-Nowoisky, J.; Pöschl, U.; Pöhlker, C.; Bagheri, G.; Bodenschatz, E.; Huffman, J. A.; S, S., and Mikhailov, E.: *Respiratory aerosols and droplets in the transmission of infectious diseases*. accepted in Reviews of Modern Physics. 2021. DOI: 10.48550/ARXIV.2103.01188.

Pöhlker, M. L.; Pöhlker, C.; Ditas, F.; Klimach, T.; De Angelis, I. H.; Araújo, A.; Brito, J.; Carbone, S.; Cheng, Y.; Chi, X.; Ditz, R.; Gunthe, S. S.; Kesselmeier, J.; Könemann, T.; Lavrič, J. V.; Martin, S. T.; Mikhailov, E.; Moran-Zuloaga, D.; Rose, D.; Saturno, J.; Su, H.; Thalman, R.; Walter, D.; Wang, J.; Wolff, S.; Barbosa, H. M.; Artaxo, P.; Andreae, M. O., and Pöschl, U.: "Long-term observations of cloud condensation nuclei in the Amazon rain forest - Part 1: Aerosol size distribution, hygroscopicity, and new model parametrizations for CCN prediction". *Atmospheric Chemistry and Physics*, 16, 24. (2016), pp. 15709–15740. DOI: 10.5194/acp-16-15709-2016.

Pöhlker, M. L.; Pöhlker, C.; Quaas, J.; Mülmenstädt, J.; Pozzer, A.; Andreae, M. O.; Artaxo, P.; Block, K.; Coe, H.; Ervens, B.; Gallimore, P.; Gaston, C. J.; Gunthe, S. S.; Henning, S.; Herrmann, H.; Krüger, O. O.; McFiggans Gordonand Poulain, L.; Raj, S. S.; Reyes-Villegas, E.; Royer, H. M.; Walter, D.; Wang, Y., and Pöschl, U.: "Global organic and inorganic aerosol hygroscopicity and its effect on radiative forcing". (2023). in review for Nature Communications.

Pöschl, U.: "Atmospheric aerosols: Composition, transformation, climate and health effects". *Angewandte Chemie - International Edition*, 44, 46. (2005), pp. 7520–7540. DOI: 10.1002/anie.200501122.

Pozzer, A.; Meij, A. de; Pringle, K. J.; Tost, H.; Doering, U. M.; Aardenne, J. van, and Lelieveld, J.: "Distributions and regional budgets of aerosols and their precursors simulated with the EMAC chemistry-climate model". *Atmos. Chem. Phys.*, 12, 2. (2012), pp. 961–987. DOI: 10.5194/acp-12-961-2012.

Pozzer, A.; Meij, A. de; Yoon, J.; Tost, H.; Georgoulias, A. K., and Astitha, M.: "AOD trends during 2001–2010 from observations and model simulations". *Atmos Chem Phys*, 15, 10. (2015), pp. 5521–5535. DOI: 10.5194/acp-15-5521-2015.

Pringle, K. J.; Tost, H.; Message, S.; Steil, B.; Giannadaki, D.; Nenes, A.; Fountoukis, C.; Stier, P.; Vignati, E., and Lelieveld, J.: "Description and evaluation of GMXe: a new aerosol submodel for global simulations (v1)". *Geosci. Model Dev.*, 3, 2. (2010), pp. 391–412. DOI: 10.5194/gmd-3-391-2010.

Prospero, J. M.: "Atmospheric dust studies on barbados". *Bulletin of the American Meteorological Society*, 49, 6. (1968), pp. 645 –652. DOI: 10.1175/1520-0477-49.6.645.

Prospero, J. M.; Blades, E.; Mathison, G., and Naidu, R.: "Interhemispheric transport of viable fungi and bacteria from africa to the caribbean with soil dust". *Aerobiologia*, 21. (2005), pp. 1573–3025. DOI: https://10.1007/s10453-004-5872-7.

Quaas, J.; Arola, A.; Cairns, B.; Christensen, M.; Deneke, H.; Ekman, A. M. L.; Feingold, G.; Fridlind, A.; Gryspeerdt, E.; Hasekamp, O.; Li, Z.; Lipponen, A.; Ma, P.-L.; Mülmenstädt, J.; Nenes, A.; Penner, J. E.; Rosenfeld, D.; Schrödner, R.; Sinclair, K.; Sourdeval, O.; Stier, P.; Tesche, M.; Diedenhoven, B. van, and Wendisch, M.: "Constraining the twomey effect from satellite observations: issues and perspectives". *Atmospheric Chemistry and Physics*, 20, 23. (2020), pp. 15079–15099. DOI: 10.5194/acp-20-15079-2020.

Quaas, J.; Gryspeerdt, E.; Vautard, R., and Boucher, O.: "Climate impact of aircraft-induced cirrus assessed from satellite observations before and during covid-19". *Environmental Research Letters*, 16, 6. (2021), p. 064051. DOI: 10.1088/1748-9326/abf686.

Quaas, M. F.; Meya, J. N.; Schenk, H.; Bos, B.; Drupp, M. A., and Requate, T.: "The social cost of contacts: theory and evidence for the first wave of the covid-19 pandemic in germany". *PLOS ONE*, 16, 3. (2021), pp. 1–29. DOI: 10.1371/journal.pone.0248288.

Querol, X.; Alastuey, A.; Viana, M.; Moreno, T.; Reche, C.; Minguillón, M. C.; Ripoll, A.; Pandolfi, M.; Amato, F.; Karanasiou, A.; Pérez, N.; Pey, J.; Cusack, M.; Vázquez, R.; Plana, F.; Dall'Osto, M.; Rosa, J. de la; Campa, A. Sánchez de la; Fernández-Camacho, R.; Rodríguez, S.; Pio, C.; Alados-Arboledas, L.; Titos, G.; Artíñano, B.; Salvador, P.; García Dos Santos, S., and Fernández Patier, R.: "Variability of carbonaceous aerosols in remote, rural, urban and industrial environments in spain: implications for air quality policy". *Atmospheric Chemistry and Physics*, 13, 13. (2013), pp. 6185–6206. DOI: 10.5194/acp-13-6185-2013.

Quinn, P. K.; Thompson, E. J.; Coffman, D. J.; Baidar, S.; Bariteau, L.; Bates, T. S.; Bigorre, S. P.; Brewer, A.; Boer, G. de; Szoeke, S. P. de; Drushka, K.; Foltz, G. R.; Intrieri, J. M.; Iyer, S.; Fairall, C. W.; Gaston, C. J.; Jansen, F.; Johnson, J. E.; Krüger, O. O.; Marchbanks, R. D.; Moran, K.; Noone, D.; Pezoa, S.; Pincus, R.; Plueddemann, A. J.; Pöhlker, M. L.; Pöschl, U.; Melendez, E. Q.; Royer, H. M.; Szczodrak, M.; Thomson, J.; Upchurch, L. M.; Zhang, C.; Zhang, D., and Zuidema, P.: "Measurements from the rv ronald h. brown and related platforms as part of the atlantic tradewind ocean-atmosphere mesoscale interaction campaign (atomic)". *Earth System Science Data*. (Apr. 29, 2021). DOI: 10.5194/essd-13-1759-2021.

Ramanathan, V. and Carmichael, G.: "Global and regional climate changes due to black carbon". *Nature Geoscience*, 1, 4. (2008), pp. 221–227. DOI: 10.1038/ngeo156.

Ramanathan, V.; Crutzen, P. J.; Kiehl, J. T., and Rosenfeld, D.: "Aerosols, climate, and the hydrological cycle". *Science*, 294, 5549. (2001), pp. 2119–2124. DOI: 10.1126/science.1064034.

Rasch, P. J.; Crutzen, P. J., and Coleman, D. B.: "Exploring the geoengineering of climate using stratospheric sulfate aerosols: the role of particle size". *Geophysical Research Letters*, 35, 2. (2008). DOI: https://doi.org/10.1029/2007GL032179.

Read, W. G.; Froidevaux, L., and Waters, J. W.: "Microwave limb sounder measurement of stratospheric so2 from the mt. pinatubo volcano". *Geophysical Research Letters*, 20, 12. (1993), pp. 1299–1302. DOI: https://doi.org/10.1029/93GL00831.

Reddington, C. L.; McMeeking, G.; Mann, G. W.; Coe, H.; Frontoso, M. G.; Liu, D.; Flynn, M.; Spracklen, D. V., and Carslaw, K. S.: "The mass and number size distributions of black carbon aerosol over Europe". *Atmospheric Chemistry and Physics*, 13, 9. (2013), pp. 4917–4939. DOI: 10.5194/acp-13-4917-2013.

Reifenberg, S. F.; Martin, A.; Kohl, M.; Bacer, S.; Hamryszczak, Z.; Tadic, I.; Röder, L.; Crowley, D. J.; Fischer, H.; Kaiser, K.; Schneider, J.; Dörich, R.; Crowley, J. N.; Tomsche, L.; Marsing, A.; Voigt, C.; Zahn, A.; Pöhlker, C.; Holanda, B. A.; Krüger, O.; Pöschl, U.; Pöhlker, M.; Jöckel, P.; Dorf, M.; Schumann, U.; Williams, J.; Bohn, B.; Curtius, J.; Harder, H.; Schlager, H.; Lelieveld, J., and Pozzer, A.: "Numerical simulation of the impact of covid-19 lockdown on tropospheric composition and aerosol radiative forcing in europe". *Atmospheric Chemistry and Physics*, 22, 16. (2022), pp. 10901–10917. DOI: 10.5194/acp-22-10901-2022.

Reyes-Villegas, E.; Panda, U.; Darbyshire, E.; Cash, J. M.; Joshi, R.; Langford, B.; Di Marco, C. F.; Mullinger, N. J.; Alam, M. S.; Crilley, L. R.; Rooney, D. J.; Acton, W. J. F.; Drysdale, W.; Nemitz, E.; Flynn, M.; Voliotis, A.; McFiggans, G.; Coe, H.; Lee, J.; Hewitt, C. N.; Heal, M. R.; Gunthe, S. S.; Mandal, T. K.; Gurjar, B. R.; Shivani; Gadi, R.; Singh, S.; Soni, V., and Allan, J. D.: "Pm_1 composition and source apportionment at two sites in delhi, india, across multiple seasons". *Atmospheric Chemistry and Physics*, 21, 15. (2021), pp. 11655–11667. DOI: 10.5194/acp-21-11655-2021.

Roberts, G. C. and Nenes, A.: "A continuous-flow streamwise thermal-gradient CCN chamber for atmospheric measurements". *Aerosol Science and Technology*, 39, 3. (2005), pp. 206–221. DOI: 10.1080/027868290913988.

Robock, A.: "Volcanic eruptions and climate". *Reviews of Geophysics*, 38, 2. (2000), pp. 191–219. DOI: https://doi.org/10.1029/1998RG000054.

Rolph, G.; Stein, A., and Stunder, B.: "Real-time environmental applications and display system: ready". *Environmental Modelling and Software*, 95. (2017), pp. 210–228. DOI: https://doi.org/10.1016/j.envsoft.2017.06.025.

Rose, D.; Gunthe, S. S.; Mikhailov, E.; Frank, G. P.; Dusek, U.; Andreae, M. O., and Pöschl, U.: "Calibration and measurement uncertainties of a continuous-flow cloud condensation nuclei counter (DMT-CCNC): CCN activation of ammonium sulfate and sodium chloride aerosol particles in theory and experiment". *Atmospheric Chemistry and Physics*, 8, 5. (2008), pp. 1153–1179. DOI: 10.5194/acp-8-1153-2008.

Rosenfeld, D.; Andreae, M. O.; Asmi, A.; Chin, M.; Leeuw, G. de; Donovan, D. P.; Kahn, R.; Kinne, S.; Kivekas, N.; Kulmala, M.; Lau, W.; Schmidt, K. S.; Suni, T.; Wagner, T.; Wild, M., and Quaas, J.: "Global observations of aerosol-cloud-precipitation-climate interactions". *Reviews of Geophysics*, 52, 4. (2014), pp. 750–808. DOI: 10.1002/2013rg000441. URL: <GotoISI>://WOS:000348452000005.

Rosenfeld, D.; Lohmann, U.; Raga, G. B.; O'Dowd, C. D.; Kulmala, M.; Fuzzi, S.; Reissell, A., and Andreae, M. O.: "Flood or drought: how do aerosols affect precipitation?" *Science*, 321, 5894. (2008), pp. 1309–1313. DOI: 10.1126/science.1160606. URL: <GotoISI>://WOS:000258914300038.

Rosenfeld, D.: "Suppression of rain and snow by urban and industrial air pollution". *Science*, 287, 5459. (2000), pp. 1793–1796. DOI: 10.1126/science.287.5459.1793.

Rosenfeld, D.; Lohmann, U.; Raga, G. B.; O'Dowd, C. D.; Kulmala, M.; Fuzzi, S.; Reissell, A., and Andreae, M. O.: "Flood or drought: how do aerosols affect precipitation?" *Science*, 321, 5894. (2008), pp. 1309–1313. DOI: 10.1126/science.1160606.

Royer, H. M.; Pöhlker, M. L.; Krüger, O.; Blades, E.; Sealy, P.; Lata, N. N.; Cheng, Z.; China, S.; Ault, A. P.; Quinn, P. K.; Zuidema, P.; Pöhlker, C.; Pöschl, U.; Andreae, M., and Gaston, C. J.: "African smoke particles act as cloud condensation nuclei in the wintertime tropical north atlantic boundary layer over barbados". *Atmospheric Chemistry and Physics*, 23, 2. (2023), pp. 981–998. DOI: 10.5194/acp-23-981-2023.

S. Raj, S.; Krüger, O. O.; Sharma, A.; Panda, U.; Pöhlker, C.; Walter, D.; Förster, J.-D.; Singh, R. P.; S., S.; Klimach, T.; Darbyshire, E.; Martin, S. T.; McFiggans, G.; Coe, H.; Allan, J.; R., R.; Soni, V. K.; Su, H.; Andreae, M. O.; Pöschl, U.; Pöhlker, M. L., and Gunthe, S. S.: "Planetary boundary layer height modulates aerosol—water vapor interactions during winter in the megacity of delhi". *Journal of Geophysical Research: Atmospheres*, 126, 24. (2021). DOI: https://doi.org/10.1029/2021JD035681.

Samset, B. H. and Myhre, G.: "Climate response to externally mixed black carbon as a function of altitude". *Journal of Geophysical Research*, 120, 7. (2015), pp. 2913–2927. DOI: 10.1002/2014JD022849.

Samset, B. H.; Myhre, G.; Schulz, M.; Balkanski, Y.; Bauer, S.; Berntsen, T. K.; Bian, H.; Bellouin, N.; Diehl, T.; Easter, R. C.; Ghan, S. J.; Iversen, T.; Kinne, S.; Kirkevåg, A.; Lamarque, J.-F.; Lin, G.; Liu, X.; Penner, J. E.; Seland, Ø.; Skeie, R. B.; Stier, P.; Takemura, T.; Tsigaridis, K., and Zhang, K.: "Black carbon vertical profiles strongly affect its radiative forcing uncertainty". *Atmospheric Chemistry and Physics*, 13, 5. (2013), pp. 2423–2434. DOI: 10.5194/acp-13-2423-2013.

Samset, B. H.: "Aerosol absorption has an underappreciated role in historical precipitation change". *Communications Earth and Environment*, 3, 1. (2022), pp. 1–8. DOI: 10.1038/s43247-022-00576-6.

Sander, R.; Kerkweg, A.; Jöckel, P., and Lelieveld, J.: "Technical note: The new comprehensive atmospheric chemistry module MECCA". *Atmos. Chem. Phys.*, 5, 2. (2005), pp. 445–450. DOI: 10.5194/acp-5-445-2005.

Sander, R.; Baumgaertner, A.; Cabrera-Perez, D.; Frank, F.; Gromov, S.; Grooß, J.-U.; Harder, H.; Huijnen, V.; Jöckel, P.; Karydis, V. A.; Niemeyer, K. E.; Pozzer, A.; Riede, H.; Schultz, M. G.; Taraborrelli, D., and Tauer, S.: "The community atmospheric chemistry box model CAABA/MECCA-4.0". *Geosci. Model Dev.*, 12, 4. (2019), pp. 1365–1385. DOI: 10.5194/gmd-12-1365-2019.

Saturno, J.; Ditas, F.; Vries, M. Penning de; Holanda, B. A.; Pöhlker, M. L.; Carbone, S.; Walter, D.; Bobrowski, N.; Brito, J.; Chi, X.; Gutmann, A.; Angelis, I. Hrabe de; Machado, L. A. T.; Moran-Zuloaga, D.; Rüdiger, J.; Schneider, J.; Schulz, C.; Wang, Q.; Wendisch, M.; Artaxo, P.; Wagner, T.; Pöschl, U.; Andreae, M. O., and Pöhlker, C.: "African volcanic emissions influencing atmospheric aerosols over the amazon rain forest". *Atmospheric Chemistry and Physics*, 18, 14. (2018), pp. 10391–10405. DOI: 10.5194/acp-18-10391-2018.

Savoie, D. L.; Arimoto, R.; Keene, W. C.; Prospero, J. M.; Duce, R. A., and Galloway, J. N.: "Marine biogenic and anthropogenic contributions to non-sea-salt sulfate in the marine boundary layer over the north atlantic ocean". *Journal of Geophysical Research: Atmospheres*, 107, D18. (2002), AAC 3–1–AAC 3–21. DOI: https://doi.org/10.1029/2001JD000970.

Scheidel, A. and Work, C.: "Large-scale forest plantations for climate change mitigation? new frontiers of deforestation and land grabbing in cambodia". In: 2016.

Schill, G. P.; Froyd, K. D.; Bian, H.; Kupc, A.; Williamson, C.; Brock, C. A.; Ray, E.; Hornbrook, R. S.; Hills, A. J.; Apel, E. C.; Chin, M.; Colarco, P. R., and Murphy, D. M.: "Widespread biomass burning smoke throughout the remote troposphere". *Nature Geoscience*, 13. (2020), pp. 422–427. DOI: 10.1038/s41561-020-0586-1.

Schmale, J.; Schneider, J.; Jurkat, T.; Voigt, C.; Kalesse, H.; Rautenhaus, M.; Lichtenstern, M.; Schlager, H.; Ancellet, G.; Arnold, F.; Gerding, M.; Mattis, I.; Wendisch, M., and Borrmann, S.: "Aerosol layers from the 2008 eruptions of mount okmok and mount kasatochi: in situ upper troposphere and lower stratosphere measurements of sulfate and organics over europe". *Journal of Geophysical Research: Atmospheres*, 115, D2. (2010). DOI: https://doi.org/10.1029/2009JD013628.

Schmidt, A. and Black, B. A.: "Reckoning with the rocky relationship between eruption size and climate response: toward a volcano-climate index". *Annual Review of Earth and Planetary Sciences*, 50, 1. (2022), pp. 627–661. DOI: 10.1146/annurev-earth-080921-052816.

Schneider, J.; Weigel, R.; Klimach, T.; Dragoneas, A.; Appel, O.; Hünig, A.; Molleker, S.; Köllner, F.; Clemen, H.-C.; Eppers, O.; Hoppe, P.; Hoor, P.; Mahnke, C.; Krämer, M.; Rolf, C.; Grooß, J.-U.; Zahn, A.; Obersteiner, F.; Ravegnani, F.; Ulanovsky, A.; Schlager, H.; Scheibe, M.; Diskin, G. S.; DiGangi, J. P.; Nowak, J. B.; Zöger, M., and Borrmann, S.: "Aircraft-based observation of meteoric material in lower-stratospheric aerosol particles between 15 and 68 °n". *Atmospheric Chemistry and Physics*, 21, 2. (2021), pp. 989–1013. DOI: 10.5194/acp-21-989-2021.

Schulz, C.; Schneider, J.; Amorim Holanda, B.; Appel, O.; Costa, A.; Sá, S. S. de; Dreiling, V.; Fütterer, D.; Jurkat-Witschas, T.; Klimach, T.; Knote, C.; Krämer, M.; Martin, S. T.; Mertes, S.; Pöhlker, M. L.; Sauer, D.; Voigt, C.; Walser, A.; Weinzierl, B.; Ziereis, H.; Zöger, M.; Andreae, M. O.; Artaxo, P.; Machado, L. A. T.; Pöschl, U.; Wendisch, M., and Borrmann, S.: "Aircraft-based observations of isoprene-epoxydiol-derived secondary organic aerosol (iepox-soa) in the tropical upper tro-

posphere over the amazon region". *Atmospheric Chemistry and Physics*, 18, 20. (2018), pp. 14979–15001. DOI: 10.5194/acp-18-14979-2018.

Schumann, U.; Bugliaro, L.; Dörnbrack, A.; Baumann, R., and Voigt, C.: "Aviation contrail cirrus and radiative forcing over europe during 6 months of covid-19". *Geophysical Research Letters*, 48, 8. (2021). e2021GL092771 2021GL092771, e2021GL092771. DOI: https://doi.org/10.1029/2021GL092771.

Schumann, U.; Poll, I.; Teoh, R.; Koelle, R.; Spinielli, E.; Molloy, J.; Koudis, G. S.; Baumann, R.; Bugliaro, L.; Stettler, M., and Voigt, C.: "Air traffic and contrail changes over europe during covid-19: a model study". *Atmospheric Chemistry and Physics*, 21, 10. (2021), pp. 7429–7450. DOI: 10.5194/acp-21-7429-2021.

Schwarz, J. P.; Gao, R. S.; Fahey, D. W.; Thomson, D. S.; Watts, L. A.; Wilson, J. C.; Reeves, J. M.; Darbeheshti, M.; Baumgardner, D. G.; Kok, G. L.; Chung, S. H.; Schulz, M.; Hendricks, J.; Lauer, A.; Kärcher, B.; Slowik, J. G.; Rosenlof, K. H.; Thompson, T. L.; Langford, A. O.; Loewenstein, M., and Aikin, K. C.: "Single-particle measurements of midlatitude black carbon and light-scattering aerosols from the boundary layer to the lower stratosphere". *Journal of Geophysical Research Atmospheres*, 111, 16. (2006), pp. 1–15. DOI: 10.1029/2006JD007076.

Schwarz, J. P.; Gao, R. S.; Spackman, J. R.; Watts, L. A.; Thomson, D. S.; Fahey, D. W.; Ryerson, T. B.; Peischl, J.; Holloway, J. S.; Trainer, M.; Frost, G. J.; Baynard, T.; Lack, D. A.; Gouw, J. A. de; Warneke, C., and Del Negro, L. A.: "Measurement of the mixing state, mass, and optical size of individual black carbon particles in urban and biomass burning emissions". *Geophysical Research Letters*, 35, 13. (2008), pp. 1–5. DOI: 10.1029/2008GL033968.

Schwarz, J. P.; Weinzierl, B.; Samset, B. H.; Dollner, M.; Heimerl, K.; Markovic, M. Z.; Perring, A. E., and Ziemba, L.: "Aircraft measurements of black carbon vertical profiles show upper tropospheric variability and stability". *Geophysical Research Letters*, 44, 2. (2017), pp. 1132–1140. DOI: https://doi.org/10.1002/2016GL071241.

Sedlacek, A. J. I.; Lewis, E. R.; Onasch, T. B.; Zuidema, P.; Redemann, J.; Jaffe, D., and Kleinman, L. I.: "Using the black carbon particle mixing state to characterize the lifecycle of biomass burning aerosols". *Environmental Science & Technology*, 56, 20. (2022), pp. 14315–14325. DOI: 10.1021/acs.est.2c03851.

Seinfeld, J. H. and Pandis, S. N.: *Atmospheric Chemistry and Physics: From Air Pollution to Climate Change*. John Wiley & Sons, Inc., 2006, p. 1232. ISBN: 9780471720188. DOI: 10.1063/1.882420.

Senande-Rivera, M.; Insua-Costa, D., and Miguez-Macho, G.: "Spatial and temporal expansion of global wildland fire activity in response to climate change". *Nature Communications*, 13, 1. (2022), pp. 1–9. DOI: 10.1038/s41467-022-28835-2.

Shi, Z.; Song, C.; Liu, B.; Lu, G.; Xu, J.; Van Vu, T.; Elliott, R. J.; Li, W.; Bloss, W. J., and Harrison, R. M.: "Abrupt but smaller than expected changes in surface air quality attributable to COVID-19 lockdowns". *Science Advances*, 7, 3. (2021). DOI: 10.1126/sciadv.abd6696.

Singh, V.; Ravindra, K.; Sahu, L., and Sokhi, R.: "Trends of atmospheric black carbon concentration over the united kingdom". *Atmospheric Environment*, 178. (2018), pp. 148–157. DOI: https://doi.org/10.1016/j.atmosenv.2018.01.030.

Squires, P.: “The microstructure and colloidal stability of warm clouds”. *Tellus*, 10, 2. (1958), pp. 256–261. DOI: https://doi.org/10.1111/j.2153-3490.1958.tb02011.x.

Steffen, W.; Grinevald, J.; Crutzen, P., and McNeill, J.: “The anthropocene: conceptual and historical perspectives”. *Philosophical Transactions of the Royal Society A: Mathematical, Physical and Engineering Sciences*, 369, 1938. (2011), pp. 842–867. DOI: 10.1098/rsta.2010.0327.

Stein, A. F.; Draxler, R. R.; Rolph, G. D.; Stunder, B. J. B.; Cohen, M. D., and Ngan, F.: “NOAA’s HYSPLIT Atmospheric Transport and Dispersion Modeling System”. *Bulletin of the American Meteorological Society*, 96, 12. (2015), pp. 2059–2077. DOI: 10.1175/BAMS-D-14-00110.1.

Stenchikov, G. L.; Kirchner, I.; Robock, A.; Graf, H.-F.; Antuña, J. C.; Grainger, R. G.; Lambert, A., and Thomason, L.: “Radiative forcing from the 1991 mount pinatubo volcanic eruption”. *Journal of Geophysical Research: Atmospheres*, 103, D12. (1998), pp. 13837–13857. DOI: https://doi.org/10.1029/98JD00693.

Stephens, M.; Turner, N., and Sandberg, J.: “Particle identification by laser-induced incandescence in a solid-state laser cavity.” *Applied optics*, 42, 19. (2003), pp. 3726–36. DOI: 10.1364/AO.42.003726.

Stevens, B.; Farrell, D.; Hirsch, L.; Jansen, F.; Nuijens, L.; Serikov, I.; Brügmann, B.; Forde, M.; Linne, H.; Lonitz, K., and Prospero, J. M.: “The barbados cloud observatory: anchoring investigations of clouds and circulation on the edge of the itcz”. *Bulletin of the American Meteorological Society*, 97, 5. (2016), pp. 787 –801. DOI: 10.1175/BAMS-D-14-00247.1.

Stevens, B. and Feingold, G.: “Untangling aerosol effects on clouds and precipitation in a buffered system”. *Nature*, 461, 7264. (2009), pp. 607–613. DOI: 10.1038/nature08281.

Stevens, B.; Giorgetta, M.; Esch, M.; Mauritsen, T.; Crueger, T.; Rast, S.; Salzmann, M.; Schmidt, H.; Bader, J.; Block, K.; Brokopf, R.; Fast, I.; Kinne, S.; Kornblueh, L.; Lohmann, U.; Pincus, R.; Reichler, T., and Roeckner, E.: “Atmospheric component of the mpi-m earth system model: echam6”. *Journal of Advances in Modeling Earth Systems*, 5, 2. (2013), pp. 146–172. DOI: https://doi.org/10.1002/jame.20015.

Stevens, B. et al.: “Eurec 4 a”. *Earth System Science Data*. (Aug. 25, 2021). DOI: 10.5194/essd-13-4067-2021.

Stier, P.; Feichter, J.; Kinne, S.; Kloster, S.; Vignati, E.; Wilson, J.; Ganzeveld, L.; Tegen, I.; Werner, M.; Balkanski, Y.; Schulz, M.; Boucher, O.; Minikin, A., and Petzold, A.: “The aerosol-climate model ECHAM5-HAM”. *Atmos. Chem. Phys.*, 5. (2005), pp. 1125–1156. DOI: 10.5194/acp-5-1125-2005.

Stjern, C. W.; Samset, B. H.; Myhre, G.; Forster, P. M.; Hodnebrog, Andrews, T.; Boucher, O.; Faluvegi, G.; Iversen, T.; Kasoar, M.; Kharin, V.; Kirkevåg, A.; Lamarque, J.-F.; Olivié, D.; Richardson, T.; Shawki, D.; Shindell, D.; Smith, C. J.; Takemura, T., and Voulgarakis, A.: “Rapid adjustments cause weak surface temperature response to increased black carbon concentrations”. *Journal of Geophysical Research: Atmospheres*, 122, 21. (2017), pp. 11,462–11,481. DOI: https://doi.org/10.1002/2017JD027326.

Szopa, S.; Naik, V.; Adhikary, B.; Artaxo, P.; Berntsen, T.; Collins, W.; Fuzzi, S.; Gallardo, L.; Kiendler-Scharr, A.; Klimont, Z.; Liao, H.; Unger, N., and Zanis, P.: "Short-lived climate forcers". In: *Climate Change 2021: The Physical Science Basis. Contribution of Working Group I to the Sixth Assessment Report of the Intergovernmental Panel on Climate Change*. Ed. by V. Masson-Delmotte; P. Zhai; A. Pirani; S. Connors; C. Péan; S. Berger; N. Caud; Y. Chen; L. Goldfarb; M. Gomis; M. Huang; K. Leitzell; E. Lonnoy; J. Matthews; T. Maycock; T. Waterfield; O. Yelekçi; R. Yu, and B. Zhou. Cambridge, United Kingdom and New York, NY, USA: Cambridge University Press, 2021, 817–922. DOI: 10.1017/9781009157896.008.

Tadic, I.; Nussbaumer, C.; Bohn, B.; Harder, H.; Marno, D.; Martinez, M.; Obersteiner, F.; Parchatka, U.; Pozzer, A.; Rohloff, R.; Zöger, M.; Lelieveld, J., and Fischer, H.: "Central role of nitric oxide in ozone production in the upper tropical troposphere over the atlantic ocean and west africa". *Atmospheric Chemistry and Physics Discussions*, 2021. (2021), pp. 1–24. DOI: 10.5194/acp-2021-52.

Tegen, I.; Neubauer, D.; Ferrachat, S.; Siegenthaler-Le Drian, C.; Bey, I.; Schutgens, N.; Stier, P.; Watson-Parris, D.; Stanelle, T.; Schmidt, H.; Rast, S.; Kokkola, H.; Schultz, M.; Schroeder, S.; Daskalakis, N.; Barthel, S.; Heinold, B., and Lohmann, U.: "The global aerosol–climate model echam6.3–ham2.3 – part 1: aerosol evaluation". *Geoscientific Model Development*, 12, 4. (2019), pp. 1643–1677. DOI: 10.5194/gmd-12-1643-2019.

Thomson, M. and Mitra, T.: "A radical approach to soot formation". *Science*, 361, 6406. (2018), pp. 978–979. DOI: 10.1126/science.aau5941.

Thornhill, G. D.; Collins, W. J.; Kramer, R. J.; Olivié, D.; Skeie, R. B.; O'Connor, F. M.; Abraham, N. L.; Checa-Garcia, R.; Bauer, S. E.; Deushi, M.; Emmons, L. K.; Forster, P. M.; Horowitz, L. W.; Johnson, B.; Keeble, J.; Lamarque, J.-F.; Michou, M.; Mills, M. J.; Mulcahy, J. P.; Myhre, G.; Nabat, P.; Naik, V.; Oshima, N.; Schulz, M.; Smith, C. J.; Takemura, T.; Tilmes, S.; Wu, T.; Zeng, G., and Zhang, J.: "Effective radiative forcing from emissions of reactive gases and aerosols – a multi-model comparison". *Atmospheric Chemistry and Physics*, 21, 2. (2021), pp. 853–874. DOI: 10.5194/acp-21-853-2021.

Tomsche, L.; Marsing, A.; Jurkat-Witschas, T.; Lucke, J.; Kaufmann, S.; Kaiser, K.; Schneider, J.; Scheibe, M.; Schlager, H.; Röder, L.; Fischer, H.; Obersteiner, F.; Zahn, A.; Zöger, M.; Lelieveld, J., and Voigt, C.: "Enhanced sulfur in the upper troposphere and lower stratosphere in spring 2020". *Atmospheric Chemistry and Physics*, 22, 22. (2022), pp. 15135–15151. DOI: 10.5194/acp-22-15135-2022.

Trenberth, K. E.: "Changes in precipitation with climate change". *Climate Research*, 47, 1-2. (2011), pp. 123–138. DOI: 10.3354/cr00953.

Tsimpidi, A. P.; Karydis, V. A.; Pozzer, A.; Pandis, S. N., and Lelieveld, J.: "ORACLE (v1.0): module to simulate the organic aerosol composition and evolution in the atmosphere". *Geosci. Model Dev.*, 7, 6. (2014), pp. 3153–3172. DOI: 10.5194/gmd-7-3153-2014.

Tsimpidi, A. P.; Karydis, V. A.; Pozzer, A.; Pandis, S. N., and Lelieveld, J.: "ORACLE 2-D (v2.0): an efficient module to compute the volatility and oxygen content of organic aerosol with a global chemistry–climate model". *Geosci. Model Dev.*, 11, 8. (2018), pp. 3369–3389. DOI: 10.5194/gmd-11-3369-2018.

Twomey, S.: “Pollution and the planetary albedo”. *Atmospheric Environment (1967)*, 8, 12. (1974), pp. 1251–1256. DOI: https://doi.org/10.1016/0004-6981(74)90004-3.

Twomey, S.: “The influence of pollution on the shortwave albedo of clouds”. *Journal of Atmospheric Sciences*, 34, 7. (1977), pp. 1149 –1152. DOI: 10.1175/1520-0469(1977)034<1149:TIOPOT>2.0.CO;2.

Vadrevu, K. P.; Lasko, K.; Giglio, L.; Schroeder, W.; Biswas, S., and Justice, C.: “Trends in Vegetation fires in South and Southeast Asian Countries”. *Scientific Reports*, 9, 1. (2019), pp. 1–13. DOI: 10.1038/s41598-019-43940-x.

Venter, Z. S.; Aunan, K.; Chowdhury, S., and Lelieveld, J.: “Covid-19 lockdowns cause global air pollution declines”. *Proceedings of the National Academy of Sciences*, 117, 32. (2020), pp. 18984–18990. DOI: 10.1073/pnas.2006853117.

Vernier, J.-P.; Kalnajs, L.; Diaz, J. A.; Reese, T.; Corrales, E.; Alan, A.; Vernier, H.; Holland, L.; Patel, A.; Rastogi, N.; Wienhold, F.; Carn, S.; Krotkov, N., and Murray, J.: “Volkilau: volcano rapid response balloon campaign during the 2018 kilauea eruption”. *Bulletin of the American Meteorological Society*, 101, 10. (2020), E1602 –E1618. DOI: 10.1175/BAMS-D-19-0011.1.

Vignati, E.; Berkowicz, R.; Palmgren, F.; Lyck, E., and Hummelshøj, P.: “Transformation of size distributions of emitted particles in streets”. *Science of The Total Environment*, 235, 1. (1999), pp. 37–49. DOI: https://doi.org/10.1016/S0048-9697(99)00188-6.

Visioni, D.; MacMartin, D. G.; Kravitz, B.; Tilmes, S.; Mills, M. J.; Richter, J. H., and Boudreau, M. P.: “Seasonal injection strategies for stratospheric aerosol geoengineering”. *Geophysical Research Letters*, 46, 13. (2019), pp. 7790–7799. DOI: https://doi.org/10.1029/2019GL083680.

Voigt, C.; Lelieveld, J.; Schlager, H.; Schneider, J.; Curtius, J.; Meerkötter, R.; Sauer, D.; Bugliaro, L.; Bohn, B.; Crowley, J. N.; Erbertseder, T.; Groß, S.; Hahn, V.; Li, Q.; Mertens, M.; Pöhlker, M. L.; Pozzer, A.; Schumann, U.; Tomsche, L.; Williams, J.; Zahn, A.; Andreae, M.; Borrmann, S.; Bräuer, T.; Dörich, R.; Dörnbrack, A.; Edtbauer, A.; Ernle, L.; Fischer, H.; Giez, A.; Granzin, M.; Grewe, V.; Harder, H.; Heinritzi, M.; Holanda, B. A.; Jöckel, P.; Kaiser, K.; Krüger, O. O.; Lucke, J.; Marsing, A.; Martin, A.; Matthes, S.; Pöhlker, C.; Pöschl, U.; Reifenberg, S.; Ringsdorf, A.; Scheibe, M.; Tadic, I.; Zauner-Wieczorek, M.; Henke, R., and Rapp, M.: “Cleaner skies during the COVID-19 lockdown”. *Bulletin of the American Meteorological Society*, 3. (2022), pp. 1–57. DOI: 10.1175/bams-d-21-0012.1.

Wang, R.; Andrews, E.; Balkanski, Y.; Boucher, O.; Myhre, G.; Samset, B. H.; Schulz, M.; Schuster, G. L.; Valari, M., and Tao, S.: “Spatial representativeness error in the ground-level observation networks for black carbon radiation absorption”. *Geophysical Research Letters*, 45, 4. (2018), pp. 2106–2114. DOI: https://doi.org/10.1002/2017GL076817.

Wendisch, M. et al.: “Atmospheric and surface processes, and feedback mechanisms determining arctic amplification: a review of first results and prospects of the (ac)3 project”. *Bulletin of the American Meteorological Society*, 104, 1. (2023), E208 –E242. DOI: 10.1175/BAMS-D-21-0218.1.

Wendisch, M.; Poschl, U.; Andreae, M. O.; MacHado, L. A.; Albrecht, R.; Schlager, H.; Rosenfeld, D.; Martin, S. T.; Abdelmonem, A.; Afchine, A.; Araujo, A. C.; Artaxo, P.; Aufmhoff, H.; Barbosa, H. M.; Borrmann, S.; Braga, R.; Buchholz, B.; Cecchini, M. A.; Costa, A.; Curtius, J.; Dollner, M.; Dorf, M.; Dreiling, V.; Ebert, V.; Ehrlich, A.; Ewald, F.; Fisch, G.; Fix, A.; Frank, F.; Futterer, D.; Heckl, C.; Heidelberg, F.; Huneke, T.; Jakel, E.; Jarvinen, E.; Jurkat, T.; Kanter, S.; Kastner, U.; Kenntner, M.; Kesselmeier, J.; Klimach, T.; Knecht, M.; Kohl, R.; Kolling, T.; Kramer, M.; Kruger, M.; Krisna, T. C.; Lavric, J. V.; Longo, K.; Mahnke, C.; Manzi, A. O.; Mayer, B.; Mertes, S.; Minikin, A.; Molleker, S.; Munch, S.; Nillius, B.; Pfeilsticker, K.; Pohlker, C.; Roiger, A.; Rose, D.; Rosenow, D.; Sauer, D.; Schnaiter, M.; Schneider, J.; Schulz, C.; De Souza, R. A.; Spanu, A.; Stock, P.; Vila, D.; Voigt, C.; Walser, A.; Walter, D.; Weigel, R.; Weinzierl, B.; Werner, F.; Yamasoe, M. A.; Ziereis, H.; Zinner, T., and Zoger, M.: "Acridicon-chuva campaign: Studying tropical deep convective clouds and precipitation over amazonia using the New German research aircraft HALO". *Bulletin of the American Meteorological Society*, 97, 10. (2016), pp. 1885–1908. DOI: 10.1175/BAMS-D-14-00255.1.

Wex, H.; Dieckmann, K.; Roberts, G. C.; Conrath, T.; Izaguirre, M. A.; Hartmann, S.; Herenz, P.; Schäfer, M.; Ditas, F.; Schmeissner, T.; Henning, S.; Wehner, B.; Siebert, H., and Stratmann, F.: "Aerosol arriving on the caribbean island of barbados: physical properties and origin". *Atmospheric Chemistry and Physics*, 16, 22. (2016), pp. 14107–14130. DOI: 10.5194/acp-16-14107-2016.

Wiedensohler, A.: "An approximation of the bipolar charge distribution for particles in the submicron size range". *Journal of Aerosol Science*, 19, 3. (1988), pp. 387–389. DOI: https://doi.org/10.1016/0021-8502(88)90278-9.

Wiesner, A.; Pfeifer, S.; Merkel, M.; Tuch, T.; Weinhold, K., and Wiedensohler, A.: "Real world vehicle emission factors for black carbon derived from longterm in-situ measurements and inverse modelling". *Atmosphere*, 12, 1. (2021), pp. 1–19. DOI: 10.3390/atmos12010031.

Williamson, C. J.; Kupc, A.; Axisa, D.; Bilsback, K. R.; Bui, T. P.; Campuzano-Jost, P.; Dollner, M.; Froyd, K. D.; Hodshire, A. L.; Jimenez, J. L.; Kodros, J. K.; Luo, G.; Murphy, D. M.; Nault, B. A.; Ray, E. A.; Weinzierl, B.; Wilson, J. C.; Yu, F.; Yu, P.; Pierce, J. R., and Brock, C. A.: "A large source of cloud condensation nuclei from new particle formation in the tropics". *Nature*, 574, 7778. (2019), pp. 399–403. DOI: 10.1038/s41586-019-1638-9.

Wilson, J. C.; Jonsson, H. H.; Brock, C. A.; Toohey, D. W.; Avallone, L. M.; Baumgardner, D.; Dye, J. E.; Poole, L. R.; Woods, D. C.; DeCoursey, R. J.; Osborn, M.; Pitts, M. C.; Kelly, K. K.; Chan, K. R.; Ferry, G. V.; Loewenstein, M.; Podolske, J. R., and Weaver, A.: "In situ observations of aerosol and chlorine monoxide after the 1991 eruption of mount pinatubo: effect of reactions on sulfate aerosol". *Science*, 261, 5125. (1993), pp. 1140–1143. DOI: 10.1126/science.261.5125.1140.

Wren, S. N.; Liggio, J.; Han, Y.; Hayden, K.; Lu, G.; Mihele, C. M.; Mittermeier, R. L.; Stroud, C.; Wentzell, J. J., and Brook, J. R.: "Elucidating real-world vehicle emission factors from mobile measurements over a large metropolitan region: A focus on isocyanic acid, hydrogen cyanide, and black carbon". *Atmospheric Chemistry and Physics*, 18, 23. (2018), pp. 16979–17001. DOI: 10.5194/acp-18-16979-2018.

Wu, H.; Taylor, J. W.; Langridge, J. M.; Yu, C.; Allan, J. D.; Szpek, K.; Cotterell, M. I.; Williams, P. I.; Flynn, M.; Barker, P.; Fox, C.; Allen, G.; Lee, J., and Coe, H.: "Rapid transformation of ambient absorbing aerosols from west african biomass burning". *Atmospheric Chemistry and Physics*, 21, 12. (2021), pp. 9417–9440. DOI: 10.5194/acp-21-9417-2021.

Wu, H.; Taylor, J. W.; Szpek, K.; Langridge, J. M.; Williams, P. I.; Flynn, M.; Allan, J. D.; Abel, S. J.; Pitt, J.; Cotterell, M. I.; Fox, C.; Davies, N. W.; Haywood, J., and Coe, H.: "Vertical variability of the properties of highly aged biomass burning aerosol transported over the southeast Atlantic during CLARIFY-2017". *Atmospheric Chemistry and Physics*, 20, 21. (2020), pp. 12697–12719. DOI: 10.5194/acp-20-12697-2020.

Yuan, J.; Modini, R. L.; Zanatta, M.; Herber, A. B.; Müller, T.; Wehner, B.; Poulain, L.; Tuch, T.; Baltensperger, U., and Gysel-Beer, M.: "Variability in the mass absorption cross section of black carbon (BC) aerosols is driven by BC internal mixing state at a central European background site (Melpitz, Germany) in winter". *Atmospheric Chemistry and Physics*, 21, 2. (2021), pp. 635–655. DOI: 10.5194/acp-21-635-2021.

Zahn, A.; Weppner, J.; Widmann, H.; Schlote-Holubek, K.; Burger, B.; Kühner, T., and Franke, H.: "A fast and precise chemiluminescence ozone detector for eddy flux and airborne application". *Atmospheric Measurement Techniques*, 5, 2. (2012), pp. 363–375. DOI: 10.5194/amt-5-363-2012.

Zauner-Wieczorek, M.; Heinritzi, M.; Granzin, M.; Keber, T.; Kürten, A.; Kaiser, K.; Schneider, J., and Curtius, J.: "Mass spectrometric measurements of ambient ions and estimation of gaseous sulfuric acid in the free troposphere and lowermost stratosphere during the cafe-eu/bluesky campaign". *Atmospheric Chemistry and Physics*, 22, 17. (2022), pp. 11781–11794. DOI: 10.5194/acp-22-11781-2022.

Zhang, K.; O'Donnell, D.; Kazil, J.; Stier, P.; Kinne, S.; Lohmann, U.; Ferrachat, S.; Croft, B.; Quaas, J.; Wan, H.; Rast, S., and Feichter, J.: "The global aerosol-climate model ECHAM-HAM, version 2: sensitivity to improvements in process representations". *Atmos. Chem. Phys.*, 12, 19. (2012), pp. 8911–8949. DOI: 10.5194/acp-12-8911-2012.

Zhang, Y.; Fan, J.; Logan, T.; Li, Z., and Homeyer, C. R.: "Wildfire impact on environmental thermodynamics and severe convective storms". *Geophysical Research Letters*, 46, 16. (2019), pp. 10082–10093. DOI: https://doi.org/10.1029/2019GL084534.

Zhu, Y.; Toon, O. B.; Jensen, E. J.; Bardeen, C. G.; Mills, M. J.; Tolbert, M. A.; Yu, P., and Woods, S.: "Persisting volcanic ash particles impact stratospheric SO2 lifetime and aerosol optical properties". *Nature Communications*, 11, 1. (2020), pp. 1–11. DOI: 10.1038/s41467-020-18352-5.

Zieger, P.; Vaisanen, O.; Corbin, J. C.; Partridge, D. G.; Bastelberger, S.; Mousavi-Fard, M.; Rosati, B.; Gysel, M.; Krieger, U. K.; Leck, C.; Nenes, A.; Riipinen, I.; Virtanen, A., and Salter, M. E.: "Revising the hygroscopicity of inorganic sea salt particles". *Nature Communications*, 8. (2017). DOI: 10.1038/ncomms15883.

Zimmermann, P. H.; Brenninkmeijer, C. A. M.; Pozzer, A.; Jöckel, P.; Winterstein, F.; Zahn, A.; Houweling, S., and Lelieveld, J.: "Model simulations of atmospheric methane (1997–2016) and their evaluation using NOAA and AGAGE surface and IAGOS-CARIBIC aircraft observations". *Atmos Chem Phys*, 20, 9. (2020), pp. 5787–5809. DOI: 10.5194/acp-20-5787-2020.

Zuberi, B.; Johnson, K. S.; Aleks, G. K.; Molina, L. T.; Molina, M. J., and Laskin, A.: "Hydrophilic properties of aged soot". *Geophysical Research Letters*, 32, 1. (2005). DOI: https://doi.org/10.1029/2004GL021496.

Abbreviations and Acronyms

Aerosol-Cloud Interactions	ACI
Aerosol-Radiation Interactions	ARI
Aerosol Optical Density	AOD
ACRIDICON-CHUVA	AC
Stratospheric Aerosol Optical Density	SAOD
Aerosol Optical Thickness	AOT
Amazon Tall Tower Observatory	ATTO
Backward Trajectory	BT
Barbados Aerosol and Chemistry Observatory	BACO
Biomass Burning	BB
Black Carbon	BC
Refractory Black Carbon	rBC
Equivalent Black Carbon	BCe
Brown Carbon	BrC
CAFE Africa	CA
CAFE Europe and BLUESKY	CE
Cloud Condensation Nuclei	CCN
Cloud Condensation Nuclei Counter	CCNC
Condensation Particle Counter	CPC
Compact Time-of-Flight Aerosol Mass Spectrometer	C-ToF-AMS
Coordinated Universal Time	UTC
EMeRGe Asia	EA
EMeRGe Europe	EM
ECHAM6.3–HAM2.3	ECHAM–HAM
ECHAM/MESSy Atmopheric Chemistry	EMAC
Fire Radiative Power	FRP
High Altitude and Long Range	HALO
Long-Range Transport	LRT
Marine Boundary Layer	MBL
Moderate Resolution Imaging Spectroradiometer	MODIS
Optical Particle Counter	OPC
Planetary Boundary Layer	PBL
Polycyclic Aromatic Hydrocarbon	PAH
Single Particle Soot Photometer	SP2
Single Scattering Albedo	SSA
Spinning Enhanced Visible and InfraRed Imager	SEVIRI
Standard Temperature and Pressure	STP (273.15 K,1013.25 hPa)
Tropical Tropopause Layer	TTL
Intergovernmental Panel on Climate Change	IPCC

Declaration of primary authorship

I, Ovid Oktavian Krüger hereby declare that I prepared this dissertation without inadmissible aid and only by the usage of the specified sources. I also declare that I marked the directly or indirectly adopted ideas from external references. Furthermore, I confirm that this dissertation is entirely the result or my own investigations except where otherwise indicated. In particular, I assure that I did not use the assistance of a doctoral consultant. I guarantee that no one has gained pecuniary advantages related to the content of this dissertation from me or from other persons on behalf of me.

I assure that this dissertation was not submitted in an identical or similar design to another examination office for the purpose of a graduation or another examination procedure. I also state that I have not been involved in another PhD procedure.

Mainz, 30.05.2023, Ovid Oktavian Krüger

Acknowledgements

I want to express my appreciation for being a part of the Max Planck Institute for Chemistry, where I have had a wonderful time and the chance to interact with and learn from some of the most talented scientists. Special thanks to my supervisors, Mira Pöhlker and Ulrich Pöschl, for giving me the opportunity to be a researcher at the MPIC and for facilitating all the exciting field campaigns. Thank you for your enthusiasm and curiosity, and for giving me the freedom to do amazing research in my own way.

For the support and the great scientific exchange I would like to thank my PhD supervisor Johannes Quaas at the University of Leipzig and his group. Especially Marc Salzmann, who provided valuable model data for my analysis.

Thanks to David Walter, who helped me a lot with my data management during these years, for sharing your brilliant Igor tools and for fixing my codes. Also all our bike rides enriched my PhD time.

This work would not have been possible without the technical support of Thomas Klimach, many thanks for all the help with the instruments, the data processing and the campaigns. We also had a lot of fun with our kicker competitions.

I would also like to thank Andrea Pozzer and his team for the great support of my research with EMAC and ERA5 results and great discussions.

I would like to thank my current and former office colleagues Leslie Kremper, Maria Prass, Florian Ditas and Luiz Merchardo for the great scientific and personal exchange. It was a great time.

My sincere thanks to both Pölker groups and Anna Lena Leifke for the daily support and cooperation, but even more for all the coffee and fun. Special thanks to Jan David for the LATEX support while writing this dissertation.

To all the MPIC staff who make our lives so much easier, Martina Peissker, Sarah Alznauer, Mark Lammeck and the other colleges in the electronics department, graphics office and mechanical workshop.

It was a great pleasure and honor to have the chance to meet such diligent and pleasant people all over the world during the EMeRGe's, CAFE's, EUREC^{4}A, CIRRUS, ATTO and BLUESKY campaigns as well as during all the lab experiments in Mainz. Special thanks to Celine and the Dududu crew, the team from the University of Bremen, especially to Lola and John, the Harder's, Fischer's, Schneider's and Williams' groups. It was also always a pleasure to work with such friendly and motivated people at DLR and ENVISCOPE, special thanks to Tommy Leder, Thomas Sprünken, Daniel Sauer, Helmut Ziereis, Frank Probst, Rolf Maser, Nicole Brehm and Dieter Schell.

Without the support of my family I would never have been where I am now, so for that and all the love and great experiences I thank you!

Last but not least I would like to thank my wife for her support and motivation, but also for all the great campaigns and research we could do together.